Investigating the potential of Photodynamic and Sonodynamic Therapy for the treatment of pancreatic cancer

Yingjie Sheng BSc(Hons)

Faculty of life and Health Sciences

Ulster University

Thesis submitted for the degree of

Doctor of Philosophy

February 2018

I confirm that the word count of this thesis is less than 100,000 words

Declaration

I hereby declare that with effect from the date on which the thesis is deposited in Ulster University Doctoral College, I permit

1. The Librarian of the University to allow the thesis to be copied in whole or in part without reference to me on the understanding that such authority applies to the provision of single copies made for study purposes or for inclusion within the stock of another library.

2. The thesis to be made available through the Ulster Institutional Repository and/or EThOS under the terms of the Ulster eTheses Deposit Agreement which I have signed.

IT IS A CONDITION OF USE OF THIS THESIS THAT ANYONE WHO CONSULTS IT MUST RECOGNISE THAT THE COPYRIGHT RESTS WITH THE AUTHOR AND THAT NO QUOTATION FROM THE THESIS AND NO INFORMATION DERIVED FROM IT MAY BE PUBLISHED UNLESS THE SOURCE IS PROPERLY ACKNOWLEDGED.

I declare that this thesis and the work presented in it are my own and have been generated by me as the result of my own original research, with the exception of the chemical synthesis of the biotinylated drugs which was performed by Dr Sukanta Kamila and animal surgery which was performed by Dr Heather Nesbitt. Magnetic field calculations were preformed by Prof Eleaner Stride at the University of Oxford. Analysis of histology sctions were performed by Dr Paul Kelly and Dr Declan O'Rourke at the Royal Victoria Hospital.

Acknowledgements

First and foremost, I would like to thank Prof John Callan for his constant support through this process and for providing me with the opportunity to pursue this line of research. My thanks also go out to my second supervisor, Prof Anthony Mchale, whose conversations and discussions definitely led to a few novel approaches to the project.

I would also like to acknowledge members of the Callan research group, both past and present, for helping make the process much more enjoyable. I would also like to acknowledge members of the Stride research group from Institute of Biomedical Engineering, University of Oxford including Estelle Beguin, Joshua Owen, Lester C. Barnsley and Eleanor Stride for incorporation work on joint project of magnetic responsive microbubbles and generously supplying Magnetic nanoparticles. I would like to acknowledge Dr Paul Kelly and Dr Declan O'Rourke from Imaging Centre of The Royal Victoria Hospital for all the help in histology scoring of liver and renal pathology. I would like to thank Dr Colin Fowley, Dr Barry Hyland, Dr Graham Hamiltion, Dr Jordan Atchison and Dr David Costley for offering guidance and assistance when required. I would also like to thank Dr Heather Nesbitt for all the help in animal surgeries and nice conversations during the animal experiments. I would like to thank Dr Chris O'Kane, Mr Dean Nicholas, Mr Keiran Logan, Mr Thomas Mckaig, Mr Jinhui Gao and Mr Conor McEwan for their moral support and good humour which helped make the past three years even more enjoyable. I would like to thank Dr Sukanta Kamila, who's never ending patience was admireable even when I had made troubles, for his help with all things in chemical synthesis and proton NMR. I would also like to thank members of the wider research group, including Ms Noorjahan Aibani and Ms Sian Farrell. I wish you all the very best in your future.

Finally, I would like to thank my family for all their support over the last 3 years. My parents Aimin and Jun, who were experts in their own fields as a professor and a nurse, supported me through it and encouraged me to pursue this career in science. Last but not the least I would like to acknowledge my wife Niky Tsz Ki Cheung and my daughter Eevee whose support was greatly appreciated and allowed me to keep my sanity through the process.

Summary

Pancreatic cancer has the lowest survival rate among the 21 most common forms of cancer with only 5 % of patients surviving five years after their initial diagnosis. Several studies have investigated the potential of neo-adjuvant chemo- and / or radiotherapy to downstage tumours and increase the number of patients eligible for resection. Unfortunately, such treatments are often associated with significant off-target effects due to the non-specific nature of the chemotherapy regimen. Therefore, the development of targeted treatments that reduce side-effects related to systemic chemotherapy have enormous potential as neo-adjuvant and palliative pancreatic cancer treatments by reducing tumour burden to either enable surgery or to provide symptom relief.

Photodynamic therapy (PDT) is a clinically approved anti-cancer treatment that involves the activation of an otherwise inactive sensitisier drug with light, which in the presence of molecular oxygen, generates cytotoxic reactive oxygen species (ROS). In contrast, Sonodynamic therapy (SDT) is an emerging anti-cancer treatment that involves the activation of an otherwise inactive sensitiser drug using low-intensity ultrasound (US). The combination of sensitiser and ultrasound, in the presence of molecular oxygen, generates cytotoxic levels of ROS causing cell death via oxidative stress. As oxygen is a key requirement for the generation of ROS in PDT or SDT and given the fact that hypoxia is a characteristic of most solid cancerous tumours, treating hypoxic tumours using PDT or SDT can be a challenge. Therefore, an area of interest in this thesis was to investigate new methods for enhancing PDT and SDT efficacy in hypoxic tumors.

Chapter 1 provided a background to current cancer treatments, PDT, SDT, improvement of tumor oxygenation and drug delivery systems while **Chapter 2** detailed the materials and methods utilised in subsequent results chapters. The first results chapter, **Chapter 3** investigated whether combined SDT / gemcitabine treatment, using intravenously delivered oxygen carrying lipid stabilised microbubbles (MBs) as delivery vehicle, can provide a significant reduction in the volume of Mia-PaCa-2 tumours compared to SDT or gemcitabine treatment alone and evaluate potential toxic effects in healthy non-tumour bearing mice. It was observed that the combination of US with the Rose Bengal, Gemcitabine and oxygen loaded Microbubbles (O_2MBs-RB/GEM) enhanced cytotoxicity when compared to either

treatment alone in a panel of four pancreatic cancer cell lines. In addition, the treatment of ectopic Mia Paca-2 tumours with the combined SDT/antimetabolite therapy resulted in a statistically significant decrease in tumour volume compared to untreated tumours. The effects of multiple treatments on tumour growth was also investigated and it was observed that a second treatment 48h following the initial treatment also provided a significant delay in tumour re-growth. This work is under revision in the Journal of Controlled Release.

The second results chapter (**Chapter 4**) evaluated whether external magnetic and low-intensity ultrasound fields can enhance the efficacy of combined antimetabolite / sonodynamic therapy, delivered using magnetically responsive microbubbles, in an orthotopic murine model of pancreatic cancer. When decorated with the sensitiser Rose Bengal (RB) and the antimetabolite 5-FU and subjected to ultrasound treatment, magnetic responsive microbubbles ($MagO_2MB$) conjugates induced a significant reduction in pancreatic cancer cell viability, of more than 50%. The combined application of external magnetic and ultrasound fields during IV delivery of the $MagO_2MB$ conjugates resulted in a 48.3% reduction in orthotopic pancreatic tumour volumes 9 days after treatment, while the application of ultrasound alone resulted in a reduction of only 27.9%. In addition, a significant increase in apoptosis was observed in tumours that were treated with the $MagO_2MB$ conjugates and exposed to both magnetic and ultrasonic fields when compared to the ultrasound treatment alone or untreated groups. This work has been published in the Journal of Controlled Release.

The third and final results chapter (**Chapter 5**) investigated the ability of calcium peroxide nanoparticles to improve oxygenation in a hypoxic environment and enhance PDT-mediated treatment of BxPc-3 pancreatic cancer cells *in vitro* and an ectopic Mia Paca-2 xenograft murine model *in vivo*. A significant elevation in tumour pO_2 was observed 10 mins following IV administration of a suspension of the particles. This increase in tumour pO_2 was also shown to have a dramatic effect on PDT efficacy with significant reductions in tumour growth observed in mice treated with the particles before PDT when compared to PDT alone. This work has also been published in the Journal of Controlled Release.

Chapter 6 summarised the conclusions of all the results chapters and provides an outlook for future work.

Abbreviation

$^1O_2$	Singlet oxygen
$^3O_2$	Triplet oxygen
5-FU	5-Fluorouracil
ATCC	American Type Culture Collection
CaO_2	Calcium Peroxide
DNA	Deoxyribonucleic acid
DMEM	Dulbecco's Modified Eagles Medium
DMF	N,N-Dimethylformamide
DCC	N,N-Dicyclohexylxarbodiimide
DMSO	Dimethyl sulfoxide
DCM	Dichloromethane
Et_2O	Diethyl ether
GEM	Gemcitabine
MBs	Microbubbles
MeOH	Methanol
EtOH	Ethanol
IP	Intraperitoneal
IV	Intravenous
LED	Light emitting diode
MagMBs	Magnetic Responsive Microbubbles
MS	Mass Spectroscopy

MTT	3-(4,5-dimethylthiazol-2-yl)-2,5-diphenyltetrazolium bromide
NIR	Near Infrared
NMR	Nuclear Magnetic Resonance
OxyMBs	Oxygen carrying microbubbles
PBS	Phosphate Buffered Saline
PDT	Photodynamic therapy
PPIX	Protoporphyrin IX
PTX	Paclitaxel
RB	Rose Bengal
SDT	Sonodynamic therapy
SEM	Scanning Electron Microscope
SOSG	Singlet Oxygen Sensor Green
SPIONs	Superparamagnetic iron oxide nanoparticles
ROS	Reactive Oxygen species
PEG	Polyethyleneglycol
ESI	Electrospray Ionization
MeCN	Acetonitrile
UV-Vis	Ultraviolet Visible
US	Ultrasound
UTMD	Ultrasound-targeted Microbubble Destruction

Table of Contents

Table of Figures

Chapter 1

Chapter 3

Chapter 4

Chapter 5

Chapter 1

General Introduction

1. General Introduction

1.1 Prologue

Cancer is the second leading cause of death worldwide, with 14.1 million people having been diagnosed with the disease and 8.2 million dying from it in 2012 alone. [1] The incidence rate of cancer is variable depending on its type, epidemiological factors and gender. In less developed countries, the most commonly diagnosed cancer in men is lung cancer while in women it is breast cancer. Breast cancer remains the most commonly diagnosed cancer for women in developed countries, while in men it is prostate cancer.[2] The occurrence of cancer in less developed countries is increasing as a result of population growth and aging, which increases the prevalence of known risk factors.

Cancer can be defined as a class of diseases characterised by the abnormal division of cells. [3] Unlike normal cells, cancer cells negatively regulate cellular proliferation by producing growth factor ligands and up-regulate expression of anti-apoptotic proteins. As such, cancer cells are able to avoid programmed cell death, otherwise referred to as apoptosis. [4]

Ten hallmarks of cancer have been proposed to provide a logical understanding of the diversified neoplastic disease. These hallmarks include (1) evasion of cell death, (2) evasion of immune destruction, (3) increasing angiogenesis, (4) resistance to growth suppressors, (5) uncontrolled cellular energetics, capability to (6) maintain proliferative signalling, (7) consistently replicate, (8) invade to normal tissue, (9) mutate the genome and (10) stimulate tumour inflammation. [4] These hallmarks encourage neoplastic growth or progression and lead to a more malignant phenotype. However, they have also provided targets for the development of anti-cancer therapeutics.

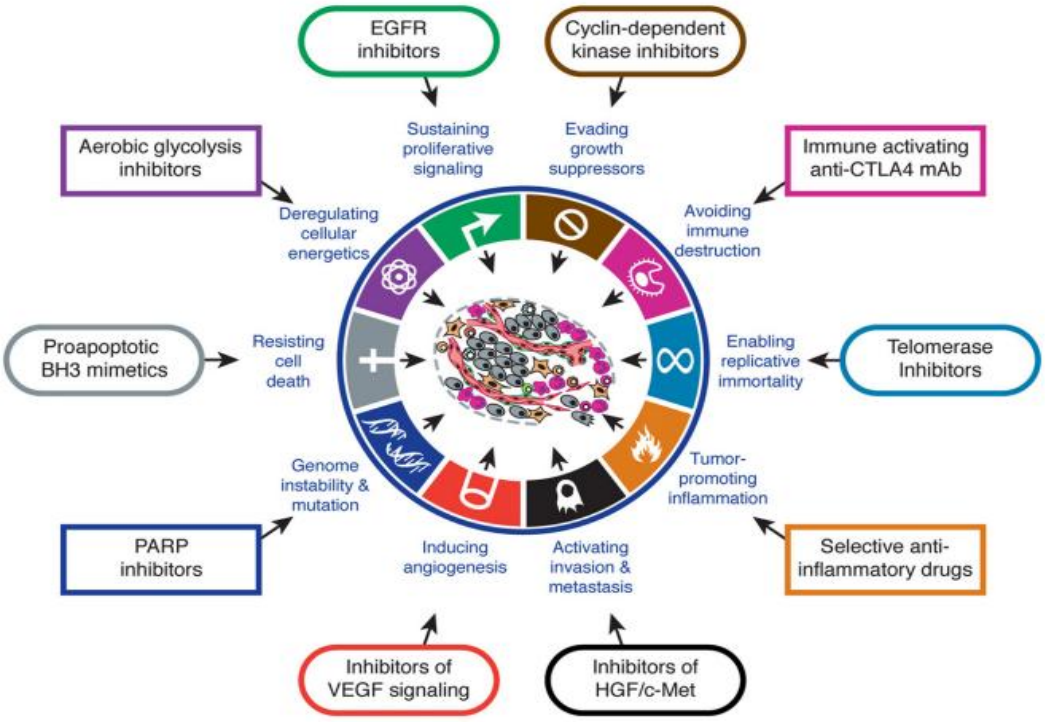

Figure 1. 1 Therapeutic targeting of the hallmarks of cancer. Reproduced from ref [4].

On the basis of increasing experimental evidence, a therapeutic targeting agent normally focuses on one major pathway in a tumour, enabling some tumour cells to survive and continue replication. Such adaptive resistance can renew the tumour functional ability and lead to clinical recurrence. In addition, tumour cells may switch their dependence from one particular hallmark to another. For example, in certain animal models of cancer, it has been observed that upon successful suppression of angiogenesis, tumours can reduce their angiogenesis dependence and switch to a more invasive and metastatic phenotype. [5] Therefore, combination treatments that target two or more of the hallmark targets can lead to much more permanent and effective cancer treatments.

The focus of the work outlined in this thesis is pancreatic cancer, which has the lowest survival statistics of the 21 most common forms of the disease.

1.2 Pancreatic Cancer

1.2.1 Incidence and epidemiology

In the UK, pancreatic cancer is the 11th most diagnosed cancer with approximately 9,000 cases per year and is the 5th most common cause of cancer related deaths. [1] According to GlobalData Pharma, the incidence for pancreatic cancer in 2017 is estimated at 20.573 cases per 100,000 population and is projected to continually increase each year with an incidence of 22.742 cases per 100,000 population by 2021.

Pancreatic cancer has a 5-year survival rate of approximately 5% and a 10-year survival rate of < 1.0% making it the most lethal of all the most common cancers. [1] Surgical resection of the pancreas remains the only cure for pancreatic cancer but only 20% of patients present with resectable disease on diagnosis. Approximately 40% of patients present with metastatic disease while the remaining 40% are in a group referred to as locally advanced or borderline resectable pancreatic cancer (LAPC/BRPC), meaning that while the cancer is still confined to the pancreas, its size or anatomical location means it is not possible for the surgeon to remove all of the tumour. [6] When surgery is possible, 5-year survival rates improve 4-fold to approximately 20%, which while still low, represents a significant survival advantage when compared to un-resectable disease. Several strategies are being investigated to improve these dismal statistics and are designed to increase the number of patients eligible for surgical resection. These are (i) improved diagnostics; (ii) neo-adjuvant chemo-radiotherapy to downstage tumours and (iii) better awareness campaigns. [7] Currently, there is no simple blood or urine test for pancreatic cancer and as the disease is largely asymptomatic until the advanced stages, late diagnosis is a major issue. A significant amount of research is being devoted to develop a simple blood/urine test that could be used as a nationwide screening tool as is the case for prostate cancer. [8] By catching patients earlier, one would assume resection rates would increase. Similarly, the 40% of patients in the LAPC/BRPC could benefit from chemo- or chemo-radiotherapy before surgery with a view of down-staging tumours to again improve resection rates. Several studies have investigated the potential of neo-adjuvant treatments with promising results. [9] Better awareness campaigns are also necessary to enable the public and practitioners to become more familiar with the red-flag symptoms of pancreatic cancer so earlier referrals are increased.

There are many risk factors associated with pancreatic cancer, including cigarette smoking, age, diabetes and obesity. Among these, cigarette smoking is the most well established risk factor. Statistical analysis has shown that nearly 30% of pancreatic cancer patients have smoking histories; even after 10 years since cessation, the risk of progress to neoplasia is still increased by 75%. [10] One study has reported a remarkable interaction between heavy smoking and an Arg399Gln polymorphism of the DNA repair gene XRCC1, which indicated that individuals with a disabled DNA repairing system possess a higher risk of pancreatic cancer. [11] In a study of oncogene mutations, specific endogenous mutagens: KRAS, a member of the RAS oncogene family, significantly induced characteristic patterns of DNA alteration in pancreatic cells. KRAS mutation has been related to lifestyle such as heavy smoking and drinking alcohol. [12] Apart from cigarette smoking, about 10% of cases of pancreatic cancer have a family history. Several genetic syndromes are related to an increased risk of pancreatic cancer. Individuals with Peutx-Jeghers syndrome, induced by germline mutations in STK11 have a substantially increased risk of pancreatic cancer. [13] Additionally, Individuals with diabetes possess an extra 30% risk of pancreatic cancer, which lasts for over 20 years after the initial diagnosis of diabetes. [14]

1.2.2 Molecular pathology and biology

A common characteristic associated with the pathogenesis of cancer is the accumulation of somatic mutations that results in this malignant disease. (Figure 1.2) [15] Oncogenes, tumour-suppressor genes, and genomic maintenance genes are the three main categories of gene mutations in the majority of pancreatic cancer cases. [16] KRAS, as the most commonly mutated oncogene, plays a key role in mediating downstream signalling by the activation of transcription factors, which has been involved in over 90% of pancreatic carcinogenesis. The prevalence of KRAS mutation in patients with pancreatic cancers has been identified as a potential early detection label. [17] CDKN2As, also known as p16 tumour-suppressor gene, regulates the major cell-cycle of the pancreas, with inactivation in over 90% of pancreatic adenocarcinomas. TP53 tumour suppressor genes are another commonly mutated gene that plays a role in the cellular stress response and its mutational frequencies are evident in 75% of pancreatic cancers. [18] Finally, MADH4 tumour suppressor genes control the downstream signalling by converting growth factor TGFβ receptor, which is inactivated in over 50% of pancreatic cancers. [19]

	Chromosomal location	Alteration frequency (%)
Oncogenes		
K-ras	12p	75–100
HER2/neu	17q	65–70
AKT2	19q	10–20
MYB	6q	10
Tumour-suppressor and genome-maintenance genes		
TP53	17p	40–75
*CDKN2A**	9p	27–98
CDKN2A†	9p	27–82
CDKN2B	9p	27–48
MADH4	18q	50–55
FHIT	3p	66–70
RBI	13q	0–10
BRCA2	13q	7–10
STK11	19q	5
MAP2K4	17p	4
ALK5	9q	1
TGFBR2‡	3p	1
TGFBR2§	3p	3
MLH1	3p	3

Figure 1. 2 Generally mutated oncogenes and tumour-suppressor genes in human pancreatic cancer. Reproduced from ref [15].

At the molecular biology level, the mechanisms correlating genetic mutations with invasive characteristic are connected not only to the activated oncogenes and inactivated tumour-suppressor genes but also the crucial stress factors like cytokines and acidosis, which have an impact on the downstream signal transduction pathways in relation to the regulation of cell growth and proliferation. [20] This diversity of influence factors offers a significant growth and survival advantage in pancreatic cancer cells so that they possess a higher chance to develop into an advanced or metastatic pancreatic cancer, which are incurable with traditional anticancer treatments. Kleeff et al have demonstrated that various cytokines such as interleukin 1, 6 and 8, tumour necrosis factor α and transforming growth factor β are up-regulated in human pancreatic neoplasm. [21] The over-expression of these growth factors result in the resistance of cell death, activation of invasion and metastasis. Shi et al have shown that a low pH microenvironment or acidosis may lead to the over-expression of vascular endothelial growth factor into the tumour tissue, especially in the area encapsulated by necrosis. [22] However, a better understanding of such factors involved in the pathophysiology of pancreatic cancer is required before innovative methods or approaches to combat it can be developed.

1.2.3 Current Pancreatic Cancer Treatments

The current treatments for pancreatic cancer include surgery, chemotherapy, radiation therapy or combination of two or more of these treatments. The chosen treatment is decided on the basis of the general health of a patient and stage of pancreatic cancer in a multi-subject pathway. (Figure 1.3) [18] According to the American Joint Committee on Cancer, pancreatic cancer is classified into three different groups for treatment purposes, which are surgically resectable, unresectable locally advanced and metastatic. [23]

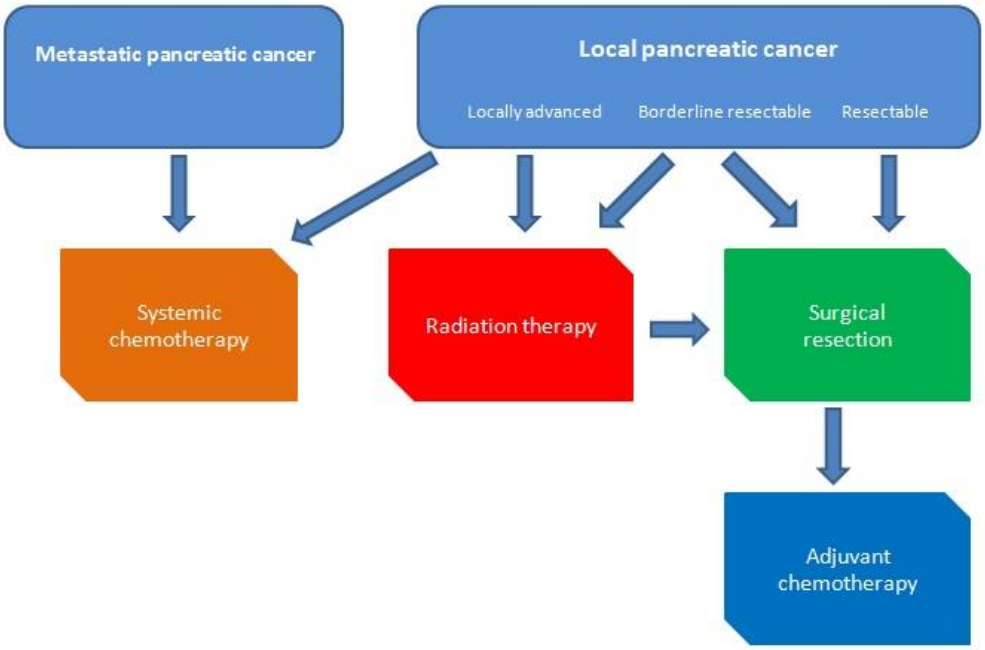

Figure 1. 3 Schematic diagrams of treatment options for pancreatic cancer. Reproduced from ref [23]

1.2.3.1 Surgery

Currently, surgical resection is the only treatment that can cure patients with pancreatic cancer. Surgical procedures for pancreatic cancer contain pancreaticoduodenectomy, distal pancreatectomy with splenectomy, and total pancreatectomy. However, all these resections may lead to a reduced quality of life as the removal of the pancreas means the patients lack important enzymes that facilitate food digestion and absorption. This means patients must take dietary supplements, such as pancrelipase (eg CREON), for the rest of their life. The overall survival rates after surgical resection is highly dependent on the expertise and techniques available in the specialist pancreatic cancer centre. [24] Laparoscopic techniques have also been applied in surgery for various types of pancreatic cancers, such as mucinous

cystadenocarcinoma, neuroendocrine carcinoma, pancreatic ductal adenocarcinoma and intra-ductal papillary mucinous carcinoma.[25] A previous study has demonstrated that laparoscopic distal pancreatectomy of left-sided pancreatic ductal adenocarcinoma has several advantages over open surgery with a view to the survival rate and dramatically reduces the duration of hospital stay with faster recovery times, which result from eliminating the need for intricate reconstructions. [26]

1.2.3.2 Chemotherapy

1.2.3.2.1 Typical antimetabolite agents for pancreatic cancer

The pyrimidine 5-fluorouracil (5-FU) has been used as an anticancer drug for over 60 years and was one of the earliest chemotherapies used in pancreatic cancer treatment.

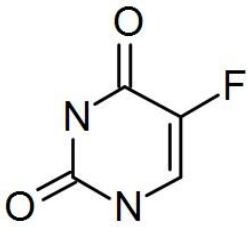

Figure 1. 4 Structure of 5-FU

The mechanism of action for 5-FU can be divided into two major pathways as shown in Figure 1.5. The first involves the conversion from 5-FU to 5-fluorouridine triphosphate (FUTP) via phosphorylation by nucleotide kinases. FUTP is then incorporated into cellular RNA and leads to the inhibition of RNA transcription. [27] An alternative activation pathway includes the thymidine phosphorylase catalysed conversion of 5-FU to fluorodeoxyuridine (FUDR) and subsequent thymidine kinase (TK) phosphorylation to the active metabolite 5-fluoro-2'-deoxyuridine monophosphate (FdUMP). [28] FdUMP is capable of inhibiting thymidylate synthase, which leads to an increased amount of deoxyuridine triphosphate (dUTP) recognised as damaged DNA. When the cell repair system is overloaded to set up a cycle of misincorporation and repair, single strand and double strand breaks result in cell death. [29] However, resistance can occur in pancreatic cancer patients when the metabolic rate of 5-FU decreases or DNA repair efficiency increases. [30] Therefore, as the response rate to 5-FU was only 20%, more effective drugs or combination treatments were required. [31]

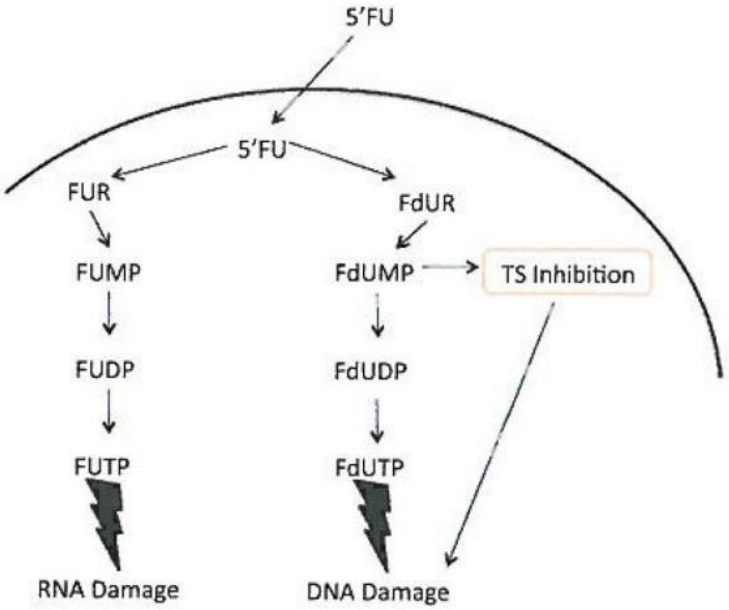

Figure 1. 5 Mechanism of 5-FU resulting in RNA and DNA damage. Reproduce from ref [29]

Gemcitabine (GEM) was first investigated as an antiviral drug but soon- after was also identified for its anti-cancer activity in solid and haematological cancer models. [32] GEM was FDA approved in 1996 as single chemotherapy agent for metastatic pancreatic cancer with a better overall survival rate when compared to 5-FU. [21] Its molecular structure is a 2'-deoxycytidine analogue where hydrogen is replaced by fluorines at the 2' position of the furanose ring as shown in Figure 1.6.

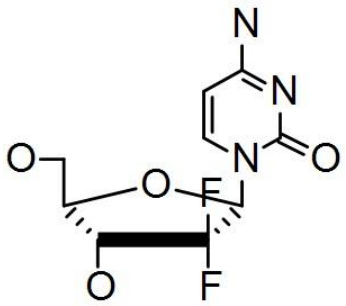

Figure 1. 6 Structure of GEM

The mechanism of GEM action depends on its phosphorylation state leading to the inhibition of DNA repair and replication enzymes that result in cell death via apoptosis. GEM is first taken into the cells via human equilibrative nucleoside transporters (hENTs) or human concentrative nucleoside transporters (hCNTs). [33] The next step involves the conversion from GEM to gemcitabine monophosphate (dFdCMP) via phosphorylation by

deoxycytidine kinase, which is further phosphorylated by nucleotide kinase into the active diphosphate (dFdCDP) and triphosphate (dFdCTP) nucleoside metabolites. [34] The major cytotoxic effect of GEM comes from the triphosphate metabolite, which is able to incorporate into the DNA strand resulting in destruction of DNA chain formation and single strand shatter via the inhibition of DNA polymerase activity. [35] Furthermore, dFdCDP and dFdCTP can inhibit the function of ribonucleotide reductase and deaminase respectively, which not only enhance the phosphorylation of GEM to the active metabolite dFdCTP but also inhibit deoxycytidylate (dCMP) deaminase activity producing mutated genes. (Figure 1.7) In spite of its broad-spectrum characteristic, resistance to this agent still exists due to several mechanisms. The main cause is the low level expression of the human equilibrative nucleoside transporter 1 (hENT1) resulting in the poor intracellular uptake of GEM. [36] In the ESPAC-3 trial study, the levels of hENT1 were discovered to have a great impact on the overall survival time of patients, where patients with lower levels of hENT1 more likely to die earlier than those with higher levels of hENT1.[36]

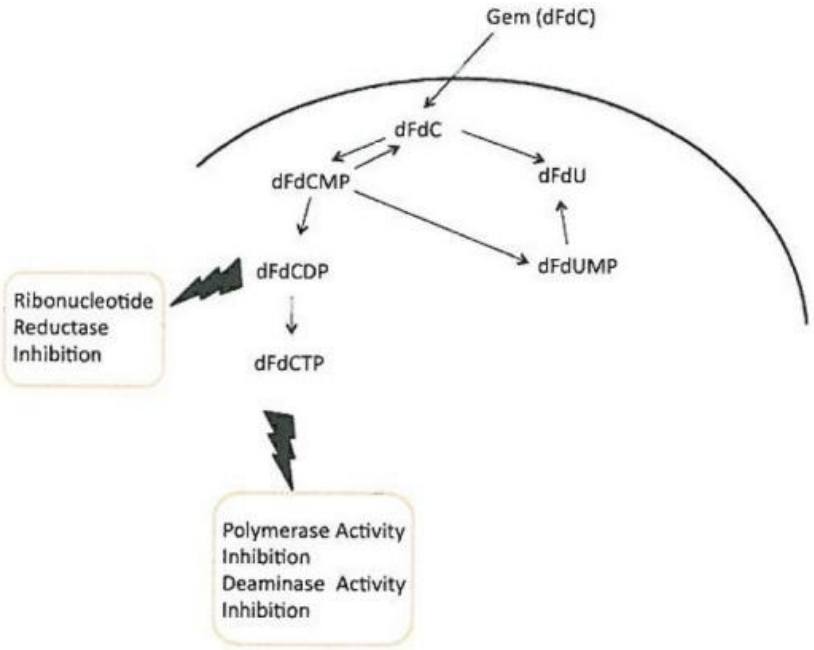

Figure 1. 7 Mechanism of GEM leading to cell death via apoptosis. Reproduced from ref [32]

1.2.3.2.2 Taxanes in Pancreatic Cancer

Abraxane (albumin-bound paclitaxcel particles for injectable suspension) is a Cremophor-free, 130 nm colloidal nanoparticle suspension that has been developed to overcome the

limitations of single-agent paclitaxel involving its poor solubility and the solvent-associated toxicities (Cremophor in this case). In September 2013, Gemcitabine plus nab-paclitaxel became a first-line therapy for metastatic pancreatic cancer (MPC) following positive outcomes from a global phase III trial (MPACT). [37]

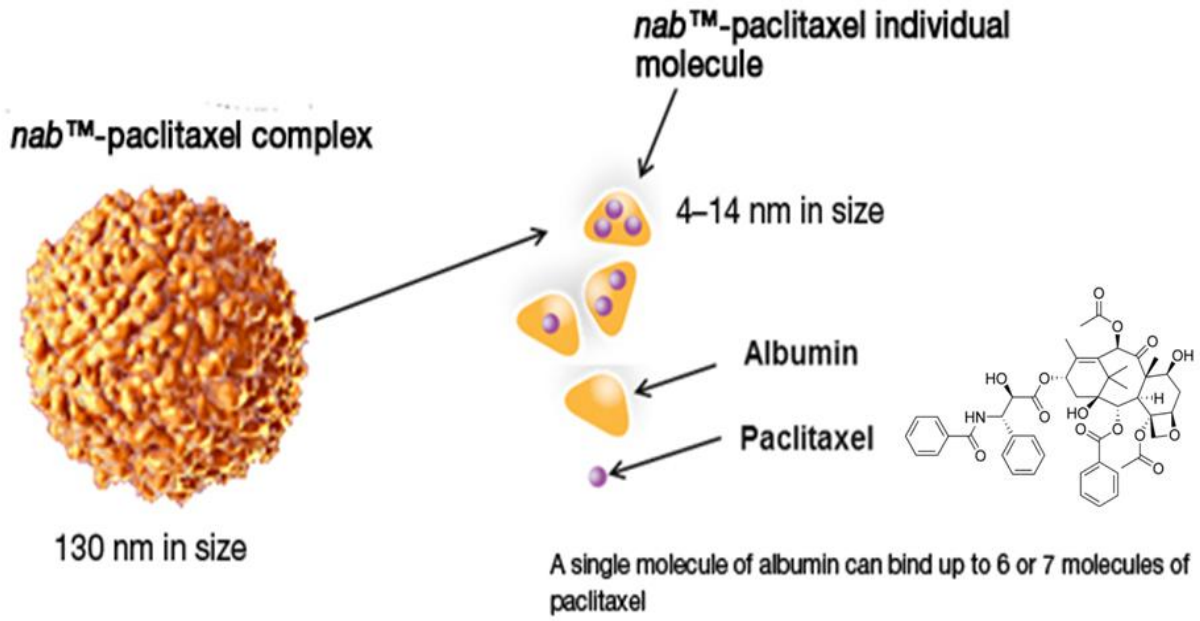

Figure 1. 8 Diagram illustrating the nab-paclitaxel complex. Reproduced from ref [38]

The intra-tumor drug delivery mechanism utilised the biological characteristic of albumin. Firstly, albumin attaches to the cell surface receptor gp60 and activates the intracellular protein caveolin-1, leading to the formation of vesicular structures. [39] Albumin-bound complexes are then transferred through these vesicles into the interstitial space. Secondly, due to the crucial role of secreted protein acidic and rich in cysteine (SPARC) as a high-affinity receptor for albumin, albumin-bound complexes are likely to accumulate in SPARC-positive areas of tumors. SPARC is over-expressed in the stroma of pancreatic tumours and this is the most likely reason for the enhanced activity of nab-paclitaxel when compared to paclitaxel delivered in a cremophor vehicle.

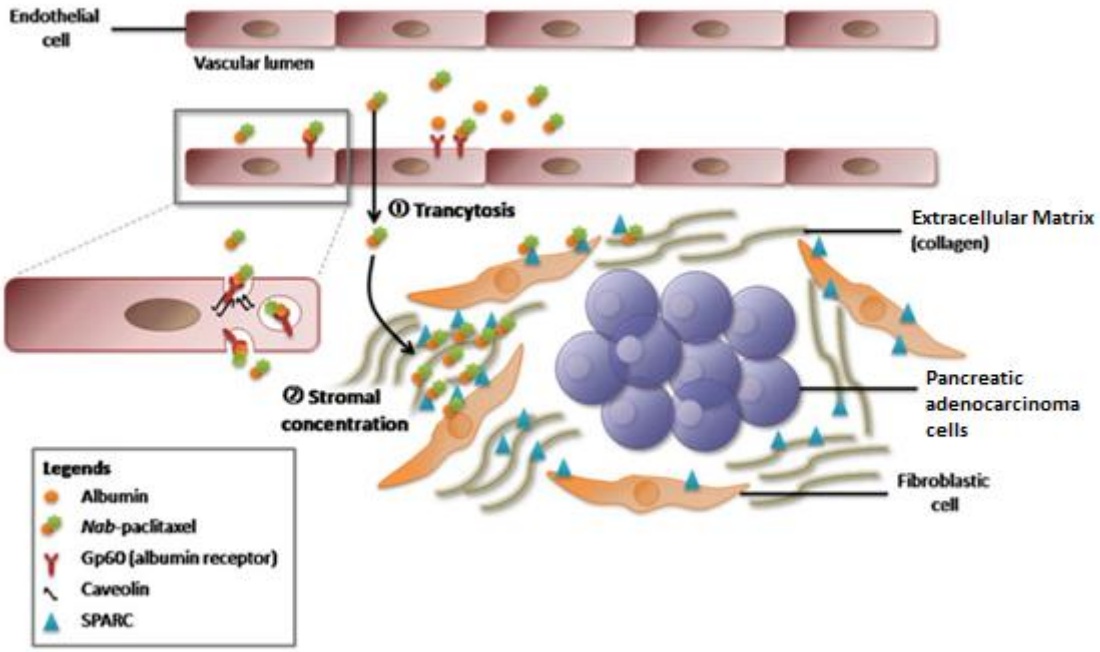

Figure 1. 9 Mechanisms of drug delivery of nab-paxclitaxel. Reproduced from ref [40]

1.2.3.2.3 FOLFIRINOX and Pancreatic Cancers

Since the result of the PRODIGE 4/ACCORD 11 trial was published in 2011, the FOLFIRINOX regimen (combination of infusional 5-FU, leucovorin, irinotecan and oxaliplatin) has emerged as a new treatment for patients with metastatic pancreatic cancer. [41] The mechanism of 5-FU delivery and metabolism has already been described in section *1.2.3.2.1.* Leucovorin or folinic acid, is a reduced form of folic acid and improves the effectiveness of 5-FU chemotherapy. With regard to the platinum compound Oxaliplatin, the excision repair cross-complementing rodent repair deficiency, complementation group 1 (ERCC1) play a crucial role in elimination of damaged DNA involving nucleotide excision repair and thus are regarded as potential biomarkers.[42] For instance, Fuereder et al. investigated the activity and safety of GEMOX (gemcitabine/oxaliplatin combination alongside erlotinib) and correlated the benefit with ERCC1 expression. The data showed that patients with higher ERCC1 staining pattern received a therapeutic effect.[43] As for irinotecan, the irinotecan target topoisomerase-I (TOP1) and carboxyl esterase-2 (CES2) were evaluated potential biomarkers in pancreatic cancer cells. For the former, a recent clinical study demonstrated that increased TOP1 copy number benefited the overall efficacy of irinotecan. [44] For the later, a more integrated study involving genetic analyses demonstrated that patients having

metastatic pancreatic cancer with over expression of CES2 had a better OS and PFS rates when treated with FOLFIRINOX. [45]

Figure 1. 10 Mechanisms of action and metabolism of the drugs in the FOLFIRINOX regimens. Reproduced from ref [46]

1.2.3.3 Management of chemotherapy to different patients based on the presentation of disease

It is important that each patient is given an appropriate treatment for their particular condition, therefore pancreatic cancer is divided into three main presentation classes, which are surgically resectable, locally advanced and unresectable, or metastatic pancreatic cancer. [47]

For surgically resectable pancreatic cancer, patients will normally first undergo Whipple's surgery to remove the tumour and then treated with adjuvant chemotherapy as soon as they are well enough to tolerate all 6 cycles, usually in the form of gemcitabine plus capecitabine or 5-FU plus leucovorin. With regards to patients who are not well enough to tolerate combination chemotherapy, adjuvant gemcitabine is recommended as the standard treatment. [48]

For locally advanced and unresectable pancreatic cancer, the recommended treatment is chemoradiotherapy using capecitabine as a radiosensitiser.[49] In addition, systemic

combination chemotherapy including FOLFIRINOX, gemcitabine plus nab-paclitaxel, or nanoliposomal irinotecan plus 5-fluorouracil and leucovorin is recommended to patients who are well enough to tolerate it. Adjuvant gemcitabine is recommended to patients who are not well enough to tolerate combination chemotherapy.

As for metastatic pancreatic cancer, FOLFIRINOX is regarded as the first-line treatment to patients with an Eastern Cooperative Oncology Group (ECOG) performance status of 0-1. Gemcitabine combination therapy is recommended to patients who are not well enough to tolerate FOLFIRINOX. With regards to patients who are not well enough to tolerate combination chemotherapy, adjuvant gemcitabine is recommended as the first-line treatment. With regards to second-line treatment, oxaliplatin-based chemotherapy is recommended to patients who have not first-line oxaliplatin; gemcitabine-based chemotherapy is recommended to patients whose cancer sustains progress even after the first-line FOLFIRINOX treatment.

1.3 Targeted Cancer Treatments

1.3.1 Photodynamic therapy (PDT)

Photodynamic Therapy (PDT) involves three specific components: (i) a photosensitiser drug (PS), (ii) molecular oxygen and (iii) light of a specific wavelength (Figure 1.11). Each component exhibits no cytotoxcity independently, however, when utilised in combination, highly reactive singlet oxygen ($^1O_2$) and other reactive oxygen species (ROS) are generated which can cause significant cytotoxicity leading to rapid cell death via apoptosis or necrosis.

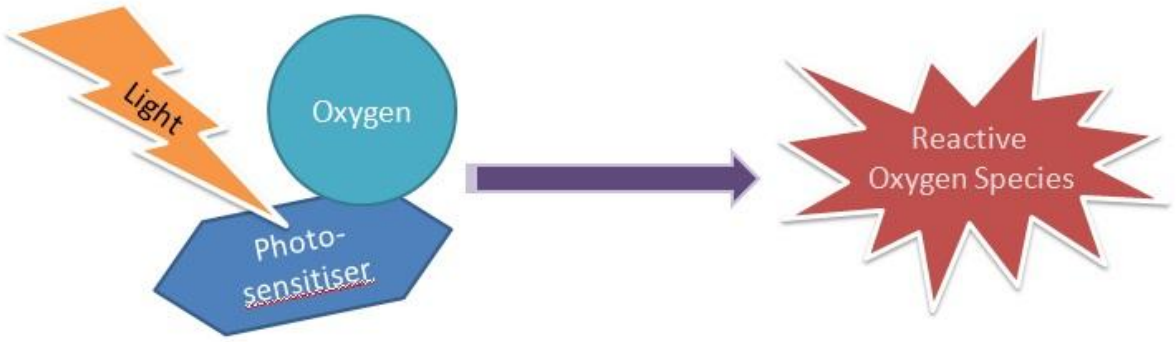

Figure 1. 11 Essential elements for the photodynamic process and the generation of cytotoxic reactive oxygen species.

The photophysical processes involved in PDT are illustrated in **Figure 1.12**.[50] First, an electron in the photosensitiser is excited by a photon of light from the singlet ground state (S_0) to the first excited singlet–state (S_1), which is relatively short-lived. Then, there are two options for the electron. One is to return to the singlet ground state, emitting a photon of light, which is known as fluorescence. Alternatively, it can change its spin state and engage in inter-system crossing (ISC), converting to the relatively long-lived first excited triplet state (T_1). There are also two options for the triplet state electron: (i) to drop back to the ground state causing emission of energy, known as phosphorescence or (ii) engage in photochemical reactions, which lead to the production reactive oxygen species (ROSs). There are two types of such photochemical reactions, Type I and Type II. In the Type I reaction, the electron interacts with a bio-molecule (or oxygen) resulting in electron transfer (re-dox) that leads to production of free radicals such as the hydroxyl radical and superoxide radical. In the Type II reaction, energy from the excited triplet state is transferred to the triplet ground state of molecular oxygen, which generates singlet oxygen. The products from both types of reaction are cytotoxic and cause cellular damage via oxidative stress. [51]

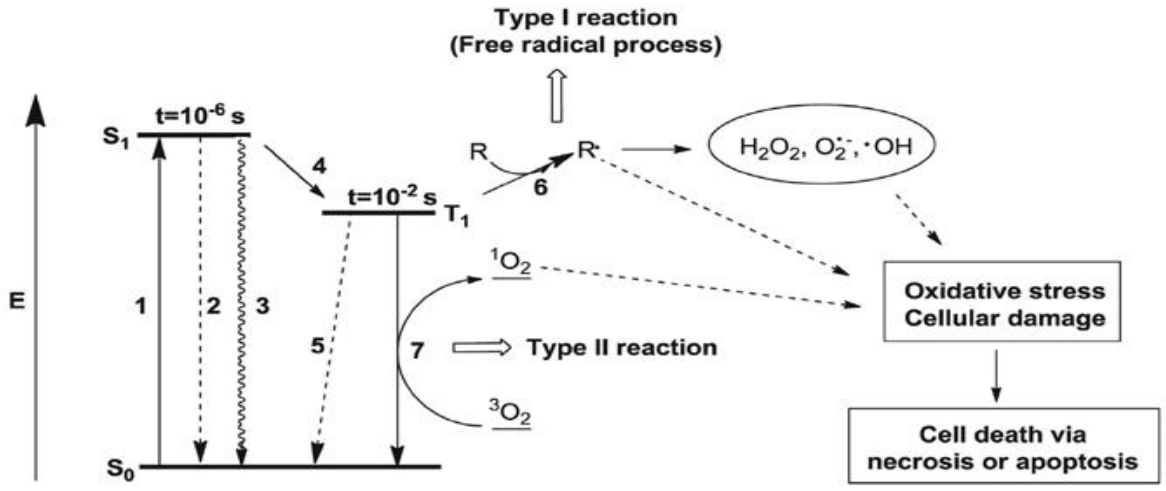

Figure 1. 12 Modified Jablonski diagram outline the photophysical processes involved in PDT. Photophysical processes involved in photodynamic therapy: 1) absorption, 2) fluorescence, 3) internal conversion, 4) intersystem crossing, 5) phosphorescence, 6) formation of free radicals by energy transfer from T_1 photosensitiser to biological substrates, and 7) formation of singlet oxygen ($^1O_2$) by energy transfer from T_1 photosensitiser to triplet oxygen ($^3O_2$). Reproduced from ref [52]

Although both type of reactions are responsible for the therapeutic effect observed in PDT, Type I reactions are dominant in hypoxic environments while Type II reactions are dominant in normoxic environments. [53] In most situations, singlet oxygen is the major product of PDT reaction amongst ROSs. Singlet oxygen is a potent cytotoxic agent due to its highly oxidative nature, participating in non-selective reactions with biological substrates such as lipids, proteins and DNA. [54] A key feature of singlet oxygen is that it has a short half-life, and therefore the diffusion distance from the treatment tumour area is limited. [55] For these reasons, singlet oxygen is an ideal anti-cancer therapeutic in combination with a controlled light source, as together they can significantly reduce any cytotoxic effect to healthy tissue. [56]

It is also believed that PDT is responsible for activating the body's antitumour immune system. [57] In contrast; most conventional treatments for cancers are non-selective killing a variety of cells, including bone marrow cells which are responsible for producing immune cells. PDT can activate B and T cells at the treatment site resulting in a positive immune response. [58] Therefore, the process of killing cancer cells via PDT can arouse the immune response, recruiting macrophages and dendritic cells to the site of treatment. Kamangar *et al*. reported an immune response aroused by PDT in both *in vitro* and *in vivo* experiments. [59] Therefore, PDT is a promising treatment as it can kill tumour cells in a specific area and can elicit an immune response in regions other than the treatment area. [60]

However, a major restriction of PDT is its ability to treat deep-seated lesions due to the poor ability of light to penetrate tissue. Tissues transparency to light is related to the wavelength, with longer wavelengths being capable of deeper penetration (Figure 1.13). [61] The near-infrared (NIR) region is where light has its maximum penetration through tissue with the region between 750nm to 900nm being described as the "optical or photo-therapeutic window". [62]

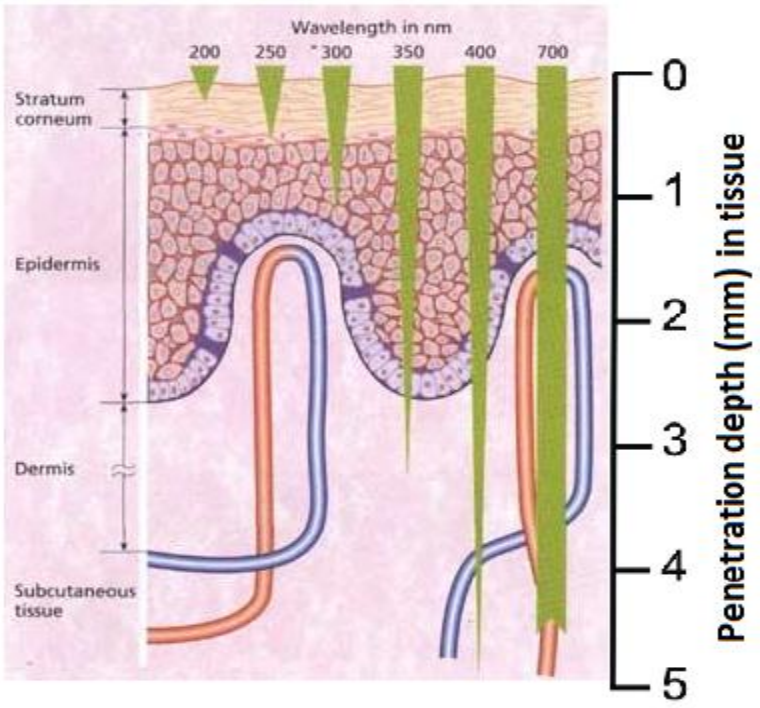

Figure 1. 13 Schematic diagram representing how tissue depth penetration is wavelength dependent. Reproduced from ref [63]

To be useful for clinical application in PDT, photosensitisers should absorb strongly in the photo-therapeutic window and possess a high singlet oxygen quantum yield. Unfortunately, currently approved photosensitisers are mostly activated using wavelengths in the visible region of the electromagnetic spectrum and thus exhibit low tissue penetration. To overcome this deficiency, a relatively new concept of two-photon excited (TPE) PDT was proposed. [64] This process involves the excitation of a fluorophore/sensitiser by two photons of long wavelength light by a femtosecond laser, which is of relatively low energy and induces the same excited state as one photon of shorter wavelength of light with high energy. However, currently utilised photosensitisers have low two-photon extinction coefficients and therefore require a high amount of energy for excitation. At such high energies resulting in photodamage to healthy tissue is problematic. [65]

1.3.1.1 First Generation Photosensitisers

Photofrin, a hematoporphyrin derivative (HpD) is regarded as the first PS developed for use in anti-cancer PDT treatment. It was first approved by Canada for treating bladder cancer

and later FDA approved for the treatment of esophageal cancer. Currently, Photofrin has been used in PDT treatment for a range of cancers including head & neck, skin, lung and intestinal cancer. [66]

Hematoporphyrin (HP) was discovered by removing the red pigment in blood (Haem). HP is able to transform to HpD following treatment with 5% sulfuric acid in acetic acid to produce a mixture of porphyrin monomers, dimers and oligomers with ether, ester, and carbon-carbon linkages. The purified Photofrin product is then extracted from HpD by removing the monomeric components. [67]

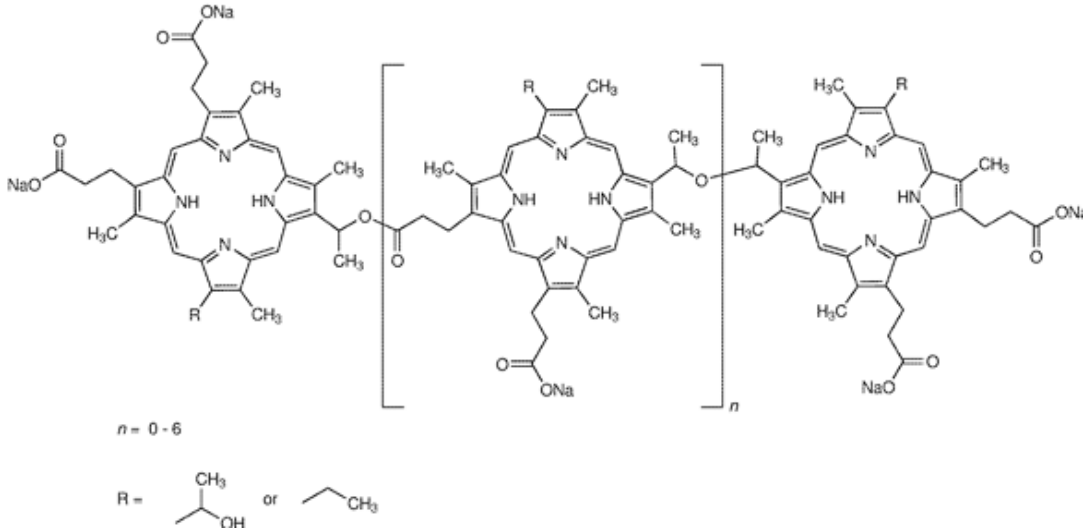

Figure 1. 14 Structure of Photofrin

The attraction of Photofrin as a PS include (1) a relatively high singlet oxygen quantum yield (Φ^1O_2 = 0.89) and (2) a favorable safety profile from various clinical trials. [68] In one clinical trial involving patients with cutaneous Kaposi's sarcoma, Photofrin was administrated to patients at 2mg/kg plus light treatment 48h post infusion at a dose of 200-300 J/cm^2. Due to its minimally-invasive nature and excellent tolerability, this trial proved PDT to be an attractive alternative to conventional chemotherapy treatment. [69] However, several deficiencies were identified that limited a more widespread application of PDT using Photofrin. Firstly, the extinction coefficient at the longest wavelength Q-band of Photofrin is low (ε at 630 nm = 3000 M^{-1} cm^{-1}), which restricted the Φ^1O_2 when excited at this wavelength. In addition, 630nm wavelength light has only moderate tissue penetration (2-3 mm) making it difficult to treat larger or more deeply-seated lesions. Furthermore, the

multicomponent nature of the mixed dimers / oligomers is not ideal. Therefore, much development work continued to identify a better PS to replace Photofrin.

1.3.1.2 Second Generation Photosensitisers

The development of second generation PS aimed to improve on the main limitations of the first generation PS, mainly absorbance inefficiency and the mixed final product composition. To enhance absorbance efficiency for a better therapeutic effect, meta-tetra (hydroxyphenyl) porphyrin (m-THPP) was developed since the enhanced conjugation resulted in more desirable characteristics. [70] Berenbauml et al. demonstrated m-THPP was 25 to 30 times as effective as HpD for PDT-induced tumour necrosis by measuring the depth of necrosis on slices of the fixed tumors after illumination. [71] However, the existence of skin hypersensitivity limited the employment of this agent into clinical use.

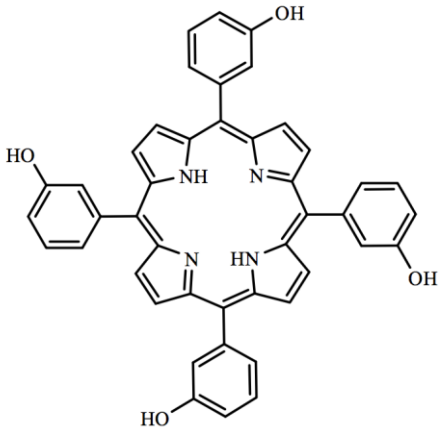

Figure 1. 15 Structure of m-THPP

Protoporphyrin IX (PPIX) is another typical second generation PS that was FDA approved for the PDT treatment of actinic keratosis in 1999. [72] This PS can also be metabolically generated from the pro-drug: 1, 5-aminolevulinic acid (ALA) by human cells. The bio-synthetic process of converting ALA to PPIX is via the heme pathway as shown in scheme 1.1 with excess ALA facilitating cellular PPIX accumulation since the final step to generate heme is limited via its slow conversion rate. As a result, a concentration gradient of PPIX is evident between neoplastic and healthy tissue. [73] Furthermore, as ALA is converted relatively slowly to PPIX (8-12h) skin photo-toxicity was greatly reduced. [74] Kennedy et al. were first

to demonstrate successful PDT treatment of skin malignancies via the transdermal application of ALA. [75] Subsequently, ALA has been widely used in anticancer therapy including skin, head and neck cancer, bladder cancer and prostate cancer despite its inefficient $^1O_2$ generation at its Q-band excitation wavelength (635nm, Φ_Δ = 0.56). [76]

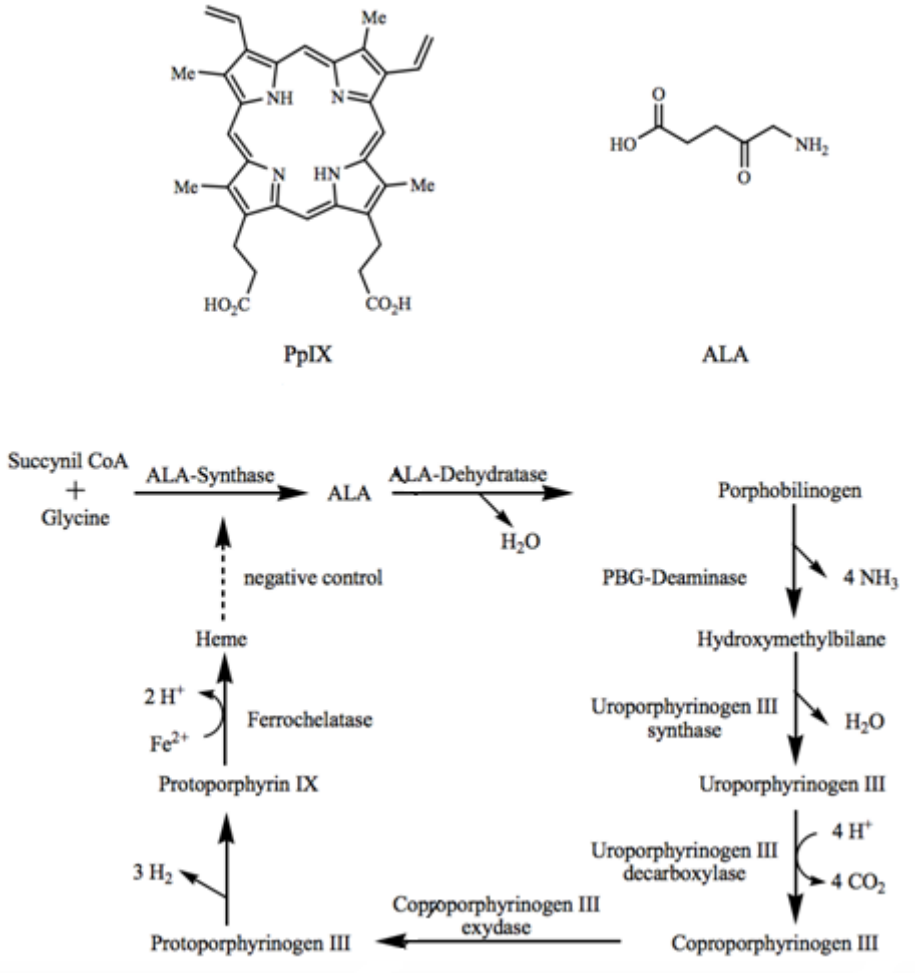

Figure 1. 16 Biosynthesis scheme for the conversion of ALA to PPIX. Reproduced from ref [72].

The discovery of the chlorin group of PS, including meta-tetra (hydroxyphenyl) chlorin (m-THPC) and NPe6 that were derived from chlorophyll a, represented another step forward in the development of second generation PS. When compared to porphyrin based PS, a double bond on one pyrrole ring was saturated in the chlorins, leading to a significant bathochromic shift (from 640nm to 700nm) in the Q-band absorbance (Figure 1.17). [77] This variation also enabled enhanced singlet oxygen quantum yields (Φ_Δ = 0.87) and much better extinction coefficient at the peak wavelength than in the porphyrins (ε_{max} ~ 35000 M^{-1} cm^{-1}). [78] Due to the efficient singlet oxygen production, a reduced dose was required for PDT treatment and m-THPC was approved in Europe for treating head & neck cancer and further clinical

trials were conducted to investigate its antitumour effect on prostate, breast and pancreatic cancers. [79] The only significant deficiency associated with m-THPC was the long circulatory half-life increasing the likelihood of skin phototoxicity.

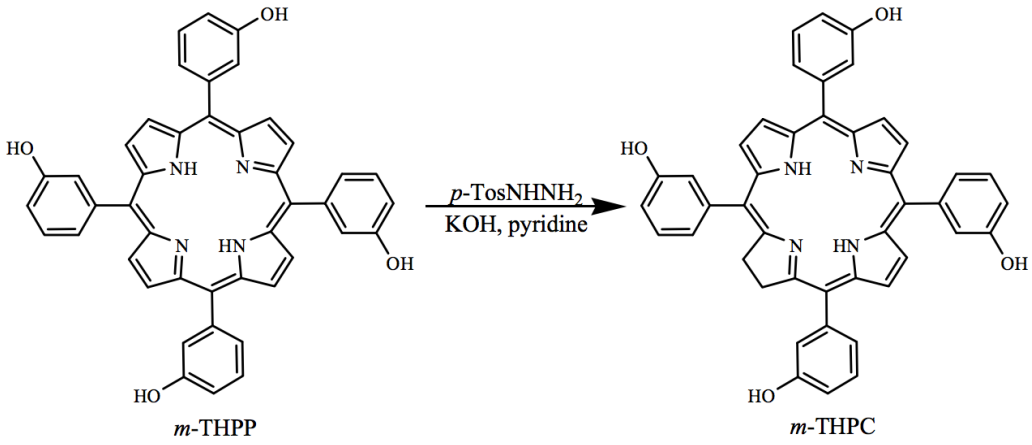

Figure 1. 17 Transformation of m-THPC from m-THPP. Reproduced from ref [77].

NPe6, is another representative second generation PS from the chlorin family and is capable of excitation using a wavelength in the red region of the spectrum (664nm) with a high extinction co-efficient (ε= 40000 M^{-1} cm^{-1}).[80] It also possesses minimal dark toxicity and skin phototoxicity owing to the fast systemic pharmacokinetics resulting in its quick elimination from the body. In a phase II clinical study, NPe6 was administrated IV at 40 mg/m^2 and following 4h light irradiation post injection at 100 J/cm^2 almost 85% of patients with endobronchial lung cancer responded to the therapy. [81] Therefore in 2003, NPe6 was approved for treating lung cancer in Japan and also demonstrated potential for treating oral, brain and liver cancer. [82]

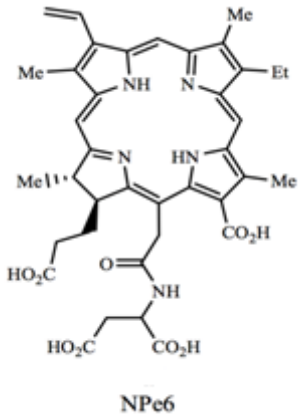

Figure 1. 18 Structure of NPe6.

Table 1.1 various photosensitisers with specific wavelength, power output of light and duration.

Photosensitisers	Wavelength	Light power	Duration	Reference
Photofrin	630nm	200-300 J/cm^2	3 hours	[69]
5-ALA	635nm	200-300 J/cm^2	2 hours	[76]
m-THPC	652nm	200 J/cm^2	2 hours	[79]
NPe6	664nm	100 J/cm^2	4 hours	[82]

Even though most of PSs have been based on a porphyrin type structures, some non-porphyrin related compounds have demonstrated promise as sensitisers for PDT. One such compound is the hydrophilic xanthene sensitiser Rose Bengal (RB). Substitution of Xanthene ring hydrogen atoms in fluorescein to halogen atoms in Rose Bengal, significantly enhanced the intersystem crossing process via the "heavy atom effect" with a corresponding dramatic increase in singlet oxygen quantum yield (Φ_Δ = 0.76). [83] In addition, RB also possessed a broad excitation band in the green region of the spectrum (480-550nm) with an excellent extinction co-efficient (ε_{max} = 99,800 M^{-1} cm^{-1} at 532nm). [84] For these reasons, RB is regarded as an efficient photosensitiser that has been applied for a variety of PDT applications. [85]

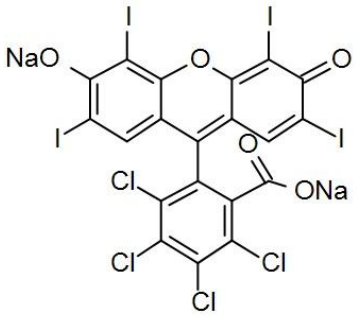

Figure 1. 19 Structure of RB

1.3.1.3 Third generation Photosensitisers

Third generation PSs differ from their 1st and 2nd generation counterparts in that they contain a tumor- targeting characteristic which can be achieved via two main approaches: 1) the attachment of biomolecules such as monoclonal antibodies (mAB) to the PS or 2) encapsulation of PS into delivery vehicles that direct the PS to their targets. For the first

approach, advantage is taken of the unique surface antigens on tumor cells in comparison with normal cells, which will selectively attach to a corresponding antibody derivativised PS without influencing surrounding tissue. [86] The avidin-biotin interaction is one common method employed to link the mAB and PS, which ensures a high dose PS delivery to the targeted site resulting in an enhanced PDT effect. [87] Wöhrle et al. have demonstrated the successful binding and excellent therapeutic effect of this mAB-PS system via an enzyme-linked immunosorbent assay (ELISA). Breast carcinoma cells and colon carcinoma cells were treated with biotinylated antibody, avidin and biotinylated zinc phthalocyanine PSs successively, followed by illumination for 30s at 5 J/cm^2 using a red light source. The results showed that cell cytolysis occurred on 90% of the breast carcinoma cells and 45% of the colon carcinoma cells respectively.[87] For the second approach, adenovirus Type 2 capsid proteins were utilised to covalently attach to an $AlPcS_4$ PS via an ester linkage. These proteins display high selectivity and strong association with integrin receptors overexpressed via various cancer types such as breast cancer and lung cancer. Although *in vitro* data was limited, *in vivo* studies using a breast cancer EMT-6 murine model demonstrated increased uptake of the adenovirus Type 2 protein labeled $AlPcS_4$ compared to the free $AlPcS_4$, indicating a promising delivery system for tumor targeting PDT treatment. [88]

1.3.2 Sonodynamic Therapy

While the use of NIR-absorbing PS and two-photon excitation schemes enables potential sensitiser excitation in the phototherapeutic window, the penetration depths are still limited to about 1 cm. [89] In this context, alternative methods for sensitiser excitation have also been explored. One such approach is Sonodynamic Therapy (SDT). Like PDT, SDT requires the combination of three individual components to enable the generation of ROS. Typically, the same sensitiser is employed and molecular oxygen is also a mandatory component. However, while light is used to excite the sensitiser in PDT, this is replaced with low-intensity ultrasound in SDT. (Figure 1.20) Ultrasound is widely used as an economical and safe imaging modality [90][91] and unlike light, its penetration depth in soft tissue enables sensitiser excitation at depths of tens of centimeters enabling the possible treatment of lesions in the abdominal or thoracic cavity. [92]

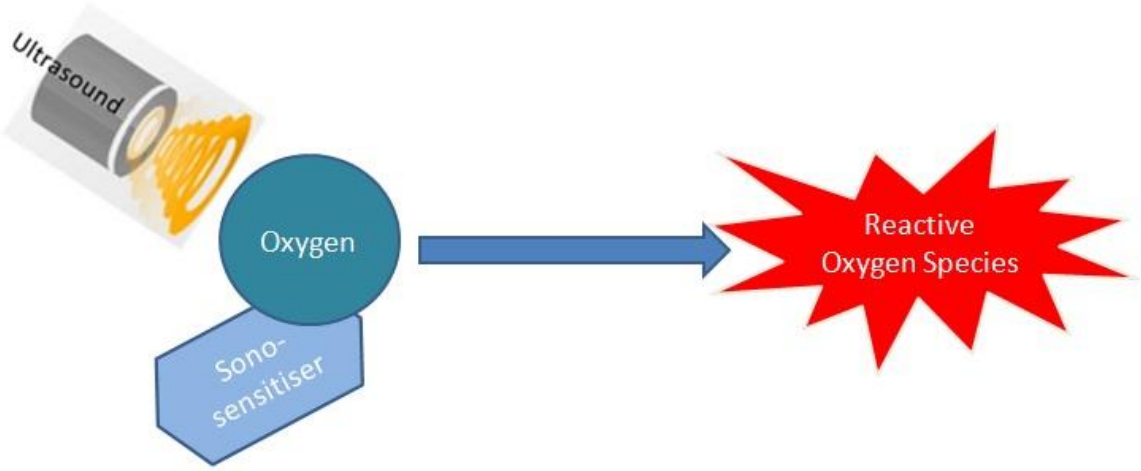

Figure 1. 20 Essential elements for SDT process and the generation of cytotoxic reactive oxygen species.

1.3.2.1 Basic physical principles of ultrasound

Ultrasound comprises sound waves with frequencies greater than 20 kHz, which exceed the upper range of human hearing. An US wave is a type of mechanical energy, which is transferred through a medium by vibrating molecules. It can be sub-divided into two types of wave: the first is a longitudinal wave, which involves the oscillation of molecules in a linear direction (in mediums such as gases, liquids, or plasma). The second is a transverse wave, which involves the oscillation of molecules vertical to the direction of the transmitted wave (such as in solids).

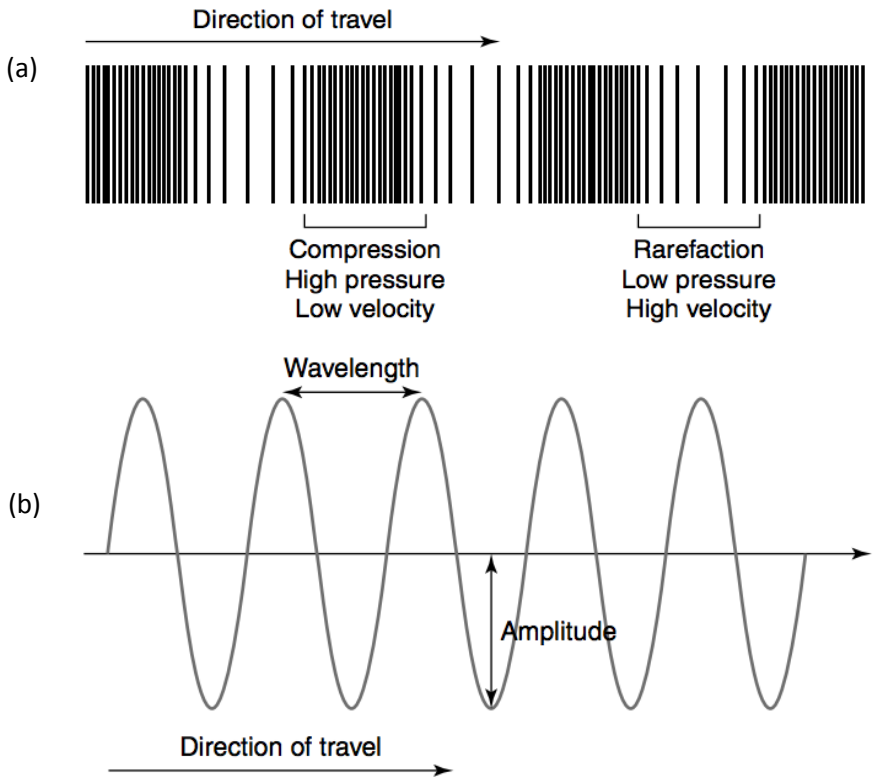

Figure 1. 21 The illustration of (a) a longitudinal sound wave and (b) a transverse sound wave

To better understand this process, a few parameters are used to describe the mechanism of how US waves propagates through tissue. The frequency (f) of an US wave includes the cycle number or the variation of pressure that occurs in one second. Frequency is not influenced by the medium which sound travels through but by the source generating US. The velocity (v) of an US wave is defined as the speed at which sound can pass through the medium. Unlike frequency, velocity is only determined by features of the medium including density and compressibility. Wavelength (λ) is described as the distance between two identical points on the US wave. It is determined by the frequency and velocity of the US wave as described in **Equation 1.1**.

$$\lambda = v/f \qquad \textbf{(Equation 1.1)}$$

Equation 1.1 shows that the wavelength and frequency of US are inversely related. In practical applications such as improving resolution in diagnostic imaging and procedural US, it is crucial to select a suitable source frequency. Generally speaking, lower frequency waves are less attenuated than high frequency waves for a given distance and thus penetrate to

deeper tissues. In contrast, a higher axial resolution image can be generated by higher frequency waves. For this reason, it is ideal to apply high-frequency sources to image superficial structures (such as for stellate ganglion blocks). [93]

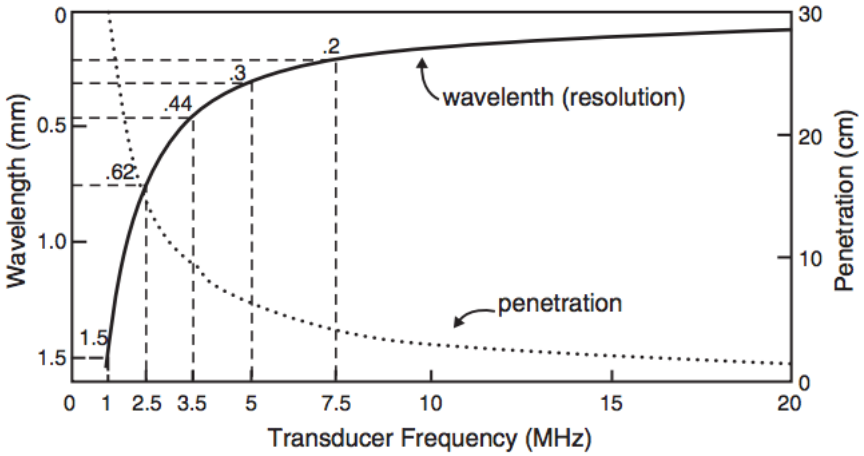

Figure 1. 22 A comparison of the resolution and penetration of various ultrasound frequencies.

For the ultrasound mediated SDT, the frequency used is typically in the region of 1-2 MHz. [94] Two further important characteristics of the ultrasound used in SDT are intensity and duty cycle. The intensity (power) of ultrasound is calculated in W/cm^2 and determines the strength grade of the energy from this sound wave. Intensity is crucial when discussing bioeffects and safety, which varies in diagnostic ultrasound since it's highest at the center of the beam and falls off near the periphery. It also varies along direction of travel due to focusing and attenuation. Spatial Peak (SP) and Spatial Average (SA) intensity are used to describe the peak intensity and the average intensity of the ultrasound output over of the area of the transducer respectively.

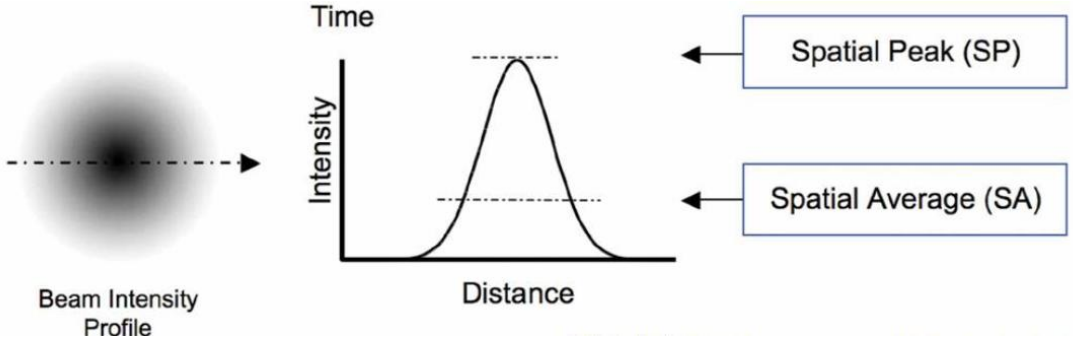

Figure 1. 23 Schematic diagrams to describe US intensity metrics in diagnostic ultrasound.

In pulsed ultrasound, intensity varies with time: it's zero between pulses and greater than zero during each pulse. Temporal peak (TP) is the greatest intensity found during a pulse, while temporal average (TA) includes the "dead" time between pulses. The pulse average (PA) is in between for a given pulse beam. PA and TA are related by the duty cycle and the duty cycle is measured as a percentage of the time in which the ultrasound is applied over the cumulative time of the treatment. This function is able to limit temperature increase in heat-sensitive applications. [95]

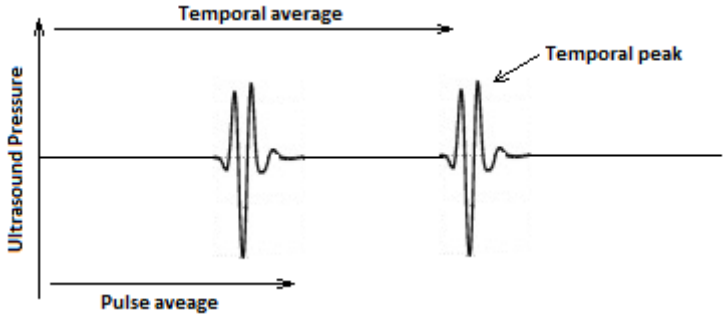

Figure 1. 24 Schematic diagram to describe US pressure and intensity metrics in pulsed ultrasound. Reproduced from ref [96]

1.3.2.2 Mechensim of ROS generation in SDT.

While the mechanism for ROS generation in PDT is well understood at the molecular level, the mechanism for its generation following ultrasound irradiation in SDT is less clear. A unique phenomenon called “cavitation” occurs when ultrasound interacts with an aqueous environment, where gas filled bubbles undergo a series of processes including their generation, expansion and collapse. Stable and inertial cavitations are terms applied to further subdivide this phenomenon. Stable cavitation leads to the generation of bubbles, which carries on oscillating and consequently stirring the surrounding media. Inertial cavitation is when the cavitation bubbles grow to a resonance size, before collapsing violently. The energy released by collapsing bubbles can transfer into extreme high temperature and pressure, which can reach up to 10,000K and 81MPa respectively. [97] These extreme micro-environmental conditions have been described as a “sonochemical reactor” [98] and forms the basis for the two main theories for ROS generation in SDT: sonoluminescence and pyrolysis.

Sonoluminescence is the process of light generation following ultrasound irradiation of a solution. Pickworth et al. have confirmed this light production by utilizing a photomultiplier tube and processing through pulse height analysis.[99] It has been suggested that the sonoluminescence generated from the process of cavitation [100] is then capable of activating sensitisers in a similar way as in PDT. The second theory of pyrolysis suggests that the sonochemcial reactor type conditions experienced by a sensitiser in the vicinity of bubble undergoing inertial cavitation results in sensitiser pyrolysis liberating reactive free radicals that subsequently react with surrounding endogenous substrates to generate ROS. [101] Mišík et al have attempted to prove this theory and confirmed the production of free radicals through the application of electron paramagnetic resonance (EPR). They also investigated that these free radicals play a great role in the water dissociation to generate hydroxyl radicals and hydrogen peroxide. [102]

Although neither mechanism has a substantial body of evidence as support, numerous studies are available to confirm that the irradiation of sensitisers with low-intensity ultrasound generates ROS with a corresponding cytotoxic effect. [103-105] However, given the exact mechanism of SDT remains uncertain, it is difficult to identify the ideal structure or characteristics of the sensitiser for optimum SDT efficiency. Despite this, various different photosensitisers, including porphyrins and xanthene derivatives, have also been identified as capable of generating ROS upon low intensity ultrasound irradiation and used as sonosensitisers in SDT. Some examples of SDT anticancer treatment are provided below.

1.3.2.3 SDT as an anti-cancer treatment.

A pioneering study by Umemura et al. in 1999 demonstrated a significant 96% reduction in cell viability of sarcoma 180 after 60s US exposure (1 MHz, 5.9 W/cm^2) in the presence of 160 µM RB, while RB alone had only a minor effect. [106] A further study involving mice bearing intracranial glioma tumours treated with focused ultrasound at 25 W/cm^2 (1 MHz) for 5min and Rose Bengal (50 mg/kg of body weight) resulted in a 80% reduction in tumor volume compared to untreated mice, without affecting surrounding brain tissues. [107] Although RB has attracted a significant amount of attention as a sonosensitiser, due to its hydrophilic nature, it suffered from a low accumulation capacity at the tumor region that seriously restricted its further development with regard to clinical use. When RB is delivered

via IV administration into systemic circulation, it is rapidly eliminated from the blood circulation and expelled through bile. [108] To overcome this deficiency, a series of amphiphilic RB derivatives were synthesised by adding a carboxyl group or alkyl chain to modify the structure as shown in Figure 1.25. The tumor uptake capability of RBD1 was evaluated in colon 26 carcinoma mice model and results demonstrated a much better uptake in tumor tissue compared to non-tumor tissue, which indicated that tumor accumulation and SDT anticancer efficiency can be enhanced via the suitable structural modification of sonosensitisers. [109] Previous work by Nomikou et al has also investigated covalently attaching RBD2 to lipid microbubbles and observed an ultrasound-induced anticancer effect in RIF-1 cells *in vitro*. *In vivo* data also demonstrated a dramatic reduction in tumor growth via the combination of the conjugate and ultrasound but no effect on tumor growth in the absence of the ultrasound stimulus in mice bearing prostate LNCaP-Luc tumours. [110]

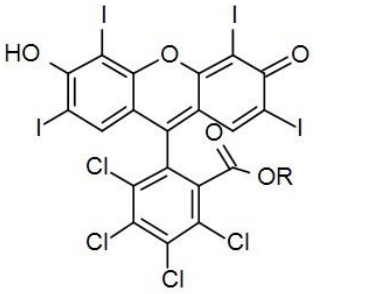

RBD1 R=$(CH_2)_7COOH$
RBD2 R=$CHCOOH(CH_2)_{11}CH_3$

Figure 1. 25 Structure of RB derivatives. Reproduced from ref [109]

As porphyrins represented the earliest class of photosensitisers used in PDT, it is no surprise they have also been investigated for use in SDT, with photofrin, HP and PPIX being proven capable of generating ROS when irradiated with ultrasound.

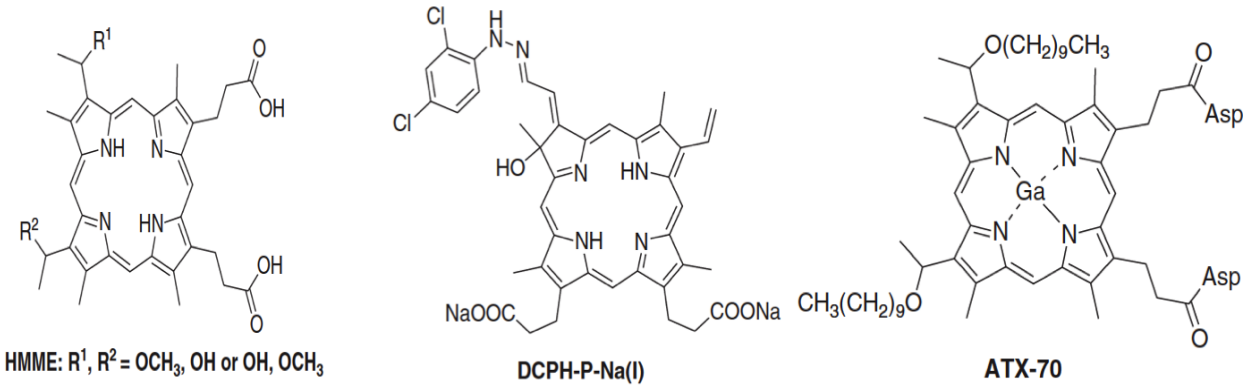

Figure 1. 26 Chemical Structure of some selected HP derivatives including Hematoporphyrin monomethyl ether (HMME), DCPH-P-Na(I) and ATX-70.

Hematoporphyrin monomethyl ether (HMME) is a recently developed HP derivative with the ability to selectively accumulate in cancer cells, is nontoxic in the absence of ultrasound and is rapidly metabolised by the body. Previous *in vitro* studies demonstrated that HMME (10 µg/mL, incubated in dark for 2 h) exhibited significant cytotoxicity on C6 glioma cells following ultrasound irradiation (1.0 MHz and 0.5 W/cm^2 for 2 min) and SDT induced cell apoptosis and necrosis was also observed as a result of ROS generation. [111][112] Furthermore, gene expression analysis indicated that HMME-mediated SDT treatment resulted in down-regulation of Bcl-2 expression, which is involved in the apoptotic signalling pathway. [113] Moreover, SDT mediated treatment of osteosarcoma in rats using HMME (20 mg/kg, IV) and ultrasound radiation (10.5 MHz) for 120 seconds at an intensity of 0.8 W/cm^2 demonstrating a significant 48.9% inhibitory rates of tumour volume compared to animals treated with drug or ultrasound alone. [114]

The previously mentioned porphyrin derivatised DCPH-P-Na(I), has also demonstrated effective SDT mediated toxicity against a panel of human cancer cells (including human lung cancer cell lines, LU65A, RERFLC-KJ, HLC-1, VMRC, and KNS-62, human gastric cancer cell lines, MKN-1, MKN-28, MKN-45, MKN-74, and KATO-III, a human pancreas cell line, QGP-1, and a human prostate cancer cell line, PC-3) *in vitro*. [94] Furthermore, it was suggested that its effective SDT efficacy was derived from ROS generation since the DCPH-P-Na (I) mediated SDT effect was drastically decreased upon the addition of L-histidine as a scavenger of ROS. In addition, efficient tumor growth inhibition was observed in MKN-45 tumor bearing mice, when tumours were exposed for 10 min to ultrasound at 1 MHz, 2 W/cm^2, 50 % duty cycle

following IV injection of DCPH-P-Na(I) (14.4 μg/kg). [94] These results suggested that DCPH-P-Na(I) mediated SDT had great potential for use in the clinical treatment of cancer located too deep to be treated utilising regular PDT.

In another study by Nakajima et al., it was demonstrated that a high concentration of the sonosensitiser ATX-70 is capable of accumulating in nitrosoamine-induced pancreatic tumours. [115] Pharmacokinetics and tissue distribution studies showed that 24h after drug administration the concentration ratio of tumor against plasma reached its peak value, indicating the optimal treatment time. [116] Furthermore, the potential ultrasound mediated effect of ATX-70 was investigated by Umemura et al. and the results showed that the damage on isolated mouse sarcoma 180 cells in air-saturated suspension was enhanced fourfold by ATX-70, compared to only twofold by the same concentration of HP upon ultrasound irradiation. [117] *In vivo* data was also impressive and suggested that the antitumor effect of ATX-70 was dramatically enhanced with an increasing dose of ATX-70 in combination with ultrasound exposure, while no obvious antitumor effect was observed for tumors treated with ultrasound or the drugs alone. [118] While still a relatively new area, the interested reader is directed to several prominent reviews on the efficacy of SDT as an anticancer treatment. [119][120][121]

1.4 Drug delivery system

1.4.1 Microbubbles as drug delivery vehicles

Microbubbles (MBs) comprise a core-shell structure with a gas core covered by a coating involving lipids, proteins or polymers. This coating influences the half-life of microbubbles and prevents the gas from escaping. [122] MBs have been widely employed in diagnostic imaging as contrast agents. The principle of this application is to make use of the large acoustic impedance difference between MBs and surrounding tissues to generate nonlinear acoustic radiation under moderate ultrasound intensities, therefore the images can provide contrast enhancement via MBs at the target region. [123]

Furthermore, MBs have been investigated as delivery vehicles through attachment of therapeutic agents into or on the MBs shell and subsequently destructing the MB using US to liberate the drugs at a target region. [124] The targeted destruction of the MBs means a

local release of the drugs at the target site reducing exposure in non-targeted tissue. This is particularly relevant when cytotoxic drugs are involved and can reduce side effects associated with treatment. In addition, microsteaming and microjetting effects as a result of MB cavitation can enhance drug diffusion through tumor tissue. [125] Furthermore, several biodegradable agents such as proteins and nucleic acids may avoid decomposing prematurely in the systemic clearance by incorporation into the shell of microbubbles.[126] Finally, drug-carrying microbubbles enables drug delivery to be tracked via ultrasound imaging if necessary. [127]

1.4.2. Ultrasound-targeted microbubble destruction (UTMD) as a drug-delivery strategy.

Several methods have been investigated to deal with the conjugation of drugs to microbubbles as shown in Figure 1.27. Drugs can be attached not only (a) inside the shell via dissolving in the oil phase, (b) in the shell via filling the shell gap but also outside the shell via (c) electrostatic, covalent and non-covalent interactions or (d) the avidin-biotin linking.

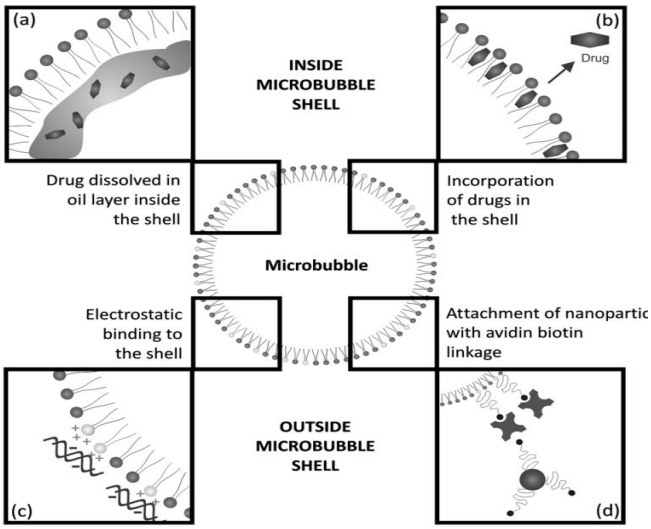

Figure 1. 27 Schematic diagram of potential conjugation of drugs with microbubbles involving (a) inside the shell, (b) in the shell but also outside the shell via (c) electrostatic, covalent and non-covalent interactions or (d) the avidin-biotin linking. Reproduced from ref[124]

Similar to film coated tablets or capsules, microbubbles are able to absorb drugs inside the shell to protect the therapeutic drugs from untimely decomposition. Unger et al. has investigated microbubbles containing acoustically active lipospheres (AALS), which involves a drug loaded oil phase acting as the intermediate layer between the gaseous core and lipid

shell. [124] This approach enabled a hundred times higher dosage of the paclitaxel (PTX) to be loaded in the oil phase when compared the standard IV injection. However, Shortencarier et al's study have shown that AALS microbubbles are harder to destruct (burst) compared to normal lipid MBs due to their thick shells reducing the efficacy of cavitation. [128]

Another pathway to protect drugs from degradation is to incorporate therapeutic agents in the microbubble shell. Frenkel et al. investigated a type of plasmid DNA (pDNA) carrying albumin microbubbles, which verified the existence of pDNA in the microbubble shell via tracking the propidium iodide labeled pDNA. Furthermore, they showed that the transfection efficacy of pDNA carrying microbubbles was significantly higher than a simple mixture of pDNA and albumin microbubbles. [129] Nevertheless, Klibanov et al reported that this type of negative charged MBs had a shorter half-life time and easily attached to the positive charged blood components leading to the premature release of agents. [122]

Electrostatic interaction is a convenient method for the attachment of charged therapeutic agents to the surface of MBs. DNA, as a polyanion with several negative charged sugar phosphate fragments, can be readily attached to the cationic microbubbles. In 1996, Kim et al. administrated pDNA attached to albumin microbubbles into murine knees and demonstrated an enhancement in the transfection rate of DNA under ultrasound excitation. [130] Borden et al had further optimised this type of MBs with increased drug loading by incorporating an extra cationic polymer layer on the MBs. [131] This modification not only improved the limited loading on the MBs' shell but also minimises the gas diffusion and subsequently enhanced the stability of MBs. On the other hand, the strong interaction between pDNA and cationic lipids on the shell may lead to the aggregation of rather large particles during MBs collapse. The size of these aggregates can be too large to pass through cell membrane and therefore decreased the transcription efficiency of the binding DNA. [132]

Avidin-biotin interactions provide another method for the attachment of drugs to the MB shell via non-covalent interactions. In brief, biotinylated lipids such as DSPE-PEG-biotin constitute the lipid shell of microbubbles, avidin is then added as a cross-linker molecule

and eventually a biotinylated drug moiety is incorporated to form a biotin-avidin-biotin complex. (Figure 1.28)

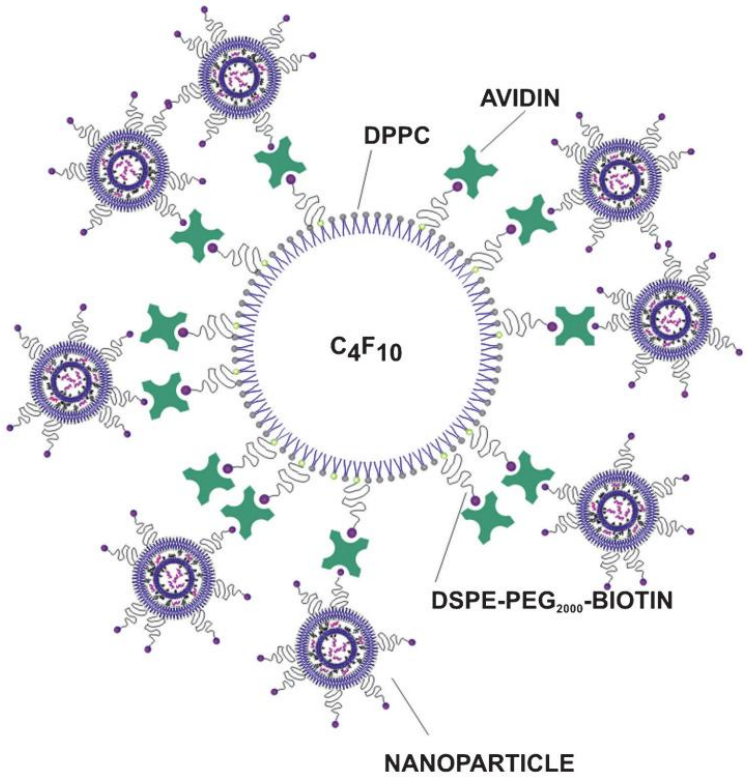

Figure 1. 28 Schematic diagram of a biotinylated MBs loading nanoparticles. Reproduced from ref [133]

Avidin is a type of functional protein extracted from the egg white of oviparous vertebrates. Biotin has high affinity for avidin (K_d of 10^{-13} to 10^{-15} M) and has only a minor effect on the host immune system. [134] Moreover, the separation half-life ($T_{1/2}$) of avidin-biotin bridges lasts for up to three months. [133] Lum et al. were the first to investigate biotinylated MBs bound with avidinylated polystyrene globules. [135] Biotinylated liposomes have also been successfully attached to biotinylated MBs by adding excess avidin as cross-linker, which resulted in approximately 10^5 liposomes bound to each MB. [136] Moreover, liposomes are well-established as drug delivery carriers for several decades. Due to their particular structure (containing a bilayer coating exterior and hydrophilic core), hydrophobic, hydrophilic and amphiphilic drugs can all be loaded into liposomes. Furthermore, there was no noticeable reduction in MB cavitation upon ultrasound excitation following attachment to liposomes or polystyrene beads. [135]

1.4.3 UTMD and SDT

In 2011, McCaughan et al. demonstrated that two conventional photosensitising drugs, methylene blue (MB) and RB activated by light can be activated by ultrasound and were able to generate higher levels of ROS and lower LD50 values in chinese hamster ovarian cells than either light or ultrasound activation alone. [137] In 2012, since RB was a promising sonosensitiser, it was successfully attached to the surface of a lipid stabilised MB using a carbodiimide based coupling protocol and the resulting conjugate produced more singlet oxygen and was more effective *in vitro* and *in vivo* than the sensitiser alone at the same concentration. [110] However, these lipid MB conjugates displayed poor physical stability limiting their potential translation to the clinic. Hence, PLGA MBs were also investigated as an alternative to lipid MBs for the delivery of sensitisers in SDT. [138] PLGA MBs have significantly better stability at fridge and body temperature than lipid MBs. In addition, they still undergo ultrasound-induced destruction at therapeutically acceptable ultrasound intensities ensuring their capability as a targeted delivery vehicle. [138] When these MBs conjugated to a rose Bengal sensitiser, the resulting constructs demonstrated selective cytotoxicity while treating a HeLa cancer cell line *in vitro* and human xenograft pancreatic tumors *in vivo*. Therefore, PLGA MBs appear as promising candidates for use with conventional sensitizing drugs to provide a minimally invasive targeted treatment of cancer using SDT. Nevertheless, PLGA MBs are not FDA approved which limits their potential translation to the clinic. [138] In 2015, to test the potential SDT effect in a simulated tumor environment, McEwan et al. have synthesised oxygen loaded MBs attached to a Rose Bengal sensitiser via an avidin-biotin linkage. [139] This approach was successful in generating significantly more singlet oxygen in a simulated hypoxic environment than similar conjugates loaded with SF_6 as the core gas. Moreover, a greater cytotoxic effect was observed when BxPc-3 cells, cultured in a hypoxic environment, were treated with the oxygen loaded MB conjugate and ultrasound compared to cells cultured under similar conditions and treated with the SF_6 loaed MB conjugate and ultrasound. Finally, mice bearing human xenograft pancreatic BxPc-3 tumours treated with the oxygen loaded MB conjugate and ultrasound showed a 45% reduction in tumour volume five days after treatment while the volume of tumours in mice treated only with the conjugate increased by 180 % over the same time period. Overall these results demonstrate that SDT may be significantly enhanced by incorporating an approach that involves ultrasound- and

microbubble-mediated delivery of oxygen to hypoxic tumours. This approach could provide the basis for less invasive treatment of more deeply-seated lesions, together with addressing hypoxia which limits sensitiser-based approaches and is associated with less favorable prognoses. It also provides the basis for a novel treatment option for pancreatic cancer which is perhaps one of the most recalcitrant forms of cancer and where existing therapeutic options are extremely limited. [139] In 2016, McEwan et al. prepared a biotin-5FU derivative suitable for attachment to the surface of a platform consisting of avidin-functionalised MBs filled with O_2 gas. [140] The MBs were shown to be more stable with respect to oxygen retention when compared to their earlier MB. Further experiments demonstrated that combining sonodynamic and antimetabolite therapy using the O_2MB conjugates provided enhanced cytotoxicity in three different pancreatic cancer cell lines cultured under anaerobic conditions when compared with cytotoxicity yielded by either treatment alone. Similarly, treatment of ectopic BxPc-3 tumors with the combined therapy led to a statistically significant reduction in tumor volume when compared with the efficacy of either therapy alone. These results suggest that combined sonodynamic and antimetabolite therapy using ultrasound-responsive O_2MBs could provide a promising alternative to chemotherapy for the treatment of locally advanced pancreatic cancer and could also be effective as a neo-adjuvant therapy. Furthermore, it is shown that the avidin-functionalised MB platform is an effective vehicle for the targeted delivery of biotinylated payloads to ectopic BxPc-3 tumours upon application of externally applied ultrasound. In addition, as the first study characterising the effect of SDT at the molecular genetic level, the results have shown that this treatment approach has an effect on the expression of immune-associated signaling pathways. [140]

1.4.4 UTMD using magnetic microbubbles

Yang et al. were the first to produce a type of lipid-stabilised microbubbles loaded with superparamagnetic iron oxide nanoparticles (SPION) for image contrast enhancement. [141]The SPION MBs demonstrated a dramatic improvement in MRI image contrast compared to SPION alone. Park et al further developed this type of MBs with various kinds of NPs via inserting specialised ligands on the MB shell as bioluminescence or fluorescence labels. [142]

MagMBs for ultrasound-mediated delivery was first conceptualised by Stride et al. [143] In this study, the shell of MBs consisted of multilayer material, where the gas core was covered with an iron oxide fluid and the outer layer comprised a L-α-phosphatidylcholine surfactant. (Figure1.29)

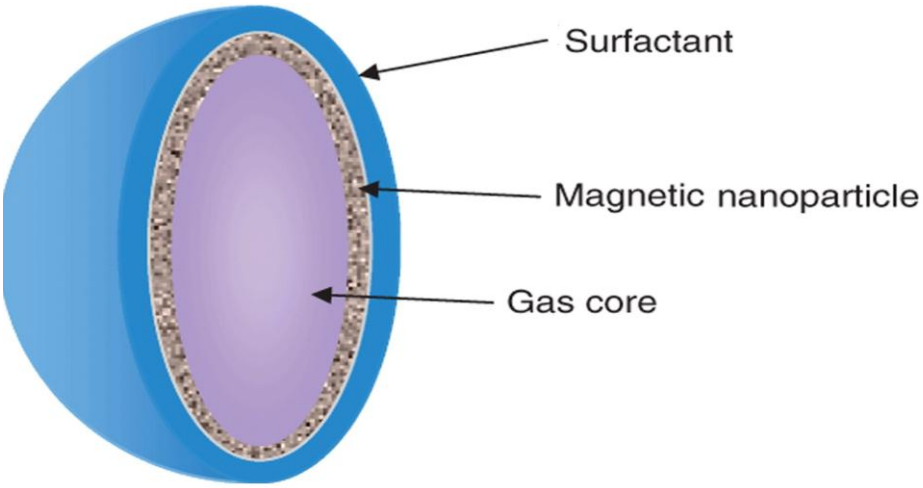

Figure 1. 29 Schematic diagram of MagMBs. Reproduced from ref [143]

The transfection efficiency of this type of MagMBs in the absence or presence of magnetic or ultrasound fields were further investigated *in vitro*. pDNAs inserted with luciferase were incorporated into each MB and the bioluminescence intensity was tested for each sample. The results demonstrated that samples treated with both ultrasound and magnetic fields revealed a dramatic enhancement in DNA transfection while treatment with US or magnetic fields alone had little impact on the improvement of transfection. [143] This approach was also tested *in vivo* in a murine model, and the results again demonstrated that the strongest bioluminescence signal was observed when both the ultrasound and magnetic fields were applied together. [144] Although MagMBs for ultrasound-mediated delivery seems to be a promising pathway for clinical use, there remains a question of whether the localization of MagMBs will be affected by the distance between magnet and target tissue. As a reference, an *in vivo* study has revealed that localization of magnetic microparticles can be achieved where the target tissue is over 10cms deep from skin surface. [145]

1.5 Improving tumour oxygenation to facilitate PDT and SDT

Both PDT and SDT require O_2 to exert their therapeutic effect. Several strategies have been investigated to improve oxygenation of tissues during therapy and each will be discussed in turn.

1.5.1 Hyperbaric oxygen therapy

Hyperbaric oxygen therapy (HBO) is described as a therapy in which 100 % oxygen is administered to patients via a face-mask or endotracheal tube. It has been recommended and applied for a variety of medical conditions such as in decompression sickness and air embolism. [146] The mechanism of HBO is not fully understood but is associated with gas laws, the physiological and biochemical effects of hyperoxia on the basis of previous studies. According to Boyle's law, the pressure and volume of gas are inversely proportional when the temperature is constant, which is the foundation for many aspects of hyperbaric therapy including a temperature increase during treatment. [146] According to Henry's law, the amount of a given gas that dissolves in a given type and volume of liquid is directly proportional to the partial pressure of that gas in equilibrium with that liquid, which is the basis for increased tissue oxygen tensions with HBO treatment. [147] For instance, tissue oxygen tension is only 55 mmHg when breathing normobaric air but increased to 500mmHg when breathing 100% oxygen at threefold atmosphere absolute, providing a 20 fold increase of oxygen level dissolved in blood. [148] However, HBO increases generation of oxygen free radicals, which oxidise proteins and membrane lipids, damage DNA and inhibit bacterial metabolic functions. HBO is particularly effective against anaerobes, and facilitates the oxygen-dependent peroxidase system by which leukocytes kill bacteria. HBO also improves the oxygen-dependent transport of certain antibiotics across bacterial cell walls. [149]

Current cancer therapy approaches that attempt to address hypoxia and enhance therapy include hyperbaric oxygen or carbogen breathing and the use of electronic affinic radio- or chemosensitisers (e.g. nitroimidazol compounds). [150] Patients have been treated with hyperbaric oxygen or carbogen in attempts to enhance tumour oxygenation. However, these depend on respiratory function, which can sometimes be compromised in elderly or weaker individuals. In addition, breathing pure oxygen has been shown to result in adverse

effects with unwanted oxidative events in off-target tissues. Therefore, these therapies have had very limited success. [151] Furthermore, the cost of HBO is quite high and not universally available. Therefore, further study is necessary to establish its safety and efficacy in clinical conditions.

1.5.2 Oxygen diffusion enhancers

Diffusion plays a key role in transferring small molecules such as oxygen in blood circulation. Furthermore, the diffusivity of oxygen is further challenged when oxygen consumption reaches a high level in situations such as shock or anoxia. [152] Enhancing the diffusivity of oxygen in hypoxic cells and tissues has been suggested as a potential route to overcome severe hypoxia in PDT treatments.

Trans-sodium crocetinate (TSC) is a carotenoid compound which owes its ability to enhance tissue oxygen levels by promoting diffusivity of oxygen and glucose in treated tissue.[153] The compound has a novel mechanism of action, first proposed in the 1970s by Professor John Gainer, and has recently become better understood. The diffusion coefficients of glucose and oxygen tested in water using various TSC concentrations are shown in Figure 1.29. Although a big difference exists with the diffusion coefficient of oxygen in water compared to that of glucose in water, when the TSC concentration is over 5μM, the diffusivities of both solutions increase by 30 % in the presence of TSC. This suggests that TSC does affect oxygen or glucose diffusion indirectly. Nevertheless, hydrogen bonding of neighbouring water molecules is increased by TSC, a mechanism known as “structure-building,” which decreases the hindrance of molecules such as oxygen and glucose. [154] Early studies with TSC involved the treatment of hemorrhagic shock in both rats and pigs. [155] For example, one study showed that TSC was capable of promoting survival in rats breathing 10% oxygen. TSC also was able to increase arterial pO_2 values in a rat model of acute respiratory distress syndrome (ARDS) caused by the injection of oleic acid.[156]

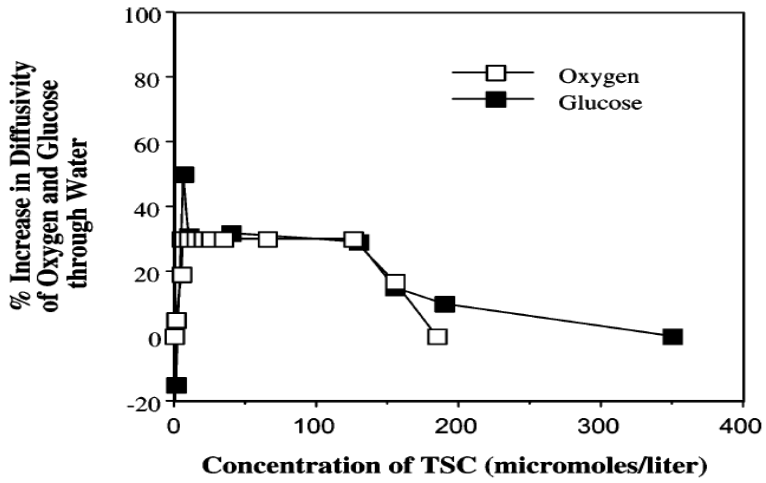

Figure 1. 30 Plot of increase of diffusivity of glucose and oxygen in TSC-water solution upon various loading of TSC. Reproduced from ref [155]

1.5.3 Oxygen generating nanoparticles

One strategy for the generation of molecular oxygen is via the hydrolytic decomposition of solid peroxides, e.g. calcium or magnesium peroxide, which occurs according to **Equation 1.2**. [157] The reaction between calcium peroxide with water first produces hydrogen peroxide (H_2O_2) which then subsequently decomposes to molecular oxygen and water.

$$2CaO_2 + 4H_2O \rightarrow 2Ca(OH)_2 + 2H_2O_2 \rightarrow 2Ca(OH)_2 + 2H_2O + O_2 \qquad \textbf{Equation 1.2}$$

When compared to other solid peroxides such as BaO_2, CaO_2 has several advantages: 1) It possesses a higher aqueous solubility and consequently faster reaction rate with water than other solid peroxides; 2) CaO_2 is easy to synthesise with high yield and purity. 3) CaO_2 powder is relatively inexpensive. [158] [159] However, the maximum rate of the decomposition reaction is dependent on particle size with smaller particles reacting faster than larger particles by virtue of their greater surface area. When CaO_2 is synthesised in nanoparticulate form, the surface area increases dramatically and thus increases the rate of reaction with water. [160]

1.6 Aims and Objectives

The major aim of the work conducted in this thesis was to develop approaches for enhanced PDT or SDT efficacy in pancreatic tumors. This involved the optimization and evaluation of oxygen carrying microbubbles or magnetically responsive microbubbles as delivery vehicles for sonodynamic and antimetabolite therapy of pancreatic cancer (Chapter 3-4) and investigating the effect of oxygen generating nanoparticles for improved photodynamic therapy of pancreatic cancer. (Chapter 5)

1.6.1 Optimisation and Safety Evaluation of Oxygen carrying microbubbles as delivery vehicles for combined sonodynamic and antimetabolite therapy.

The main aim for the work undertaken in Chapter 3 was to determine whether combined SDT / gemcitabine treatment, using intravenously delivered oxygen carrying lipid stabilised microbubbles as delivery vehicle, can provide a significant reduction in the volume of Mia-PaCa-2 tumours compared to SDT or gemcitabine treatment alone and cause no significant toxicity to healthy non-tumour bearing mice.

1.6.2 Magnetically Responsive Microbubbles as Delivery Vehicles for Targeted Sonodynamic and Antimetabolite Therapy of Pancreatic Cancer

The main aim of the work undertaken in Chapter 4 was to evaluate whether external magnetic and low-intensity ultrasound fields can enhance the efficacy of combined antimetabolite / sonodynamic therapy, delivered using magnetically responsive microbubbles, in an orthotopic murine model of pancreatic cancer.

1.6.3 Oxygen Generating Nanoparticles for Improved Photodynamic Therapy of Hypoxic Tumours

The main aim of the work undertaken in Chapter 5 was to prepare and characterise CaO_2 NPs capable of oxygen generation upon decomposition in water. A pH-responsive methacrylate based terpolymer was also synthesised, characterised and used to coat the CaO_2 NPs. The ability of the particles to improve oxygenation in hypoxic environments and enhance PDT-mediated treatment was also evaluated using BxPc-3 pancreatic cancer cells *in vitro* and an ectopic Mia Paca-2 xenograft murine model *in vivo*.

Chapter 2

Materials and Methods

2 Materials and Methods

2.1 Reagents and Materials:

Chemicals were purchased from commercial sources at the highest possible grade. Panc-1, BxPc-3 and Mia Paca-2 cells were obtained from the American Type Culture Collection (ATCC) and matrigel from BD Biosciences, Erembodegem, Belgium. SCID mice (C.B-17/IcrHanHsd-PrkdcSCID) were bred in house. SPION was generously supplied from the Stride research group, Institute of Biomedical Engineering, University of Oxford. MBs were formed using a Microson ultrasonic cell disruptor, 100 W, 22.5 kHz, from Misonix Inc. (NY, USA). Optical microscope images were obtained using a Leica DM500 optical microscope. MB concentration and size were determined using purpose-written MATLAB software (2010B, MathWorks, Natick, MA, USA). Scanning electron microscopy (SEM) analysis was conducted using an "FEI Quanta" scanning electron microscope while dynamic light scattering (DLS) measurements were performed using a Malvern Zetasizer 3000HSA (Malvern, Worcs., UK). Dissolved oxygen measurements were recorded using a Thermo Scientific™ DO Probe Orion™ 083005MD (Fisher Scientific, Ottawa, ON, Canada) while nanoparticle solutions were mixed using a Silverson homogeniser (Silverson Machines Ltd., Chesham, U.K.). UV-Vis spectra were recorded with a Varian Cary spectrometer, using quartz cells with a path length of 1cm. Fluorescence measurements were undertaken using a Cary Eclipse spectrophotometer in aerated solutions with slits = 5 nm while 96 well plates were analysed using a Fluostar Omega plate reader. Tumour pO_2 measurements were performed using an Oxylite oxygen electrode sensor (Oxford Optronics, Oxford, UK). NMR spectra were obtained on Varian 500 MHz instrument at 25.0 ± 1 °C and processed using Bruker software. Mass spectra were obtained using a Finnegan LCQ-MS instrument. HPLC analysis was carried out on a Shimadzu LC-8 preparative pump system (Shimadzu Corp., Kyoto, Japan). Error in measurements was expressed as % standard error of the mean while statistical analysis was undertaken using 2-tailed Students t-test.

2.2. Preparation of biotinylated Rose Bengal, biotinylated 5-FU and biotinylated Gemcitabine

2.2.1. Synthesis of alcohol-functionalised biotin derivative (2) *N-(2-hydroxyethyl)-5-(2-oxohexahydro-1H-thieno[3,4-d]imidazol-4-yl)pentanamide:* To an ice-cooled solution of biotin-N-hydroxysuccinimide ester (prepared by the reaction between biotin and Di(Nsuccinimidyl)carbonate), (3.75 g, 11 mmol) in anhydrous DMF (40 mL), was added 2-aminoethanol (1.0 ml, 16.4 mmol) and the mixture stirred at 25 °C for 30 min. The reaction was monitored by thin layer chromatography (TLC) (Merck Silica 60, HF 254, 20:80 methanol-dichloromethane v/v). The biotin-Nhydroxysuccinimide ester (Rf = 0.76) was consumed within 15 min with the concomitant formation of the alcohol product (Rf = 0.47). The reaction mixture was concentrated under reduced pressure and the residue co-evaporated with DMF to remove excess amounts of 2-aminoethanol. The white residue was recrystallised from water to yield **2** as a light yellow solid (1.7 g, 38%). An analytical sample was obtained from a second recrystallization, m.p. 192-195 °C, 1H NMR (500 MHz, D_2O) 4.49-4.47 (m, 1H, -CH), 4.31-4.30 (m, 1H, -CH), 3.53-3.51 (m, 2H, CH_2), 3.23-3.18 (m, 3H, CH and CH_2), 2.85-2.64 (m, 2H, CH_2), 2.15 (t, 2H, -CH_2), 1.62-1.46 (m, 4H, CH_2 X 2), 1.32-1.26 (m, 2H, CH_2). ^{13}C NMR (125 MHz, D_2O) 177.09 (C=O), 61.98 (CH_2), 60.19 (CH), 59.91 (CH), 55.24 (CH), 41.29 (CH_2), 39.61 (CH_2), 35.42 (CH2), 27.77 (CH2), 27.56 (CH2), 25.02 (CH2). ESMS ($M+H^+$): found 288.70, calculated for $C_{12}H_{21}N_3O_3S$ = 287.13.

2.2.2. Synthesis of Biotin-Gem conjugate (5) *(2R,3R,5R)-5-(4-amino-2-oxopyrimidin-1(2H)-yl)-4,4-difluoro-3 hydroxytetrahydrofuran-2-yl)methyl (2-(5-(2-oxohexahydro-1H-thieno[3,4-d]imidazol-4-yl)pentanamido)ethyl) carbonate):* The synthesis of intermediate **2** has been described in **section 2.2.1.** To a DCM (10 mL) solution of **2** (0.28g, 0.9 mmol), 4-nitrophenyl chloroformate (0.59g, 2.9 mmol), DIPEA (0.50g, 3.9 mmol) and a catalytic amount of pyridine were added at 0^oC and then stirred for 24 hrs at 18^oC. The reaction mixture was then concentrated to dryness and the crude residue containing **3** dissolved in 20 mL of DMF. To this solution, Gem (0.88g, 2.9 mmol) in DMF (5 mL) and TEA (1 mL) were added and the mixture stirred for a further 24 hrs at 18 ^oC. After completion of reaction (monitored by TLC), excess diethyl ether (200 mL) was added to the reaction mixture and stirred for further 45 min at 18^oC. The yellowish oil obtained was separated and washed three times with cold

diethyl ether (50 mL x 3). The crude compound was purified by preparative TLC using DCM / MeOH (9 : 1) as eluent to afford the target compound **5** (0.12g, 22% yield). ^{1}H NMR, 500MHz (DMSO-d_6): δ 7.99-7.91 (m, 3H, CH, NH_2), 6.41-6.33 (m, 1H, CH), 6.12-6.01 (m, 3H, CH, NH X 2), 4.30-4.16 (m, 1H, CH), 4.19-4.12 (m, 3H, CH, CH_2), 3.90-3.75 (m, 2H, CH_2), 3.69-3.58 (m, 2H, CH_2), 3.12-3.09 (m, 1H, CH), 2.93-2.88 (m, 2H, CH_2), 2.83 (brs, 1H, OH), 2.82-2.77 (m, 2H, CH X2), 2.72 (brs, 1H, NH),2.49-2.04 (m, 2H, CH_2), 1.49-1.28 (m, 6H, CH_2 X 3). ^{13}C NMR, 125 MHz (DMSO-d_6): 175.0 (C=O), 166.3 (C), 165.5 (C=O), 156.3 (C=O), 156.1 (C=O), 141.3 (CH), 125.3 (C), 95.2 (CH), 79.2 (CH), 67.2 (CH), 61.9(CH), 60.2 (OCH_2), 55.5 (OCH_2), 39.6 (CH), 37.8 (CH_2), 35.2 (CH), 28.3 (CH_2), 28.0 (CH_2), 25.3 (CH_2). ESI-MS: cald for $C_{22}H_{30}F_2N_6O_8S$, 576.18; found 577.2 ($M + H^+$).

2.2.3 Synthesis of Rose Bengal amine (6) *2-Aminoethyl 2,3,4,5-tetrachloro-6-(6-hydroxy-2,4,5,7-tetraiodo-3-oxo-3H-xanthen-9-yl)benzoate:* To a solution of Rose Bengal sodium salt (1.0 g, 1.0 mmol) in anhydrous DMF (10 mL) was added 2-bromoethylamine (0.32 g, 1.5 mmol) and the mixture was stirred at 80 C for 7 h. The DMF was then removed under reduced pressure and the residue stirred for 18 h in diethyl ether (200 mL). The solution was filtered and the resulting solid stirred in water (200 mL) for 18 h. The solution was filtered and the solid crystallised from MeOH to yield the product as a dark red solid. ^{1}H NMR (500 MHz, DMSO-d6): 2.42 (t, CH2, 2H), 3.80 (t, OCH2, 2H), 7.26 (s, ArH, 2H), 7.60 (s, NH2, 2H). 13C NMR (500 MHz, DMSO-d6): 19.0, 37.5, 49.3, 56.5, 62.7, 76.6, 97.9, 129.6 130.6, 132.4, 133.4, 10.6, 110.9, 134.7, 135.7, 136.4, 137.0, 139.6, 157.5, 163.2, 172.3. HRMS: calculated for $C_{22}H_9Cl_4I_4NO_2$ = 1016.5384, found 1016.1376. I.R. ν_{max} (cm^{-1}) 3430, 2925, 2366, 1615, 1546, 1450, 1337.

2.2.4. Synthesis of biotin–Rose Bengal (7) *2-(5-(2-Oxohexahydro-1H-thieno[3,4-d]imidazol-4-yl)pentanamido)ethyl2,3,4,5-tetrachloro-6-(6-hydroxy-2,4,5,7-tetraiodo-3-oxo-3H-xanthen-9-yl)benzoate:* To a solution of Rose Bengal amine (74 mg, 74 µmol) in 2 mL DMSO, NHS Biotin (25 mg, 74 µmol) dissolved in PBS buffer 2 mL (pH 9) was added. Triethylamine (10 µl, 0.71 µmol) was added to the mixture which was then stirred at room temperature for 12 h. The resulting solution was placed in a solution of hexane: chloroform (200 ml 8:2) and stirred for 24 h at room temperature. The solution filtered and the filtrate retained. The filtrate was washed three times with diethyl ether and dried in a vacuum oven to yield the product as a red powder (14 mg, 10%). ^{1}H NMR (500 MHz, DMSO-d6): 1.28 (m, CH_2, 2H),

1.45 (m, CH_2, CH, 3H), 1.57 (m, CH, 1H), 1.60 (t, CH_2, 2H), 2.52 (q, CH, 1H), 2.58 (m, CH, 1H), 2.79 (q, CH, 1H), 2.97 (t, CH_2, 2H), 3.10 (m, SCH, 1H), 3.85 (t, OCH_2, 2H), 4.09 (t, CH, 1H), 4.28 (t, CH, 1H), 6.34 (s, NH, 1H), 6.41 (s, NH, 1H), 7.46 (s, ArH, 2H), 7.56 (brs, NH, 1H). ^{13}C NMR (125 MHz, DMSO-d_6): 8.98, 9.03, 25.52, 28.57, 29.45, 31.72, 35.52, 37.34, 46.07, 53.13, 55.86, 59.66, 61.48, 64.65, 76.50, 97.69, 110.56, 124.271, 129.37, 130.48, 132.34, 134.79, 135.50, 136.41, 139.79, 157.42, 163.13, 163.57, 172.23, 172.68, 228.31, 230.86 –ve ESMS: calculated for $C_{32}H_{23}Cl_4I_4N_3O_7S$ = 1243.0 found = 1241. I.R. v_{max} (cm^{-}1) 3425, 2924, 2369, 1683, 1576, 1541, 1342. M.P. 188–191 °C.

2.2.5. Synthesis of 5-fluorouracil-1-carboxylic acid (9): *2-(5-Fluoro-2,4-dioxo-3,4-dihydropyrimidin-1(2H)-yl)acetic acid:* A mixture of 5-Fluorouracil (5 g, 38.4 mmol), potassium hydroxide (9.07 g, 161.6 mmol) and chloroacetic acid (3.63 g, 38.4 mmol) in 100 mL of water was refluxed for 2 h at 70 °C. After cooling to room temperature, the pH of the solutionwas adjusted to 5.5 by the addition of concentrated hydrochloric acid. The reaction mixture was then kept in a refrigerator (5 °C) for 18 h and the resulting white crystals isolated by filtration and washed with cold water to produce **9** in 52.5% yield. mp > 200 °C, ^{1}H NMR (500 MHz, D_2O) 7.76 (d, 1H, J = 6 Hz, CH), 4.29 (s, 2H, CH_2). ^{13}C NMR (D_2O):173.58 (C=O), 159.97 (C=O), 150.80 (C=O), 141.20 (C), 131.74 (CH), 51.48 (CH_2). ESMS ($M\text{-}H^+$): found 187.10, calculated for $C_6H_5O_4N_2F$ = 188.11.

2.2.6. Synthesis of biotinylated 5-FU (10) *2-(5-(2-Oxohexahydro-1H-thieno[3,4-d]imidazol-4yl)pentanamido) ethyl 2-(5-fluoro-2,4-dioxo-3,4-dihydropyrimidin-1(2H)-yl)acetate:* N-(2-Hydroxyethyl)-5-(2-oxohexahydro-1H-thieno[3,4-d]imidazol-4-yl)pentanamide (0.5 g, 1.7 mmol), 5-Fluorouracil-1-carboxylic acid (4) (0.4 g, 2.1 mmol), DMAP (0.023 g, 0.17 mmol) and HOBT (0.023 g, 0.17 mmol) were added to 20 mL of anhydrous DMF in a 100 mL 2-neck round bottom flask under a N_2 atmosphere. The mixture was heated at 40 °C and stirred until a homogeneous solution was obtained. DCC (0.4 g, 1.9 mmol) was then added to the reaction mixture and allowed to stir at room temperature for 12 h. The DMF was removed under reduced pressure, diethyl ether (50 mL) added and the contents stirred for 20 min. The resulting white semi-solid product was removed by filtration and after removing excess diethyl ether under reduced pressure, the crude product was purified by preparative HPLC (C-18 column) using acetonitrile/water (80:20 v/v) as mobile phase. The product **10** was obtained after lyophilisation of the desired fractions as a white semi-solid (0.24 g, 30 %

Yield). 1H NMR (500 MHz, D2O): 7.67 (d, 1H, J =6.0 Hz, CH), 4.50-4.47 (m, 1H, CH), 4.31-4.29 (m, 1H, CH), 4.19(s, 2H, CH_2), 3.54 (t, 2H, CH_2), 3.22-3.19 (m, 2H, CH2), 2.89-2.86 (m,1H, CH), 2.67-2.64 (m, 2H, CH_2), 2.17-2.14 (m, 2H, CH_2), 1.61-1.47(m, 4H, CH_2 X 2), 1.47-1.28 (m, 2H, CH_2). ^{13}C NMR 125 MHz, D_2O):177.12 (C=O),173.74 (C=O), 165.33 (C=O), 160.01 (C=O), 159.81(C=O), 141.14 (C), 131.71 (CH), 62.00(CH_2), 60.22 (CH), 59.94 (CH), 55.26 (CH), 51.53 (CH_2), 41.31 (CH_2), 39.64 (CH_2), 35.45 (CH_2), 27.79(CH_2), 27.58 (CH_2), 25.14 (CH_2). ESMS (M-H^+) found 456.20, calculated for $C_{18}H_{24}FN_5O_6S$ = 457.48.

2.3. Preparation of O_2 loaded microbubbles: For the preparation of DBPC MBs, DBPC (4.0 mg, 4.43 mmol), DSPE-PEG (2000) (1.35 mg, 0.481 mmol) and DSPE-PEG (2000)-biotin (1.45 mg, 0.481 mmol) in a molar ratio of 82:9:9 were dissolved in chloroform and placed in a glass vial. The solution was heated at 40 ^oC until all the chloroform had evaporated. PBS (pH 7.4 ± 0.1) (5 ml) was added to the dried lipid film and the contents heated above the lipid phase transition temperature (>70 ^oC) under constant magnetic stirring for 30 min. The suspension was then sonicated with a Microson ultrasonic cell disruptor for 1.5 min (100 Watts, 22.5 kHz at power setting 4), the headspace filled with perfluorobutane (PFB) gas and the gas/liquid interface sonicated (power 19) for 20 s producing PFBMBs. The MB suspension was cooled in an ice bath for approximately 10 min. An aqueous solution of avidin (50 mL, 10 mg/mL) was then added to the cooled MB suspension and stirred for a further 10 min. The suspension was then centrifuged (300 RPM, 10 min) and the resulting MB “cake” concentrated into 1 mL of PBS (pH 7.4 ± 0.1). This was divided into two freeze drying vials. For the PFBMBs the vials were then crimped (sealed with a metal cap). To create oxygen filled MBs the headspace of the vial and the MB suspension was sparged under a positive pressure of oxygen gas for 2 min and the vial was then crimped. Following preparation as described above, MB samples were imaged under conventional optical microscopy to determine their size distribution and concentration. 10 mL samples were removed from each suspension and diluted in 90 mL of PBS (pH 7.4 ± 0.1) followed by examination on a haemocytometer (Bright-Line, Hausser Scientific, Horsham, PA, USA). Images were obtained with a 40 X objective lens with a Leica DM500 optical microscope. The MB size distribution and concentration were then obtained using purpose written image analysis software in Matlab (2010B, The MathWorks, Natick, MA, USA).

2.4 Preparation of O_2MB-Gem, O_2MB-5FU and O_2MB-RB: Saturated solutions of biotin-RB, biotin-5FU and biotin-GEM were prepared in a 0.5% DMSO solution in PBS (pH 7.4 ± 0.1). A 0.3 mL aliquot of these stock solutions were then added separately to three 2 mL suspensions of avidin functionalised PFBMBs (2.1 x 10^9 MB/mL) and the contents vortex mixed for 15 min. The suspensions were then centrifuged (900 rpm) for 5 min and the MB conjugates isolated as a milky suspension floating on top of the solution. The solution was removed and replaced with a further 0.3 mL of stock solution containing either biotin-RB, biotin-5FU or biotin-GEM and the mixing/centrifugation steps repeated. The MB suspensions were then washed with PBS (5 mL), centrifuged (900 rpm) for 5 min and the MBs transferred to a clean centrifuge tube. This washing procedure was repeated again and the isolated PFBMB-RB, PFBMB-5FU and PFBMB-GEM conjugates placed in glass vial. The PFBMB-RB, PFBMB-5FU and PFB-GEM conjugates were then sparged with oxygen gas for 2 min and the resulting O_2MB-RB, O_2MB-5FU and O_2MB-GEM conjugates were then crimped in the vials and ready to use. The MB number and size were determined by withdrawing 10 µL samples of the O_2MB-RB, O_2MB-5FU and O_2MB-Gem conjugates and diluting them separately in 90 µL of PBS (pH 7.4 ± 0.1) followed by analysis using a haemocytometer (Bright-Line, Hausser Scientific, Horsham, PA, USA). Images were obtained with a 40 x objective lens using a Leica DM500 optical microscope. The MB size distribution was then obtained following processing using ImageJ software. Where appropriate, the O_2MB-RB and O_2MB-Gem conjugates were mixed together in a 1:1 ratio for combined chemo-sonodynamic therapy treatments. A fluorescence image of the mixed MB suspension was obtained using a Nikon Eclipse E400 epi-fluorescence microscope equipped with a B2A and G2A filter set using an excitation wavelength of 548nm with emission collected at 565nm. The drug loading on the surface of the MB conjugates was determined using UV-Vis spectroscopy for biotin-RB and reverse phase HPLC for biotin-5FU and biotin-GEM, using a Phenomenex C18 column (250 x 4.6 mm, 5 µm), a mobile phase consisting of acetonitrile: 1.5 mM potassium phosphate monobasic (5:95 v/v), a flow rate of 1.0 mL/min^{-1} using 206 nm as the detection wavelength.

2.5 Preparation of avidin functionalised magnetic microbubbles (MagPFBMBs): Avidin functionalised magnetic MBs were prepared by following the procedure discussed in section **2.3** except after the lipid suspension stirred for 30 min in a water bath, FluidMAG-Lipids NPs

(150 µL) were then added to the solution and the mixture was sonicated with a handheld sonicator probe for 1.5 min (100 W, 22.5 kHz, power setting 4). MagPFBMBs were analyzed using a Leica DM500 optical microscope to obtain the size distribution and concentration. For this, 10 µL of suspension was diluted in 190 µL of PBS and examined using a haemocytometer (Bright-Line, Hausser Scientific, Horsham, PA, USA). 30 images were obtained with a 40 x objective lens and analysed with customised image analysis package in MATLAB (2010B, MathWorks, Natick, MA, USA). The iron content in the MagPFBMBs was determined by atomic absorption spectroscopy using a Varian fast sequential atomic absorption spectrometer. A calibration curve was constructed using known concentrations of Fe(III) in 0.5 M HCl. Readings were taken at 248.3 nm, 0.5 nm slit width, 10.0 mA lamp current, with the following flame settings; flame type: air/acetylene, air flow: 13.50 L/min, acetylene flow: 2.00 L/min, burner height: 13.5 mm. A 300 µL sample of MagMBs was sonicated to destroy the bubbles and dissolved in 0.5 M HCl. The amount of Fe (III) present in the sample was calculated by reference to the calibration curve and the total iron content determined using a magnetite (Fe_3O_4) Fe(III):Fe(II) ratio of 2:1.

2.6. Preparation of $MagO_2MB$-Rose Bengal and $MagO_2MB$-5FU conjugates: The synthesis of biotin functionalised Rose Bengal and biotin functionalised 5-FU have been described in section **2.2.2** and **2.2.5**. Saturated solutions of biotin-RB and biotin 5-FU were prepared in a 0.5% (v/v) DMSO: PBS (pH 7.4 ± 0.1) solvent mixture. 100 µL of biotin-5FU and biotin-RB were added to separate samples (2 mL each) of MagPFBMBs and allowed to mix for 5 min on a rotary shaker. Both samples were centrifuged (100 RCF, 5 min) to remove unbound material and PFBMB conjugates were re-suspended in 1 mL of PBS solution (pH 7.4 ± 0.1). This conjugation/centrifugation process was repeated three times. The final PFBMB-RB and PFBMB-5FU conjugates were transferred to glass vials. $MagO_2MB$-RB and $MagO_2MB$-5FU conjugates were obtained by sparging the MagPFBMB-RB and MagPFBMB-5FU with pure O_2 gas for 2 min and sealing the vial via crimping. A small sample (100 µL) of both the $MagO_2MB$-RB and $MagO_2MB$-5FU conjugates was retained and the MB number again counted using a haemocytometer. The remaining sample was sonicated in an ultrasonic bath for 5 min to burst the MBs and the Rose Bengal and 5-FU concentration determined using UV–Vis (ultraviolet–visible) spectroscopy and HPLC (high performance liquid chromatography) respectively.[161]

2.7. Retention of MagMBs in a flow cell using an external magnetic field: MagPFBMBs without payload were used in this study to reduce wastage of biotin-5FU and biotin-RB. 1 x 10^7 MagPFBMBs were placed in a 1 mL syringe, connected to an ibidi μ-Slide VI flow chamber using silicone tubing (1.6 mm internal diameter) and placed in a peristaltic syringe pump. A single N52 grade NdFeB permanent magnet cube (12.7 mm) with an internal magnetization of 1.14 x 10^6 A/m was positioned 1 mm from the base of the flow chamber. Values for a field of 0.46 T and gradient of 83.1 T/m inside the flow chamber were calculated using a model described and experimentally verified previously, [162] whereby the field was determined by breaking the magnet into a 3-dimensional lattice of evenly-distributed point moments, and summing the contributed dipole field from each moment. The MagPFBMBs were pumped through the flow chamber at a rate of 0.6 mL/min. Once the syringe was empty, the magnetic field was removed and 1 mL of PBS (pH 7.4 ± 0.1) added to the syringe to flush the flow chamber's content into a clean vial. Collected MBs were counted using the method described above. As a control, the experiment was repeated in the absence of a magnetic field but under otherwise identical conditions. The number of MBs collected during the PBS flush was again recorded.

2.8. Preparation of uncoated CaO_2 NPs: CaO_2 nanoparticles were prepared following the method described by Khodaveisi et al. [163] Ammonia solution (15.0 mL, 1 M) and PEG 200 (120.0 mL, 0.6744 mol) was added to a stirred solution of calcium chloride (3.0 g, 0.027 mol) in distilled water (30 mL). A solution of 35% H_2O_2 (15 mL, 0.17 mol) was then added to the mixture at a rate of 3 drops per minute and the colourless solution stirred for a further 2 h at room temperature. A NaOH solution (0.1 M) was then added until a pH value of 11.5 was achieved when the solution changed to a white coloured suspension. The precipitate was separated by centrifugation (8000 g, 5 min) and the resulting pellet washed three times with NaOH (25 mL, 0.1 M). The precipitate was then washed with distilled water until the filtrate pH reached 8.4 and the resulting solid dried in vacuo at 80 °C for 2 h. The resulting particles were suspended in ethanol and sonicated for 5 min. The suspension was passed through a Millex Filter Unit (0.45 μm) to isolate larger particles and the filtrate concentrated to dryness providing the uncoated CaO_2 nanoparticles as a white powder. The size of the nanoparticles was determined by SEM and DLS.

2.9. Determination of CaO_2 content in the uncoated CaO_2 NPs: The active CaO_2 content of the NPs was determined by reaction with luminol in PBS. A chemiluminescence/concentration calibration curve for the reaction of H_2O_2 with luminol was performed according to the procedure adopted by Komagoe et al. [164] CaO_2 NPs suspended in ethanol (50 µL, 35.6 µM) were added to a luminol solution (50 µL, 10 mg/mL in PBS) and the luminescence intensity determined using a plate reader. The CaO_2 content was determined by indirectly measuring the number of moles of H_2O_2 produced (by reference to a calibration graph) from the fixed mass of CaO_2 powder and assuming all the available CaO_2 was converted to H_2O_2.

2.10. Determination of singlet oxygen generation: The ability of the CaO_2 NPs to enhance PDT mediated singlet oxygen generation was determined using the singlet oxygen probe SOSG. CaO2 NPs (2 mg) in de-oxygenated ethanol (1 mL) were added to a de-oxygenated PBS solution containing SOSG and RB resulting in final concentrations of 2.5 µM (SOSG), 5.0 µM (RB) and 35.6 µM (CaO_2 NPs). The solutions were then exposed to white light for 5 min (Fenix LD01 LED, 50 mW output, 113.0 J/cm^2) Control experiments were also undertaken and included (i) CaO_2 NP + light and (ii) RB +light. The intensity of SOSG fluorescence at 525 nm upon excitation at 505 nm was recorded at the beginning and at the end of each experiment.

2.11. Preparation of polymer 11: 2-(Dimethylamino) ethyl methacrylate (157.2 mg, 1 mmol), methyl methacrylate (100.1 mg, 2 mmol) and ethyl acrylate (100.1 mg, 1 mmol) and a catalytic amount of the free radical initiator (ABCN) were dissolved in anhydrous THF (5 mL) and placed in a Carious reaction vessel. The contents were then subjected to three freeze-pumpthaw cycles, sealed under vacuum and placed in a Carious oven at 80 °C for 72 h. The contents were removed and hexane (20 mL) added to the facilitate precipitation followed by centrifugation for 5 min at 3500 g. The supernatant was removed, the pellet containing **11** re-dissolved in anhydrous THF, precipitated again using hexane and centrifuged at 3743 × g. This purification procedure was repeated twice further before the pellet was dried in vacuo at 80 °C and characterised by ^{1}H NMR spectroscopy.

2.12. Coating of CaO_2 NPs with polymer 11 to form CaO_2-11 NPs: CaO_2 NPs were coated with **11** using a modified single emulsion method. [165] CaO_2 NPs (10 mg) were dispersed in

hexane (10 mL) and sonicated for 5 min. The NP suspension was then added dropwise at a rate of 2 mL/min to a solution of **11** (100 mg, 0.36 μmol) in ethanol (40 mL) using a Silverson homogeniser at 8000g for 5 min to ensure efficient mixing. After a further mixing period of 6 h, excess solvent was allowed to slowly evaporate and the CaO_2-**11** NPs reconstituted in sterile water. Particle size was then determined using SEM and DLS.

2.13. Dissolved oxygen experiments: For the dissolved oxygen experiments involving the uncoated CaO_2 NPs, an ethanol solution containing the NPs (10.0 mg, 24 mmol) was added to 10 mL of de-oxygenated PBS solvent. The dissolved oxygen was then measured and recorded every minute using a dissolved oxygen meter. For dissolved oxygen experiments involving the CaO_2-**11** NPs, separate solutions of de-oxygenated water were pH adjusted to pH 7.4 or 6.2. The CaO_2-**11** NPs (2 mg) were then added to each solution and the dissolved oxygen measured using a dissolved oxygen meter 3 min following addition. Results were compared against identical solutions in the absence of CaO_2-**11** NPs. Both sets of experiments were repeated in triplicate.

2.14. Solubility of CaO_2-11 NPs with change in pH: The pH of an aqueous suspension containing CaO_2-**11** NPs (2 mg in 10 mL) was lowered from pH 7.4 to pH 6.2 in approximate 0.1 pH increments following the addition of very small aliquots of 0.1 M HCl. Photographs of the resulting suspensions/solutions were taken at pH 7.4, 6.9 and 6.2.

2.15 In vitro cytotoxicity of O_2MB-GEM, O_2MB-5FU and O_2MB-RB*:* The human primary pancreatic carcinoma cell lines Mia Paca-2 and PANC-1 were maintained in Dulbecco's Modified Eagle's Medium (DMEM) while adenocarcinoma BxPc-3 cells were maintained in RPMI-1640 medium, all of which were supplemented with 10% (v/v) foetal bovine serum in a humidified 5% CO_2 atmosphere at 37^{o}C. A mouse pancreatic cancer cell line T110299 (KPC and a gift from Prof. J. Siveke, Technical University of Munich, Germany) was derived from a primary pancreatic tumour of genetically modified KPC mouse model. T110299 cells were maintained in high glucose DMEM with 10% FBS, 1% Non-Essential Amino Acids, 1% L-glutamine and 1% Pen/Strep. $5x10^3$ cells were seeded in 96 well plates and placed in an incubator (37 ^{o}C, 5% CO_2) and 24 h later were treated with a suspension of either O_2MB-Gem, O_2MB-RB or a combination of O_2MB-Gem / O_2MB-RB [MB] = 2.7×10^6; [RB] = [Gem] = 5 μM. After 3 hours, selected wells were treated with ultrasound delivered using a Sonidel

SP100 sonoporator (1 MHz, 30 seconds, 3 Wcm^{-2}, duty cycle = 50%). Untreated cells and cells treated with ultrasound only were used for comparative purposes. After 24 hours, cell viability was determined using a MTT assay. For the efficacy comparison between Gem and Biotin-Gem (**5**), $5x10^3$ BxPc-3 and Mia Paca-2 cells were seeded in 96 well plates, placed in an incubator (37 ^oC, 5% CO_2) and 24 h later were treated with 0, 5, 10, 25 100 and 100 µM of Gem or 4 and cell viability determined using a MTT assay 48h later.

2.16 In vitro cytotoxicity of $MagO_2MB$-GEM, $MagO_2MB$-5FU and $MagO_2MB$-RB: Human primary pancreatic adenocarcinoma cell lines Mia Paca-2 and Panc-1, were maintained in DMEM medium. The mouse primary pancreatic adenocarcinoma T110299 derived from a GEM mouse, was also maintained in DMEM medium while the human primary pancreatic adenocarcinoma cell line BxPc-3 was maintained in RPMI-1640 medium, all of which were supplemented with 10% (v/v) foetal bovine serum and grown in a humidified 5% CO_2 atmosphere at 37 °C. These cells were plated into the wells of a 96-well tissue culture plate at a concentration of 5×10^3 cells per well and incubated for 24 h at 37 °C in a humidified 5% CO_2 atmosphere. The media was then removed from each well and replaced with 100 µL of treatment suspension and 100 µL of fresh medium. This resulted in a final MB count and RB or 5-FU concentration as follows: $MagO_2$MB-RB: 106 MB, [RB] = 5µM; $MagO_2$MB-5FU; 107 MB, [5-FU] = 100 µM and combined $MagO_2$MB-RB/$MagO_2$MB-5FU: 107 MB, [RB] = 5 µM, [5-FU] = 100 µM. Where required, individual wells were then placed in direct contact with the emitting surface a Sonidel SP100 sonoporator with ultrasound gel used to mediate contact. Each well was treated with ultrasound for 30 s, using a frequency of 1 MHz, an ultrasound power density of 3.0 W cm^{-2} (ISATP; spatial average, temporal peak) corresponding to a peak to peak pressure of 0.8 MPa in water and 0.5 MPa inside the well as measured with a needle hydrophone (Precision Acoustics, Dorset, UK); and a duty cycle of 50% (pulse frequency =100 Hz). The solution was then removed from the wells and fresh medium added (200 µL). Plates were incubated in a humidified 5% CO_2 atmosphere at 37 °C for 21 h and cell viability determined using an MTT assay. Results were compared with those obtained using untreated cells and cells exposed to ultrasound treatment alone.

2.17. In vitro PDT experiments for uncoated CaO_2 NP: BxPc-3 cells were seeded in a 96 well plate at a density of 5×10^4 cells per well and incubated in a hypoxic chamber at 37 °C ($O_2/CO_2/N_2$, 0.1: 5: 94.9, v/v/v) for 3 h. The cells were then treated with either (i) RB or (ii)

RB with CaO_2 NPs to reach a final concentration per well of 1 µM (RB) and 25 µM (CaO_2) respectively. The CaO_2 NPs were initially prepared in EtOH that was diluted 1:1 v/v with PBS (100 µL total volume) immediately before addition to wells containing 100 µL media leading to a total EtOH concentration of 25% v/v. Control wells containing untreated cells or cells treated with vehicle alone (i.e. EtOH/PBS 1:1 v/v 100 µL) were undertaken for comparative purposes. The cells were allowed to incubate with the drug/NPs/vehicle for 5 mins; the medium was then removed and replaced with fresh media. The cells were then exposed to white light treatment for 30 s (Fenix LD01 LED, 50 mW output, 11.3 J/cm^2). Following light treatment cells were incubated for a further 3 h in the hypoxic chamber and then for a further 24 h under normoxic conditions in a humidified 5% CO_2 atmosphere at 37 °C. Cell viability was then determined using a MTT assay.

2.18 In vivo cytotoxicity of O_2MB-GEM, O_2MB-5FU and O_2MB-RB: All animals employed in this study were treated in accordance with the licenced procedures under the UK Animals (Scientific Procedures) Act 1986. Experimental procedures were approved by Ulster University ethic committee: Chair Finbarr O'Hart. All animal experiments were carried out under Professor Anthony McHale's project licence (2733) and my personal licence number (PIL 1660). Mia Paca-2 cells ($5x10^6$) in 100 uL Matrigel were sub-cutaneously implanted into the rear dorsum of SCID (C.B-17/IcrHan®Hsd-*Prkdcscid)* mice. Tumours started to form approximately 1-2 weeks after cell implantation. Once the tumour became palpable, dimensions were measured using Vernier callipers. The geometric mean diameter was used to determine tumour volume using the equation $4\pi R^3/3$.

The optimum US exposure conditions SCID mice was identified by the following procedures: Mice bearing ectopic Mia paca-2 tumours (241 ± 6 mm^3) were randomly allocated into 12 groups (n=5). **Group 1** received no treatment; **Group 2** the O_2MB-Gem/RB conjugate alone; **Group 3** the O_2MB-5-FU/RB conjugate alone; **Group 4** received US treatment alone at 1 MHz, 3.5 W/cm^{-2} and 30% duty cycle; **Group 5** received US treatment alone at 1 MHz, 3.5 W/cm^{-2} and 50% duty cycle; **Group 6** received US treatment alone at 1 MHz, 4.0 W/cm^{-2} and 30% duty cycle. **Group 7** received O_2MB-Gem/RB conjugate + US treatment at 1 MHz, 3.5 W/cm^{-2} and 30% duty cycle; **Group 8** received O_2MB-Gem/RB conjugate + US treatment at 1 MHz, 3.5 W/cm^{-2} and 50% duty cycle; **Group 9** received O_2MB-Gem/RB conjugate + US treatment at 1 MHz, 4.0 W/cm^{-2} and 30% duty cycle; **Group 10** received O_2MB-5-FU/RB conjugate + US

treatment at 1 MHz, 3.5 W/cm^{-2} and 30% duty cycle; **Group 11** received O_2MB-5-FU/RB conjugate + US treatment at 1 MHz, 3.5 W/cm^{-2} and 50% duty cycle and **Group 12** received O_2MB-5FU/RB conjugate + US treatment at 1 MHz, 4.0 W/cm^{-2} and 30% duty cycle. MB conjugates were administered by tail vein injection (100 µL) containing 1.6*10^8 MB/mL with [5-FU] = 344 µM; [Gem] = 442 µM and [RB] = 557 µM. Ultrasound application occurred during and for 3.5 min following injection with a second US treatment applied 30 min following the first. Tumours were measured daily using callipers and the tumour volume plotted for each group as a function of time.

The effect of a second treatment on the tumour growth was done by following procedures. SCID mice bearing ectopic Mia Paca-2 tumours (213 ± 7 mm^3) were randomly allocated into 6 groups (n=5) as follows. **Group 1** received no treatment; **Group 2** US only; **Group 3** the O_2MB-Gem/RB conjugate only; **Group 4** the O_2MB-Gem/RB conjugate + US; **Group 5** the O_2MB-5FU/RB conjugate only and **Group 6** the O_2MB-5FU/RB conjugate + US. MB conjugates were again administered by tail vein injection (100 µL) (7.5*10^8 MB/mL with [5-FU] = 2.02 mM; [Gem] = 2.55 mM and [RB] = 879 µM). Ultrasound application occurred for 3.5 min during injection and a further 3.5 min following injection using the optimised parameters. Tumours were measured daily using callipers and the tumour volume plotted for each group as a function of time.

2.19 In vivo cytotoxicity of MagO$_2$MB-GEM, MagO$_2$MB-5FU and MagO$_2$MB-RB*:* BxPc-3 Luc cells were maintained in RPMI-1640 medium supplemented with 10% foetal calf serum as described above. Cells (1 × 10^6) were re-suspended in 100 µL of Matrigel® and orthotopically implanted into the head of the pancreas of female Balb/c SCID (C·B-17/IcrHan®Hsd-Prkdcscid) mice. 19 days after implantation, animals were randomly distributed into 3 groups (n = 4). Following induction of anaesthesia (intraperitoneal injection of Hypnorm/ Hypnovel), a 100 µL mixture of PBS containing MagO$_2$MB-RB/ MagO$_2$MB-5FU (MB = 1.6 × 10^8, [RB] = 350 µM and [5-FU] = 700 µM) was administered by tail vein injection to Groups 2 & 3 while Group 1 received vehicle only. For Group 2, ultrasound (frequency =1 MHz, ultrasound power density= 3.5 W cm^{-2} ISATP; spatial average temporal peak, corresponding to a free field peak to peak pressure of 0.85 MPa, duty cycle = 30% and pulse repetition

frequency =100 Hz) was directed to the tumour region (determined using prior bioluminescent imaging) via the abdomen for 3.5 min during and after injection (3.5 min total). For Group 3, in addition to ultrasound using the above parameters, a stack of permanent magnet discs (arranged to deliver the optimal magnetic force to the tumour region) [5] was directed to the tumour region (again via the abdomen) for 3.5 min during and after injection (3.5 min total), resulting in an approximate magnetic field at the tumour of 0.10 T and gradient 14.9 T/m. Treatments using the above conditions were repeated on Days 20 and 21 with animals sacrificed on Day 28. Tumours were then surgically excised and tumour volumes determined by direct measurement.

2.20 Molecular Biology + qPCR analysis of tumour cells suspension in Chapter 3: To establish the effect of combined chemo-sonodynamic therapy on the expression of specific genes involved in the development and progression of pancreatic cancer, tumours in mice from groups 1 and 5 mentioned in **section 2.18** were removed post-mortem following the final measurement on Day 8. Tumours were snap-froze using liquid nitrogen and RNA was extracted using Trizol reagent (Life Technologies) in accordance with the manufacturer's instructions.[166] 1 µg of RNA per tumour was reverse transcribed using First Strand cDNA synthesis kit (Roche) in accordance with manufacturer's instructions [167] and the cDNA from the tumours in each group were pooled. Samples were analysed in duplicate on Roche RealTime Ready custom 96 well panels (Roche) analysing nine specific genes involved in pancreatic cancer. The genes investigated were vascular endothelial growth factor (VEGFC), interleukin 8 (IL8), SMAD family member 4 (SMAD4), hypoxia inducible factor 1 (HIF1A), von Hippel-Lindau (VHL), runt-related transcription factor (RUNX2), sex determining region Y-box 2 (SOX2), NANOG, epithelial cell adhesion molecule (EPCAM). The results were normalised to a reference gene set (Beta actin, 18s ribosomal RNA and GAPDH). The percentage changes in gene expression for treated tumours were compared against untreated tumours.

2.21 Molecular Biology + qPCR analysis of tumour cells suspension in Chapter 4: Following the determination of tumour volume a single cell suspension was prepared from the excised tumours. This involved homogenising the tumour tissue in 4% FCS in RPMI 160 µL (30 mg/mL) collagenase type II, 50 µL (2 µg/mL) DNAse and stirring for 15 min at room temperature. A further 160 µL of collagenase II was subsequently added and the contents

stirred for a further 15 min. The mixture was filtered through a 100 µm filter, centrifuged at 400 RCF for 5 min and re-suspended in 1 mL of Red Cell Lysis Buffer (RCLB) for 10 min. RCLB was neutralised by adding media containing FCS and cells were recovered by centrifuging at 400 RCF. The pellet was washed twice with PBS, centrifuged and re-suspended in 700 µL PBS buffer. For BAX expression, 300 µL of single cell suspension in staining buffer was permeabilised using BD permeablisation buffer (BD Biosciences UK). Permeabilised cells were re-suspended in 300 µL of staining buffercontaining BAX antibody (Cell Signalling Technology, D2E11) (10 µg/mL) and incubated for 30 min at room temperature. The cells were washed in ice cold PBS and the cell pellet was re-suspended in FITC secondary antibody (Abcam, ab6717-1) for 1 h. Cells were washed three times by centrifugation at 400 RCF for 5 min in ice cold PBS, resuspended in 650 µL of PBS buffer nd analysed by flow cytometry. For active caspase expression, the Pan Caspase NIR probe kit (Vergent Bioscience) was used according to the manufacturer's instructions. The kit utilises the caspase family inhibitor VAD-FMK conjugated to a near IR dye (780-VAD-FMK) as a marker that irreversibly binds to activated caspases in apoptotic cells. Essentially, 300 µL of tumour single cell suspension diluted in staining buffer was centrifuged, the pellet resuspended in 300 µL of 1XCAS-MAP NIR probe and incubated at room temperature in the dark for 1 h. Cells were washed three times by centrifugation at 400 RCF for 5 min in ice cold PBS and re-suspended in 650 µL of staining buffer and analysed by flow cytometry. qRT-PCR was used to investigate the expression of TMBIM1 in tumours as previously described [8]. Briefly, RNA was extracted from microdissected slides using the RecoverAll Kit (Life Technologies, Paisley, UK). cDNA synthesis was carried out using the Superscript III First Strand cDNA synthesis kit (Life Technologies, Paisley, UK) using the reverse primer of each of TMBIM1 (transmembrane BAX inhibitor motif containing 1) and the two housekeeping genes;18S rRNA and b-actin. qRT-PCR was carried out using the SYBR Green kit on the CFX96 instrument (BioRad, UK). The qRT-PCR cycle was as follows: 95 °C for 3 min, 95 °C for 10 s, 60 °C for 45 s for 40 cycles. For analysis, the geometric mean of 18S rRNA and b-actin was taken as the single housekeeping value. Statistical comparison between the groups was carried out using two-way ANOVA with Bonferroni post-hoc analysis. The primers used to investigate the TMBIM1 expression are shown in the table below.

Primer	Sequence
TMBIM1 Forward	CATCACTGCGGTGGTATCCA
TMBIM1_Reverse	GTATTGGAAGTAGAGCACAATGCTAGT
β-Actin Forward	CGTGGGCCGCCCTAGGCACCA
β-Actin Reverse	TTGGCCTTAGGGTTCAGGGGGG
18SrRNA_Forward	TGACTCAACACGGGAAACC
18SrRNA_Reverse	TCGCTCCACCAACTAAGAAC

2.22 Determining the toxicity of O_2MB-RB / O_2MB-Gem and MagO_2MB-RB / MagO_2MB-5FU treatment in healthy non-tumour bearing mice: For O_2MB-RB / O_2MB-Gem treatment, Healthy MF1 mice (8 week old) were randomly distributed into 4 groups (n=10; 5 female and 5 male). Group 1 received no treatment; Group 2 received a 100 µL IV (tail vein injection) of the mixed O_2MB-RB / O_2MB-Gem suspension containing (2.6 X10^8 MB / mL^{-1}, 480.0 µM Gem and 610.0 µM RB) while groups 3 & 4 received 100 µL IV (tail vein injections) of Gem (57.0 mM) or RB (1.0 mM) respectively. A second treatment was also administered 3 days after the initial treatment. For MagO_2MB-RB / MagO_2MB-5FU treatment, healthy MF1 mice (8 weeks old) were randomly distributed into four groups (n= 10). Group 1 received no treatment; Groups 2 & 3 received a tail vein injection (100 µL) of 5-FU (115 mM) or RB (1.03 mM) respectively and Group 4 received a tail vein injection (100 µL) containing a suspension of MagO_2MB-RB/MagO_2MB-5FU ([MB] = 2.3 × 10^8, [RB] =570 ± 15 µM, and [5FU] = 503 ± 7 µM)) on Day 1 and Day 8. Pre-treatment tail vein bleeds (0.10 mL) were collected in lithium heparinised tubes on Day 0 with the post-treatment bleeds taken in a similar manner on Day 15. Blood samples were taken 15 days following treatment and transferred to CTDS Ltd (Garforth, UK) for whole blood and plasma biochemistry analysis including urea test, Alanine Aminotransferase (ALT) test, Red Blood Cell Count (RBC), Haemoglobin test, Haematocrit test, Mean Corpuscular Volume (MCV) test, Mean corpuscular haemoglobin concentration (MCHC) test, Platelets count test, White Blood Cell Count (WBC), neutrophils count and

lymphocytes count. After harvesting blood samples, animals were sacrificed and the liver / kidneys were placed in formalin free fixative for 24 hours. The tissues were then placed in an automated tissue processor, Leica TP1020 system, passed between increasing concentrations of ethanol followed by xylene treatment and paraffin wax embedding. The following day, the wax embedded tissue samples were placed in moulds containing paraffin wax. Once the wax blocks had solidified, 5 μm sections were cut, placed on a glass slide and stained with haematoxylin and eosin (H&E) using an automated staining protocol. In some cases, additional stains (i.e. reticulin, Masson's trichrome, Perl's Prussian blue stain) were used when necessary. The stained sections were reviewed histologically by pathologists with expertise in liver and renal pathology. Liver architecture was initially assessed to establish if there was significant remodelling or fibrosis. The various liver compartments were subsequently examined for pathological changes. Portal tract and lobular inflammation grading was adapted from the Ishak (modified HAI) system. [168] Portal tract inflammation was graded numerically from 1 (none) to severe, affecting all portal tracts. Lobular inflammation was assessed at x10 magnification and graded as 1 (none) to 4 (severe, typically averaging >10 foci per x10 field). Fatty liver disease grading, referred to as steatosis/steatohepatitis, was undertaken based on parameters assessed in the NAFLD activity score. [169] In short, steatosis was graded based on a visual estimate of the percentage of liver cells affected as 1 = none or less than 5%; 2 = mild, (5- 33%); 3 = moderate (34 – 66%) and 4 = severe (greater than 67%). Kidney analysis was undertaken following a similar approach assessing the glomerular cellularity, glomerular basement membrane, tubular vacuolation, interstitial inflammation, interstitial fibrosis, vessel integrity and the collecting system. Statistical analysis was undertaken using a student's t-test where the O_2MB-Gem / O_2MB-RB group or the MagO_2MB-RB/MagO_2MB- 5FU group was compared directly with the Gem, RB and untreated groups.

2.23. Determination of tumour pO_2 for CaO_2-11 NPs experiments in vivo: All animals employed in this study were treated humanely and in accordance with licenced procedures under the UK Animals (Scientific Procedures) Act 1986. The ability of the CaO_2-**11** NPs to influence tumour hypoxia was examined in a mouse xenograft tumour model of human pancreatic cancer. Mia Paca-2 cells were maintained in RPMI- 1640 medium supplemented with 10% foetal calf serum. Cells were cultured at 37 °C under 5% CO_2 in air. The cells (5 ×

10^6) were resuspended in 100 µL of Matrigel® (BD Biosciences, Erembodegem, Belgium) and implanted subcutaneously into the rear dorsum of male SCID mice. Tumour formation occurred approximately 5 weeks after implantation and tumour measurements were taken every other day using callipers. Once the tumours had reached an average volume of 254 ± 17 mm^3 calculated from the geometric mean diameter using the equation tumour volume = (W X H X L/2), animals were randomly distributed into two groups (n = 3): (i) CaO_2-**11** NPs and (ii) vehicle only. Following induction of anaesthesia via intraperitoneal injection of Hyponym/Hypnovel (150 µL, i.p) of a mixture of 2:1:1; PBS: Hypnorm (0.315 mg/mL fentanyl citrate and fluanisone 10 mg/mL, VetaPharma Ltd., U.K.): Hypnovel (10 mg/mL midazolom, Roche, UK), the oxygen partial pressure (pO_2) of tumours was recorded using an Oxylite oxygen electrode sensor. A fibre optic probe was inserted into a 21-gauge needle before insertion into the centre of the tumour tissue. The needle was withdrawn and the probe readings allowed to stabilise for 5 min. The pO_2 in the tumours was recorded every second for 20 min. 100 µL aliquots of CaO_2-**11** NPs in a PBS vehicle (2 mg/mL) or PBS alone were administered to the respective groups by tail-vein injection with pO_2 recorded every second for a further 40 min. This time period was chosen to avoid the need for re-administering anaesthesia.

2.24. Effect of CaO_2-11 NPs on PDT efficacy in vivo: Mia Paca-2 xenograft tumours were established as described above. Once the tumours had reached an average volume of 254 ± 17 mm^3 the mice were randomly separated into 4 groups (n = 5). Group 1 involved untreated animals, group 2 the PDT only group, Group 3 the CaO_2-**11** NPs only group and group 4 the PDT + CaO_2-**11** NPs group. For group 2 mice received an intratumoural injection (100 µL) of Rose Bengal (0.1 mg/mL) in a PBS solvent and the tumour was then exposed to a LED-based white light source for 3 × 3 min treatments (Fenix LD01 LED,50 mW output,205 J/cm^2) with a 1 min interval between each treatment. Group 3 received a tail vein injection (100 µL) of CaO_2-**11** NPs in a PBS vehicle (2 mg/mL) while group 4 also received a tail vein injection (100 µL) of CaO_2-**11** NPs in a PBS vehicle (2 mg/mL) in addition to an intratumoural injection (100 µL) of Rose Bengal (0.1 mg/mL) and light exposure administered 20 min after NP injection using the same conditions as described for group 2. The tumour volume was measured daily over the course of 6 days using callipers.

Chapter 3

Optimisation and Safety Evaluation of Oxygen carrying microbubbles as a delivery vehicle for combined sonodynamic and antimetabolite therapy

Chapter 3 Optimisation and Safety Evaluation of Oxygen carrying microbubbles as a delivery vehicle for combined sonodynamic and antimetabolite therapy.

3.1 Introduction

As mentioned in **section 1.4.3**, previous work by McEwan et al. has demonstrated the ability of oxygen carrying lipid stabilised microbubbles to deliver combined sonodynamic and antimetabolite therapy for the treatment of pancreatic adenocarcimona (PDAC) in a murine model of the disease. [140] While successful in demonstrating the feasibility of this approach, the study had several limitations restricting translation of the technology to the clinic. These include: (1) the use of an intratumoural injection of the MB conjugates during the *in vivo* study. The clinical treatment of pancreatic cancer would require the MB-conjugates to be delivered by intravenous injection and to be disrupted in the tumour vasculature using an externally applied ultrasound stimulus. (2) A single set of ultrasound exposure conditions was investigated to disrupt the MBs and activate the sensitiser in that study. It would be beneficial to determine the optimum ultrasound exposure conditions to ensure efficient activation of the sensitiser for maximum SDT effect. (3) A safety study was not undertaken to evaluate any toxic effects exhibited by the combined MB mediated treatment. Such safety information would form a significant component of any pre-clinical data package. (4) Treatment efficacy was only demonstrated in a single xenograft model (BxPc-3). It would be preferable to demonstrate efficacy in a second xenograft model such as Mia Paca-2. (5) The combined treatment involved the use of 5-FU as the antimetabolite drug of choice. This was primarily for synthetic convenience as the biotin derivative of 5-FU was easier to prepare than the biotin derivative of the more commonly used gemcitabine. However, it would be beneficial to determine the efficacy of MB delivered combined SDT / antimetabolite therapy using gemcitabine as the antimetabolite drug. In addition to the above, it would also be of interest to investigate effects of the treatment at the genetic level to determine how the treatment effects expression of a selected array of gene targets including those involved in signalling pathways driving processes such as apoptosis/autophagy, angiogenesis, and resistance.

In this chapter, studies will be undertaken to address each of the above limitations to identify the optimum treatment conditions and determine the safety of the treatment.

3.2 Aims and Specific Objectives

The major aim for the work undertaken in this chapter was to determine if combined SDT / gemcitabine treatment, using intravenously delivered oxygen carrying lipid stabilised microbubbles as delivery vehicle, will provide a significant reduction in the volume of Mia-PaCa-2 tumours compared to SDT or gemcitabine treatment alone and cause no significant toxicity to healthy non-tumour bearing mice. The specific objectives were:

1. To synthesise biotinylated RB (biotin-RB), biotinylated 5-FU (biotin-5FU) and biotinylated GEM (biotin-GEM) and prepare oxygen loaded MB conjugates of each biotin functionalised compound i.e. (O_2MB-RB, O_2MB-5FU and O_2MB-GEM conjugates).

2. To investigate the efficacy of O_2MB-RB, O_2MB-5FU, O_2MB-GEM, O_2MB-RB / O_2MB-5FU and O_2MB-RB / O_2MB-GEM in a panel of three human pancreatic (Panc-1, Mia Paca-2 and BxPc-3) and one mouse primary (T110299) pancreatic cancer cell lines in the presence and absence of low intensity ultrasound.

3. To determine the efficacy of the above treatments in mice bearing human xenograft Mia Paca-2 tumours using a range of US exposures.

4. To determine the safety of the MB formulations in healthy non-tumour bearing mice.

5. To determine the expression of selected genes in harvested tumour tissues from treated and control animals using tailored arrays (e.g. RT-qPCR).

3.3 Results and discussion

3.3.1 Synthesis and Characterisation of biotin-Gem, biotin-RB and biotin-5FU.

Three separate MB conjugates were required for the experiments to be conducted in this chapter. Two of these, O_2MB-RB and O_2MB-5FU have been prepared before by McEwan et al. [Figure 3.1 (a) and (b)]. [139,140] The remaining conjugate, O_2MB-Gem [Figure 3.1 (c)] has not been previously prepared. Each conjugate utilised a generic avidin-biotin interaction to make a non-covalent bond between the surface of the MB and the drug compound itself and therefore it was necessary to prepare biotinylated derivatives of the target drug compounds to enable their attachment to the MB surface (Figure 3.1).

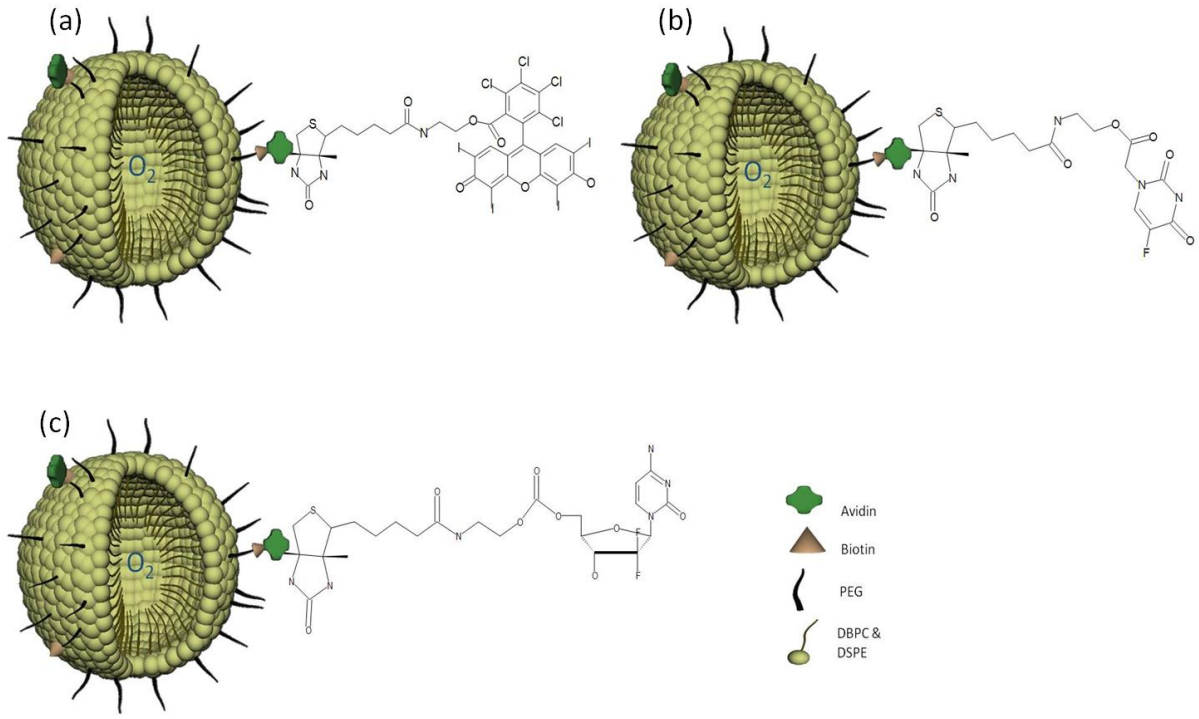

Figure 3. 1 Schematic representation for the structure of the (a) O_2MB-RB, (b) O_2MB-5FU and (c) O_2MB-GEM conjugates.

3.3.3.1 Preparation of biotinylated-Gemcitabine.

Biotinylated Gemcitabine (Biotin-GEM) was synthesised according to the three step procedure shown in Figure 3.2.

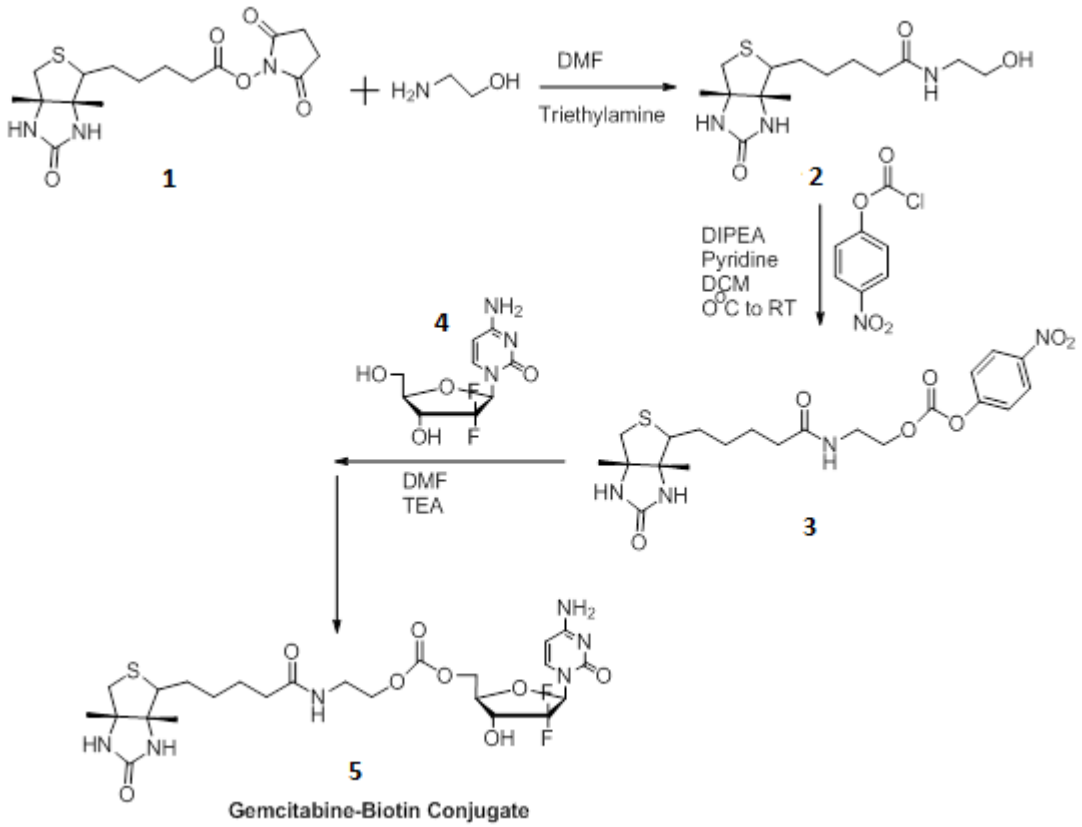

Figure 3. 2 Synthetic procedure to Biotin-GEM from non-biotinylated GEM

In the first step, the alcohol-functionalised biotin derivative **2** was prepared following a nucleophilic substitution reaction between 2-amino ethanol and biotin-NHS **1**. Nitrophenyl chlorofomate was then reacted with **2** to form the alcohol reactive carbonate ester functionalised biotin **3**. In the final step, **3** was reacted with gemcitabine to form biotin functionalised gemcitabine **5** (Biotin-Gem), with a carbonate ester linkage between the sugar hydroxyl and the biotin.

The structure of the final product was confirmed by ^{1}H-NMR, ^{13}C-NMR and electrospray mass spectroscopy (ESMS) which are shown in **Figures 3.3, 3.4** and **3.5** respectively. In the ^{1}H-NMR spectrum, the aliphatic protons from the butyl chain, biotin and sugar moiety were attributed to the upfield resonances from 1.2-4.2 ppm, while the urea protons from biotin were observed in the downfield region at 6.4 and 6.0 ppm. The protons of the GEM pyrimidinone ring appeared on resonances at 7.8 and 6.1 ppm, while the broader resonance at 7.9 ppm was attributed to the amine protons of the pyrimidinone ring. In the ^{13}C NMR spectrum, the one alkene carbon of the pyrimidinone ring and the aliphatic carbons

appeared in the upfield region between 79 ppm and 23 ppm, while the one alkene carbon and one imine carbon of the pyrimidinone ring were observed further downfield at 166 ppm and 141 ppm. The four carbonyl carbons were also observed in the downfield region between 175 ppm and 156 ppm. ESMS, recorded in the positive mode, also confirmed the structure of biotin-Gem with a base peak at 577.2 Da consistent with the molecular weight of the $[M+H]^+$ ion calculated to be 576.18 Da. Combined, these analytical data confirmed the successful formation of biotin-gemcitabine **5**.

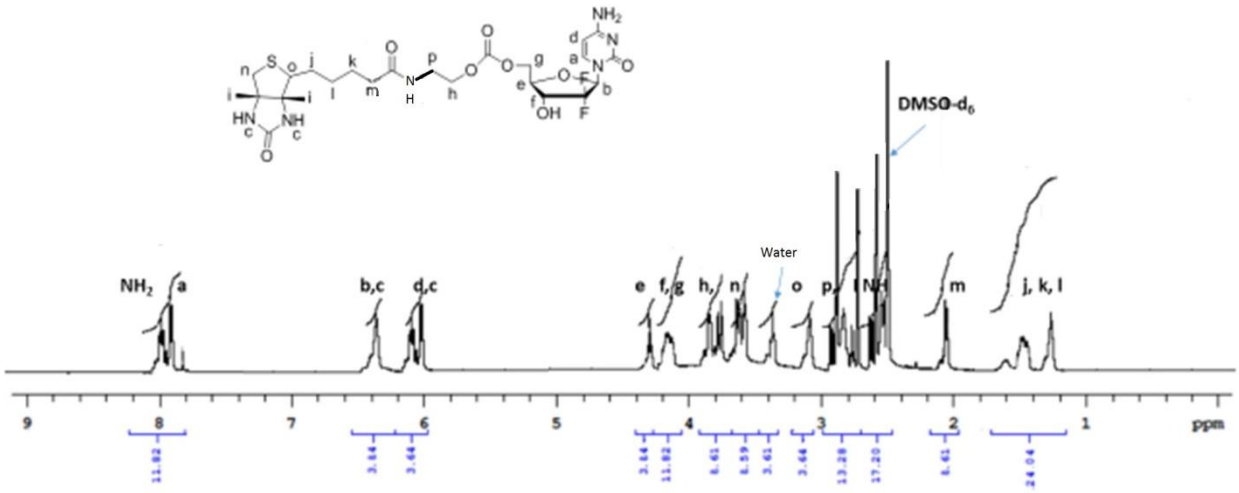

Figure 3. 3 ^{1}H-NMR of Biotin-GEM recorded in DMSO-d6.

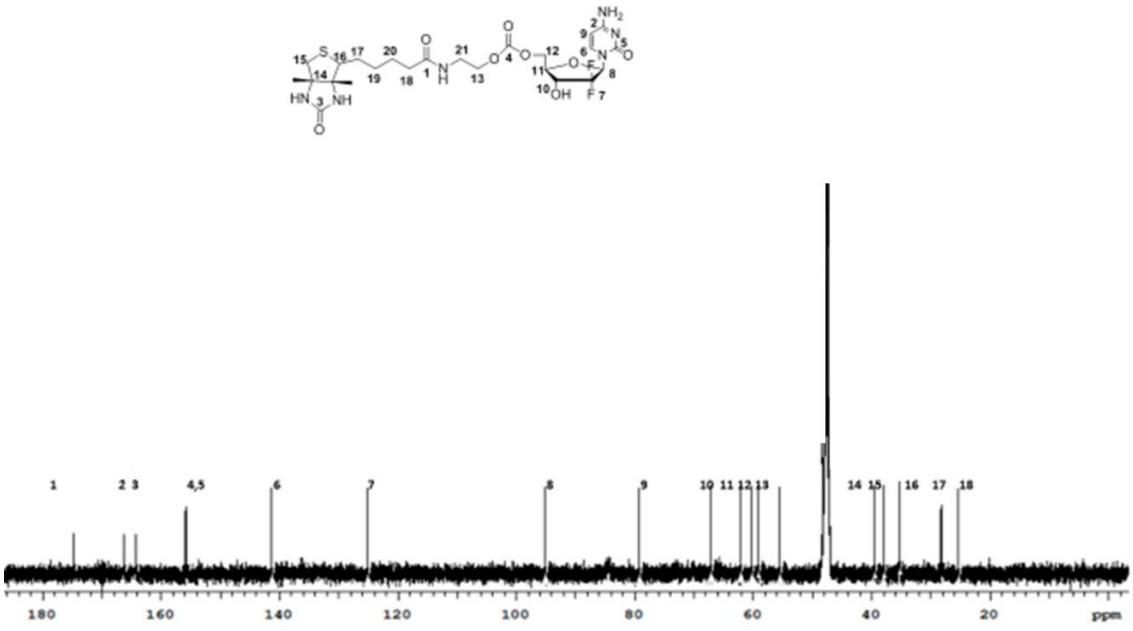

Figure 3. 4 ^{13}C-NMR of Biotin-GEM recorded in DMSO-d6.

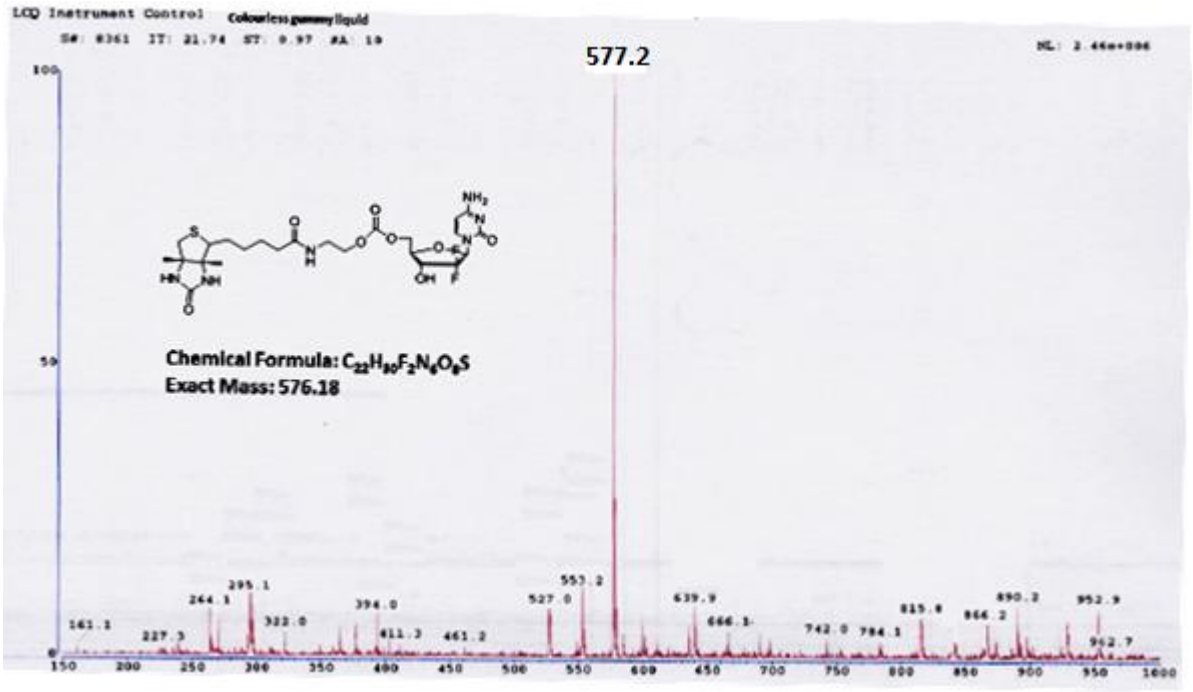

Figure 3. 5 Positive mode ES/MS of Biotin-GEM.

3.3.1.2 Preparation of Biotin-Rose Bengal

The synthesis of biotin-RB has been reported previously and the same scheme (Figure 3.6) was used here for its preparation. [139]

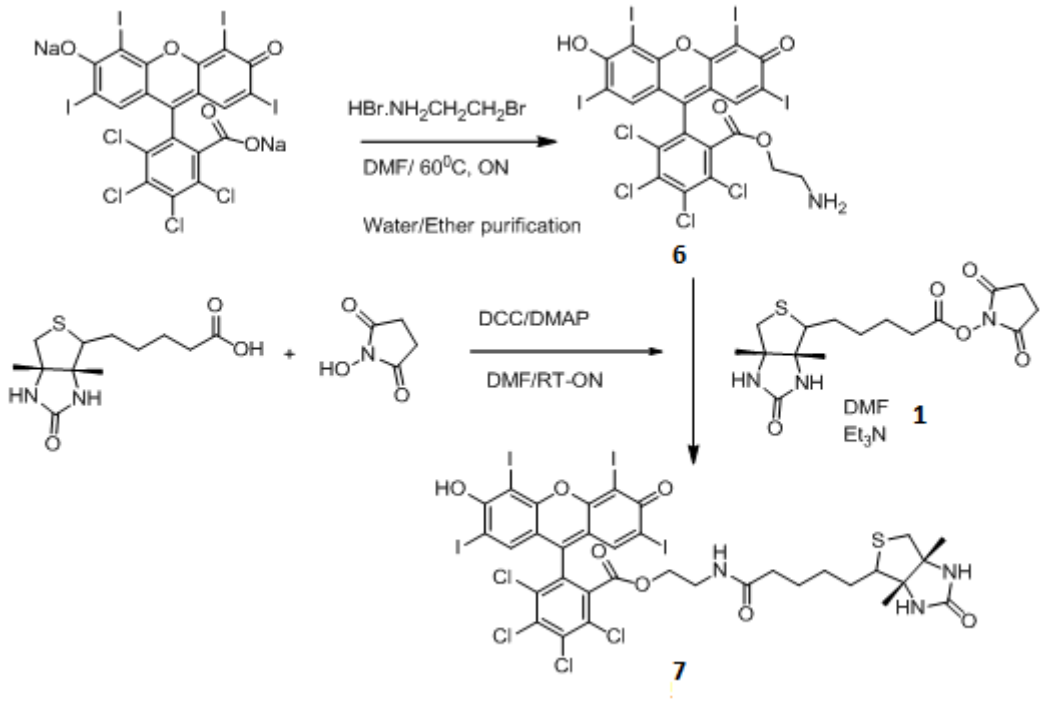

Figure 3. 6 Synthetic procedure for Biotin-RB.

In the first step, amine functionalised Rose Bengal **6** was formed by a nucleophilic substitution reaction between Rose Bengal sodium salt and bromoethylamine. **7** was then reacted with biotin-NHS **1** in the presence of TEA to form an amide linkage between the RB and biotin units. The final product was again confirmed by ^{1}H-NMR, ^{13}C-NMR and mass spectroscopy as shown in **Figure 3.7, 3.8 and 3.9**. The ^{1}H-NMR spectrum reveals one sharp resonance at 7.30 ppm resulting from the Rose Bengal aromatic protons, with the urea protons of biotin observed slightly further upfield at 6.40 and 6.30 ppm. The methylene protons from the aliphatic chain appeared on a collection of resonances from 0.80-3.90 ppm that aslo included the two methylene protons of the biotin unit (E) at 2.95 ppm. Methine protons B, both attached to chiral carbons were observed on separate resonances at 4.05 and 4.15 ppm. In the ^{13}C-NMR, the resonances in the upfield region between 22 and 61 ppm were assigned to the aliphatic carbons, while the aromatic and carbonyl carbons were observed between 70 and 200 ppm. The molecular weight of **7** was confirmed by positive ESMS with a base peak at 1241.4 Da corresponding to the $[M+H]^{+}$ ion. Again, these analytical data were consistent with those reported previously and confirm the successful synthesis of **7**.

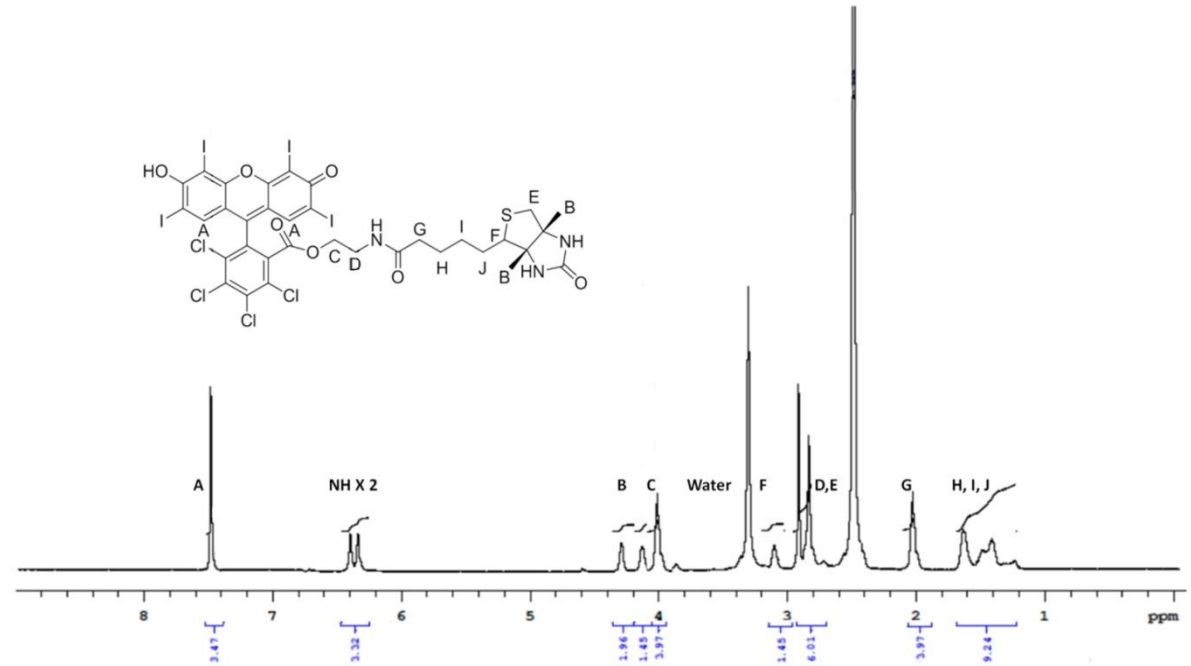

Figure 3. 7 ^{1}H-NMR spectrum recorded in DMSO-d6 for the Biotin-RB.

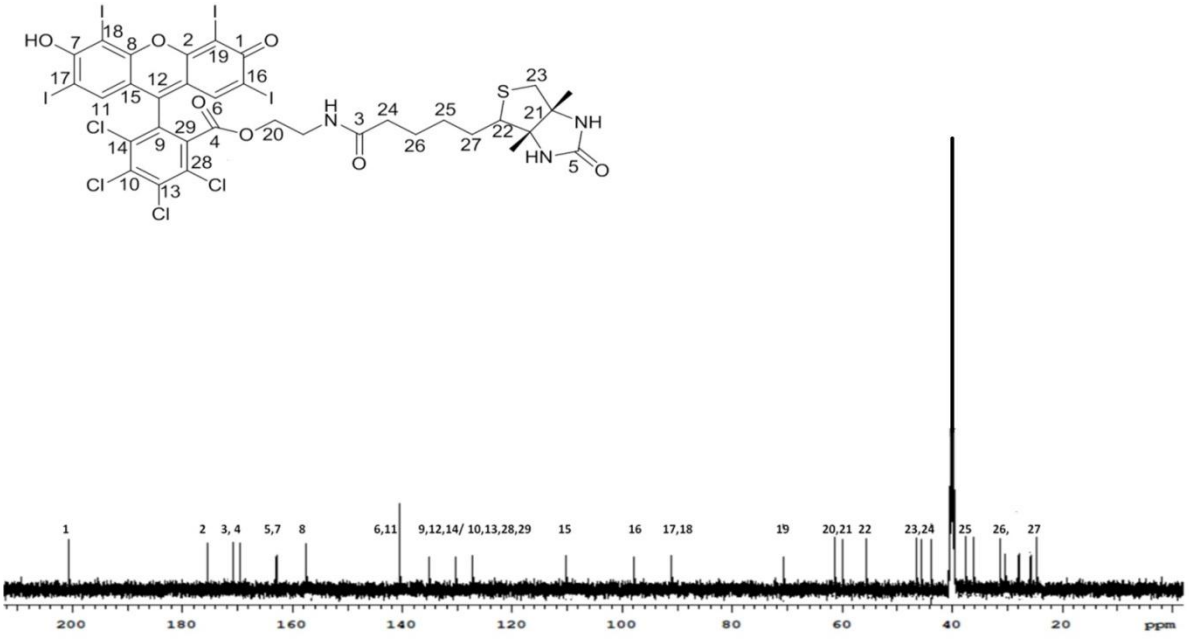

Figure 3. 8 ^{13}C-NMR of Biotin-RB recorded in DMSO-d6.

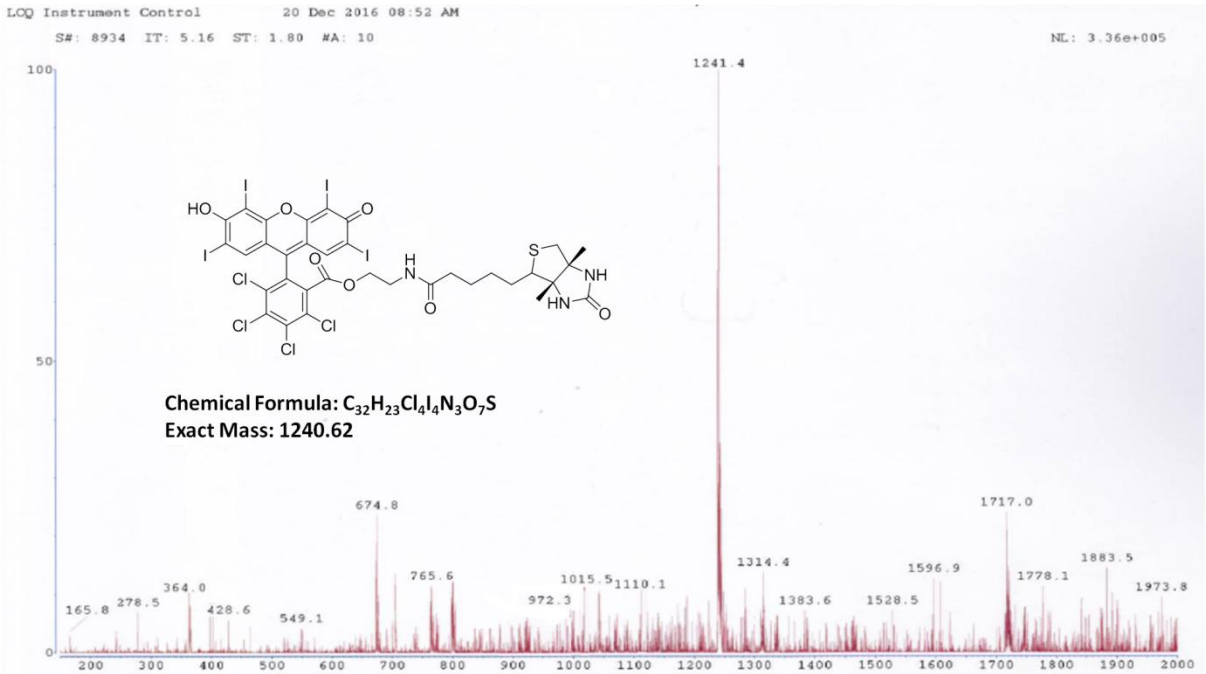

Figure 3. 9 Positive mode ES/MS of biotin-RB.

3.3.1.3 Preparation of Biotin-5FU

As for compound **10**, the synthesis of biotin-5FU **10** has also been reported before and the same synthetic protocol was followed for its preparation (Figure 3.10). [140]

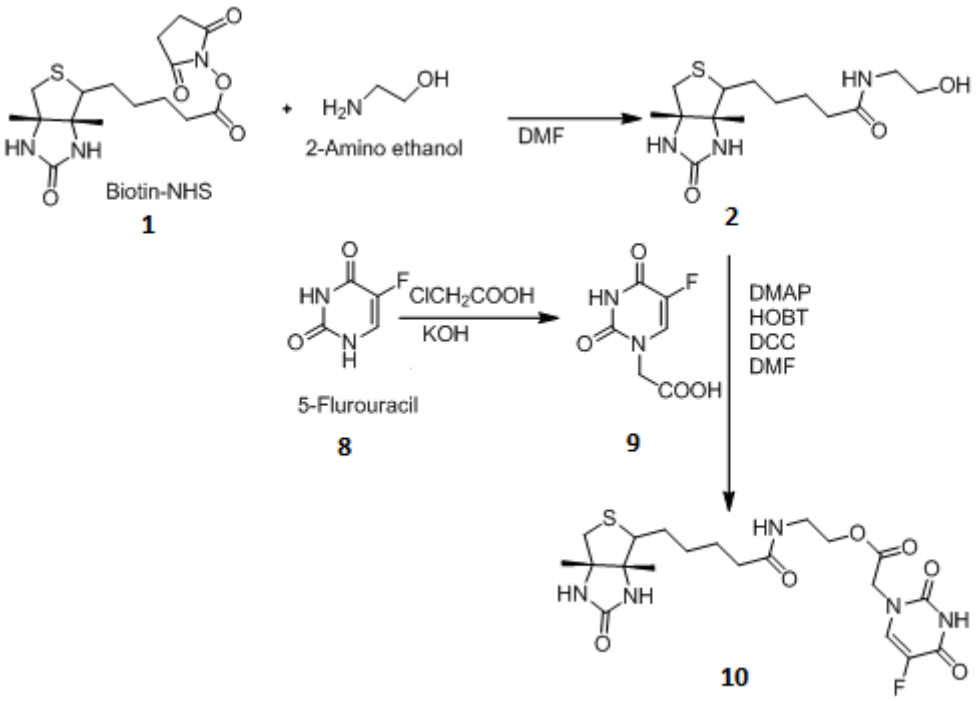

Figure 3. 10 Synthetic procedure for biotin-5FU from 5-FU.

Alcohol-functionalised biotin derivative **2** was prepared as described in Figure 3.2. In parallel, 5-FU was N-alkylated using chloro-acetic acid to produce the carboxylic acid functionalised 5-FU intermediate **9**.

Compound **9** then underwent an amidation reaction with **2** under the assistance of HOBt, DCC and DMAP to form the target compound biotin-5FU **10**, and the pure compound isolated following purification using preparative HPLC. The ^{1}H-NMR, ^{13}C-NMR and ESMS of the final product Biotin-5FU are shown in **Figures 3.11, 3.12 and 3.13** respectively. The ^{1}H-NMR spectrum revealed broad resonances in the upfield region (1.0-2.3 ppm) corresponding to the methylene protons from the butyl chain. The methylene protons from the short ethyl spacer unit were observed at 2.7 and 3.5 ppm, while the methylene protons adjacent to the uracil ring were observed at 4.2 ppm. The two methylene protons of biotin (G) are diasteriotopic and again appear as separate resonances at 4.3 and 4.5 ppm due to their proximity to the chiral centre. The singlet resonance in the downfield region (7.6 ppm) resulted from the single aromatic proton of the uracil ring. In the ^{13}C-NMR the aliphatic carbons were observed on the upfield region between 62 ppm and 25 ppm, while the two non-carbonyl carbons of the uracil ring appeared further downfield at 131 ppm and 141

ppm. The five carbonyl carbons were also observed in the downfield region between 177 ppm and 159 ppm. The molecular weight of **7** was confirmed by ESMS recorded in the negative mode with a base peak at 456.2 corresponding to $[M-H]^-$ ion calculated to be 457.48 Da. Again, these analytical data were consistent with those previously reported and confirm the successful preparation of **10**.

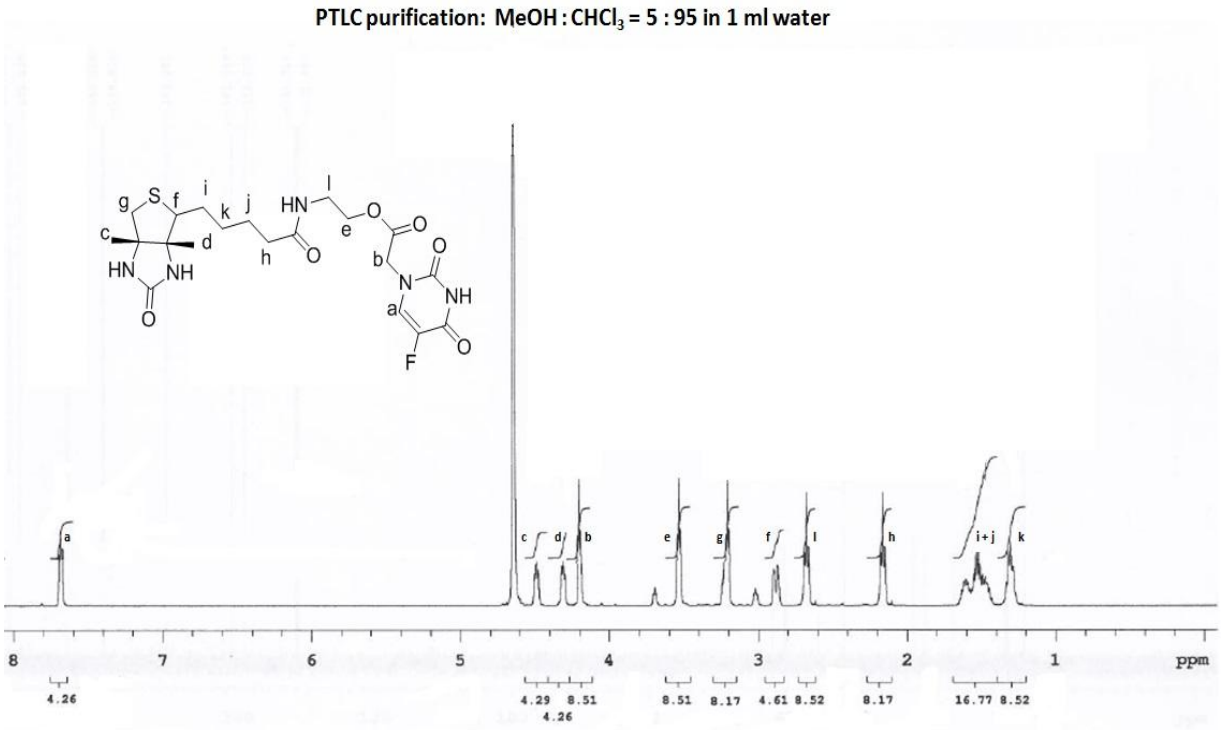

Figure 3. 11 ^{1}H-NMR of biotinlyated 5-FU recorded in D_2O.

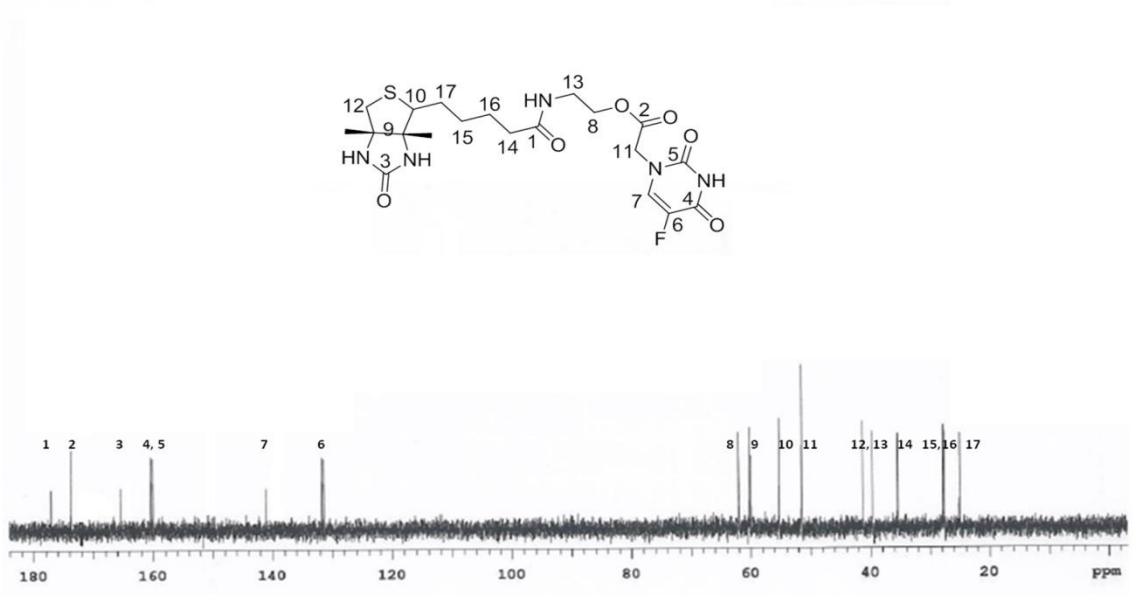

Figure 3. 12 ^{13}C-NMR of Biotin-5FU recorded in D_2O.

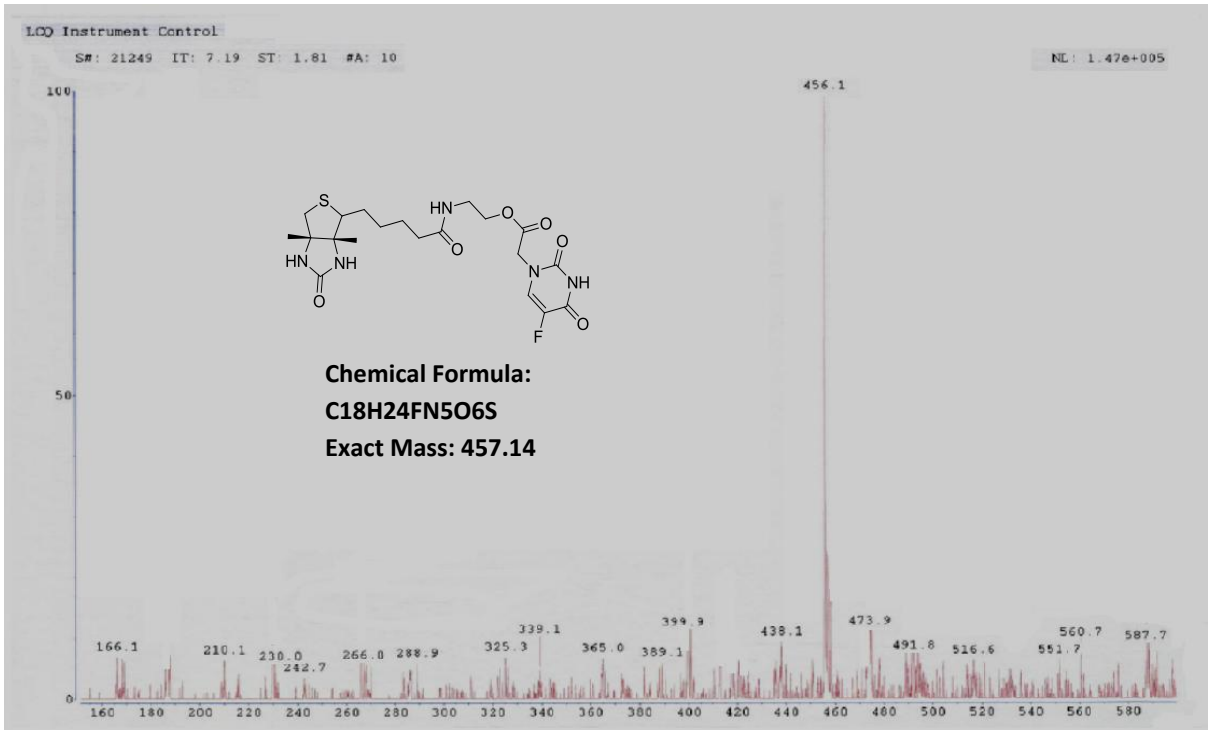

Figure 3. 13 Negative mode ES/MS of Biotin-5FU.

3.3.2 Preparation of O_2MB-RB, O_2MB-5FU and O_2MB-Gem conjugates.

As mentioned previously, the method chosen for attachment of Rose Bengal, 5-FU and Gemcitabine to the MB surface was the avidin-biotin interaction. This involved first preparing lipid stabilised MBs with the lipids DBPC, DSPE-PEG (2000) and DSPE-PEG (2000)-biotin in a molar ratio of 82:9:9. The incorporation of DSPE-PEG (2000)-biotin in the shell of the MBs at 9% molar equivalence enables the subsequent attachment of avidin to the shell of the MB via a biotin-avidin interaction. As avidin has four binding sites for biotin, this also allows the subsequent attachment of biotinylated payloads (i.e. biotin-RB, biotin-5FU and biotin-Gem) to the remaining biotin binding sites on avidin. Therefore, avidin effectively functions as a crosslinking bridge between the MB and the biotinylated payload. One possible complication that may be encountered using this approach is that two separate MBs become crosslinked together via the avidin bridge. However, the possibility of this occurring is significantly reduced by using an excess of avidin to ensure all the MB biotin sites are saturated with avidin and not available for linking with other MBs. A schematic of the conjugation process is shown in Figure 3.14.

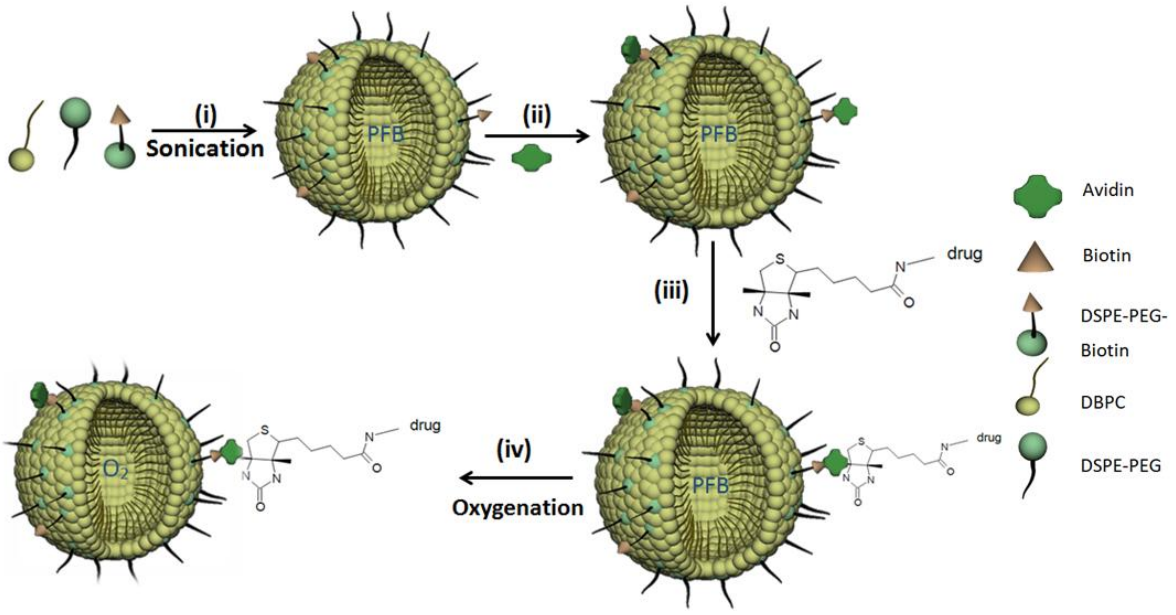

Figure 3.14 Synthetic procedure for biotin functionalised O_2-MBs

The MBs used in this chapter were prepared according to the protocol outlined in section **2.3** and shown in Figure3.14(i). A representative image of the MBs shown in Figure 3.15 (a) displays a spherical morphology with an average particle diameter calculated from analyses of the image and found to be 1 µm.

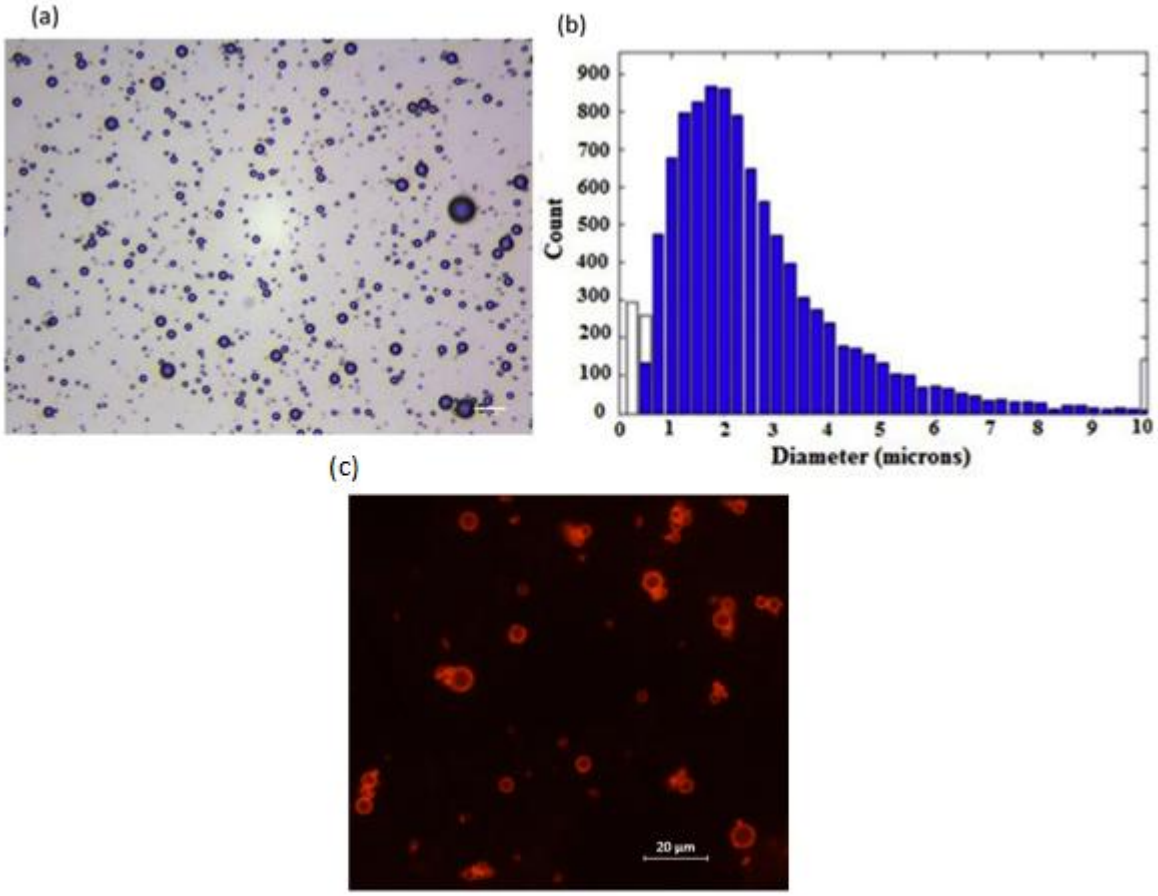

Figure 3. 15 (a) Optical microscope image taken with a 40 × objective lens of RB/GEM MB after dilution (1:10) in PBS. Scale bar is 20 µm; (b) size distribution of RB/GEM MB after centrifugation obtained from analysis of the optical microscope images. (c) Fluorescent microscope image taken with a 40 × objective lens of RB/GEM MB after dilution (1:10) in PBS, excited at 560nm. Scale bar is 20 µm.

Avidin was then added to these MBs [Figure 3.14 (ii)] and the avidin coated MBs isolated by centrifugation. While not confirmed here, the successful attachment of avidin to the MB surface using this approach has been demonstrated previously by McEwan et al when a fluorescently labelled avidin was used instead of normal avidin and MBs with bright fluorescent shells were observed. [139]

The next step in the preparation of the O_2MB-RB, O_2MB-5FU and O_2MB-Gem conjugates was to attach the biotinylated drugs onto the surface of the avidin functionalised PFBMBs [Figure 3.14 (iii)]. This was accomplished by mixing the MBs with the biotinylated drugs and removing unbound drug using centrifugation and washing steps. The final PFBMB-drug conjugates were then sparged with oxygen [Figure 3.14 (iv)] gas for 2 min to generate the

O_2MB-RB, O_2MB-5FU and O_2MB-Gem conjugates, the structures of which are shown in Figure 3.1. Confirmation of the attachment of biotinylated payloads to the surface of the avidin MBs is seen in Figure 3.15(c). The image reflects MBs loaded with RB, and clearly reveals bright red RB fluorescene from the shell of the MBs indicating successful attachment.

3.3.3 Preparation of Drug Loaded MBs and quantifying drug loading attached to the O_2MB.

Following the development work mentioned above and the protocol outlined in **section 2.4**, batches of O_2MB-RB, O_2MB-5FU and O_2MB-Gem were prepared. The drug concentration and MB number used in each of the subsequent biological studies will be presented in each relevant section.

3.3.3.1 Rose Bengal

To determine the amount of Biotin-RB present on the O_2MBs, a UV-Vis calibration curve for biotin-RB stock solution was constructed [Figure 3.16(a)]. Following the procedure described in section 2.4, the UV-Vis spectra of the various biotin-RB standard solutions were recorded at 560 nm and a calibration curve of Intensity vs. concentration generated. [Figure 3.16(b)] Good linearity was observed in the 0-20 µM range with a R^2 value of 0.99. By using the equation of the line of the calibration curve, it was possible to determine the amount of RB attached to the MBs by recording the UV-Vis spectrum of a sample following their destruction by sonication.

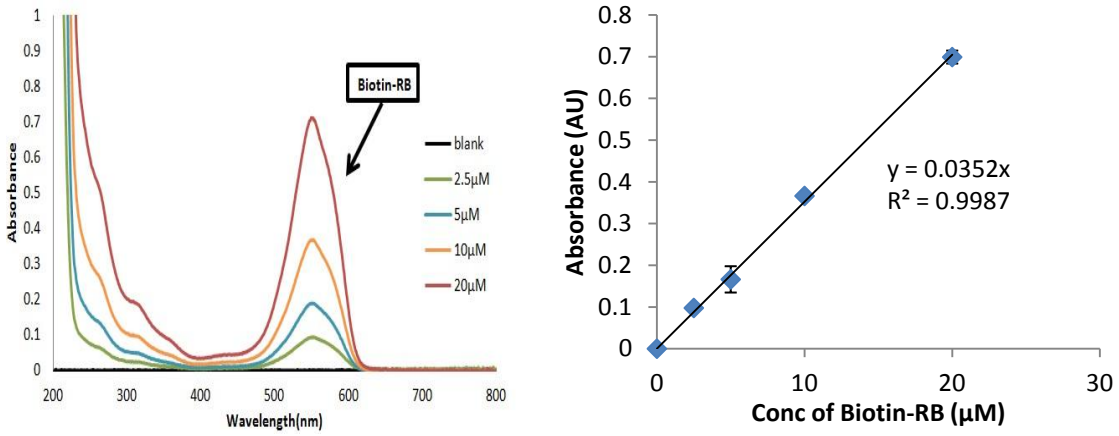

Figure 3. 16(a) UV-Vis spectra for increasing concentrations of Biotin-RB and (b) Plot of absorbance of RB at 560 nm against concentration for Biotin-RB, constructed utilizing the spectra shown in Figure 3.11(a).

3.3.3.2 5-Flurouracil

Due to the absence of a suitable chromophore within the structure of the 5-FU molecule, and the possible interference by other low wavelength absorbing components of the MB shell, UV-Vis spectroscopy was not deemed suitable to determine the concentration of 5-FU on the MB surface. Instead, high-performance liquid chromatography (HPLC) was used to separate and quantify 5-FU in samples of O_2MB-5FU. Following the procedure described in **section 2.4**, a calibration curve was again constructed using increasing concentrations of biotin-5FU. The HPLC traces are shown in Figure 3.17(a) and reveal a concentration dependent increase in concentration at a retention time of 4.5 min. An intensity / concentration plot is shown in Figure 3.17(b) and displays good linearity in the 0-0.4 µM range with an R^2 value of 0.99.

Again, using the equation of the calibration line, samples of O_2MBs-5FU were analysed for 5-FU content by HPLC following preparation.

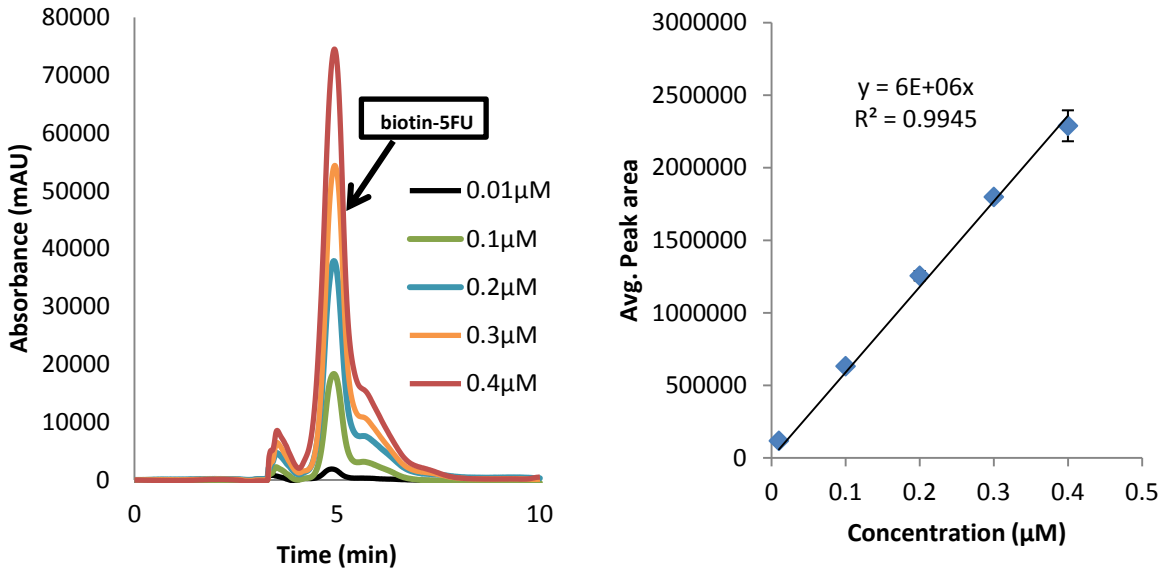

Figure 3. 17 (a) HPLC chromatograms for increasing concentrations of biotin-5FU and (b) Plot of peak area against concentration for biotin-5FU, constructed utilizing the average peak area of trace shown in Figure 3.12(a).

3.3.4.3 Gemcitabine.

For the same reasons as outlined for 5-FU above, the biotin-GEM loading was also determined by HPLC. Following the procedure described in **section 2.4**, the HPLC chromatograms of increasing concentrations of biotin-GEM (0.01, 0.1, 0.2, 0.3, 0.4 µmol) were recorded. A structured peak was observed for biotin-Gem with a retention time centred at 3.3 min. While this was not ideal, when the area of the peak was plotted as function of concentration, good linearity was obtained (R^2 = 0.98) in the 0 to 0.4 µM range and it was decided the method was acceptable for the determination of gemcitabine concentration in O_2MB-Gem samples.

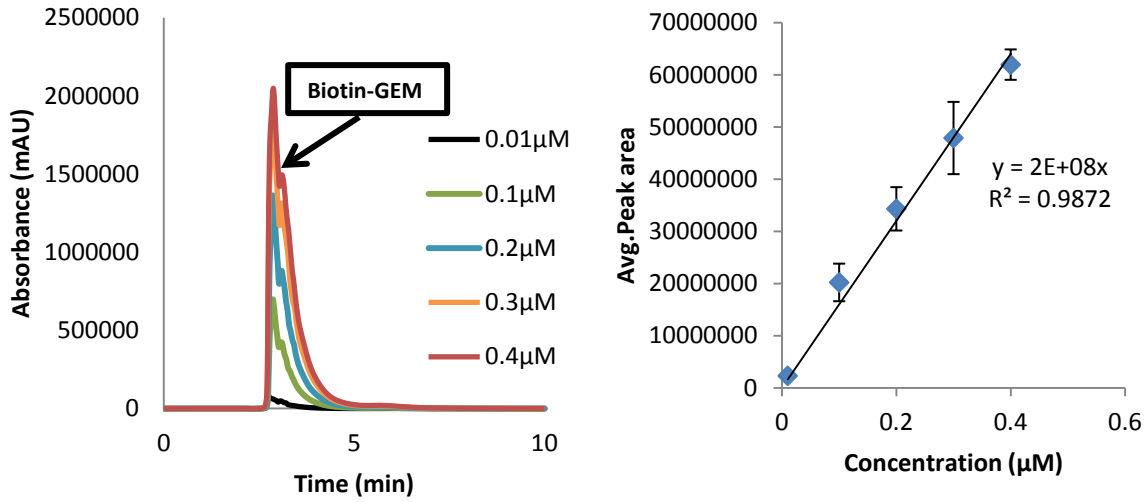

Figure 3. 18(a) HPLC chromatograms for increasing concentrations of biotin-GEM and (b) Plot of peak area against concentration for biotin-GEM, constructed utilizing the average peak area of trace shown in Figure 3.13(a).

3.3.4.4 Optimization of biotinylated drug loading on the MBs

When preparing the MB-drug conjugates it is advantageous to maximise the drug loading on the MB surface. This can be achieved in several ways: (i) increase the amount of DSPE-PEG (2000)-biotin in the MB shell (ii) ensure all the MB biotin sites are bound to avidin and (iii) ensure all the remaining avidin sites are bound with drug. It is also advantageous to keep the number of coupling, washing and centrifugation steps to a minimum in order to retain a high yield of drug loaded MBs. Previous work has suggested that 9 % of DSPE-PEG (2000)-biotin incorporation within the MB shell was optimum in terms of MB stability and oxygen retention. [140] Therefore, to optimise drug loading, the effect of the avidin coupling and the biotin-drug loading steps were investigated to identify the optimum protocol for maximum conjugation.

The first experiment undertaken involved the amount of avidin added to the MBs post preparation. 250, 500 and 750 µL aliquots of a saturated avidin solution (75.8 µM) were added in a single coupling step to separate PFBMB suspensions and the amount of biotin-RB that could be attached to the surface of the PFBMBs determined. Biotin-RB was used as the payload in these studies as the UV-Vis method for its quantification was the most straightforward to undertake. The amount of RB on the surface of the PFBMBs mixed with

the different volumes of avidin is shown in **Figure 3.19** and revealed a significant increase in loading from 182 µM to 287 µM when the avidin volume increased from 250 µL to 500 µL but no significant increase was observed when the volume increased from 500 µL to 750 µL. Therefore a single coupling using 500 µL of avidin was identified as the optimum.

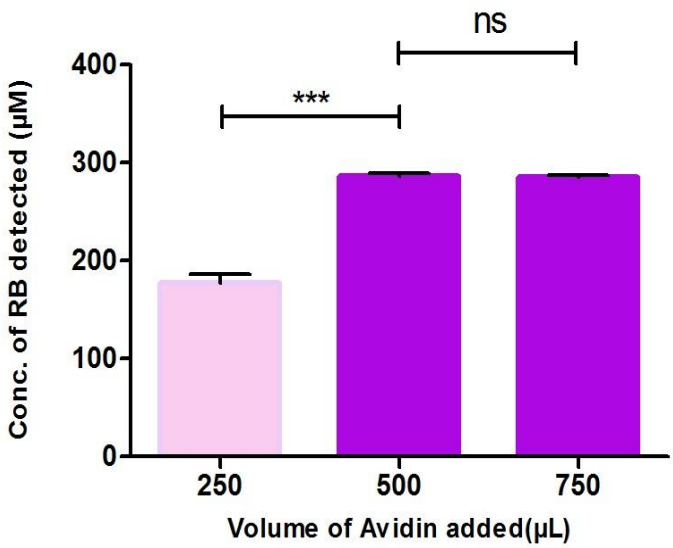

Figure 3. 19 Plot of the concentration of biotin-RB present in batches loaded with 250, 500 and 750µL of avidin saturated solution.

The number of biotin-drug couplings to the MB surface was investigated next. A saturated solution of biotin-RB (10 mM) was prepared and the amount loaded to the MB surface following 1, 2, 3, 4 or 5 sequential coupling steps using 100 µL of the ligand determined. Following each coupling step the MB number was also counted. The results [**Figure 3.20 (a) and (b)**] reveal a steady increase in biotin-RB concentration from 264 µM to 875 µM on increasing the number of couplings from 1-4 but the 5th coupling step had no significant effect. In addition, the MB number was also found to decrease steadily from 2.3 x 10^{9} MB per mL to 1.1 x10^{9} MB per mL from 1-4 couplings but reduced only slightly following the 5th coupling step.

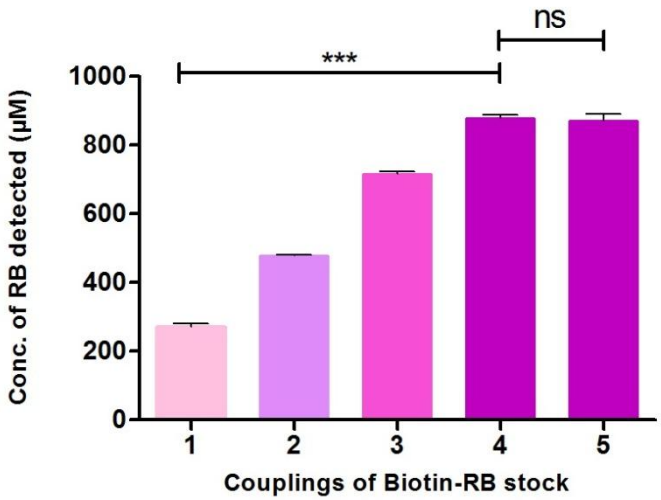

Figure 3. 20 (a) Plot of the concentration of biotin-RB present in batches loaded with 1-5couplings of biotin-RB saturated solution (5mg/mL, 100µL).

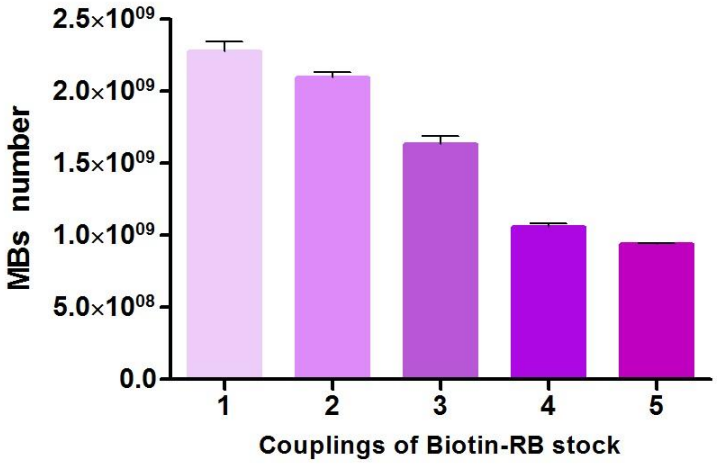

Figure 3.15(b) Plot of each couplings of biotin RB solution with the decrease in total MB number.

While 4 coupling steps appear advantageous in terms of increasing the drug loading on the MB surface, this can be counterproductive if the overall MB number also decreases. Therefore, the effect of performing two coupling steps involving 200 µL biotin-RB compared to four coupling steps involving 100 µL was also investigated to determine if this could maintain a high loading while minimising the reduction in MB number. The results are shown in **Figure 3.21** and reveal no significant variation in the loading between the two experiments suggesting two 200 µL couplings of biotin-drug to be optimum. Using these parameters of a single 500 µL of 75.8 µM avidin followed by two 200 uL couplings of

saturated biotin drug solution, batches of O_2MB-RB, O_2MB-5FU and O_2MB-Gem were prepared.

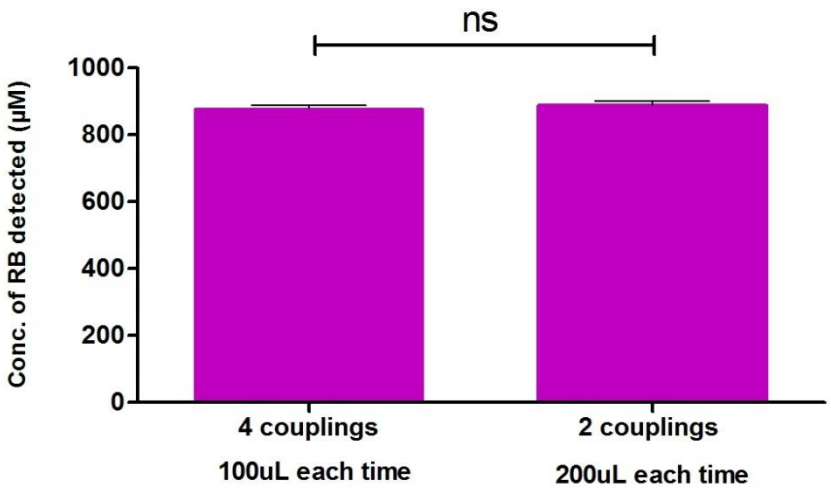

Figure 3. 21 Plot of the concentration of biotin-RB present in batches loaded with 4 couplings of biotin-RB saturated solution (5mg/mL, 100µL) and 2 couplings of biotin-RB saturated solution (5mg/mL, 200µL).

3.3.4 Evaluation of Combined SDT / Antimetabolite treatment in vitro.

Having successfully prepared batches of O_2MB-RB, O_2MB-5FU and O_2MB-Gem conjugates, the next step was to determine the efficacy of combined SDT /antimetabolite treatment in a panel of pancreatic cancer cell lines. In advance of this however, it was first necessary to ensure that the newly prepared biotin-Gem ligand displayed similar activity to the parent compound gemcitabine giving its modification at the sugar hydroxyl position. A range of biotin-Gem concentrations were tested in human pancreatic BxPc-3 cells against similar concentrations of unmodified Gemcitabine and cell viability determined by a MTT 24 h later. The results are shown in **Figure 3.22** and reveal no significant difference in efficacy between biotin-Gem over the concentration range tested with 5 µM resulting in 78% reduction in viability for both compounds.

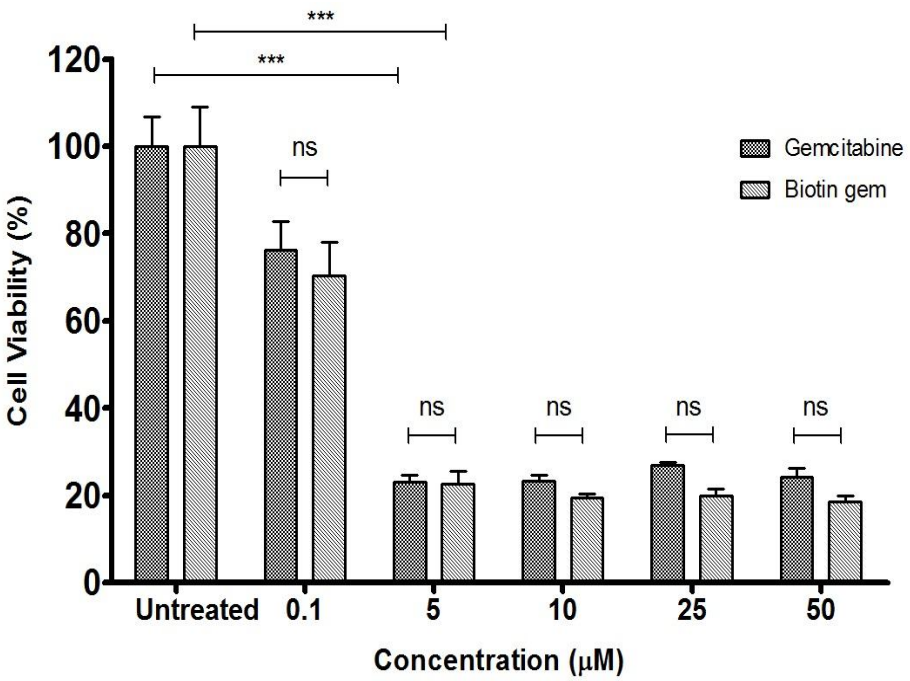

Figure 3. 22 Plot of viability for BxPc-3 cells treated with GEM and Biotin-GEM (0.1, 5, 10, 25, 50 μM). Error bars represent ± the standard error where n=6.Statistically significance versus untreated cells : $p < 0.001$

In addition to ensuring that the biotin modified Gemcitabine (**5**) possessed similar efficacy to Gemcitabine alone, the optimum ultrasound exposure conditions required to minimise dark toxicity and maximise SDT efficacy of Rose Bengal was also investigated in advance of testing in the four different cell lines. BxPc-3 cells was chosen as the candidate cell line and the cell viability determined following treatment with O_2MBs-RB (5 μM, $1.2x10^9$/mL) in the absence and presence of 4 different ultrasound conditions using a frequency of 1 MHz, a power of 3 W/cm^2 but differing in treatment duration and duty cycle. The four US exposure conditions are listed below:

1. 1MHz 3W/cm^2 30% duty cycle for 20s,

2. 1MHz 3W/cm^2 30% duty cycle for 30s,

3. 1MHz 3W/cm^2 40% duty cycle for 20s,

4. 1MHz 3W/cm^2 40% duty cycle for 30s.

The results are shown in **Figure 3.23** and reveal the optimum treatment time to be 30 sec with a duty cycle of 40 % as the differential between US only and SDT was the greatest using these conditions. Therefore, US exposure conditions using a frequency of 1 MHz, a power density of 3 W/cm^2, 40% duty cycle and 30 sec treatment duration were used to investigate the effect of combined SDT / antimetabolite therapy on the panel of four pancreatic cancer cell lines.

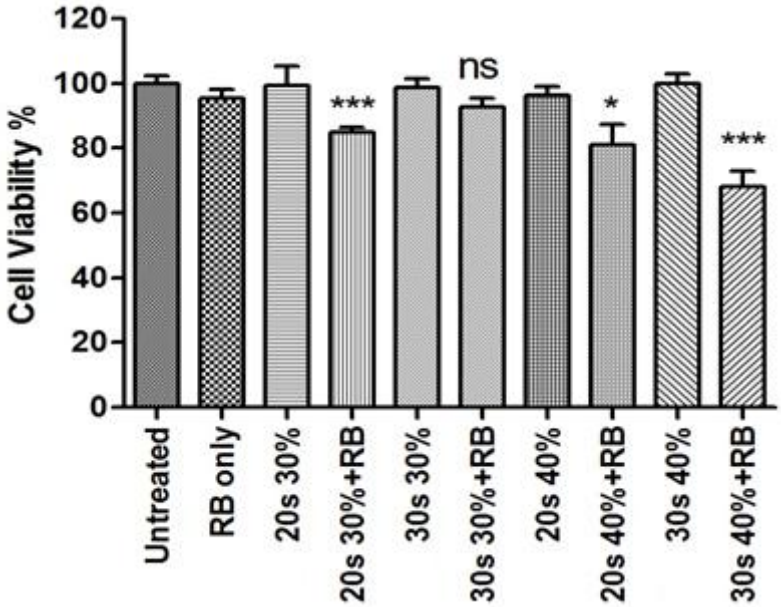

Figure 3. 23 Plot of cell viability for cells treated with O_2MB-RB (5 µM, RB) and then exposed to various ultrasound exposures. Cells treated with Ultrasound only and O_2MB-RB only used for control purposes. US at 1MHz, 3W/cm^2 was used for various times at a duty cycle of 30% or 40%. Statistically significant difference versus untreated cells: * $p < 0.05$, *** $p < 0.001$. Error bars represent ± the standard error where n=6.

3.3.4.1 Efficacy of combined SDT/antimetabolite therapy in BxPc-3, Mia-Paca2, Panc-01 and KPC cell lines.

Human primary pancreatic adenocarcinoma cell lines, BxPc-3, Panc-01 cells, human primary carcinoma cell line Mia Paca-2 and the mouse T110299 pancreatic (KPC) were investigated as target cell lines. [170] 5 x 10^3 cells were seeded in 96 well plates and incubated for 24 h with a suspension of either PFBMB-5FU, PFBMB-RB, PFBMB-GEM as well as combined PFBMB-5FU / PFBMB-RB or PFBMB-GEM / PFBMB-RB under normoxic conditions. In each case the concentrations of drugs were as follows: [RB] = 5 µM, [5-FU] = 100 µM and [Gem] = 5 µM. Following the 24h incubation period, selected wells were treated with US using the

conditions identified above. Untreated cells and cells treated with US only were also utilised as controls. The results are shown in **Figure 3.24 a-d** and reveal that combined chemo-sonodynamic therapy using the MB platform was more effective than chemotherapy or SDT alone in all four cell lines. In addition, chemo-sonodynamic therapy using gemcitabine MBs proved more efficacious than the analogous treatment using 5-FU MBs in the BxPc-3, Panc-1 and Mia Paca-2 cell lines, while in the KPC cell line the efficacy was similar. These results confirm those from similar studies [140,171] and illustrate the complimentary nature of antimetabolite and SDT treatments where the cancer cells are attacked using two different mechanisms, with the former causing cellular death by disrupting the synthesis of DNA and the latter through oxidative stress.

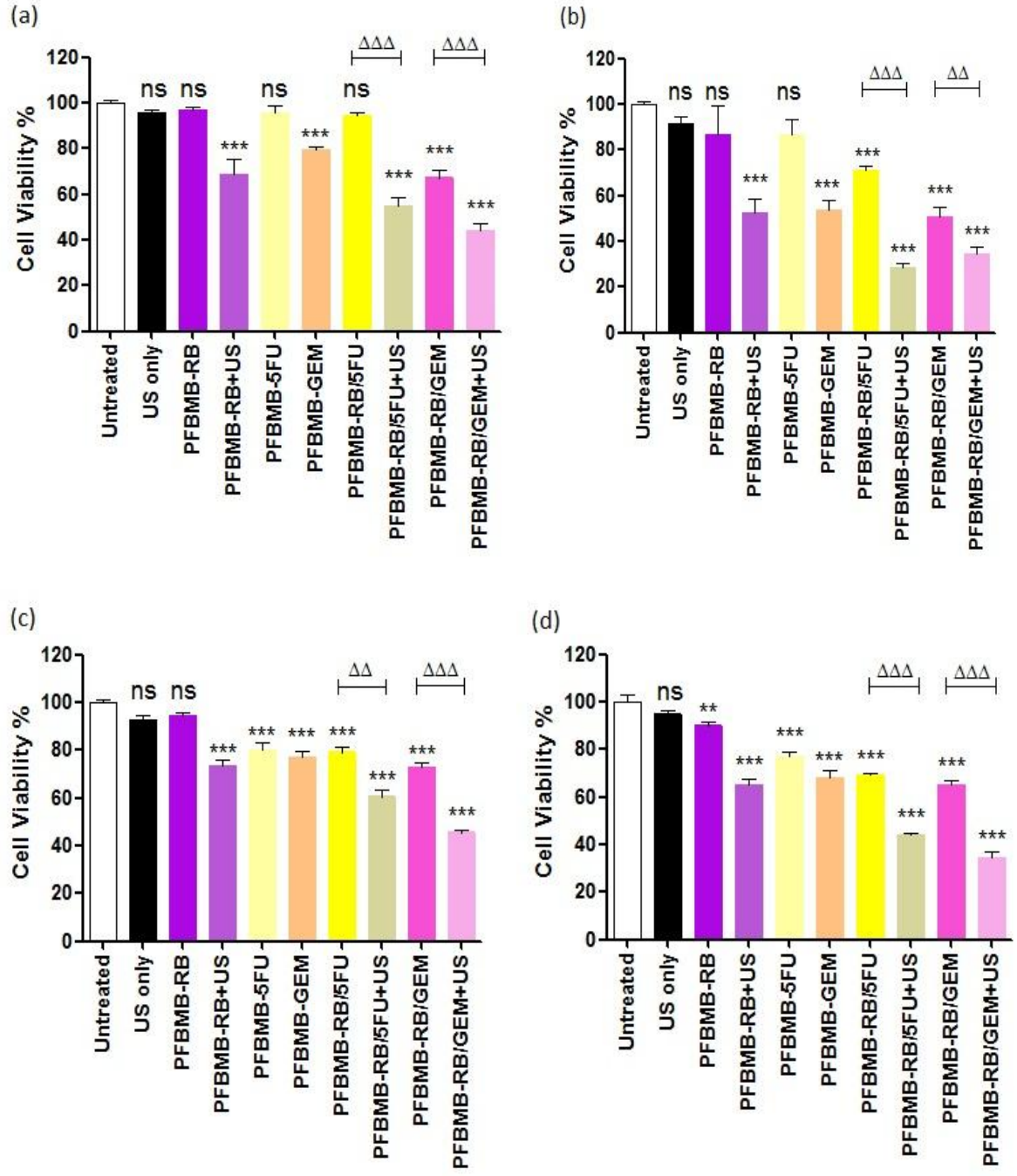

Figure 3. 24 Plot of % cell viability for (a) BxPc-3 (b) T110299 (c) Mia Paca-2 and (d) Panc-01 after treatment with (i) untreated, (ii) ultrasound only, (iii) PFBMB-RB only, (iv) PFBMB-RB plus ultrasound, (v) PFBMB-5FU only, (vi) PFBMB-GEM only, (vii) combined PFBMB-RB and PFBMB-5FU, (viii) combined PFBMB-RB and PFBMB-5FU plus ultrasound, (ix) combined PFBMB-RB and PFBMB-GEM, (x) combined PFBMB-RB and PFBMB-GEM plus ultrasound. Statistically significant difference versus untreated cells: ** $p < 0.01$, *** $p < 0.001$, ΔΔ $p < 0.01$, ΔΔΔ $p < 0.001$. Error bars represent ± the standard error where n=6.

3.3.5 Effect of US exposure conditions on the efficacy of combined chemo-sonodynamic therapy using O_2MBs as delivery vehicles.

Previous work by McEwan et al has established the benefit of chemo-sonodynamic therapy using O_2MB as the delivery vehicle for the treatment of pancreatic tumours in mice. [140] However, these studies involved direct intra-tumoural injection of the O_2MB conjugates and 5-FU as the antimetabolite drug. In addition, the animal model utilised in those studies was an ectopic BxPc-3 xenograft that does not carry the KRAS mutation. As mentioned in **section 3.1**, it is advantageous to demonstrate efficacy following intravenous injection of the MB conjugates instead of intratumoural injection as this is the route that would be used in the clinic should this technology undergo clinical translation. In addition, it is also beneficial to demonstrate efficacy in two different xenograft models. As chemo-sonodynamic therapy using gemcitabine MBs also proved more efficacious than the analogous treatment using 5-FU MBs in the *in vitro* studies discussed above, it was of interest to determine how the treatments would compare *in vivo*. Therefore, ectopic Mia Paca-2 tumours were established in the dorsum of SCID mice. This cell line carries the KRAS mutation and has been used extensively as an *in vivo* model in pancreatic cancer research. [172] Once tumours reached an average volume of 241 mm^3, they were randomly allocated into 12 groups. Where appropriate, the MB-conjugates were administered by tail vein injection and ultrasound applied to the tumour for 3.5 minutes during the injection to disrupt the MBs and release the oxygen gas and attached payloads (**Figure 3.25**).

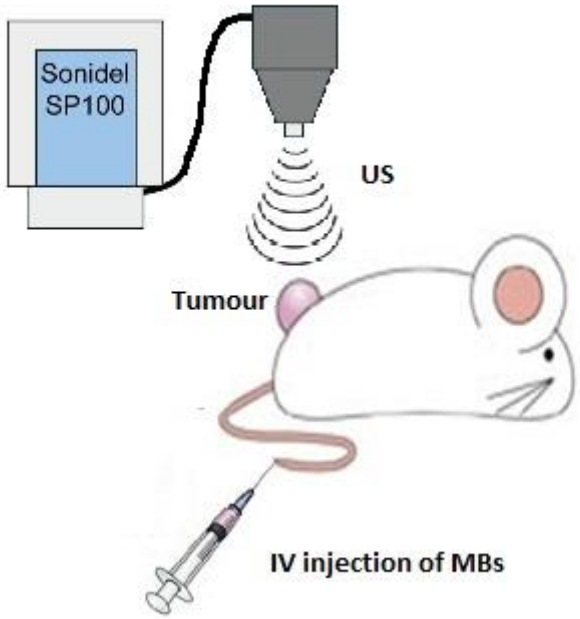

Figure 3. 25 A schematic diagram showing combined chemo-sonodynamic therapy using O_2MBs as delivery vehicles in an ectopic model.

A second US administration using the same parameters was applied 30 min following the first US application, the function of which was to activate the Rose Bengal (i.e. SDT). Tumour volume was measured each day for a total of 9 days following treatment. In these studies, three different US exposures were investigated involving various power densities (3.5 or 4 W/cm^2) and duty cycles (30 % and 50 %) to identify the optimum in terms of tumour growth control. Untreated animals and those treated with the various conjugates alone or ultrasound alone were used for comparative purposes. The exact conditions used for each of the 12 groups are shown in Table 3.1

Table 3.1 the list of different treatment groups on SCID mice bearing ectopic Mia Paca-2 tumours (n=5).

Group	Treatment condition
1	Untreated
2	the O_2MB-Gem/RB conjugate alone
3	the O_2MB-5FU/RB conjugate alone
4	US treatment alone at 1 MHz, 3.5 W/cm^{-2} and 30% duty cycle
5	US treatment alone at 1 MHz, 3.5 W/cm-2 and 50% duty cycle
6	US treatment alone at 1 MHz, 4.0 W/cm^{-2} and 30% duty cycle
7	O_2MB-Gem/RB conjugate + US treatment at 1 MHz, 3.5 W/cm^{-2} and 30% duty cycle
8	O_2MB-Gem/RB conjugate + US treatment at 1 MHz, 3.5 W/cm^{-2} and 50% duty cycle
9	O_2MB-Gem/RB conjugate + US treatment at 1 MHz, 4.0 W/cm^{-2} and 30% duty cycle
10	O_2MB-5FU/RB conjugate + US treatment at 1 MHz, 3.5 W/cm^{-2} and 30% duty cycle
11	O_2MB-5FU/RB conjugate + US treatment at 1 MHz, 3.5 W/cm^{-2} and 50% duty cycle
12	O_2MB-5FU/RB conjugate + US treatment at 1 MHz, 4.0 W/cm^{-2} and 30% duty cycle

The results from the 12 groups are shown in three separate plots for clarity (**Figures 3.26(a)-(c)**). Figure 3.21(a) shows the results for the untreated, ultrasound only and MB conjugate only treated groups (i.e. Gps 1-6) while **Figure 3.26(b)** and **(c)** show results for treatments with mixed MB preparation containing either GEM (**Figure 3.26(b)**) or 5-FU (**Figure 3.26(c)**) plus ultrasound. No significant differences were observed for the MB-conjugates only (Gps 2 & 3) or US stimulus only treatments (Gps 4-6) when compared against the untreated controls. For animals treated with the mixed MB preparation containing Gemcitabine, all three US exposures resulted in statistically significant reductions in tumour growth when compared to the control 8 days following treatment with both the 3.5W/cm^2 & 30% DC (Gp 7) and 4.0 W/cm^2 & 30% DC (Gp 9) exposures producing greater tumour reductions than the 3.5W/cm^2 & 50% DC (Gp 8) exposure, although this difference was not statistically significant. For animals treated with the mixed MB preparation containing 5FU, only those animals treated with a US exposure of 3.5W/cm^2 & 30% DC (Gp 10) produced a significant reduction ($p < 0.01$) in tumour volume 8 days following treatment when compared to the untreated control, although the magnitude of the tumour reduction and the tumour delay profile was similar to Gps 7 & 9. These results suggest that US exposure conditions of

3.5W/cm^2 & 30% DC provide the best tumour response no matter if the antimetabolite drug attached to the MBs was 5-FU or GEM.

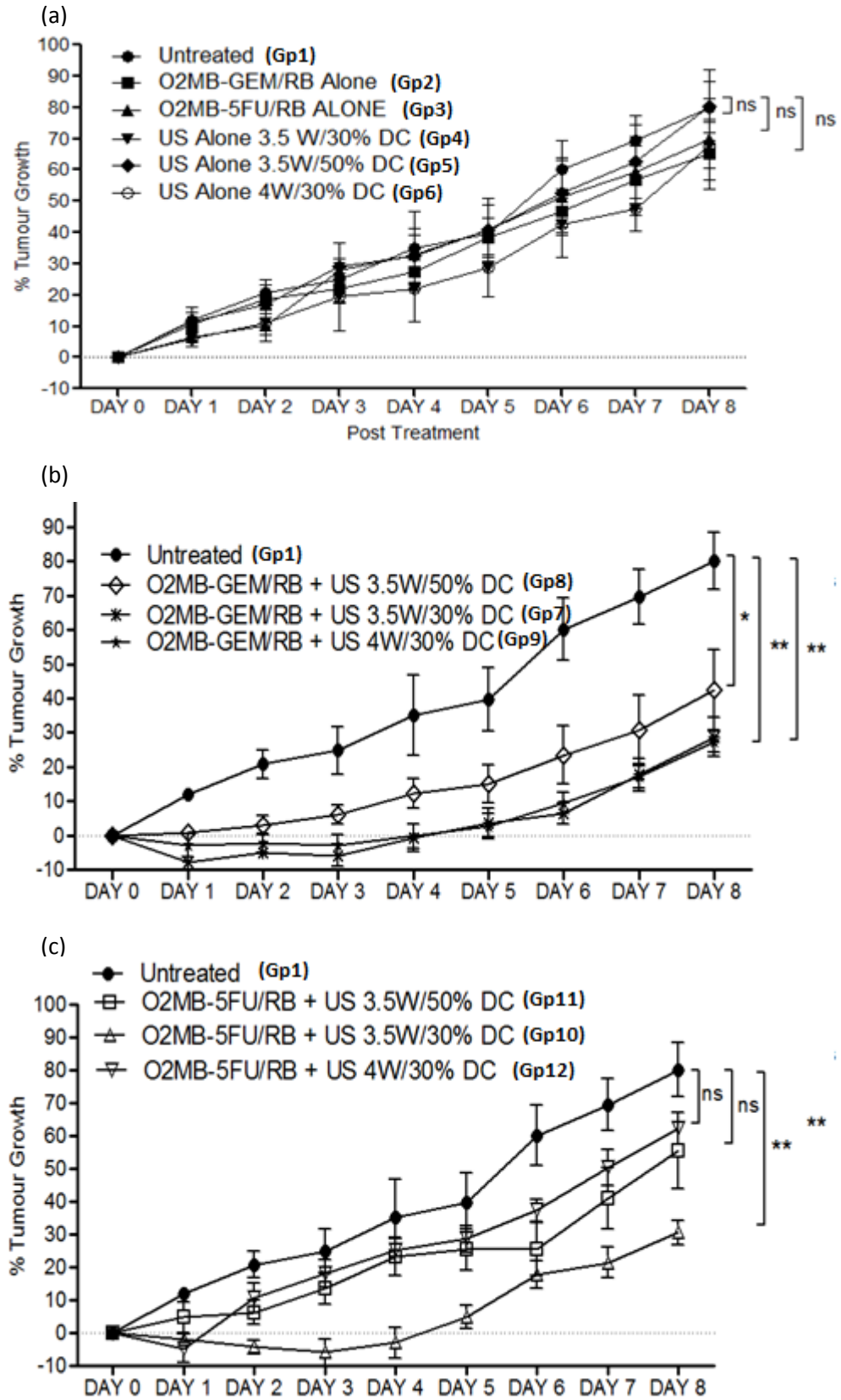

Figure 3. 26 Tumour growth plots of mice exposed to O2MB-Gem/RB or to O_2MB-5-FU/RB conjugates using different US exposures. The control groups (a), O_2MB-Gem/RB groups (b) and O_2MB-5-FU/RB groups (c) are shown.

3.3.6 Effect of treatment schedule on the efficacy of combined chemo-sonodynamic therapy using O_2MBs as delivery vehicles.

Having established the optimum US exposure conditions, the next step was to investigate the effect of adding an additional chemo-sonodynamic therapy treatment on the tumour growth delay. From the results of the single chemo-sonodynamic therapy treatment discussed above, it was observed that for Gps 7, 9 & 10, while the tumour volume initially reduced below the pre-treatment value for 3 days following treatment it then subsequently increased. Therefore, it was decided to administer a second treatment on day 3 following the initial treatment to identify if the tumour growth delay period could be extended.

Animals were randomly allocated into 6 groups and once the tumours reached an average volume of 213 mm^3 they were treated as described in **table 3.2**. Group 1 received no treatment, group 2 the optimum US stimulus, groups 3 & 4 received the mixed MB preparation containing either 5FU or Gemcitabine respectively while groups 5 & 6 received the same mixed MB preparations as groups 3 & 4 but also received the optimum US stimulus. Treatments were administered on Days 0 and Day 3 with the tumour volumes recorded for 8 days following the initial treatment.

Table 3.2 the list of different treatment groups on SCID mice bearing ectopic Mia Paca-2 tumours (n=5).

Group	Treatment condition
1	Untreated
2	US only
3	the O_2MB-Gem/RB conjugate only
4	the O_2MB-Gem/RB conjugate + US
5	the O_2MB-5-FU/RB conjugate only
6	the O_2MB-5-FU/RB conjugate + US

The results are shown in **Figure 3.27** and again show no significant impact on tumour growth for animals treated with ultrasound alone (Gp 2) or the mixed MB preparations (Gps 3 & 4). However, the results do highlight the value of the second chemo-sonodynamic

therapy treatment with the tumour volume of animals treated in groups 5 & 6 remaining below their pre-treatment value for 6 days following the initial treatment compared to the 3 days observed following a single treatment. Interestingly, there was no significant difference in the tumor growth delay profile for either Gp 5 or Gp 6, indicating a similar cytotoxic effect for either 5-FU or Gemcitabine when part of the mixed MB preparation. To better illustrate the impact of the second treatment, two further plots were constructed that included the tumor growth delay data for both the single and double treatments [**Figure 3.27(b) and Figure 3.27(c)**] and reveals a significant reduction in tumour volume 8 days following the initial treatment for the twice treated animals compared to those receiving a single treatment.

Combined, the above *in vivo* data suggests that there is no statistically significant difference for chemo-sonodynamic therapy of ectopic Mia Paca-2 tumours using either the O_2MB-RB / O_2MB-5FU or O_2MB-RB / O_2MB-Gem mixed MB preparations and the optimum US conditions (frequency = 1MHz, power density = 3.5 W/cm^2, duty cycle = 30% and pulse repetition = 100 Mz). However, the O_2MB-RB / O_2MB-Gem mixed MB preparation was more responsive across a wider range of US exposures compared to the O_2MB-RB / O_2MB-5FU mixed MB preparation. Importantly, a significant benefit was observed in terms of tumour growth delay when animals were treated for a second time 3 days after the first treatment. This is highly significant as it indicates the tumours do not become quickly resistant to the combined antimetabolite / SDT treatment. Future work should explore the benefit of further treatments to determine how much longer the tumour growth delay can be maintained.

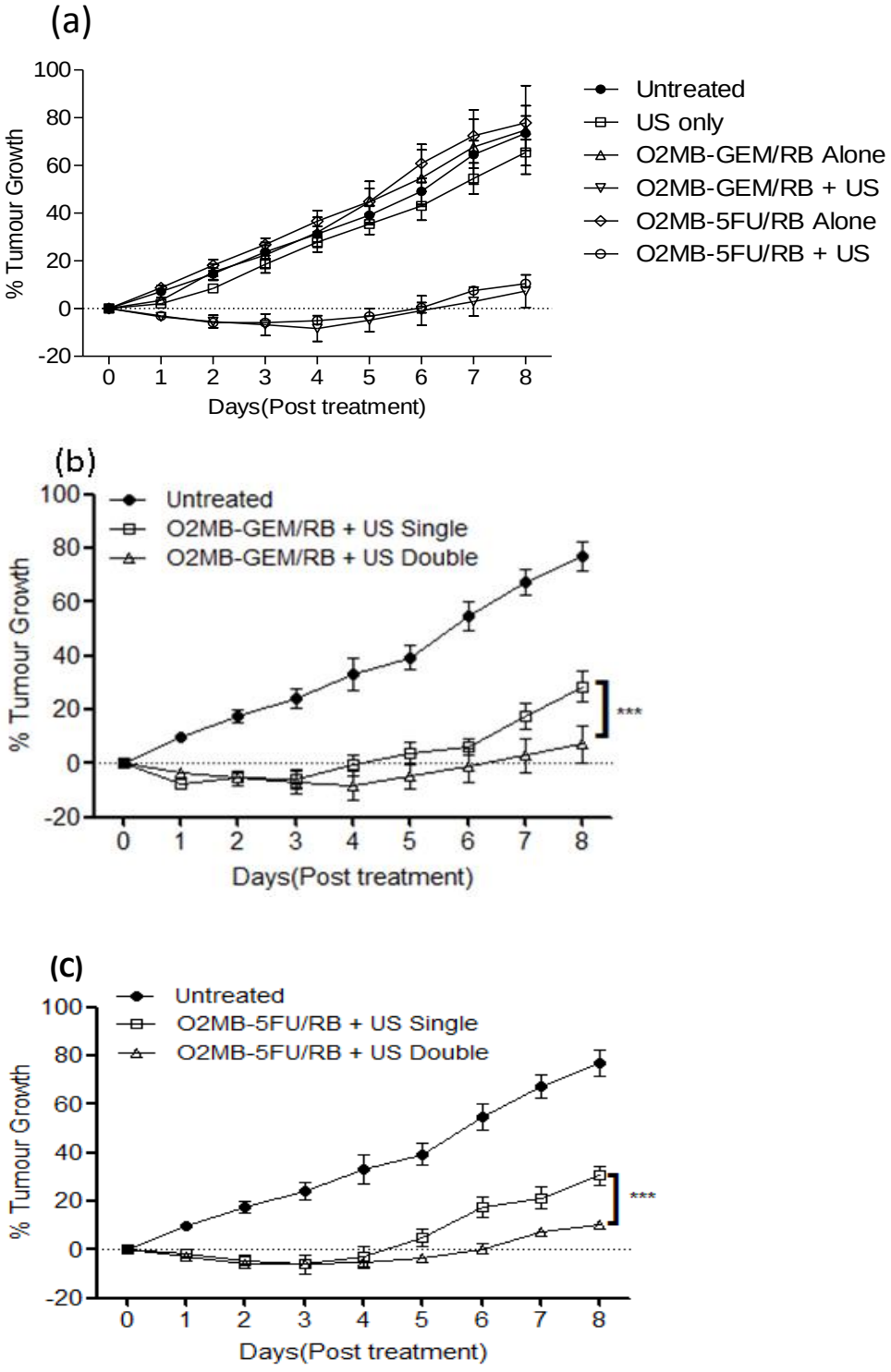

Figure 3. 27 (a) Tumour growth plots following two treatments on Days 0 and 3 using the O_2MB-GEM/RB and O_2MB-5-FU/RB conjugates. Control groups also shown. (b) Plot showing overlay of tumour growth following a single and double treatment using the O_2MB-GEM/RB conjugate + US. (c) Plot showing overlay of tumour growth following a single and double treatment using the O_2MB-5-FU/RB conjugate + US. *** $p < 0.001$ for untreated compared to O_2MB-5-FU/RB conjugate + US double treatment and O_2MB-5-FU/RB conjugate + US single treatment compared to O_2MB-5-FU/RB conjugate + US double treatment. * $p < 0.05$ for O_2MB-GEM/RB conjugate + US single treatment compared to O_2MB-GEM/RB conjugate + US double treatment.

3.3.7 Determination of how combined antimetabolite / SDT treatment affects the expression of genes involved in pancreatic cancer.

Given the impressive results observed for the combined antimetabolite / SDT in the *in vitro* and *in vivo* studies discussed above, it was also of great interest to identify any changes in the expression of genes involved in apoptosis, autophagy, angiogenesis, hypoxia, resistance and malignant progression pathways in pancreatic cancer. [173] To determine this, SCID mice bearing ectopic Mia Paca-2 tumours with an average volume of 273 mm^3 were randomly allocated into 3 groups (n=3). Animals in group 1 received no treatment, those in groups 2 received an IV injection (100 µL) of the mixed O_2MB-RB and O_2MB-Gem conjugate containing (2.6 $X10^8$ MB / mL, 480.0 µM Gem and 610.0 µM RB) while animals in group 3 received an IV injection (100 µL) of the mixed O_2MB-RB and O_2MB-5FU conjugate containing 3.2 $X10^8$ MB / mL, 2.1 mM 5FU and 700 µM RB. Animals in groups 2 and 3 were also exposed to US using the optimum parameters as determined in **section 3.3.5**. 8 days following treatment, the animals were euthanised and the tumours removed. The tumours were processed as described in **section 2.21** and the cellular suspension analysed using qRT-PCR. The results for the expression of selected genes in tumours harvested from groups 2 and 3 were compared directly against the same genes in tumours harvested from the untreated control group 1. The results are shown in **Figures 3.28(a)** and **(b)** for Group 2 and Group 3 respectively for 18 different genes associated with apoptosis, hypoxia, stem cell differentiation, apoptosis and autophagy in pancreatic cancer. Mia Paca-2 tumours are known to be extremely hypoxic [139] and hypoxic stress selects for resistant cancer cells to become established and present a more malignant genotype/phenotype. Hypoxia insult up-regulates pro survival genes associated with proliferation, stem cell maintenance and malignant progression. [174-176] Expression of the hypoxic markers HIF-1α and VHL were significantly reduced in both the treatment groups, suggesting that treated tumours were less hypoxic than the untreated tumours. Furthermore, a significant decrease was also observed for the pro-angiogenic gene VEGFC in both treatment groups suggesting that a decrease in endothelial cell recruitment prevents support of the tumour vascular. RUNX2 is a master regulator of bone formation [177] but also has pro-oncogenic functions. Under hypoxic stress, RUNX2 becomes elevated to help cancer cells survive [178,179]. The presence of RUNX2 has been noticed in several cancer types including, prostate, breast, pancreatic and melanoma [178,180-182]. High expression of RUNX2 in tumours contributes

to a more resistant aggressive phenotype by targeting genes associated with metastasis, apoptosis and angiogenesis [22,178,179,183]. In this study, both treatments caused a reduction in RUNX2, although the reduction was not statistically significant for Group 2.

Cancer stem cells (CSC) are a small population of cells that exist within a cancer tumour. [184] Recently it has been noted that CSCs are involved in tumour initiation, growth, metastasis and resistance to therapy. [184-187] The data reveals a reduction in CSC associated genes (NANOG and EPCAM) in both treatment groups, with group 3 demonstrating a significant decrease in all three genes examined (SOX2, NANOG and EPCAM). NANOG has been positively identified in human pancreatic adenocarcinoma cells [188] and this CSC marker was reduced to 63% and 11% for groups 2 and 3 respectively.

The expression of three pro-apoptotic (BID, BAX andBAD) and two anti-apoptotic genes (BCL2 and BCL2L1) were also analysed. BCL2 is an anti-apoptotic gene that is highly expressed in human primary pancreatic tumours. The expression of BCl2 was reduced in both treatment groups although the magnitude of decrease was greater for Group 3 compared to Group 2. Interestingly, it was significantly decreased by 50% in O_2MB-5FU/RB + US compared to untreated, which has also been noted in a previous communication.[140] The data reveals that three out of four of the autophagy marker genes (TFE3, ARL8B and CLCN7) were up regulated in both treatment groups. Autophagy is a stress response, correlated to the apoptosis pathway that can enhance survival of cells that have been damaged. [189] From a mechanistic perspective, the results demonstrate that autophagy is clearly playing a role in providing residual cancer cells with survival capabilities after treatment. These observations could suggest that targeting autophagy could provide additional therapeutic benefit. In general, these results indicate that the combined SDT/antimetabolite treatment does not involuntary stimulate any factors that could lead to more aggressive disease and the further study should be focused on utilizing more specific molecular targeted modalities.

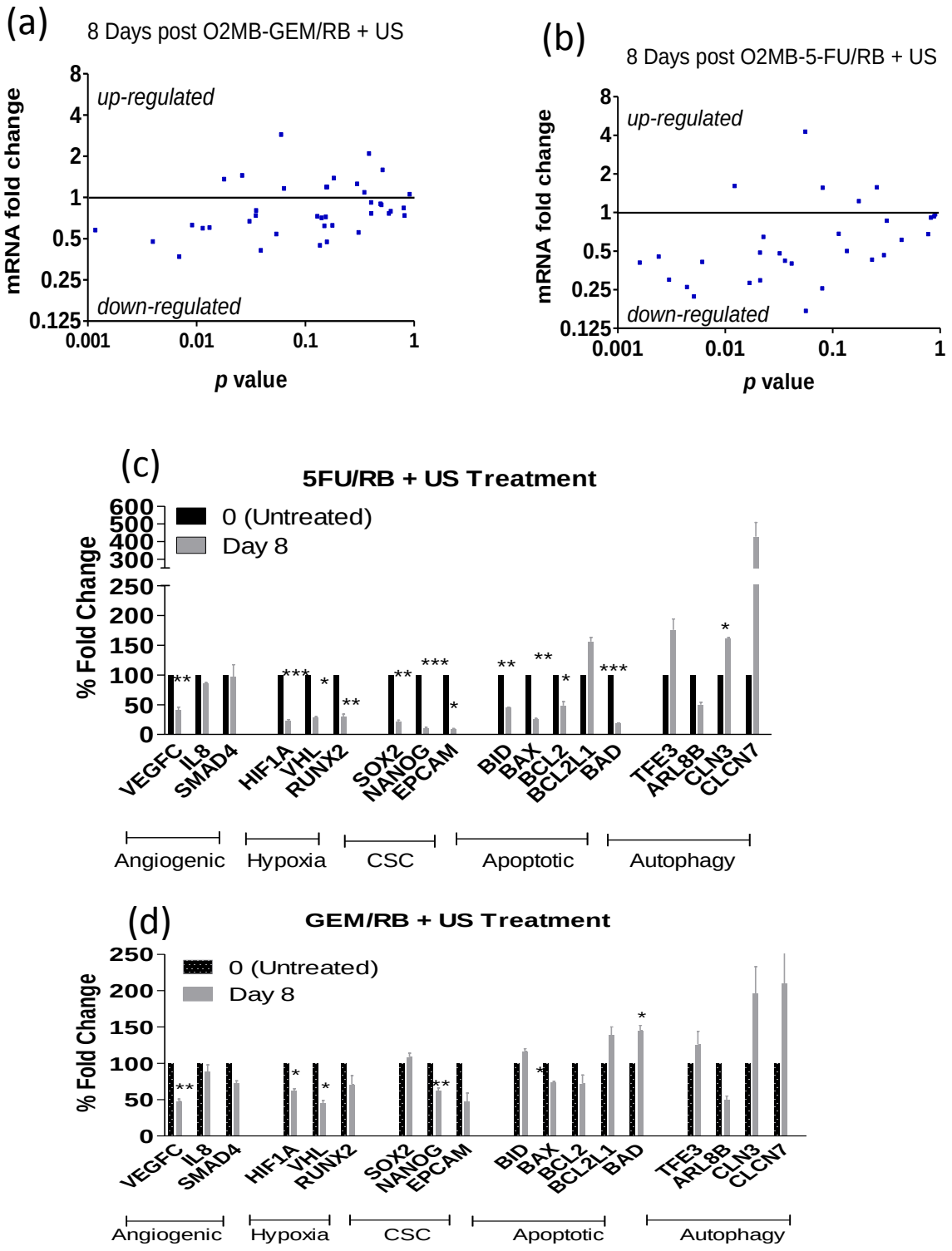

Figure 3. 28 Comparison of gene expression in tumours excised on days 8 from mice treated with (a) O_2MB-GEM/RB + US or (b)O_2MB-5FU/RB + US compared to untreated. Data in scatter plots were generated using quantitative PCR arrays, which were carried out on pooled RNA from tumours excised at each time point (*n* =3 per group). Comparison of gene changes on day 8 between untreated and (c) O_2MB-5FU/RB + US or (d) O_2MB-GEM/RB + US.

3.3.8 Identification of any toxic effects of combined Chemo-Sonodynamic therapy in Healthy Non-Tumour Bearing Mice.

While the active agents used in combined chemo-sonodynamic therapy treatment (i.e. Rose Bengal, 5-FU, Gemcitabine and phospholipid based MBs) are approved agents with established pharmacokinetic / safety profiles, and given that the targeted nature of the MB delivered treatment means that the amount administered is considerably less than that used for systemic treatment, it was still deemed prudent to ensure no deleterious interaction occurred when the MBs were combined with the active agents. Therefore, healthy non-tumour bearing MF1 mice (8 weeks old) were randomly allocated into nine groups (n=10; 5 male and 5 female) and treated as described in Table 3.3.

Table 3.3 the list of different treatment groups on healthy MF1 mice (n=10; 5 male and 5 female to identify gender specific effects)

Group	Treatment condition
1	Untreated
2	a tail vein injection of the O_2MB-RB conjugate
3	a tail vein injection of the O_2MB-Gem conjugate
4	a tail vein injection of the O_2MB-5-FU conjugate
5	a tail vein injection of the O_2MB-Gem-RB mixed conjugate
6	a tail vein injection of the O_2MB-5-FU/RB mixed conjugate
7	a tail vein injection of free RB
8	a tail vein injection of free 5-FU
9	a tail vein injection of free Gem

Mice were treated on day 0 and 8 via IV injection with either O_2MB-5FU, O_2MB-RB, O_2MB-GEM, O_2MB-RB / O_2MB-5FU, O_2MB-RB / O_2MB-Gem and a clinically relevant murine dose of the free drugs (RB, 5FU and GEM). Blood samples were taken on Days 8 and 15 mice and analysed for key biochemical markers in both the whole blood and serum. Following blood collection on Day 15, the liver and kidneys were removed. The body weights of the animals in each group were also analysed on a daily basis throughout the study. The results of the

body weight analysis are shown in **Figure 3.29** and reveal no significant difference between any of the groups indicating a lack of acute adverse effects of free drugs or MB based treatments. The blood biochemistry results are presented in **Figure 3.30** and again reveal no major differences between the free drugs or MB based treatments for any of the key biochemical markers. Meanwhile, it was noteworthy that alanine aminotransferase levels (ALT) were lower, while neutrophil were slightly higher in the O_2MB-Gem / O_2MB-RB group, relative to the Gem or RB treated groups. Elevated ALT levels are an indicator of liver damage while low platelet and neutrophil levels are commonly observed following chemotherapy treatment. [190,191]These differences are most likely lower due to the lower dose of Gem and RB delivered using the MB platform. In addition, one would expect neutrophil counts to be lower following administration of gemcitabine and the trend suggests this to be the case in the studies. However, it was interesting to note that neutrophil counts were higher in animals treated with the microbubble preparations. It is belived that this is again a consequence of targeted delivery of the chemotherapeutic drug and administration of overall lower doses to these animals. Similarly, histological analysis of liver and kidney sections also revealed no significant changes between the free drugs and MB based treatment groups, although there was a slight increase in hepatic lobular inflammation and steatosis for these groups relative to the untreated group. Analysis of kidney sections showed slightly raised levels of tubular vacuolation for the O_2MB-Gem / O_2MB-RB group, but again these levels were raised in the Gem and RB groups and the differences were non-significant. It is worth to notice that the mean score for the liver and kidney histology never exceeded 2, which is considered mild. These results reveral that O_2MB with a sensitiser or antimetabolite payload is safe and nono-toxic and is able to be applied for potentially achievement of better patient outcome.

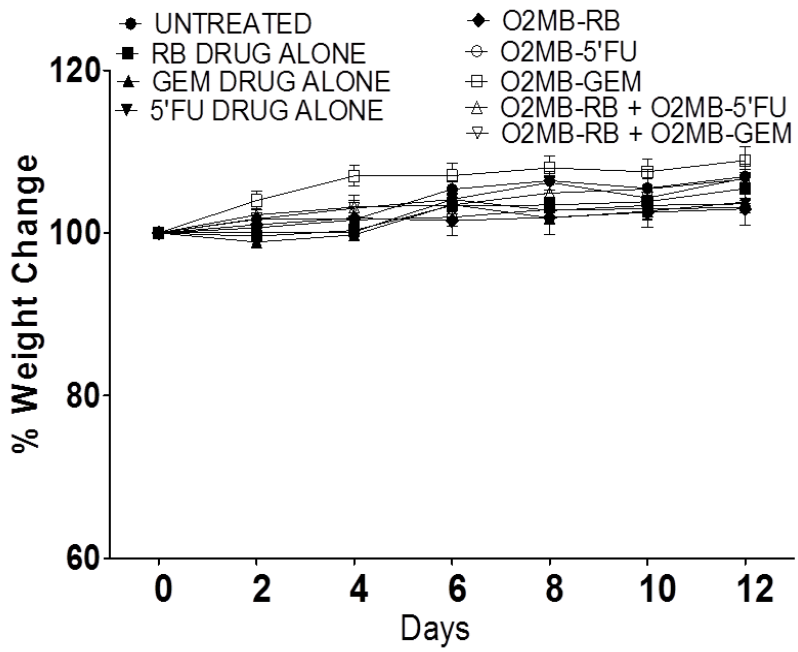

Figure 3. 29 Plot of % change in body weight against time during treatment, group1 untreated, group2,3,and 4 were clinically relevant doses of RB, GEM and 5FU, group 5, 6 and 7 were O_2MB-RB, O_2MB-5FU and O_2MB-GEM. Group 8 was treated with O_2MB-RB + O_2MB-5FU and group 9 received O_2MB-RB + O_2MB-GEM.

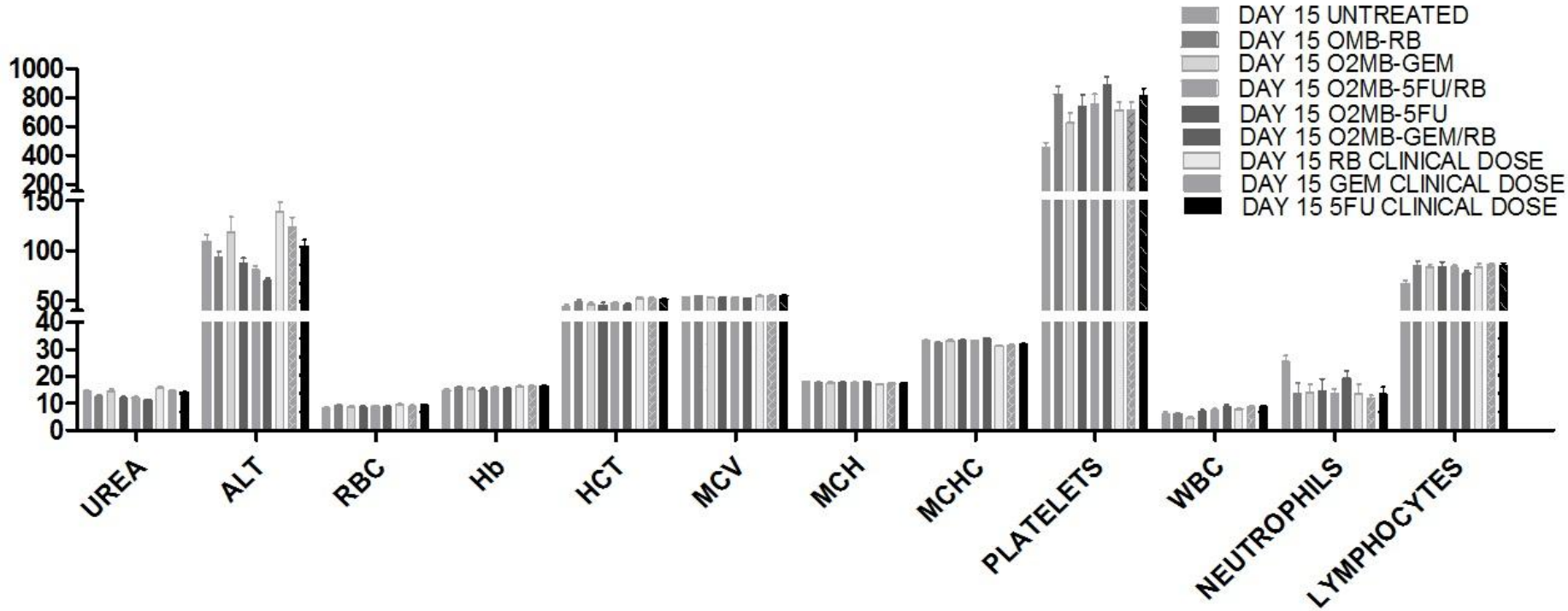

Figure 3.30 Whole blood and serum biochemistry markers analysis from healthy MF1 mice. Mice were divided into 8 groups and then biochemical markers such as urea, ALT etc were analysed 15 days after the treatment.

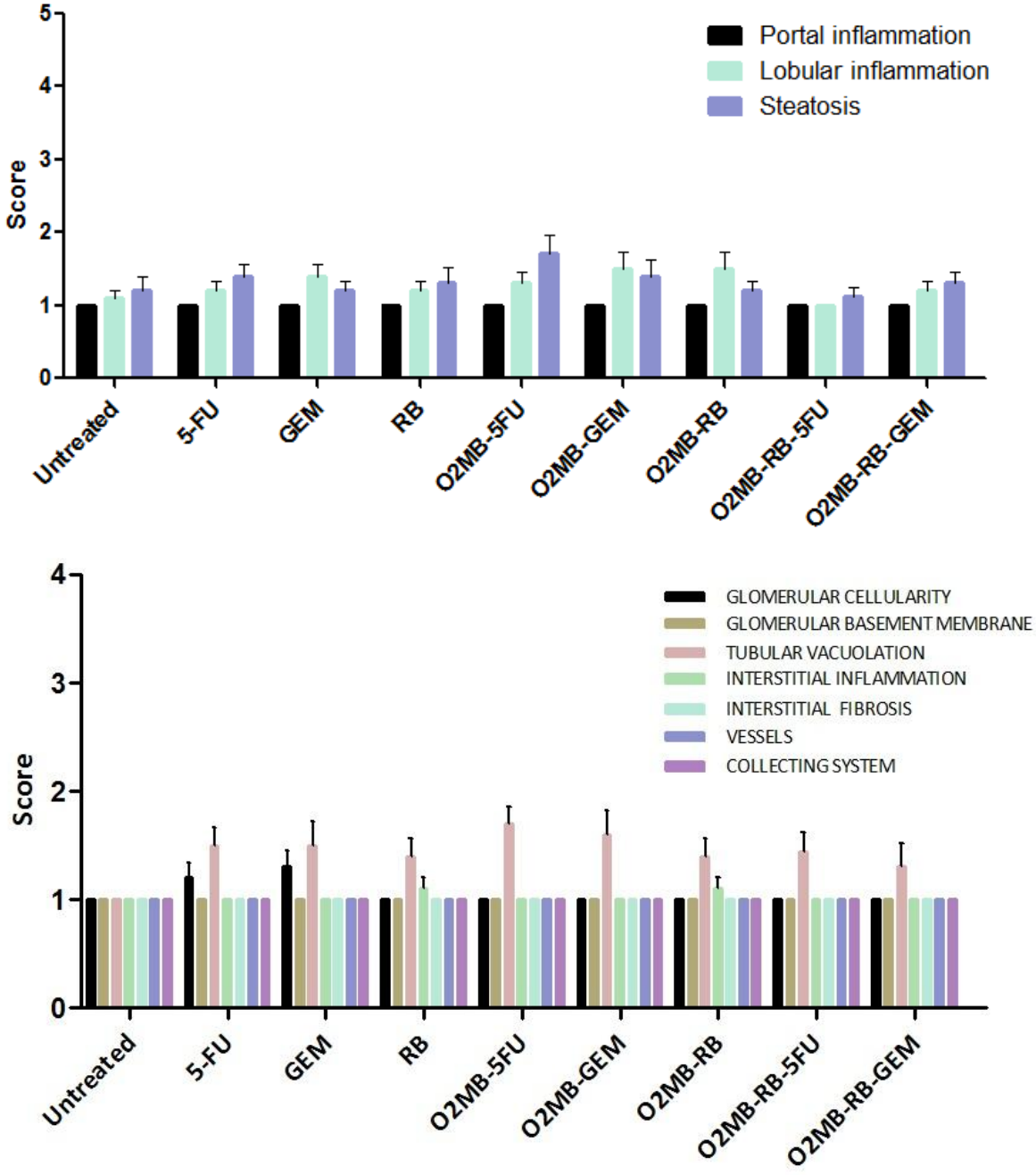

Figure 3. 31 Mean score of liver (top) and kidney (bottom) sections harvested from healthy MF1 mice treated with drugs according to Ishak (modified HAI) system.

3.4 Conclusion

The results obtained in this chapter demonstrate the potential of combined SDT/antimetabolite therapy, delivered using O_2MBs as a potential treatment of pancreatic cancer. SDT involves the activation of RB using low intensity ultrasound. Therefore, in the absence of US stimulation, RB is inactive with minimal dark toxicity. The use of O_2MBs to target gemcitabine delivery to pancreatic tumours also means that much less gemcitabine can be used when compared to systemically delivered gemcitabine, also reducing off-target toxic effects. Therefore, this approach is not only efficacious but also promises to be significantly less toxic than systemic GEM or 5-FU treatment.

Results from the *in vitro* experiments demonstrated that the newly prepared biotin-GEM ligand could been successfully attached to the avidin functionalised MBs. Combined SDT/antimetabolite treatment using O_2MB-RB/GEM formulation was generally more efficacious when used to treat pancreatic cancer cell lines than the corresponding formulation comprising O_2MB-RB/5FU. The optimum US conditions for treatment *in vivo* was identified as 3.5W/cm^2 & 30% DC for 3.5 mins. However, the efficacy of both O_2MB-RB/GEM and O_2MB/5FU were similar when activated using these US conditions. Currently, there is no explanation as to why these particular US conditions appear to be best for activating the combined treatment *in vivo* and this is currently an area of on-going investigation. Genetic analysis of treated tumours also generated significant difference in several genes involved in pancreatic tumour progression when compared to untreated tumours. These changes may provide the opportunity for the addition of adjuvants to enhance further the efficacy of the treatment. Results from the safety study demonstrated no evidence of toxicity for the MBs treatment highlighting the potential of this treatment for clinical translation.

Chapter 4

Magnetically Responsive Microbubbles as Delivery Vehicles for Targeted Sonodynamic and Antimetabolite Therapy of Pancreatic Cancer

Chapter 4 Magnetically Responsive Microbubbles as Delivery Vehicles for Targeted Sonodynamic and Antimetabolite Therapy of Pancreatic Cancer

4.1 Introduction

The work undertaken in **Chapter 3**, investigated the ability of combined antimetabolite and sonodynamic therapy (SDT), delivered using oxygen loaded lipid stabilised MBs to cause tumour growth delay in an ectopic murine model of the disease. While the study involved IV delivery of the MB conjugation and investigated a range of treatment conditions on efficacy and safety, the ectopic model used was not reflective of the true clinical situation. Efficacy data obtained from ectopic murine models is acceptable for submission as part of a pre-clinical dossier to regulators such as the MHRA for clinical trial approval. However, to fully test the suitability of a delivery vehicle, particularly MBs, to treat internal tumours, an orthotopic tumour model presents a greater challenge. Therefore, in this chapter, the ability of lipid stabilised microbubbles to deliver combined antimetabolite / sonodynamic therapy to orthotopic pancreatic tumours will be assessed. To enable the deposition of more payload than would be possible with ultrasound mediated MB destruction alone, the MB shell was also functionalised with magnetic lipids to add an additional layer of targeting to the delivery platform.

4.2 Aims and Specific Objectives

The major aim of the work undertaken in this chapter was to determine if external magnetic and low-intensity ultrasound fields can enhance the efficacy of combined antimetabolite / sonodynamic therapy, delivered using magnetically responsive microbubbles, in an orthotopic murine model of pancreatic cancer. The specific objectives were:

1. To prepare lipid stabilised O_2MBs with magnetic lipids embedded in the shell (MagO_2MB) and loaded with Rose Bengal (MagO_2MB-RB) or 5-FU (MagO_2MB-5FU).

2. To determine the ability of the MagMB conjugates to be retained during flow using an externally applied magnetic field.

3. To investigate the efficacy of $MagO_2MB$-RB, $MagO_2MB$-5FU and $MagO_2MB$-RB / $MagO_2MB$-5FU conjugates *in vitro* using a panel of three human pancreatic (Panc-1, Mia Paca-2 and BxPc-3) and a mouse primary (T110299) pancreatic cancer cell lines both in the presence or absence of ultrasound.

4. To determine the efficacy of the combined $MagO_2MB$-RB / $MagO_2MB$-5FU conjugates in mice bearing orthotopic BxPc-3 Luc tumours in the presence of external ultrasound and / or magnetic fields.

5. To evaluate the effect of the combined antimetabolite / sonodynamic therapy on the expression of selected genes and proteins in harvested tumour tissues.

6. To determine the safety of the $MagO_2MBs$ formulations in healthy non-tumour bearing mice.

4.3 Results and Discussion

4.3.1 Preparation and Characterisation of MagMBs.

As described in **section 2.5**, MagMBs were prepared by sonication of DBPC, DSPE-PEG (2000) and DSPE-PEG(2000)-biotin lipids in the presence of PFB gas and superparamagnetic iron oxide nanoparticles (SPIONs). The magnetic nanoparticle formulation comprised an iron oxide core with a lipid coating to facilitate incorporation of the magnetic nanoparticles into the MB shell. A schematic representation of the MagMBs is shown in **Figure 4.1(a)** and indicates how the lipid nanoparticles (red sphere) embed in the MB shell. The PFB containing MagMBs (MagPFBMBs) had an average diameter of 1–2 µm with a concentration of approximately 1.97×10^9 MB/mL as determined by analysis of optical microscopy images. **(Figure 4.1(b))**

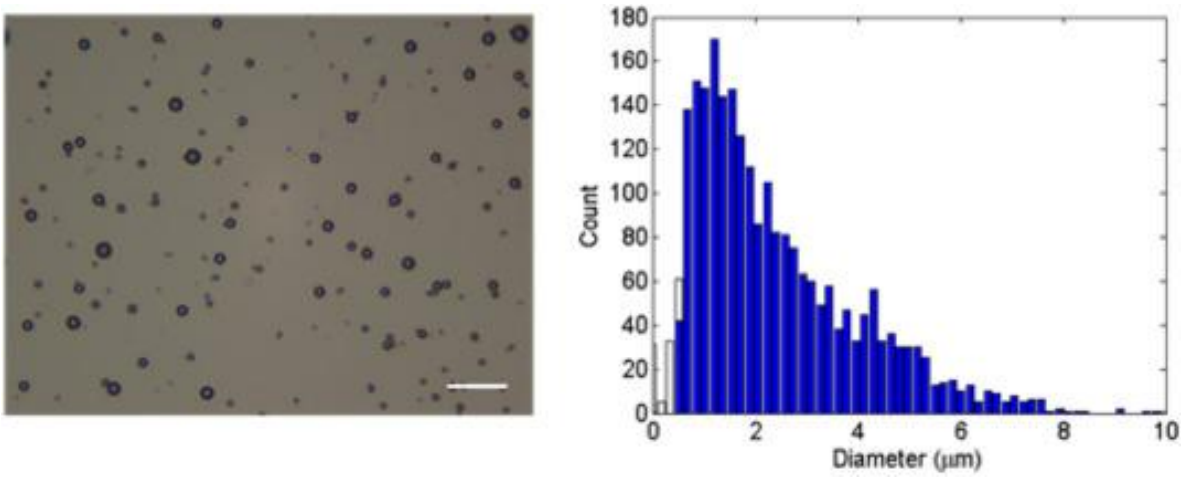

Figure 4. 1(a) Photomicrograph taken with a 40x objective lens of MagMBs after centrifugation (300 RCF, 5 min) and dilution (1:10) in PBS. Scale bar is 20µm. (b) Size distribution of MagMBs obtained from analysis of the optical microscope images detected by ImageJ analysis software.

Following isolation of the MagPFBMBs by centrifugation and surface coating with avidin, biotin-RB and biotin 5-FU were added to separate batches of the MagPFBMBs to generate RB loaded MagPFBMBs (MagPFBMB-RB) and 5-FU loaded MagPFBMBs (MagPFBMB-5FU) respectively. The PFB core gas was then exchanged with oxygen by sparging a MagMB conjugate suspension with pure oxygen gas for 2 min generating the $MagO_2$MB-RB and $MagO_2$MB-5FU conjugates (**Figure 4.2**).

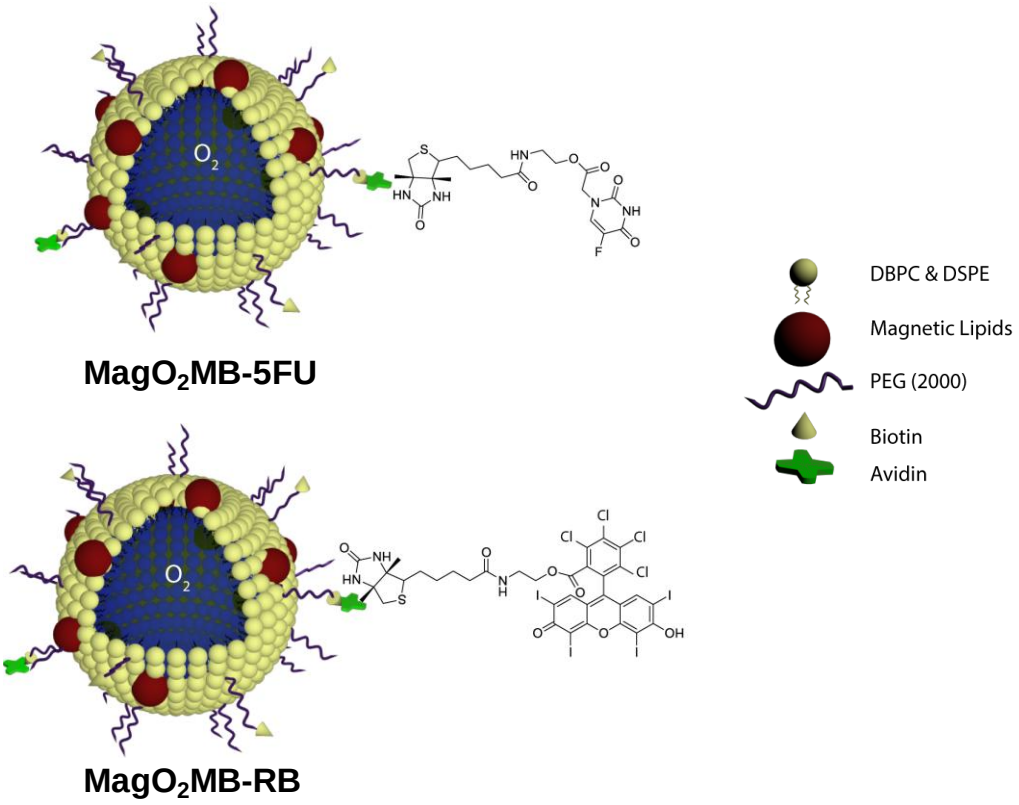

Figure 4. 2 Schematic representation of the $MagO_2MB$-5FU and $MagO_2MB$-RB conjugates.

4.3.1.1 Determination of Iron NPs loading on MagMBs

To determine the loading of the SPIONs in the MagMB shell, the Iron (III) content was determined using atomic absorption spectroscopy (AAS). A calibration curve was first constructed by measuring the Fe (III) intensity at 248.3 nm in standard samples (**Figure 4.3**) and good linearity (R^2 = 0.99) observed in the 0 – 6 mg/L range. The amount of Fe (III) in a fixed amount of the MagMBs was then determined. As the SPIONs are formed from magnetite (Fe_3O_4) which is a mixture of Fe (III) and Fe (II) oxides in a ratio of 2:1, the total iron content was determined by multiplying the Fe (III) value obtained from AAS (190.8

mg/L)by 1.5 to obtain a final value of 286.2mg/L corresponding to 0.286 mg per 10^9 MB.

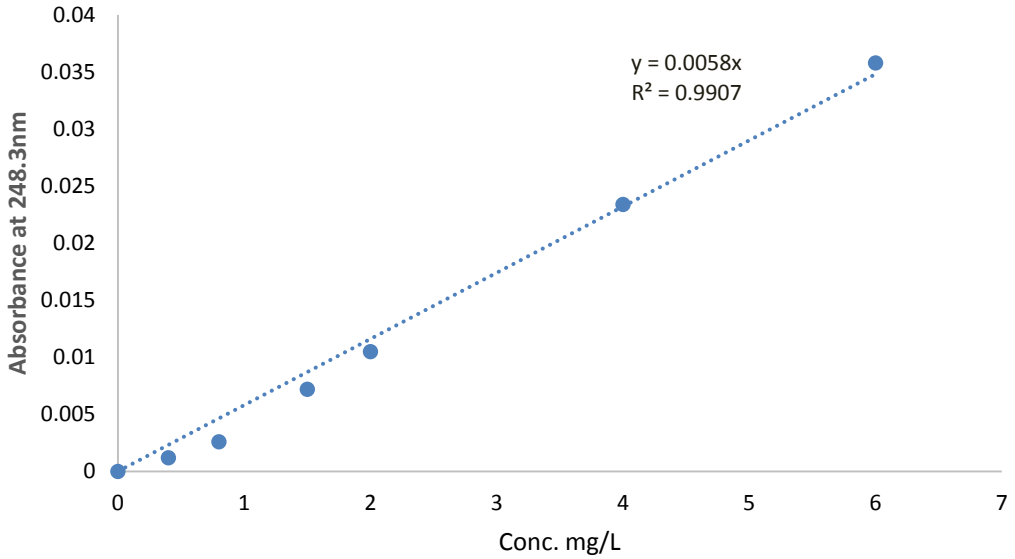

Figure 4. 3 Plot of Atomic absorbance intensity against Fe (III) concentration for a range of Fe (III) standard solutions.

4.3.1.2 Retention of MagMBs in a flow-phantom using an external magnetic field.

In order to determine the magnetic response of the platform, suspensions of $MagO_2MBs$ (1 mL) were placed in a syringe and pumped through a flow chamber (0.6 mL/min) with a fixed magnet (0.46 T) positioned on the underside of the flow chamber during the course of the experiment. (**Figure 4.4**)

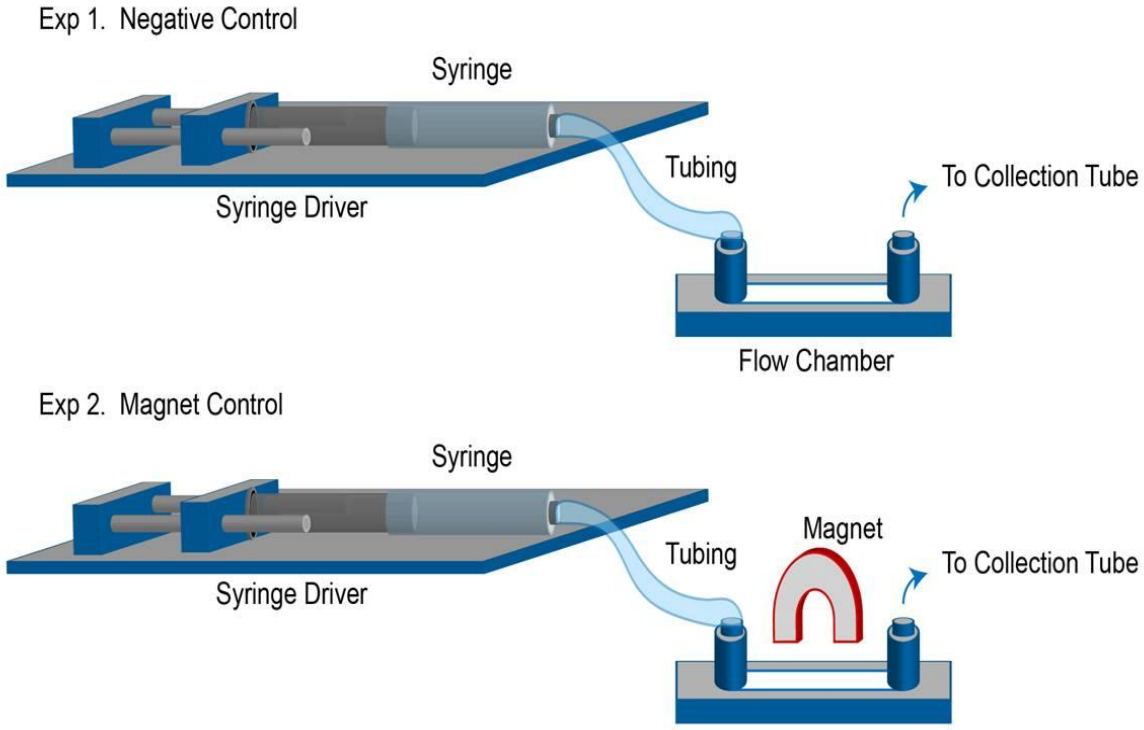

Figure 4. 4 Schematic of the syringe driver and flow chamber, in the absence (top) and presence (bottom) of a fixed magnet, to determine magnetic responsiveness of the MBs flowing through the flow chamber.

A control study was also performed in the absence of a fixed magnet but under identical conditions. At the end of each experiment, the number of $MagO_2$MBs retained in the flow cell was counted as shown in **Figure 4.5**. A significant increase in $MagO_2$MBs number ($p<0.01$) was observed when the fixed magnet was present indicating the ability of the $MagO_2$MBs to be retained against flow using an external magnetic field. Blood flow rates within the human body vary considerably depending on vessel type and size with blood leaving the aorta (2400 cm min^{-1}) at a flow rate approximately 3 orders of magnitude greater than in capillaries (1.8 cm min^{-1}).[192] In tumours, the increased viscous and geometrical resistance presented by the vasculature can compromise its blood flow, meaning the average velocity of blood in tumour vessels can be an order of magnitude lower than in normal vessels.[193] Therefore, the flow rate used in the current study was towards the upper limit of rates chosen to study tumour perfusing resistivity which suggests that magnetic targeting may be effective in helping MBs retain in the tumour vasculature and allowing a greater proportion to be destroyed in an applied acoustic field.

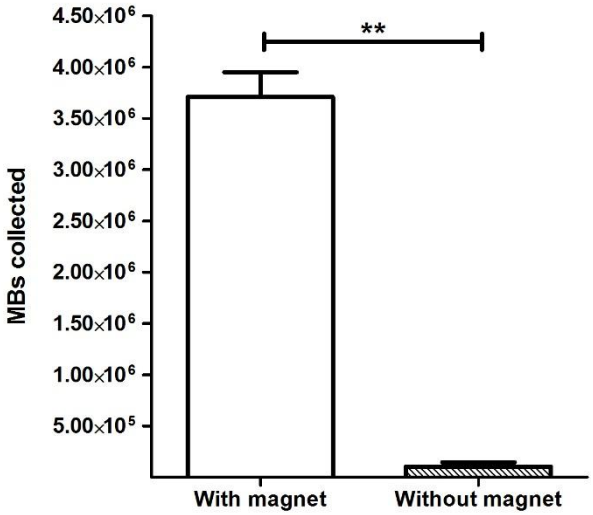

Figure 4. 5 Plot of MBs retained after injection through a flow-cell in the presence and absence of a fixed magnet.

In order to retain a useful proportion (10%) of injected microbubbles at these blood flow rates, an estimated magnetic field gradient of 0.15 T/m would provide sufficient force to capture superparamagnetic particles flowing the capillary vessels. [194] When considering the possible translation of such technology to the clinic, both transabdominal and endoscopic sources are viable methods for the delivery of magnetic fields to the pancreas. In the context of the above capillary flow rates, optimised permanent magnet designs with a volume of 1.02 cm^3 [195] would be capable of targeting a tumour through the duodenal wall as part of an endoscopic probe, where the approximate distance to the head of the pancreas is in the region of 10 mm. (This was informed by our clinical colleagues.) In the case of transabdominal delivery, where the distances are more variable depending on the patient's body to mass index (BMI), the optimised permanent magnet volume would be in the region of 1.66 cm^3, based on a distance of 50 mm from the outside of the abdomen to the pancreas. Even at flow rates 5 times higher than the capillary flow rate used above, the estimated field gradient to retain the same fraction of MBs would be 2.48 T/m, requiring permanent magnet volumes in the region of 1.5 cm^3 for an endoscopic device, which is readily achievable. [197] Given endoscopic ultrasound (EUS) analysis is a common diagnostic tool used in staging pancreatic cancer, a EUS device configured to deliver both magnetic and ultrasonic fields is one possibility for the translation of this technology to clinic.

4.3.2 In vitro cytotoxic efficacy of sonodynamic treatment with $MagO_2NPs$

The efficacy of combined antimetabolite / sonodynamic therapy has previously been established in a range of pancreatic cancer cell lines by McEwan et al [140] and also in **Chapter 3** of this thesis. These experiments were also repeated in this chapter to ensure the presence of the redox active Fe (II) or Fe (III) does not negatively impact on the SDT or 5-FU efficacy. This is particularly valid for SDT as the active agent is ROS that could potentially be impacted by Fe (II) or Fe (III) by participating in electron transfer reactions. Human pancreatic BxPc-3, Mia Paca-2 and Panc-01 cancer cells were chosen as targets in addition to a mouse primary T110299 cell line. [170] 5000 cells per well were seeded in 96 well plates and treated with a suspension of either $MagO_2$MB-5FU, $MagO_2$MB-RB or combined $MagO_2$MB-5FU / $MagO_2$MB-RB with selected wells then exposed to low-intensity ultrasound (3.5W/cm^2 & 30% DC for 3.5 mins). Untreated cells and cells treated with ultrasound only were used as controls. Cell viability was then determined 24h later using a MTT assay. A magnetic field was not used in this *in vitro* study as the purpose of the fixed magnetic field was simply to retain the MagMBs during flow and not to add any additional toxicity in its own right.

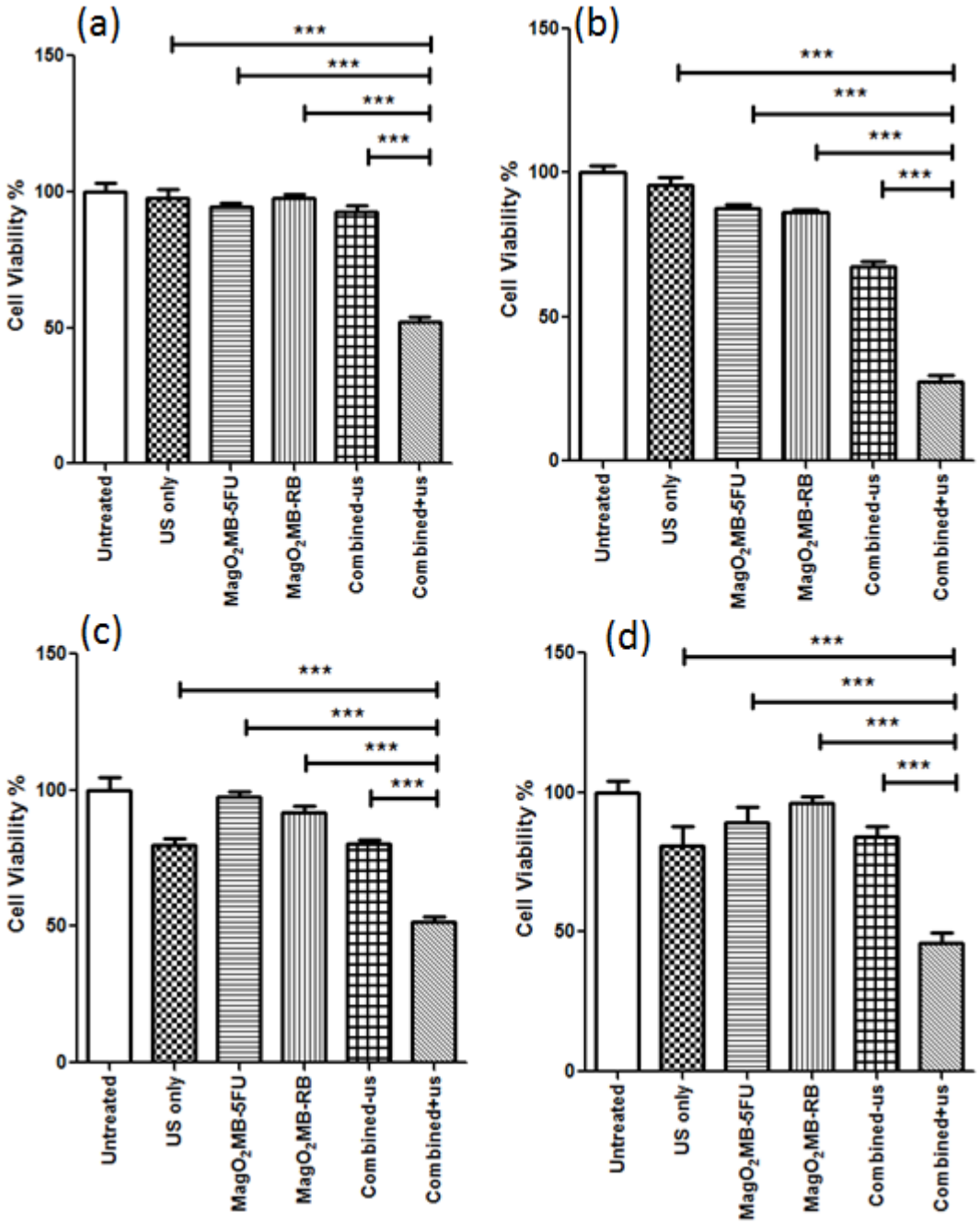

Figure 4. 6 Plot of % cell viability for (a) BxPc-3 (b) T110299 (c) Mia Paca-2 and (d) Panc-01 after treatment with (i) untreated, (ii) ultrasound only (iii) $MagO_2$MB-5FU only (iv) $MagO_2$MB-RB only, (v) combined $MagO_2$MB-RB and $MagO_2$MB-5FU and (vi) combined $MagO_2$MB-RB and $MagO_2$MB-5FU plus ultrasound. Significance of (vi) versus (ii), (iii), (iv), or (v): *** $p < 0.001$.

A significant reduction ($p<0.001$) in cell viability was observed in all cell lines that received the combined treatment (i.e. $MagO_2$MB-RB / $MagO_2$MB-5FU + US) (**Figure 4.6**). In contrast, both the $MagO_2$MB-5FU and $MagO_2$MB-RB alone (i.e. no US) demonstrated only a slow cell proliferation reduction (<10%) meaning it was possible to control the generation of cytotoxicity using the ultrasound stimulus. Therefore, these results suggest that application

of ultrasound not only facilitates at the same time the release of encapsulated O_2 gas with the attached RB/5-FU into the extracellular medium but is also able to activate RB after sonostimulation, leading as consequence to ROS generation. [140] It is also possible that application of the ultrasound could be enhancing the action of 5-FU by means of sonoporation. Indeed, it has been shown that this strategy can be employed to enhance the action of cancer chemotherapeutics by affording transient intracellular access of the drug via sonoporation. [198]

4.3.3 Investigating the effect of combined 5-FU / SDT treatment using MagO_2MBs for therapeutic effect in an orthotopic pancreatic cancer murine model.

After obtaining promising results with the combined antimetabolite/SDT therapy using the MagO_2MB platform in the *in vitro* studies outlined above, the next step was to evaluate the benefit of magnetic targeting in an *in vivo* model. For this purpose, orthotopic human xenograft BxPc-3-Luc pancreatic tumours were established in SCID mice.

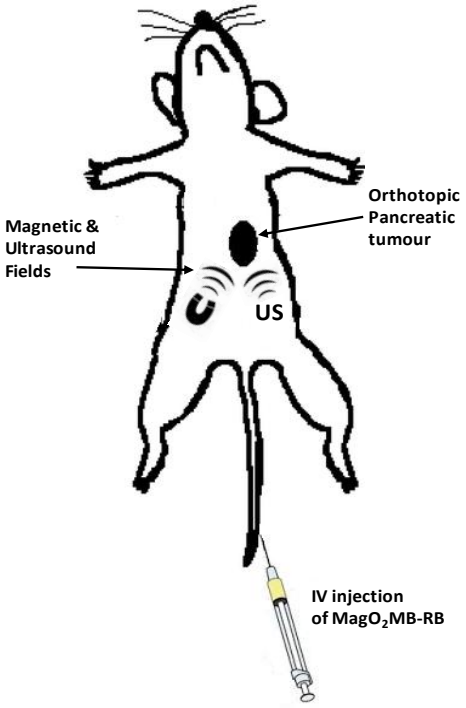

Figure 4. 7 A schematic diagram showing magnetic MBs to improve targeting further in an orthotopic model.

This was achieved by surgically implanting BxPC-3-Luc cells into the head of the pancreas. Nineteen days following implantation the mice were randomly divided into three groups

(n=4): group 1 received no treatment; group 2 received a $MagO_2MB$-5FU / $MagO_2MB$-RB suspension administered intravenously with the tumour region exposed to low-intensity ultrasound during and following injection for a total exposure of 3.5 min; group 3 also received an IV injection of the $MagO_2MB$-5FU / $MagO_2MB$-RB suspension but in addition to ultrasound treatment, a permanent magnet was also directed at the tumour during ultrasound treatment. Treatments were repeated on days 20 and 21 with the mice sacrificed on day 28. [199] This treatment schedule was determined on the basis that as the main use of this technology will be as a neo-adjuvant treatment to downstage tumours in advance of surgery, an aggressive treatment of the tumours with three successive administrations was the preferred choice.

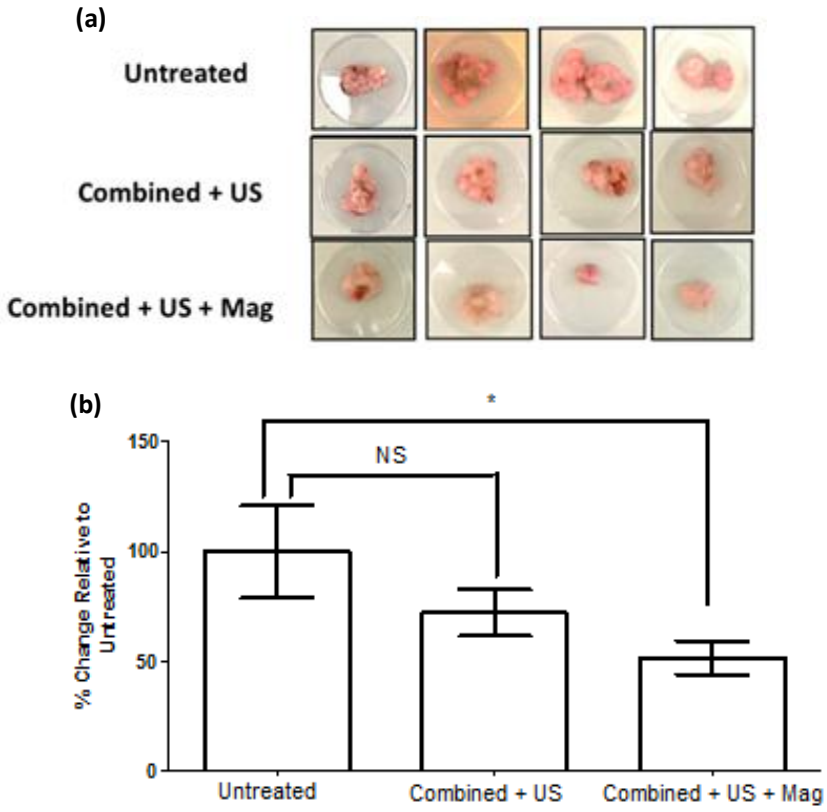

Figure 4. 8 (a) Photograpies of orthotopic BxPc-3 Luc tumours removed from SCID mice 28 days following implantation after (i) no treatment (top), (ii) treatment with combined $MagO_2MB$-RB and $MagO_2MB$-5FU plus ultrasound (middle) or (iii) treatment with $MagO_2MB$-RB and $MagO_2MB$-5FU plus ultrasound and magnet (bottom). Treatments were administered on day(s) 19, 20 and 21. (b) Plot of % change in tumour volume relative to untreated for mice treated with (ii) or (iii) above. * $p < 0.05$ for (iii) compared to (i).

A statistically significant reduction in tumour volume of 48.3% ($p < 0.05$) was observed in mice treated with $MagO_2MB$-5FU / $MagO_2MB$-RB and the permanent magnet directed at the tumour during ultrasound treatment, compared to untreated mice. For mice treated with $MagO_2MB$-5FU / $MagO_2MB$-RB and ultrasound but no magnet, the tumours were 27.9% smaller than untreated tumours although the reduction was not statistically significant. This improvement in efficacy in the presence of a magnetic field could be due to more MBs being retained in the tumour microenvironment, so that ultrasound exposure can enable enhanced deposition of MB payloads and subsequent activation of the sensitiser. These results suggest a benefit of incorporating magnetic targeting into the MB platform to enhance the combined chem-sonodynamic therapy of orthoptic tumours.

4.3.4 Investigation of the treatment efficacy on the expression of Caspase and Bax biomarkers

Since the combined antimetabolite / sonodynamic therapy using the $MagO_2MB$ conjugates showed encouraging results both in the *in vitro* and *in vivo* experiments, the effect of the treatment on caspase and BAX protein expression was investigated. For this purpose, mice from *in vivo* experiments described in **section 4.3.3** were euthanized following treatment, a single cell suspension was prepared from the excised tumours. The cell suspension was analysed for active caspase and BAX protein expression using flow cytometry. RNA was also extracted from tissue and gene expression analysed using qRT-PCR for relative expression of TMBIM1 (Transmembrane BAX Inhibitor Motif-Containing Protein 1). The results are shown in **Figure 4.9** and reveal that activated caspase and BAX protein levels were both significantly elevated in tumours treated with the combined $MagO_2MB$-RB / $MagO_2MB$-5FU conjugates and ultrasound / magnetic fields compared to expression of those proteins in tumours from either of the other 2 groups ($p < 0.05$)

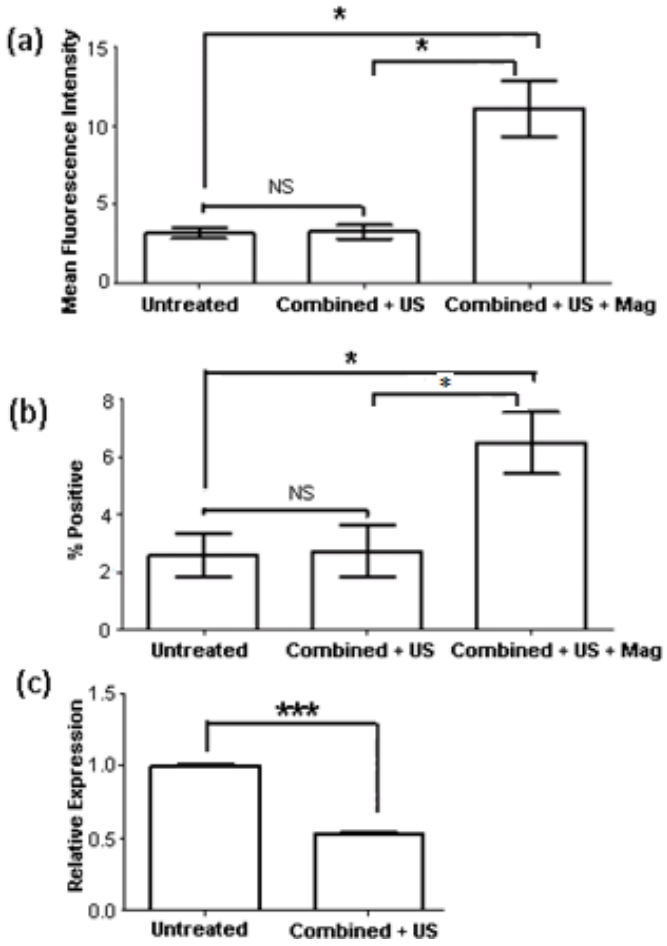

Figure 4. 9 (a) Plot showing presence of active caspase in single cell suspensions derived from tumours removed from SCID mice 28 days following implantation and left untreated (i), (ii) or treated with combined $MagO_2MB$-RB and $MagO_2MB$-5FU plus ultrasound (middle) or (iii) $MagO_2MB$-RB and $MagO_2MB$-5FU plus ultrasound and magnet fields (right). Caspase activity, reflective of apoptosis, was performed evaluating Pan Caspase probe fluorescence intensity via flow cytometry. (b) Plot of evaluation of BAX protein expression via flow cytometry. *$p < 0.05$ for (iii) compared to (i). (c) Plot of relative expression of TMBIM1 in untreated control tumours and those receiving combined treatment. ***$p<0.001$.

Increases in activated caspase and BAX protein levels are indicative of increased apoptosis [200] and consistent with the increased treatment efficacy observed for Group 3. Although BAX and caspase were not significantly increased in group 2, a trend in tumour size reduction was observed for this group (**Figure 4.9**). Previous studies by MecEwan et al have shown that ectopic BxPc-3 tumours receiving combined antimetabolite / SDT treatment in the absence of a magnetic field resulted in decreased tumour size and expressed markers for increased apoptosis. [140] Although significant differences exist in the manner in which

this and the previous study done by McEwan et al [171] were performed both from the perspective of the model type (orthotopic vs. ectopic) and that of the dosing regimen (multiple vs. single), it was felt that the reduction 'trend' observed in group 2 in the current study (**Figure 4.9**) warranted further consideration. To this end, qRT-PCR analysis demonstrated that TMBIM1 was significantly downregulated in tumours receiving the combined treatmentand exposed to US only (i.e. in the absence of a magnetic field) (**Figure 4.9**). Since TMBIM1 is an inhibitor of BAX, [201] its down regulation in these tumours could lead to enhanced BAX-mediated apoptosis without an observable change in BAX concentration. However, it is realised that the data presented **in Figures 4.9(b) and (c)** were derived from tumours removed at a specific time point (9 days) following treatment and these data may differ if longer or shorter time-points were chosen. Continuing studies will include a more in-depth examination of gene expression at various time points in order to more clearly elucidate the interplay between both of these genes and their role in treatment-induced apoptosis.

4.3.5 Determining the safety of $MagO_2MB$ conjugates-in a healthy mouse model

It was also observed during the above studies that animals who received the magnetically-responsive platform treatment did not suffer any overt adverse effects and no significant change in body weight was observed over the course of the experiment [**Figure 4.10(a)].** As undertaken in **Chapter 3**, a more detailed toxicology study was performed to investigate this safety aspect further by administering the $MagO_2MB$-5FU / $MagO_2MB$-RB suspension to 10 healthy non-tumour bearing MF1 mice by tail vein injection on Days 0 and 8. Similar experiments were undertaken involving MF1 mice treated with 5-FU or RB alone at concentrations higher than those present on the $MagO_2MB$s in order to reflect clinical doses. Blood samples were harvested from each group of animals on Day 15 and analysed for a range of key biochemical markers [**Figure 4.10(b)**]. No major differences in profile were observed between $MagO_2MB$-5FU / $MagO_2MB$-RB group and the other groups, which would raise any concern regarding toxicity of the combined MB-based treatment. Indeed ALT activity, which is a measure of liver function, was lower in the $MagO_2MB$-5FU / $MagO_2MB$-RB group compared to the other groups. While there was an increase in platelet and lymphocyte levels for the $MagO_2MB$-5FU / $MagO_2MB$-RB group relative to the untreated

group, levels were also raised in 5-FU and Rose Bengal treated animals and the differences between these groups were not significant.

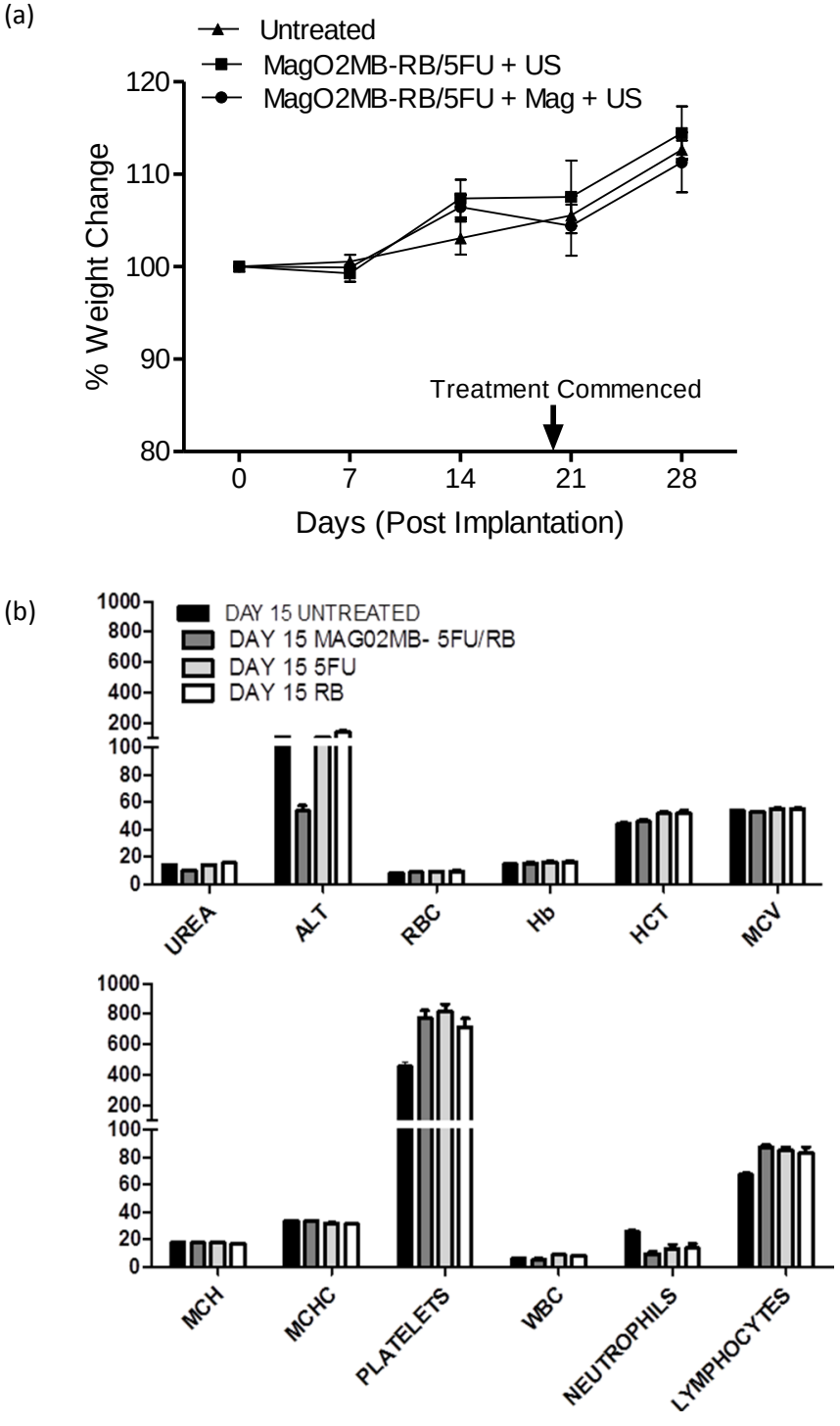

Figure 4. 10 (a) Average body weight of mice following treatment with vehicle only, i.e. $MagO_2MB$, a suspension of $MagO_2MB$-RB / $MagO_2MB$-5FU + ultrasound, or a suspension of $MagO_2MB$-RB / $MagO_2MB$-5FU + ultrasound + magnet. (b) Whole blood and serum biochemistry analysis from healthy MF1 mice (i) untreated control, or treated with (ii) a suspension of $MagO_2MB$-RB / $MagO_2MB$-5FU, (iii) 5-FU alone, or (iv) RB alone.

Similarly, there was evidence of mild neutropenia in the three treatment groups relative to the untreated group, but again the difference between the $MagO_2MB$-5FU / $MagO_2MB$-RB group and the 5-FU and RB groups was not significant. Furthermore, histological analysis of liver and kidney sections removed post-mortem on Day 16 also revealed no significant changes between the $MagO_2MB$-5FU/$MagO_2MB$-RB group and the 5-FU or RB treated groups (**Figure 4.11**).

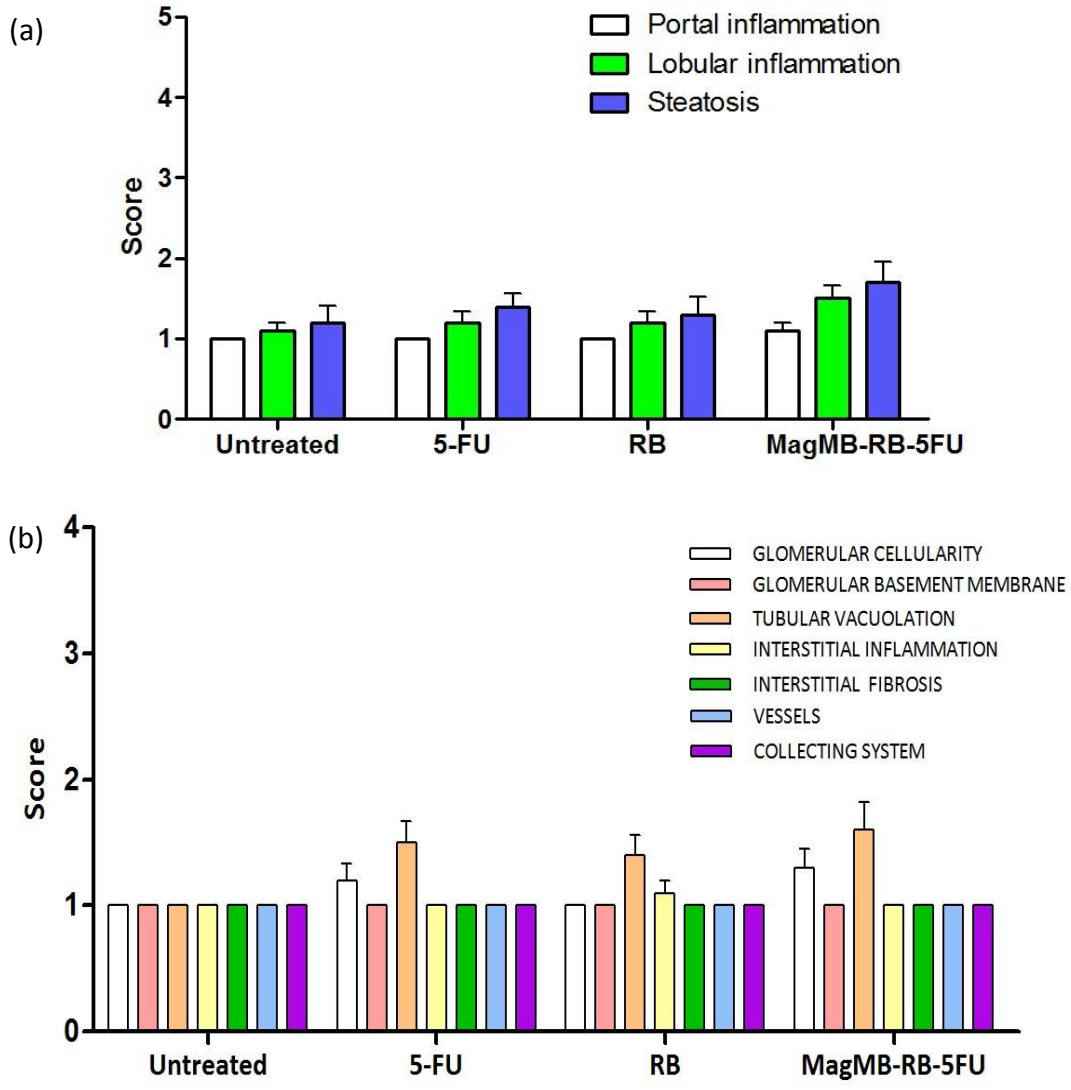

Figure 4. 11 Scoring for sections of (a) liver and (b) kidney following (i) no treatment, or treatment with (ii) 5-FU alone, (iii) RB alone, or (iv) a suspension of $MagO_2MB$-RB / $MagO_2MB$-5FU conjugates. Portal inflammation scored 1-5 while all other parameters were scored from 1-4. In each case a score of 1 = normal.

A slight increase in liver steatosis score was observed in $MagO_2$MB-5FU/$MagO_2$MB-RB group but this was not significant when compared to the 5-FU or RB groups. It has been reported in literature that liver steatosis, also known as fatty liver disease, can also be influenced by certain chemotherapeutic drug treatment, including antimetabolites. [202] The slight increase in score for the $MagO_2$MB-5FU / $MagO_2$MB-RB group relative to 5-FU or RB may be due to the uptake and metabolism of the lipid component of the MBs and on that basis is likely a transient change of limited clinical significance. Analysis of kidney sections showed slightly raised levels of glomerular cellularity and tubular vacuolation for the $MagO_2$MB-5FU/$MagO_2$MB-RB group also observed in the 5-FU and RB groups. It must be stressed, however, that any effect observed in the liver or kidney histology analysis was deemed to be mild and in no case the mean score exceeded 2. Collectively, these results indicate the potential of $MagO_2$MBs as a safe and effective platform for the delivery of combined antimetabolite and SDT treatment of pancreatic cancer.

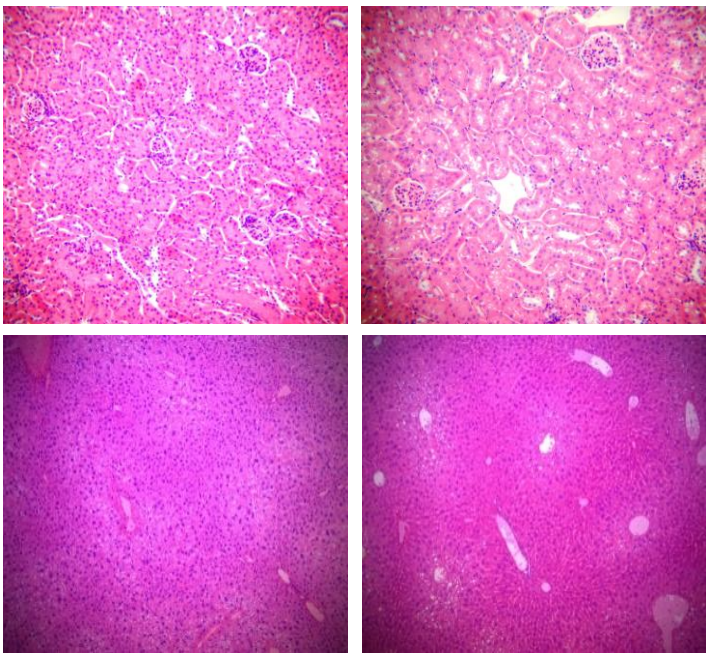

Figure 4. 12 Representative H&E images of liver (top) and kidney (bottom) sections taken from animals sacrificed on day 15 following treatment with a suspension of $MagO_2$MB-RB / $MagO_2$MB-5FU (right) or untreated (left).

4.4 Conclusions

Magnetically responsive MBs were successfully prepared and shown to be retained at a target site in the presence of an externally applied magnetic field. When decorated with the sensitiser RB and the antimetabolite 5-FU and subjected to ultrasound treatment, $MagO_2MB$ conjugates induced a significant reduction of pancreatic cancer cell viability, greater than 50%. The combined application of external magnetic and ultrasound during IV delivery of the $MagO_2MB$ conjugates resulted in a 48.3% reduction in orthotopic pancreatic tumour volumes 9 days after treatment, while the application of ultrasound alone resulted in a reduction of only 27.9%. In addition, a significant increase in apoptosis was observed in tumours that were treated with the $MagO_2MB$ conjugates and exposed to both magnetic and ultrasound fields when compared to the ultrasound treatment alone or untreated groups. The results presented in this chapter confirm the effectiveness of combined sonodynamic/antimetabolite therapy using $MagO_2MB$ as delivery platform in a pancreatic cancer model.

Chapter 5

Oxygen Generating Nanoparticles for Improved Photodynamic Therapy of Hypoxic Tumours

Chapter 5 Oxygen Generating Nanoparticles for Improved Photodynamic Therapy of Hypoxic Tumours

5.1 Introduction

Combatting hypoxia is a major challenge in the treatment of solid tumours using PDT or SDT as oxygen is a key requirement for the generation of ROS using these techniques. This is particularly true for tumours of the pancreas [203] and hypoxia is now recognised as an indicator of poor prognosis for many types of cancer.[204,205] Inefficient gas and mass transfer resulting from atypical vascularisation together with elevated oxygen demand by hyper-proliferating tissues results in hypoxia in most solid tumours. Once a hypoxic environment develops in the tumour, cell populations become resistant to many conventional cancer chemotherapeutic agents through a variety of adaptive survival mechanisms. Similarly, for radiotherapy, oxygen has been shown to play a very significant role in enhancing radiation induced damage to nucleic acid in target tissues. [139] One of the major challenges associated with the latter has been to provide oxygen to the target tissues during therapy. A number of approaches have been employed including, hyperbaric oxygen breathing and breathing pure oxygen or carbogen at atmospheric pressure. [157] Such approaches, however, have delivered limited success and there is still a significant un-met need in this area. Previously, work by McEwan et al, has demonstrated that the selective destruction of oxygen loaded microbubbles in the tumour microenvironment using low intensity ultrasound provided a temporary boost in tumour oxygen levels that enhanced the sonodynamic therapy (SDT) treatment of pancreatic tumours [158] and this approach was adopted in **Chapters 3 & 4**. However, in this chapter, the development of *in situ* oxygen generating nanoparticles as an alternative method to improve tumour oxygenation during PDT will be explored.

The principle of O_2 generation using CaO_2 NPs has been discussed in **section 1.5.3**. However, if CaO_2 NPs are to be used in biological applications and in particularly *in vivo*, it is imperative they remain stable in circulation until taken up by target tissue (i.e. tumour) so

that inadvertent systemic activation is limited. In theory, it should be possible to coat the NPs with a polymer that has low aqueous solubility at physiological pH (i.e. 7.4) but possesses increased solubility in environments where the pH is mildly acidic. Tumour tissue interstitial fluid is known to be more acidic (pH = ~6.0) than normal tissue, as hypoxia generates an overproduction of acid by inducing the production of energy from glycolysis via the Pasteur effect. [206] This difference in pH has been utilised in numerous pH-responsive cancer therapeutics and diagnostic probes. [207] In the context of using CaO_2 NPs as a means for *in situ* oxygen generation, it may be possible to use this difference in pH to facilitate targeted oxygen delivery during PDT and enhance its effectiveness in hypoxic environments.

The aim of the work presented in this chapter was to develop a pH responsive coating for CaO_2 NPs that would protect the particles from rapid decomposition at neutral pH but facilitate the process in a mildly acidic environment. Eudragit E was chosen as a starting point as this polymer has been shown to suppress drug release at pH 7.4 when used as a tablet coating but rapidly dissolves in acidic medium to release the active drug. [208] Eudragit E contains a tertiary amine that ionises in acidic medium facilitating its dissolution. Therefore, in this chapter, a pH responsive polymer **11**, similar in structure to Eudragit E was developed to coat the CaO_2 NPs and protect them from decomposition in water at pH 7.4 but facilitate their dissolution when the pH reduced to 6.0. The effect of this oxygen generation on the efficacy of PDT was also determined.

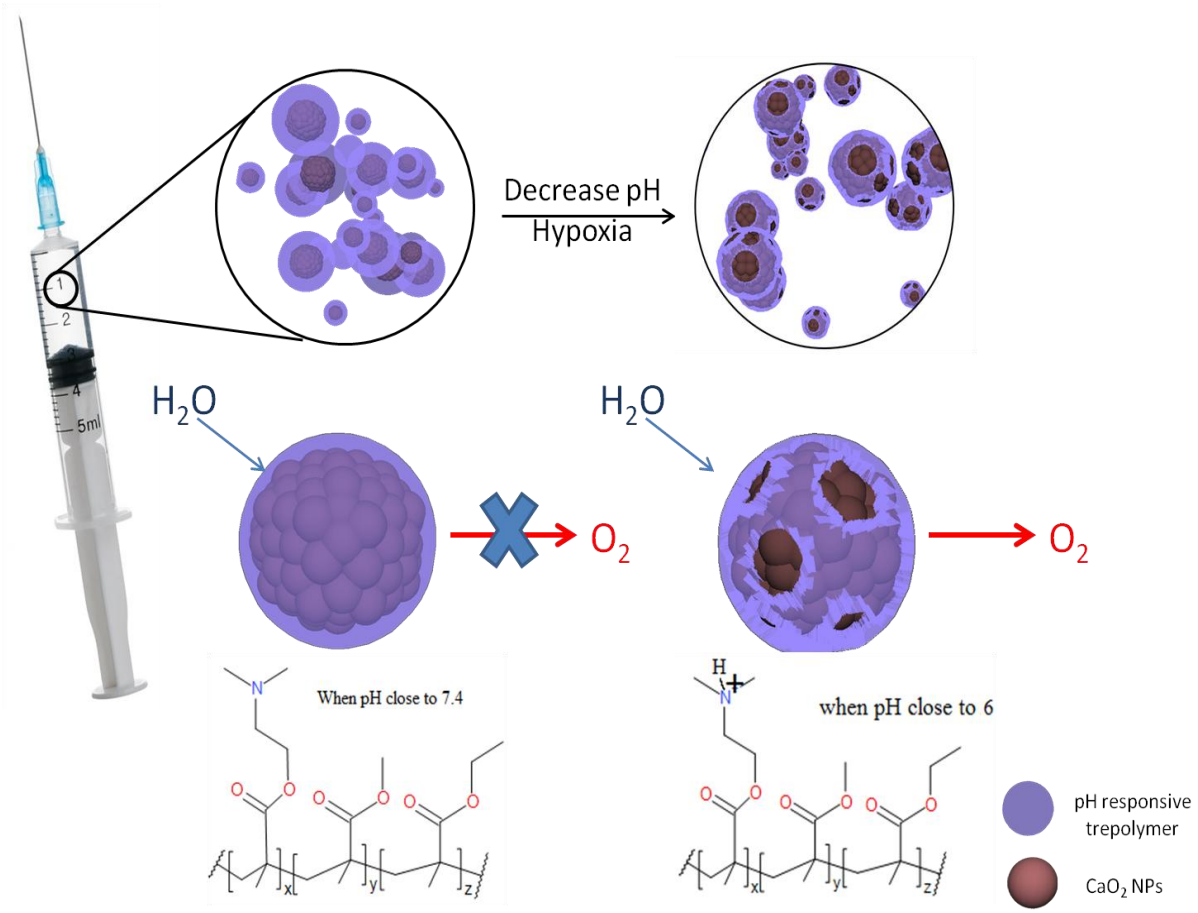

Figure 5. 1 Schematic representation of core-shell based NPs, where CaO_2 comprises the core with pH-responsive methacrylate based co-polymer coating

5.2 Aims and objectives

The main aim of the work undertaken in this chapter was to prepare and characterise CaO_2 NPs capable of oxygen generation upon decomposition in water. A pH-responsive methacrylate based terpolymer was also synthesised, characterised and used to the coat CaO_2 NPs. The ability of the particles to improve oxygenation in hypoxic environments and enhance PDT-mediated treatment has been evaluated using BxPc-3 pancreatic cancer cells *in vitro* and an ectopic Mia Paca-2 xenograft murine model *in vivo*.

The specific aims were:

1. To synthesise and characterise uncoated CaO_2 NPs.

2. To determine the ability of the uncoated CaO_2 NPs to generate molecular oxygen upon contact with water and improve oxygen levels in the immediate environment.

3. To determine the ability of the CaO_2 NPs to improve PDT mediated ROS production in BxPc-3 pancreatic cells cultured in a hypoxic environment.

4. To synthesise the pH-responsive methacrylate based terpolymer (**11**) and coat the CaO_2 NPs using a modified oil-in-water emulsion technique.

5. To determine the ability of the CaO_2-**11** particles to generate oxygen as a function of solution pH by monitoring the increase in dissolved oxygen.

6. To determine the ability of the CaO_2-**11** particles to enhance tumour oxygenation in an *in vivo* model and improve the efficacy of PDT *in vivo.*

5.3 Results and Discussion

5.3.1 Synthesis of bare CaO_2 nanoparticles

CaO_2 NPs were prepared following a hydrolysis-precipitation procedure similar to that developed by J. Khodaveiside et al. [163] that utilised $CaCl_2$ as a calcium precursor and polyethylene glycol 200 (PEG200) as a surface modifier. The $CaCl_2$ and PEG200 were stirred in an aqueous ammonium solution to ensure the solution was basic. Hydrogen peroxide, unstable in basic pH, was added dropwise to the $CaCl_2$ solution, oxidising the $CaCl_2$ to form CaO_2. As a molar excess of hydrogen peroxide was used relative to calcium chloride and ammonia, upon completion of the stirring period the solution was made basic using NaOH which decomposed the remaining hydrogen peroxide and also precipitated the CaO_2 nanoparticles that were collected by centrifugation. An equation for reaction is shown in **equation 5.1**

$$CaCl_2 + 2H_2O_2 + 2NH_4OH \rightarrow CaO_2 + 2NH_4Cl + 2H_2O \qquad \textbf{Equation 5.1}$$

5.3.2 Characterisation of bare CaO_2 nanoparticles

5.3.2.1. Particle size determination.

Dynamic light scattering (DLS) and scanning electron microscopy (SEM) were used to determine the size of CaO_2 nanoparticles. The principle behind DLS is derived from the Brownian motion of particles in solution interacting with coherent light irradiation leading to light scattering at a particular frequency. This frequency change, known as a Doppler shift, is linearly associated with the size of the particles. [209] The average hydrodynamic diameter of the CaO_2 NPs, recorded in pure ethanol solution to reduce the possibility of degradation, was determined as 20.3 ± 6.2 nm. (**Figure 5.2a**) To further confirm the particle size, the NPs were also analysed by SEM which identified spherical particles with an average diameter of 116.0 ± 7.6 nm. (**Figure 5.2b**), much greater than observed by DLS. This was surprising as DLS normally yields larger diameters than SEM due to the attraction of solvent molecules to the particle surface. Closer inspection of the particle morphology in the SEM image, however, revealed the appearance of several smaller particles coalesced together to form the larger sized NPs. One possible explanation for the variation in particle daimaeter

using the two techniques is that when dispersed in ethanol, the larger particles detected by SEM disaggregate into the smaller particles observed by DLS in solution.

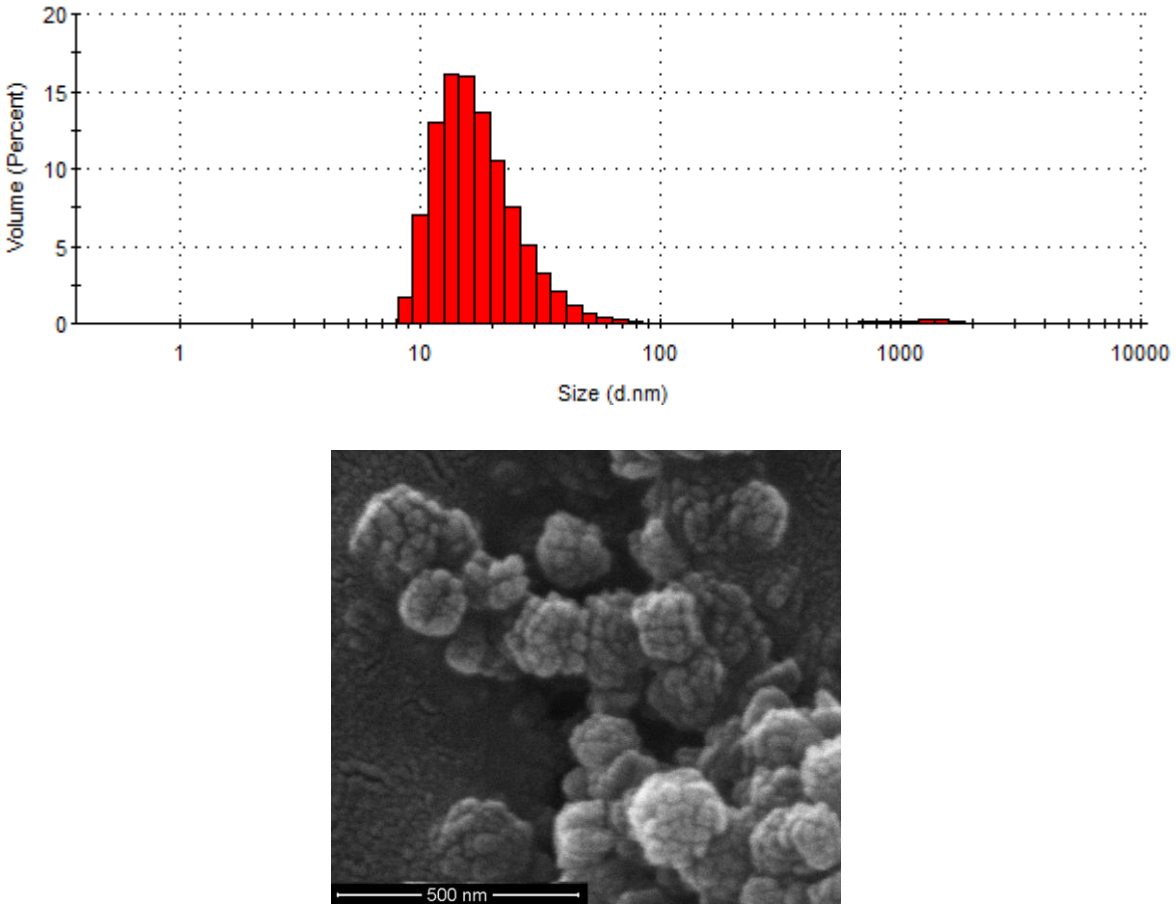

Figure 5. 2 Representative (a) DLS plot and (b) SEM image of CaO_2 NPs.

5.3.2.2 Active CaO_2 present in nanoparticle powder

In order to quantify the percentage of CaO_2 present in the NPs, the reaction between luminol and H_2O_2 was utilised (Figure 5.3). Chemiluminescence (λ_{max}=458nm) production relies on the reaction between luminol and H_2O_2 to generate the electronically excited product amino phthalate, which generates luminescence when it returns to the ground state. [210] Hence, active CaO_2 can be determined by reacting the NPs with water first to generate H_2O_2 in equimolar amounts that can be determined upon reaction with luminol.

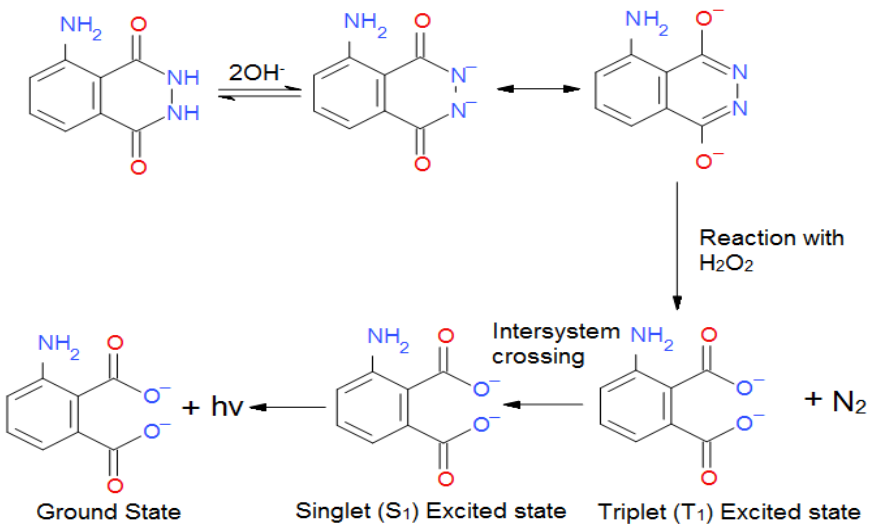

Figure 5. 3 Reaction scheme of luminol and H_2O_2. Reproduced from ref[210]

A calibration curve for the reaction H_2O_2 with luminol was constructed following the procedure described in **section 2.10**. The plot, shown in **Figure 5.4**, displayed good linearity (R_2 = 0.99) in the 0-0.4 µmol range for H_2O_2.

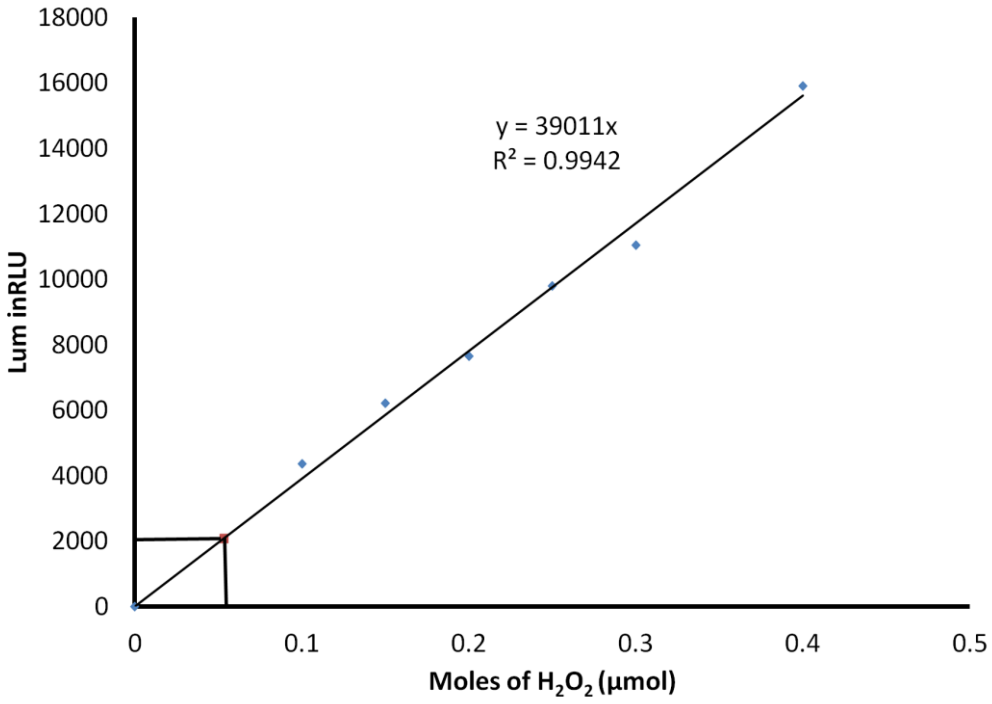

Figure 5. 4 Calibration curve for 0.035% H_2O_2 in NaOH/EtOH solution

Using the equation of the line from **Figure 5.4** and the stoichiometric ratio identified in **equation 5.1**, it was possible to calculate the amount of active CaO_2 present in a fixed amount of NP powder.

A solution (50 µL) of dried nanoparticle powder (8.5×10^{-3} mg) in ethanol was reacted with luminol generating a luminescent signal that corresponded to 0.053 mmol H_2O_2.

From **equation 5.1**:

$2CaO_2 + 4H_2O \rightarrow 2\ Ca(OH)_2 + 2H_2O_2 \rightarrow 2\ Ca(OH)_2 + 2H_2O + O_2$

2 moles of CaO_2 reacts to produce 2 moles of H_2O_2.

Therefore, 8.5×10^{-3} mg of dried nanoparticle powder produced H_2O_2 (0.053 mmol) that resulted from an equimolar amount of CaO_2. Using the RMM of CaO_2 = 72 g, the weight of active CaO_2 is 0.053 mmol x 72 = 3.82×10^{-3} mg (44.9%). Using this approach, the active CaO_2 content of the NPs was determined as 44.9 ± 2.1 %, with the remainder most likely comprising the other main excipient PEG (200) used in preparation of the NPs.

5.3.2.3 Oxygen generating capability of CaO_2 nanoparticles in de-oxygenated PBS solution.

To identify the capability of the unmodified CaO_2 NPs to generate oxygen upon reaction with water, a PBS solution (pH = 7.4 ± 0.1) was de-oxygenated to generate a simulated hypoxic environment. After determining the baseline % dissolved oxygen reading, a known quantity of the CaO_2 NP powder was added to the solution and the change in % dissolved oxygen monitored over time. The results are shown in **Figure 5.5(a)** and reveal a rapid increase in dissolved oxygen level (37.25%) 10 minutes after NP addition with no further increase observed over the next 10 min suggesting all the CaO_2 NPs were used up. In contrast, a deoxygenated PBS solution that was exposed to the open atmosphere increased by only 4.10 % over the same time period. When a second bolus of CaO_2 NP was added to the solution at t = 20 min, the dissolved oxygen reading again increased 2.5 min later and levelled off 5 min after the addition, suggesting the solution became saturated with oxygen **[Figure 5.5(b)]**. These results demonstrate that the CaO_2 NPs rapidly decompose when they come into contact with aqueous medium generating a significant enhancement in the oxygen levels of their immediate environment.

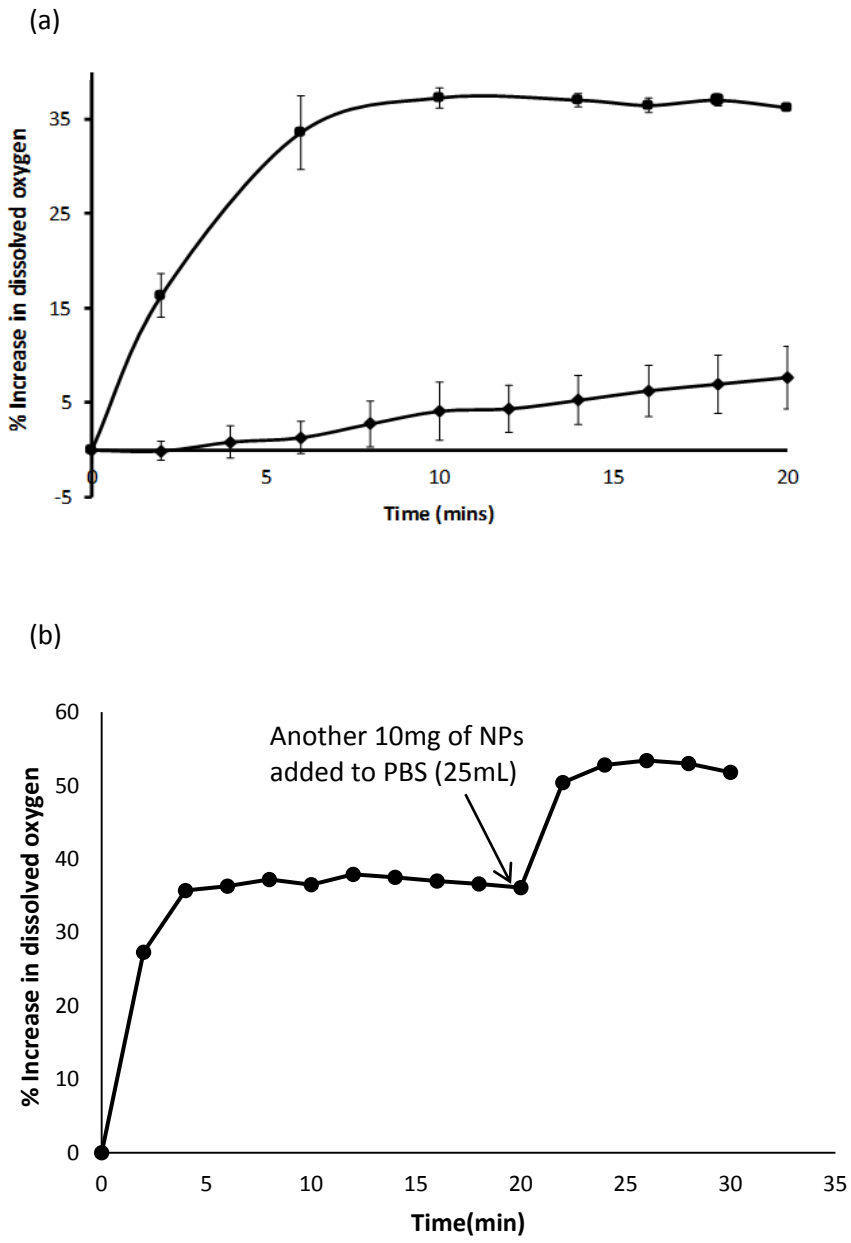

Figure 5. 5 (a) Plot of dissolved oxygen for a solution of deoxygenated PBS over a period of 20 min in the absence (diamonds) or presence (circles) of CaO_2 NPs. (b) Showing the effect of a second bolus of CaO_2 NPs 20mins after the first bolus was added.

5.3.2.4 Ability of CaO_2 NPs to enhance singlet oxygen generation in PDT.

It has been widely recognised that ROS generation is highly dependent on adequate oxygen supply in different biological systems and, in particular, in photodynamic therapy (PDT) of solid tumours. [211] To identify if the improved dissolved oxygen levels generated by the CaO_2 NPs would also translate to an increase in PDT mediated singlet oxygen quantum yield,

the singlet oxygen probe sensor green (SOSG) was utilised. SOSG is inherently non-fluorescent but reacts with singlet oxygen to generate a fluorescent product with the fluorescence intensity being proportional to the amount of singlet oxygen generated (**Figure 5.6**). [212]

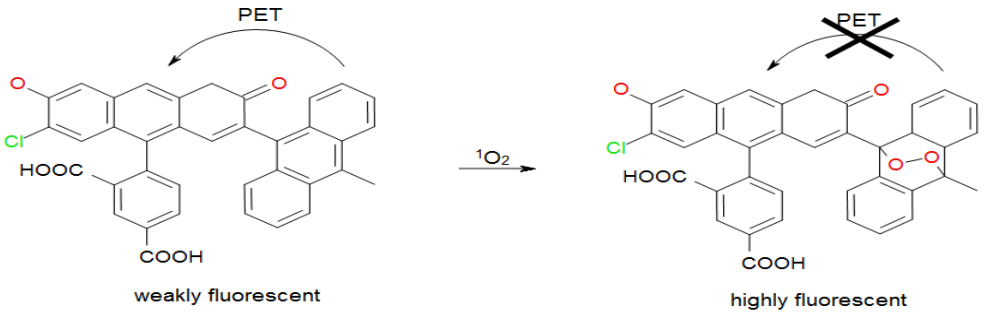

Figure 5. 6 Schematic graph of SOSG reaction with singlet oxygen. PET= photoinduced electron transfer. Reproduced from ref [212]

A deoxygenated PBS solution (2:98; EtOH: H_2O) containing SOSG (2.5µM) and the sensitiser RB (5 µM) was added to an ethanol solution containing CaO_2 NPs added to reach a final concentration of 35.6 µM. The solution was then irradiated with white light for 5 min at which point the fluorescence intensity at 530 nm was measured. Control experiments in the absence of the CaO_2 NPs (i.e. RB, SOSG and light) and CaO_2 NPs only (i.e. CaO_2 NPs, SOSG, and light) were also conducted for comparative purposes. The results are shown in Figure 5.5 and reveal a significant increase in the amount of SOSG fluorescence observed for the solution containing CaO_2 NPs, RB and treated with light compared to either the CaO_2 NPs+ light (324.8 % less) or the RB + light (112.9 % less) control groups, indicating the ability of the NPs to provide oxygen during the photodynamic event and enhance ROS generation in this simulated hypoxic environment.

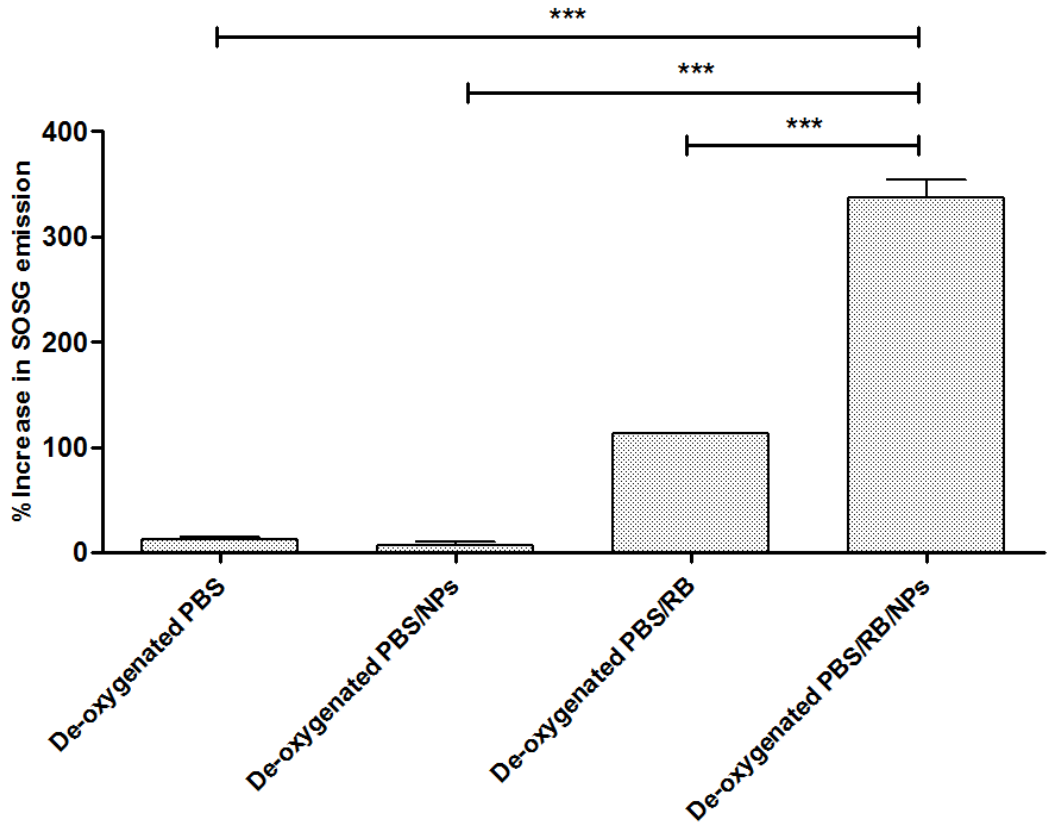

Figure 5. 7 Plot of % increase in SOSG fluorescence at 510 nm for solutions containing (i) deoxygenated PBS (ii) deoxygenated PBS and CaO_2 NPs (iii) deoxygenated PBS and Rose Bengal (RB) and (iv) deoxygenated PBS, RB and CaO_2 NPs. Groups (ii)-(iv) also received light treatment. Statistically significance of deoxygenated PBS/RB/NPs versus deoxygenated PBS, RB and CaO_2 NPs: ***p <0.001.

5.3.3 Ability of unmodified CaO_2 NPs to enhance PDT efficacy in BxPc-3 cells cultured in an anaerobic cabinet.

Having determined the ability of the CaO_2 NPs to improve the light induced ROS generation of RB in a simulated hypoxic environment, the next step was to determine if this improved ROS generation would also result in increased RB mediated PDT induced toxicity using human BxPc-3 pancreatic cancer cells as a target. However, in advance of undertaking the PDT experiments, it was first necessary to identify the optimum CaO_2 concentration to use. This involved treating BxPc-3 cells with a range of CaO_2 concentrations (0-1.0 mM) and determining cell viability using a MTT assay. The results are shown in **Figure 5.8** and reveal no significant reduction in viability for cells treated with either 25 or 50 µM CaO_2 NP concentrations. At higher concentrations, the cell viability reduced from 84 % at 100 µM to

80 % at 1000 µM. Therefore, a 50 µM concentration was identified as optimum for use in the PDT experiments.

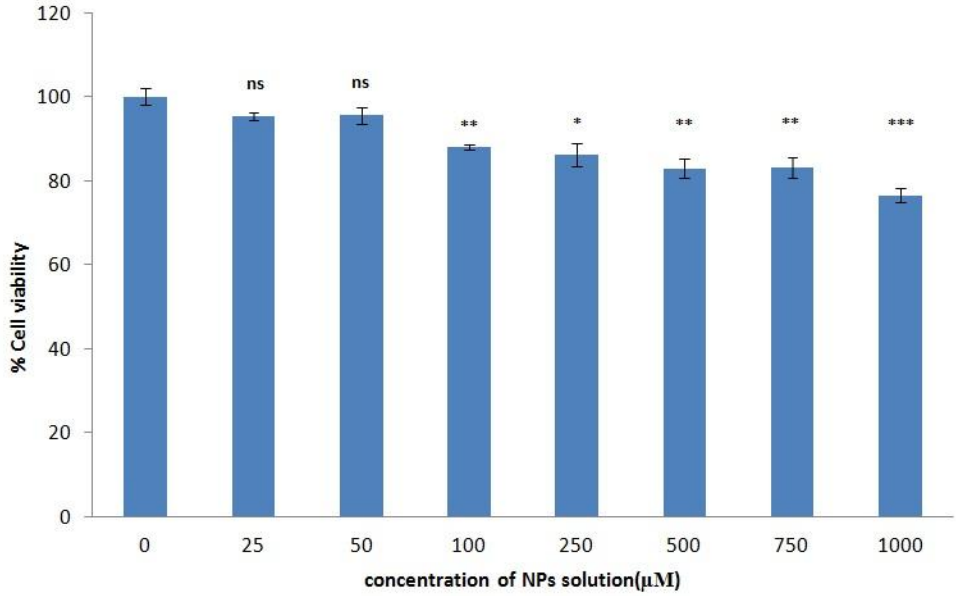

Figure 5. 8 Plot of cell viability for BxPc-3 cell line after exposure to different concentration of CaO_2 NPs solutions (25, 50, 100, 250, 500,750, 1000µM). Error bars represent ± the standard error where n=6. Statistically significance versus untreated cells (represented by 100%): ns $p>0.05$, *$p < 0.05$, **$p < 0.01$, ***$p < 0.001$.

In addition to identifying the maximum amount of unmodified CaO_2 NP that could be used without producing a significant reduction in the viability of BxPc-3 cells, it was also necessary to identify the ideal concentration of Rose Bengal and light dose to be used. "Ideal" in this context refers to the conditions required to generate a sub-lethal PDT effect for Rose Bengal + light (i.e. in the absence of CaO_2 NPs) so that any beneficial effect afforded by the NPs could be determined. PDT experiments were undertaken using a range of RB concentrations (0.5, 1.0, 2.0, 2.5 and 3.0 µM) and two different light doses (λ=532nm ± 10nm, fluency 15.92 or 31.84 $J/S \cdot m^2$) corresponding to 30s or 1 min irradiation time. 24h following treatment, the cell viability was determined by MTT assay with the results presented in **Figure 5.9**. A concentration dependent reduction in cell viability was observed for cells treated with Rose Bengal and light with the maximum Rose Bengal concentration of 3.0 µM producing 46% and 52% reductions following 30 sec or 60 sec irradiation

respectively. However, 60 sec irradiation in the absence of Rose Bengal was also found to produce a substantial 18% reduction in viability while 30 sec produced a much less 5% reduction. Based on this finding, 30 sec irradiation was identified as the optimum to be used. As mentioned above, the goal of these experiments was to identify conditions that produced a sub-lethal PDT effect i.e. that produced a moderate but not maximum reduction in viability so that any beneficial improvement of the CaO_2 NPs could be identified. Upon analysis of the results it was decided that 1 µM Rose Bengal and 30 sec irradiation time would be the ideal conditions as they provided a significant 22% reduction in cell viability with scope remaining for further reduction. Therefore, conditions involving 1 µM Rose Bengal, 30 sec irradiation time, and 50 µM CaO_2 NPs were chosen to determine the effect of the CaO_2 NPs to improve PDT mediated efficacy in a hypoxic environment.

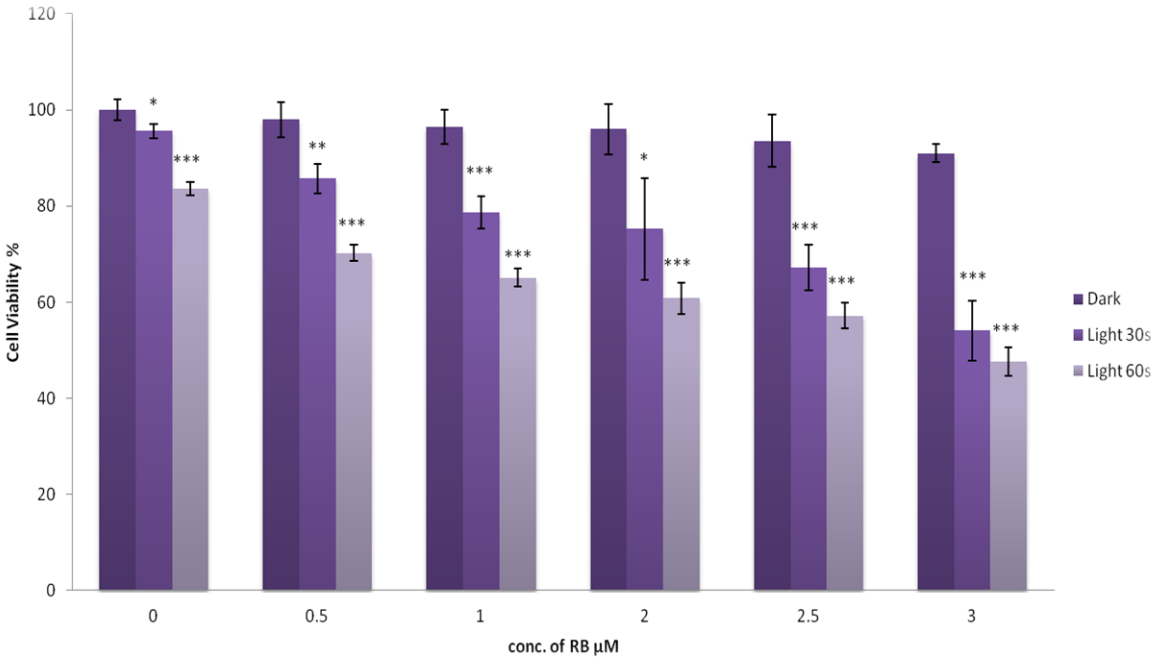

Figure 5. 9 Plot of cell viability for BxPc-3 cells grown in normoxic conditions and then incubated with different condition of RB (0.5, 1, 2, 2.5 and 3 µM) and exposed to green light source (Wavelength 532nm ± 10nm, output power 15.92 J/S.m^2) for 30 or 60 seconds. Error bars represent ± the standard error where n=6. Statistically significance versus untreated cells: ns $p>0.05$, *$p < 0.05$, **$p < 0.01$, ***$p < 0.001$.

BxPc-3 pancreatic cancer cells were cultured in an anaerobic cabinet ($O_2/CO_2/N_2$, 0.1: 5: 94.9 v/v/v) for 3h to generate a hypoxic environment and then treated with RB (1µM) and incubated for a further 3h under anaerobic conditions. The cells were then incubated with

an ethanol: PBS (50:50) suspension of the NPs (50 µM) for 5 min before being subjected to light treatment for 30 sec. The NP suspension was then removed, the cells washed with fresh PBS and incubated in fresh medium under normoxic conditions for a further 21 h before cell viability was determined using a MTT assay. The use of a 25% v/v ethanolic NP suspension in these experiments was not ideal but care was taken to ensure that contact time with the cells was kept to a minimum. Controls involving RB only, light only and NP only were also undertaken for comparative purposes. The results are shown in **Figure 5.10** and reveal a significant ($p < 0.01$) reduction in viability for those cells treated with PDT in the presence of CaO_2 NPs (33.3%) compared to PDT treatment alone (10.8%). These results suggest that treatment of hypoxic BxPc-3 with CaO_2 NPs prior to PDT can enhance oxygen levels improving the PDT mediated efficacy.

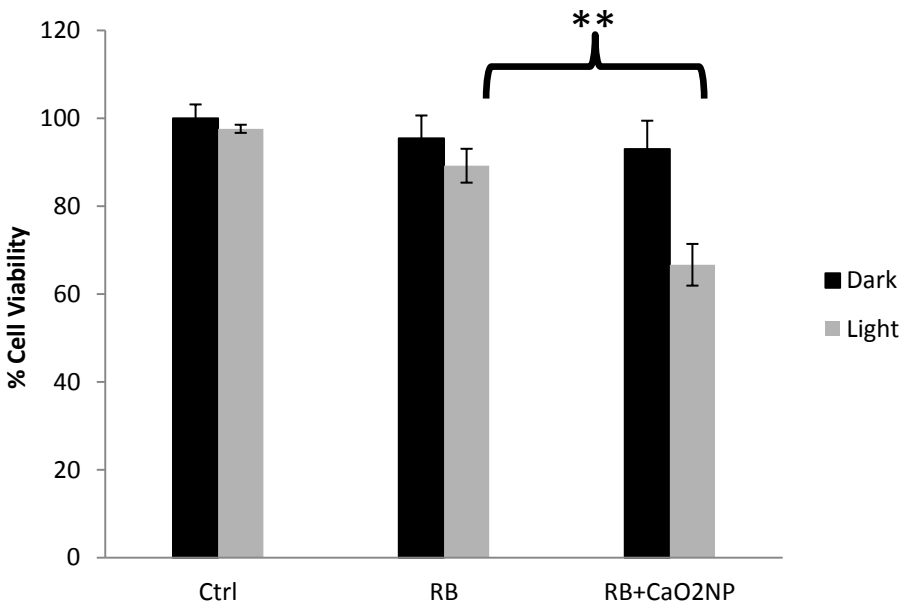

Figure 5. 10 Plot of cell viability for BxPc-3 cells grown in hypoxic conditions and then treated with RB (50 µM) or RB + NPs (50 µM) and then exposed for 30 seconds to green light sources (Wavelength 532nm ± 10nm, output power 15.92 J/S.m^2). Error bars represent ± the standard error where n=12. Statistically significance of cells treated with RB + EtOH versus cells treated with RB + NPs: **p<0.01

5.3.4 Synthesis and Characterisation of pH responsive terpolymer

If CaO_2 NPs are to be used *in vivo* it is imperative they remain stable in circulation until taken up by tumour tissue so that inadvertent systemic activation is avoided. Terpolymer **11**, similar in structure to Eudragit E, was prepared by the free radical co-polymerisation of 2-(dimethylamino) ethyl methacrylate, methylmethacyrlate and ethylmethacrylate in a 2:1:1

ratio. **11** contains a tertiary amine side chain making it possess low aqueous solubility as the free base but were soluble once ionised. [213] The successful preparation of Polymer **11** was confirmed by ^{1}H NMR spectroscopy with the stacked spectra of each monomer and **11** shown in **Figure 5.11**. The olefinic protons present in the spectra of the monomers between 5.5 and 6.5 ppm were not present in **11** indicating they had been successfully polymerised to form the backbone of **11**. The peak at 0.81 ppm, not present in the spectra of the monomers but present in the spectrum of **11** most likely corresponds to the newly created methylene protons of the polymer backbone. In addition, the peaks were generally much broader in the spectrum of **11** than in the monomers, which is characteristic of protons in or near the backbone of polymers due to an ineffective averaging of their chemical shift anisotropies. [214] The proton NMR spectra shown in **Figure 5.11** reveal the successful preparation of polymer **11**. However, it was not possible to obtain an accurate molecular weight for this polymer.

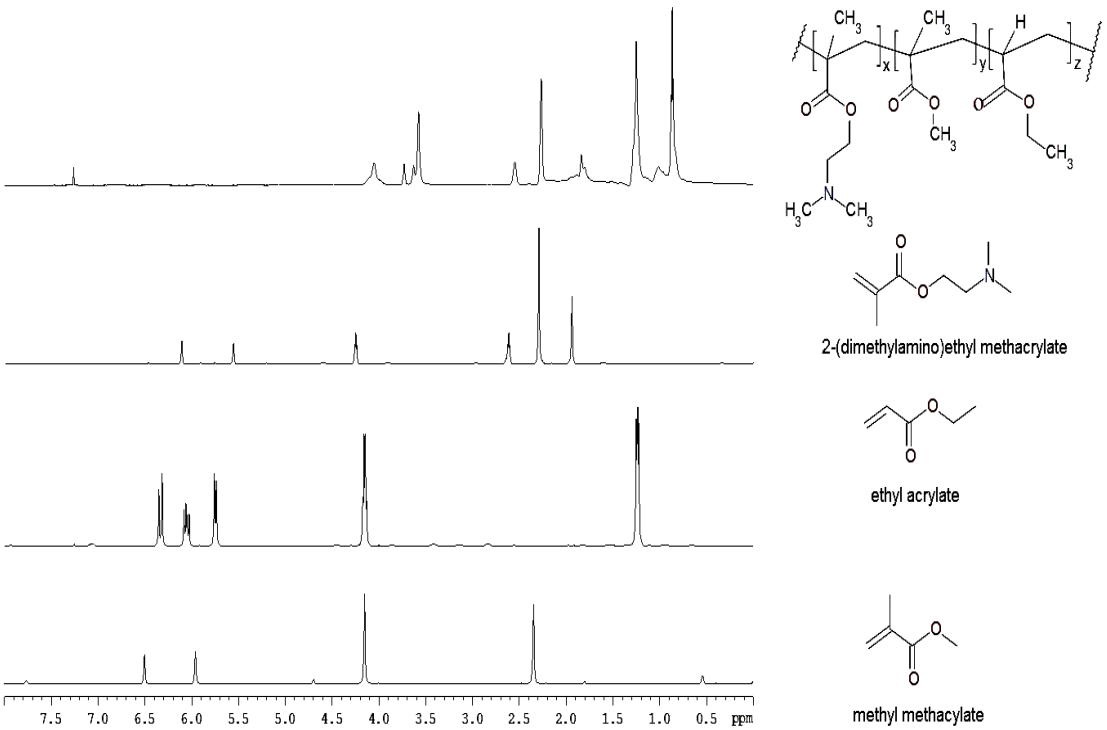

Figure 5. 11 Stacked ^{1}H NMR spectra of (i) methyl methacrylate (ii) ethyl acrylate (iii) 2-(dimethylamino)ethyl methacrylate and (iv) pH responsive polymer **11**.

5.3.5 Synthesis and characterization of 11 coated CaO_2 NPs

To coat the CaO_2 NPs with polymer **11**, a modified single emulsion method was utilised. CaO_2 NPs were dispersed in hexane and homogenised at 9000 RPM for 5 minutes. In parallel, polymer **11** was dissolved in ethanol and also homogenised at 5000 RPM for 2 min. The CaO_2 NPs/hexane suspension was added dropwise with at 2mL/min to the polymer/ethanol solution with continuous mixing at 9000 RPM. Once all the NP suspension was added the suspension was mixed for a further 6 h when the solvents were removed by evaporation. The polymer coated NPs (CaO_2-**11** NP) were then dispersed in aqueous solution and their size determined by DLs and SEM.

(a)

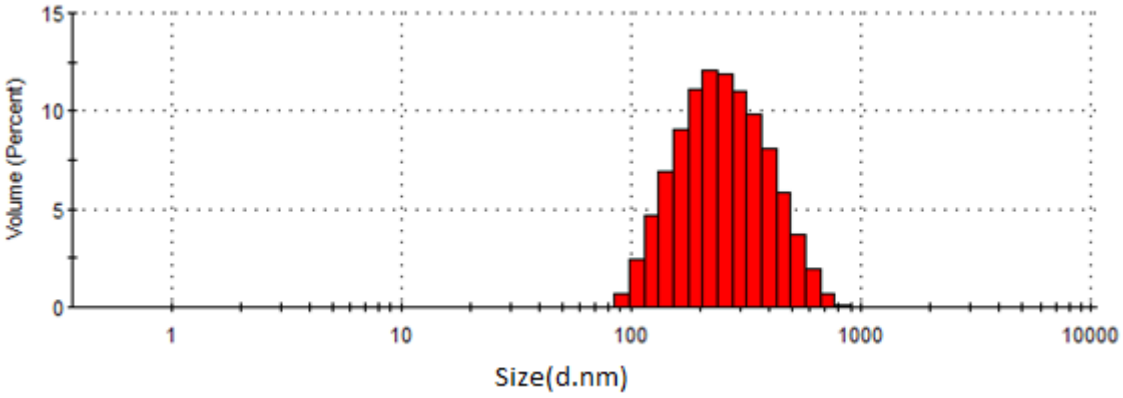

(b)

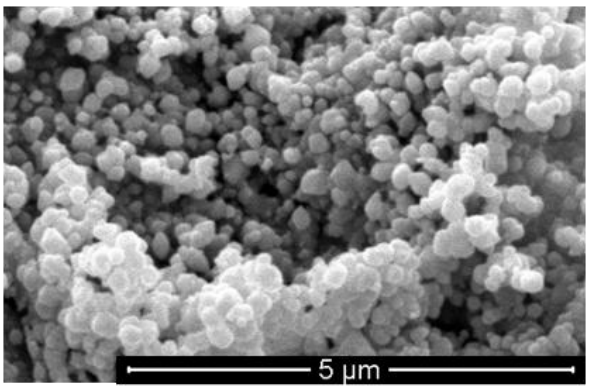

Figure 5. 12 (a) DLS plot of polymer CaO_2-**11** NPs in EtOH solution, (b) SEM image of polymer CaO_2-**11** NPs. The bar is 5µm.

The SEM image is shown in **Figure 5.12(b)** and again reveals spherical particles with an average diameter of 248 ± 17 nm which was similar to the hydrodynamic diameter (278 ± 71

nm) determined by DLS. In addition, the particle morphology in SEM was uniform and did not appear to be a collection /aggregation of smaller particles as observed for the uncoated particles. **[Figure 5.12(b)]** This increase in size, relative to the uncoated NPs can be attributed to the polymeric coating.

5.3.6 Ability of CaO_2-11 NPs to elevate dissolved oxygen levels upon response to lowering solution pH.

The ability of the CaO_2-**11** NPs to generate oxygen as a function of solution pH was determined by monitoring the increase in dissolved oxygen. Degassed aqueous solutions containing CaO_2-**11** NPs (1 mg/mL) were pH adjusted to either pH 7.4 or pH 6.2 and the change in dissolved oxygen measured at each pH stable for 5 minutes later. The results are shown in **Figure 5.13(a)** and reveal a 45% increase in dissolved oxygen at pH 6.2 compared to only 7% increase at pH 7.4. This increase in dissolved oxygen results from dissolution of the polymer coat at lower pH that exposes the CaO_2 core to the aqueous environment. Indeed, when an aqueous suspension containing CaO_2-**11** NPs was pH adjusted from pH 7.4 to pH 6.2, the visual appearance changed from a milky suspension to a more transparent solution. These results suggest that the CaO_2**-11** NPs should remain stable in the systemic circulation at pH = 7.4 but become activated to release O_2 when in the more acidic tumour microenvironment.

(a)

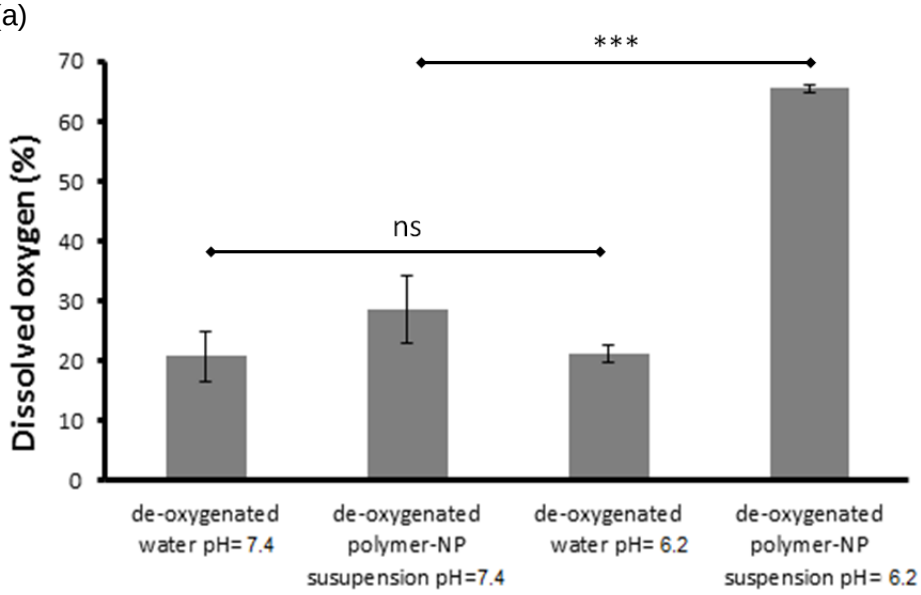

(b)

Figure 5. 13 (a) Plot of the percentages of dissolved oxygen in de-oxygenated water at pH 6.2 and pH 7.4 in the absence or in presence of polymer CaO_2-**11** NPs. (b) Representative photograph showing an aqueous suspension of the polymer **11** coated CaO_2 NPs at pH 7.44, 6.88 and 6.19. Statistical significance of polymer CaO_2-**11** NPs in pH 6.2 versus polymer CaO_2-**11** NPs in pH 7.4: *** $p \leq 0.001$.

5.3.7 Ability of CaO_2-11 NPs to improve tumour oxygenation in vivo.

To determine the ability of the CaO_2-**11** NPs to enhance tumour oxygenation in an *in vivo* model, ectopic human xenograft Mia Paca-2 tumours were established in SCID mice. The Mia Paca-2 model is known to form hypoxic tumours and has previously been used in therapeutic efficacy experiments involving hypoxia activated prodrugs. [215] Unlike the

BxPc-3 cell line, Mia Paca-2 cells also express the KRAS mutation making it a more representative model of the disease *in vivo*. Once the tumours reached an average volume of 254 ± 17 mm^3, the mice were separated into two groups (n=3). The treatment group received a tail vein injection of the CaO_2-**11** NP suspension in a PBS buffer vehicle (pH 7.4 ± 0.1), with the control group receiving the same volume of vehicle only. Tumour pO_2 readings were recorded using an Oxylite oxygen electrode sensor for 20 min before and 40 min after injection. The results are shown in **Figure 5.14(a)** and reveal no significant change in the pO_2 reading in the 20 min period before injection for either group with a mean pO_2 reading of ~ 2.0 mmHg. However, approximately 10 min after injection, tumour pO_2 levels in the CaO_2-**11** NP group increased dramatically reaching a peak of 16 mmHg before levelling off at ~6 mmHg 30 min after injection. In contrast, mice treated with vehicle alone showed no noticeable change in tumour pO_2 over the time course of the experiment. To put the above results in context, previous studies have indicated that the response to radiotherapy treatment is highly dependent upon tumour oxygenation with an increase from 2.5 mmHg to 6 mmHg significantly affecting loco-regional tumour control in advanced squamous cell head and neck carcinoma. [216] While similar data are not available for PDT, the technique is known to be negatively impacted by hypoxia and the increase in tumour pO_2 levels provided by the CaO_2-**11** NPs would be expected to have a beneficial effect on PDT mediated efficacy *in vivo*.

(a)

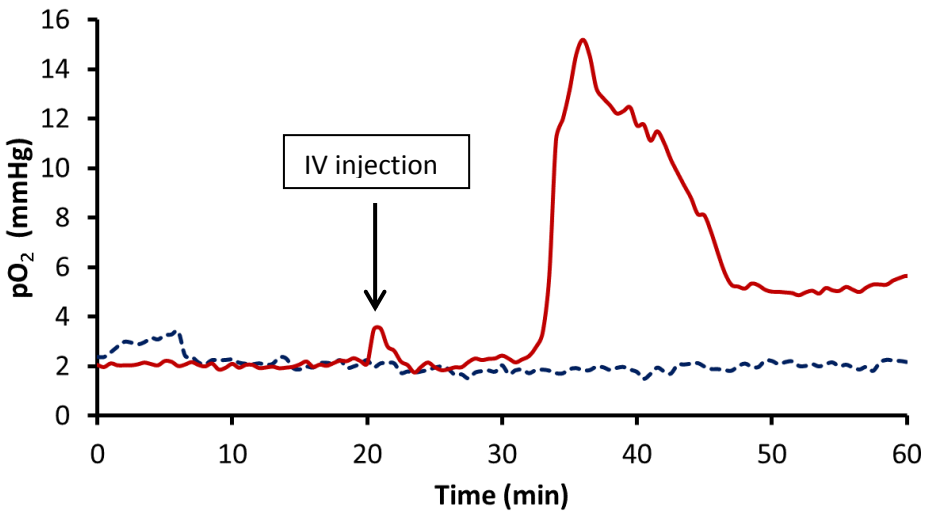

(b)

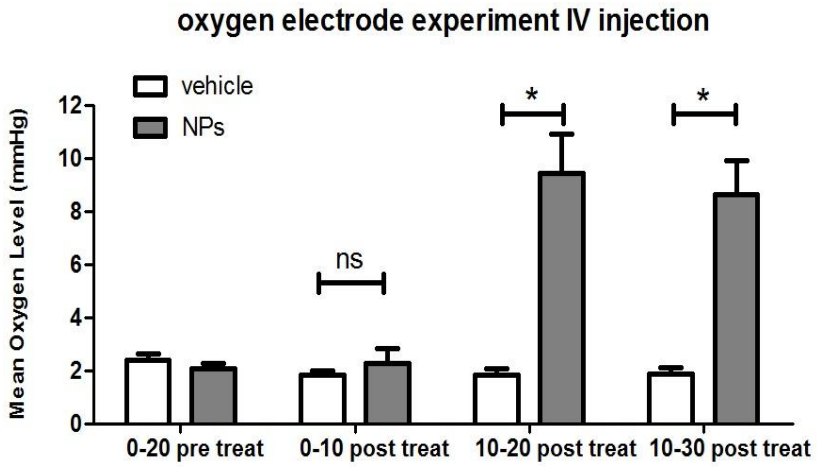

Figure 5. 14 (a) Tumour pO_2 plot in mice bearing ectopic Mia Paca-2 pancreatic tumours. pO_2 was recorded for 20 min before and 40 min following an IV injection of CaO_2-**11** NPs in a PBS (pH 7.4 ± 0.1) (red line) or an IV injection of vehicle only, i.e CaO_2-**11** NPs, (blue dashed line). Arrow indicates when the injection occurred. (b) Plot showing the integration of mean oxygen level obtained from the plot (a). the mean tumour pO_2 for various time intervals before and following IV administration of CaO_2-**11** NPs or vehicle only, i.e. CaO_2 NPs, obtained from integration of the plot shown in (a).Statistical significance of CaO_2-**11** NPs versus vehicle only: *p≤ 0.05.

5.3.8 Effect of CaO_2-11 NPs on the PDT efficacy of Rose Bengal in an in vivo model of pancreatic cancer.

To identify the benefit afforded by the CaO_2-**11** NPs on improving PDT mediated efficacy *in vivo*, the same Mia Paca-2 tumour model described in the pO_2 study above, was treated with PDT using a Rose Bengal sensitiser in the presence and absence of the CaO_2-**11** NPs. Untreated animals and those treated with CaO_2-**11** NPs alone were used as controls. The NPs were again delivered by IV injection while Rose Bengal was administered by intratumoral injection, to ensure a consistent dose was administered to all of the tumours. Twenty minutes following IV administration of the CaO_2-**11** NPs, tumours were exposed to light treatment for 3 min. Tumour volume was monitored for 5 days following treatment and the results are shown in **Figure 5.15(a).** The results demonstrate that there was no significant difference in tumour volume for mice treated with PDT alone or with CaO_2-**11** NPs alone 5 days after treatment, relative to the untreated control animals. In contrast, a significant reduction ($p \leq 0.001$) of 70.5 % was observed for animals treated with the CaO_2-8 NPs and PDT over the same time period. In addition, there was no significant change in body weight in animals treated with the CaO_2-**11** NPs alone or in combination with PDT suggesting the treatment was well tolerated [Figure 5.15(b)]. These results highlight the benefit of CaO_2-**11** NPs in improving the PDT mediated treatment of hypoxic tumours such as pancreatic adenocarcinoma and may provide benefit in other treatments that are also compromised by hypoxia, most notably radiotherapy.

(a)

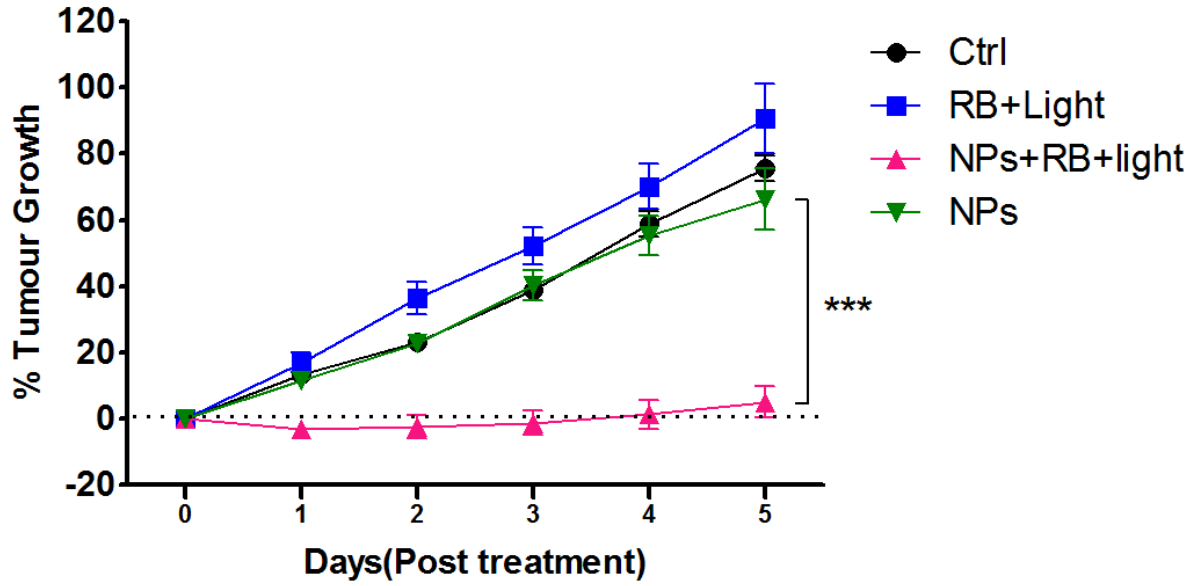

(b)

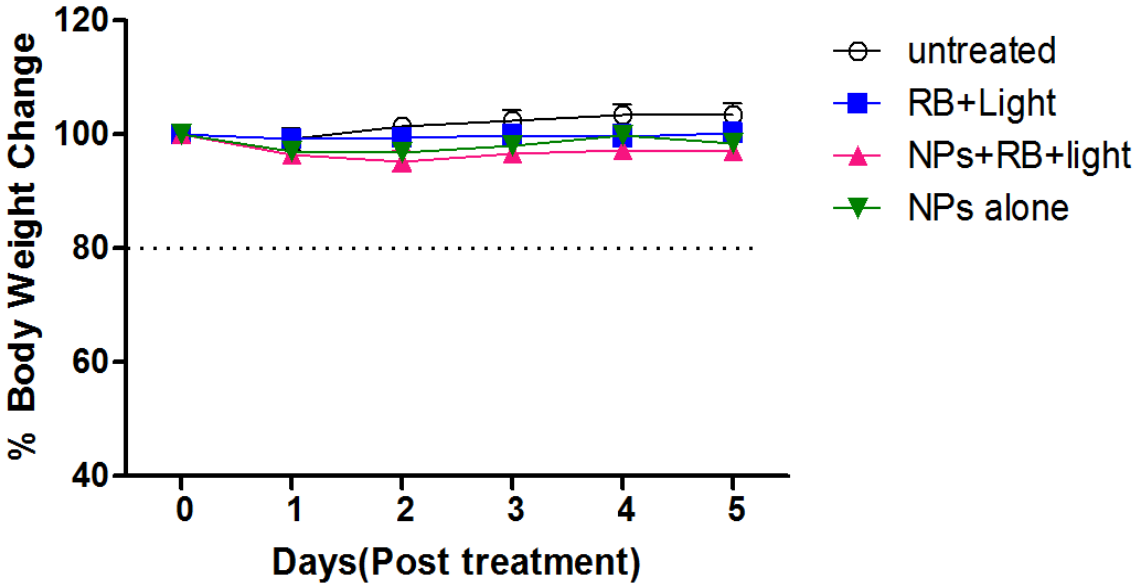

Figure 5. 15 (a) Plot of % change in tumour volume against time for SCID mice bearing human xenograft Mia Paca-2 pancreatic tumour treated with (i) no treatment (squares) (ii) PDT only (circles) (iii) CaO_2-**11** NPs only (diamonds) and (iv) CaO_2-**11** NPs and PDT (triangles). (b) Plot of average body weight for each group of mice over the time course of the experiment. ***$p \leq 0.01$.

5.4 Conclusion

In summary, a CaO_2 NPs formulation comprising a pH-responsive coating that enables the generation of molecular oxygen in response to environmental pH changes has been developed. Specifically, the polymer coat maintains its integrity in aqueous solution at pH 7.4, but it rapidly dissolves when the pH is lowered to pH 6.2, exposing the CaO_2 particles to water resulting in oxygen generation. The ability of the coated particles to elevate tumour oxygen levels was also demonstrated in an *in vivo* model using mice bearing human xenograft Mia Paca-2 pancreatic tumour. A significant elevation in tumour pO_2 was observed 10 mins following IV administration. This increase in tumour pO_2 was also shown to have a dramatic effect on PDT efficacy with significant reductions in tumour growth observed in mice treated with CaO_2-**11** NPs prior to PDT.

Hence, it can be concluded that the use of these coated NPs could not only be applied for used in PDT but could show other benefit versus other treatment negatively impacted by hypoxia such as SDT or radiotherapy.

Chapter 6

Conclusions and future work

6. Conclusions and future work

The work described in this this thesis explored new approaches for the treatment of pancreatic cancer, which is one of the most recalcitrant forms of the disease and one in which survival statistics have barely changed in over 40 years. **Chapters 3 and 4** explored the use of non-magnetic and magnetically responsive MBs respectively, to deliver combined SDT and antimetabolite treatment to pancreatic tumours. In **Chapter 3**, chemo-sonodynamic therapy using Gemcitabine as the antimetabolite was marginally better *in vitro* and responded to a broader range of US conditions *in vivo* when compared to the analogous treatment involving 5-FU as the antimetabolite. However, there was no significant difference in tumour growth delay when the optimum US exposure conditions were used in each case. Importantly, however, tumour growth delay was extended following a second treatment meaning resistance to treatment did not develop quickly. Interesting effects were also observed when a panel of genes associated with a poor outcome in pancreatic cancer were analysed following treatment, with significant changes observed for treated tumours relative to untreated tumours. The effect this treatment on non-tumour bearing healthy mice was also investigated and the results confirmed MB mediated chemo-sonodynamic therapy to be well tolerated.

The work described in **Chapter 3** was extended in **Chapter 4** to investigate the benefit of adding an additional layer of targeting to the MB platform and to determine efficacy of the treatment in an orthotopic mouse model of pancreatic cancer. The O_2MBs were functionalised with SPIONs and shown capable of being retained during flow using an externally applied magnetic field. Treatment of orthotopic BxPc-3 Luc tumours in SCID mice demonstrated that efficacy was improved when combined US / magnetic fields were applied to the tumour during treatment compared to a US field alone, although the difference was non-significant. Again, the MagO_2MB conjugates displayed no observable toxic effects when used to treat non-tumour bearing healthy mice.

Combined, the results from **Chapters 3 and 4** demonstrate the potential of chemo-sonodynamic therapy using the MB platform as a minimally invasive targeted treatment for pancreatic cancer. Moving forward, one perceived drawback of the approach used in

Chapters 3 and 4 is that two separate MBs were required to deliver the combined SDT and antimetabolite treatment. This required mixing the MBs before injection, which effectively halves the concentration of each agent. Future work should explore designing a single biotinylated ligand carrying both the sensitiser and antimetabolite drug to enable chemo-sonodynamic therapy to be delivered using a single MB formulation. Another possible area that could be explored is to incorporate a third payload within the hydrophobic oil layer of the MB, in addition those attached via the biotin-avidin interaction to the shell. One such candidate payload is paclitaxel as it is not only extremely hydrophobic but also commonly used in pancreatic cancer treatment.

In **Chapter 5**, oxygen generating nanoparticles were developed and demonstrated pH dependent oxygen release when coated with a pH responsive polymer. A significant elevation in tumour pO_2 was observed when a suspension of the particles was delivered by IV injection and this increase in tumour oxygen was shown to enhance the efficacy of PDT treatment using Rose Bengal as the sensitiser. While these results were exciting, future work should also explore the concentration dependence of the nanoparticles on tumour pO_2 increase. Although no overt acute toxic effects were observed following administration of the particles to mice, a more detailed safety study like that undertaken in **Chapters 3 and 4** should also be conducted. The possibility of further modifying the pH responsive polymer to carry a photo-, sono- or radio-senitiser is also an area that could be explored in the future work and would enable these agents to be passively targeted to the tumour by virtue of the nanoparticle mediated EPR effect.

Both the oxygen generating particles and oxygen carrying MBs have the potential to elevate tumour oxygen and increase the efficacy of treatments that depend on an adequate supply of oxygen to be effective. Previous work by McEwan et al. [217] has demonstrated the positive effect of MB mediated oxygen delivery on SDT efficacy while a recent study has shown a similar effect on external beam radiotherapy (EBR) efficacy. [218] Therefore, it would also be interesting to explore the effect of combing EBR with the oxygen generating nanoparticles or O_2MB delivered chemo-sonodynamic therapy in future studies.

References

Reference List

[1] L.A. Torre, F. Bray, R.L. Siegel, J. Ferlay, J. Lortet-Tieulent, A. Jemal, Global cancer statistics, 2012, CA: a cancer journal for clinicians. 65 (2015) 87-108.

[2] F. Bray, B. Møller, Predicting the future burden of cancer, Nature Reviews Cancer. 6 (2006) 63-74.

[3] T. Seufferlein, J. Ahn, D. Krndija, U. Lother, G. Adler, G. von Wichert, Tumor biology and cancer therapy–an evolving relationship, Cell Communication and Signaling. 7 (2009) 19.

[4] D. Hanahan, R.A. Weinberg, Hallmarks of cancer: the next generation, Cell. 144 (2011) 646-674.

[5] J.M. Ebos, C.R. Lee, W. Cruz-Munoz, G.A. Bjarnason, J.G. Christensen, R.S. Kerbel, Accelerated metastasis after short-term treatment with a potent inhibitor of tumor angiogenesis, Cancer cell. 15 (2009) 232-239.

[6] W.L. Shaib, A. Ip, K. Cardona, O.B. Alese, S.K. Maithel, D. Kooby, J. Landry, B.F. El-Rayes, Contemporary Management of Borderline Resectable and Locally Advanced Unresectable Pancreatic Cancer, Oncologist. 21 (2016) 178-187.

[7] D. Li, K. Xie, R. Wolff, J.L. Abbruzzese, Pancreatic cancer, The Lancet. 363 (2004) 1049-1057.

[8] A. Rasooly, J. Jacobson, Development of biosensors for cancer clinical testing, Biosensors and Bioelectronics. 21 (2006) 1851-1858.

[9] S. Gillen, T. Schuster, C.M. Zum Büschenfelde, H. Friess, J. Kleeff, Preoperative/neoadjuvant therapy in pancreatic cancer: a systematic review and meta-analysis of response and resection percentages, PLoS medicine. 7 (2010) e1000267.

[10] S. Iodice, S. Gandini, P. Maisonneuve, A.B. Lowenfels, Tobacco and the risk of pancreatic cancer: a review and meta-analysis, Langenbeck's Archives of Surgery. 393 (2008) 535-545.

[11] E.J. Duell, E.A. Holly, P.M. Bracci, M. Liu, J.K. Wiencke, K.T. Kelsey, A population-based, case–control study of polymorphisms in carcinogen-metabolizing genes, smoking, and pancreatic adenocarcinoma risk, J. Natl. Cancer Inst. 94 (2002) 297-306.

[12] M. Porta, N. Malats, M. Jariod, J.O. Grimalt, J. Rifà, A. Carrato, L. Guarner, A. Salas, M. Santiago-Silva, J.M. Corominas, Serum concentrations of organochlorine compounds and K-ras mutations in exocrine pancreatic cancer, The Lancet. 354 (1999) 2125-2129.

[13] F.M. Giardiello, S.B. Welsh, S.R. Hamilton, G.J.A. Offerhaus, A.M. Gittelsohn, S.V. Booker, A.J. Krush, J.H. Yardley, G.D. Luk, Increased risk of cancer in the Peutz–Jeghers syndrome, N. Engl. J. Med. 316 (1987) 1511-1514.

[14] C. Bosetti, V. Rosato, D. Li, D. Silverman, G.M. Petersen, P. Bracci, R. Neale, J. Muscat, K. Anderson, S. Gallinger, Diabetes, antidiabetic medications, and pancreatic cancer risk: an analysis from the International Pancreatic Cancer Case-Control Consortium, Annals of oncology. 25 (2014) 2065-2072.

[15] T. Sohn, C. Yeo, The molecular genetics of pancreatic ductal carcinoma:: a review, Surg. Oncol. 9 (2000) 95-101.

[16] G.H. Sakorafas, G.G. Tsiotos, Molecular Biology of Pancreatic Cancer, BioDrugs. 15 (2001) 439-452.

[17] F. Wenger, J. Zieren, F. Peter, C. Jacobi, J. Müller, K-ras mutations in tissue and stool samples from patients with pancreatic cancer and chronic pancreatitis, Langenbeck's archives of surgery. 384 (1999) 181-186.

[18] L.D. Wood, R.H. Hruban, Pathology and molecular genetics of pancreatic neoplasms, Cancer J. 18 (2012) 492-501.

[19] S.A. Hahn, M. Schutte, A. Hoque, C.A. Moskaluk, L.d. Costa, E. Rozenblum, C.L. Weinstein, A. Fischer, C.J. Yeo, R.H. Hruban, DPC4, a candidate tumor suppressor gene at human chromosome 18q21. 1, SCIENCE-NEW YORK THEN WASHINGTON-. (1996) 350-352.

[20] M. Goggins, R.H. Hruban, S.E. Kern, BRCA2 is inactivated late in the development of pancreatic intraepithelial neoplasia: evidence and implications, The American journal of pathology. 156 (2000) 1767-1771.

[21] J. Kleeff, T. Ishiwata, H. Maruyama, H. Friess, P. Truong, M. Büchler, D. Falb, M. Korc, The TGF-β signaling inhibitor Smad7 enhances tumorigenicity in pancreatic cancer. Oncogene. 18 (1999).

[22] J. Pratap, A. Javed, L.R. Languino, A.J. van Wijnen, J.L. Stein, G.S. Stein, J.B. Lian, The Runx2 osteogenic transcription factor regulates matrix metalloproteinase 9 in bone metastatic cancer cells and controls cell invasion, Mol. Cell. Biol. 25 (2005) 8581-8591.

[23] J. Li, M.G. Wientjes, J.L. Au, Pancreatic cancer: pathobiology, treatment options, and drug delivery, The AAPS journal. 12 (2010) 223-232.

[24] D.B. Evans, M.B. Farnell, K.D. Lillemoe, C. Vollmer, S.M. Strasberg, R.D. Schulick, Surgical treatment of resectable and borderline resectable pancreas cancer: expert consensus statement, Annals of surgical oncology. 16 (2009) 1736-1744.

[25] G. Klöppel, Histological Typing of Tumours of the Exocrine Pancreas, Springer Science & Business Media, 1996.

[26] S.H. Shin, S.C. Kim, K.B. Song, D.W. Hwang, J.H. Lee, D. Lee, J.W. Lee, E. Jun, K. Park, Y. Lee, A comparative study of laparoscopic vs open distal pancreatectomy for left-sided ductal adenocarcinoma: a propensity score-matched analysis, J. Am. Coll. Surg. 220 (2015) 177-185.

[27] D.B. Longley, D.P. Harkin, P.G. Johnston, 5-fluorouracil: mechanisms of action and clinical strategies, Nature Reviews Cancer. 3 (2003) 330-338.

[28] J. Van Laar, Y. Rustum, S. Ackland, C. Van Groeningen, G. Peters, Comparison of 5-fluoro-2'-deoxyuridine with 5-fluorouracil and their role in the treatment of colorectal cancer, Eur. J. Cancer. 34 (1998) 296-306.

[29] P. Noordhuis, U. Holwerda, C. Van der Wilt, C. Van Groeningen, K. Smid, S. Meijer, H. Pinedo, G. Peters, 5-Fluorouracil incorporation into RNA and DNA in relation to thymidylate synthase inhibition of human colorectal cancers, Annals of oncology. 15 (2004) 1025-1032.

[30] M. Tsujie, S. Nakamori, S. Nakahira, Y. Takahashi, N. Hayashi, J. Okami, H. Nagano, K. Dono, K. Umeshita, M. Sakon, M. Monden, Human equilibrative nucleoside transporter 1, as a predictor of 5-fluorouracil resistance in human pancreatic cancer, Anticancer Res. 27 (2007) 2241-2249.

[31] D. Thomas, J. Zalcberg, 5-Fluorouracil: A pharmacological paradigm in the use of cytotoxics, Clinical and experimental pharmacology and physiology. 25 (1998) 887-895.

[32] E. Mini, S. Nobili, B. Caciagli, I. Landini, T. Mazzei, Cellular pharmacology of gemcitabine, Annals of Oncology. 17 (2006) v7-v12.

[33] J. Bachet, R. Marechal, J. Van Laethem, Treatment of pancreatic cancer: what can we really predict today? Cancers. 3 (2011) 675-699.

[34] V. Heinemann, Y.Z. Xu, S. Chubb, A. Sen, L.W. Hertel, G.B. Grindey, W. Plunkett, Inhibition of ribonucleotide reduction in CCRF-CEM cells by 2',2'-difluorodeoxycytidine, Mol. Pharmacol. 38 (1990) 567-572.

[35] D.D. Ross, D.P. Cuddy, Molecular effects of 2′, 2′-difluorodeoxycytidine (Gemcitabine) on DNA replication in intact HL-60 cells, Biochem. Pharmacol. 48 (1994) 1619-1630.

[36] C.W. Michalski, M. Erkan, D. Sauliunaite, T. Giese, R. Stratmann, C. Sartori, N.A. Giese, H. Friess, J. Kleeff, Ex vivo chemosensitivity testing and gene expression profiling predict response towards adjuvant gemcitabine treatment in pancreatic cancer, Br. J. Cancer. 99 (2008) 760-767.

[37] D. Goldstein, R.H. El-Maraghi, P. Hammel, V. Heinemann, V. Kunzmann, J. Sastre, W. Scheithauer, S. Siena, J. Tabernero, L. Teixeira, nab-Paclitaxel plus gemcitabine for metastatic pancreatic cancer: long-term survival from a phase III trial, J. Natl. Cancer Inst. 107 (2015) dju413.

[38] E. Miele, G.P. Spinelli, E. Miele, F. Tomao, S. Tomao, Albumin-bound formulation of paclitaxel (Abraxane ABI-007) in the treatment of breast cancer, Int. J. Nanomedicine. 4 (2009) 99-105.

[39] R.D. Minshall, C. Tiruppathi, S.M. Vogel, W.D. Niles, A. Gilchrist, H.E. Hamm, A.B. Malik, Endothelial cell-surface gp60 activates vesicle formation and trafficking via G(i)-coupled Src kinase signaling pathway, J. Cell Biol. 150 (2000) 1057-1070.

[40] W.W. Ma, M. Hidalgo, The winning formulation: the development of paclitaxel in pancreatic cancer, Clin. Cancer Res. 19 (2013) 5572-5579.

[41] M. Ychou, T. Conroy, J. Seitz, S. Gourgou, A. Hua, D. Mery-Mignard, A. Kramar, An open phase I study assessing the feasibility of the triple combination: oxaliplatin plus irinotecan plus leucovorin/5-fluorouracil every 2 weeks in patients with advanced solid tumors, Annals of oncology. 14 (2003) 481-489.

[42] S.G. Chaney, A. Sancar, DNA repair: enzymatic mechanisms and relevance to drug response, JNCI: Journal of the National Cancer Institute. 88 (1996) 1346-1360.

[43] T. Fuereder, J. Stift, I. Kuehrer, N. Stranzl, D. Hoeflmayer, G. Kornek, W. Scheithauer, Response to GEMOX plus erlotinib in pancreatic cancer is associated with ERCC1 overexpression, Eur. J. Clin. Invest. 44 (2014) 958-964.

[44] M. Grunnet, D. Calatayud, N.A. Schultz, J.P. Hasselby, M. Mau-Sørensen, N. Brünner, J. Stenvang, TOP1 gene copy numbers are increased in cancers of the bile duct and pancreas, Scand. J. Gastroenterol. 50 (2015) 485-494.

[45] M. Capello, M. Lee, H. Wang, I. Babel, M.H. Katz, J.B. Fleming, A. Maitra, H. Wang, W. Tian, A. Taguchi, Carboxylesterase 2 as a determinant of response to irinotecan and neoadjuvant FOLFIRINOX therapy in pancreatic ductal adenocarcinoma, J. Natl. Cancer Inst. 107 (2015) djv132.

[46] C. Caparello, L.L. Meijer, I. Garajova, A. Falcone, T.Y. Le Large, N. Funel, G. Kazemier, G.J. Peters, E. Vasile, E. Giovannetti, FOLFIRINOX and translational studies: Towards personalised therapy in pancreatic cancer, World journal of gastroenterology. 22 (2016) 6987.

[47] D. Li, K. Xie, R. Wolff, J.L. Abbruzzese, Pancreatic cancer, The Lancet. 363 (2004) 1049-1057.

[48] N. Lubezky, M. Papoulas, Y. Lessing, G. Gitstein, E. Brazowski, I. Nachmany, G. Lahat, Y. Goykhman, A. Ben-Yehuda, R. Nakache, J.M. Klausner, Solid pseudopapillary neoplasm of the pancreas: Management and long-term outcome, Eur. J. Surg. Oncol. 43 (2017) 1056-1060.

[49] national institute for health and care excellence, **Pancreatic cancer: diagnosis and management in adults**, (2018).

[50] C. Triantaphylides, M. Krischke, F.A. Hoeberichts, B. Ksas, G. Gresser, M. Havaux, F. Van Breusegem, M.J. Mueller, Singlet oxygen is the major reactive oxygen species involved in photooxidative damage to plants, Plant Physiol. 148 (2008) 960-968.

[51] I.J. Macdonald, T.J. Dougherty, Basic principles of photodynamic therapy, Journal of Porphyrins and Phthalocyanines. 5 (2001) 105-129.

[52] M. Ethirajan, Y. Chen, P. Joshi, R.K. Pandey, The role of porphyrin chemistry in tumor imaging and photodynamic therapy, Chem. Soc. Rev. 40 (2011) 340-362.

[53] T. Dai, Y. Huang, M.R. Hamblin, Photodynamic therapy for localised infections—state of the art, Photodiagnosis and photodynamic therapy. 6 (2009) 170-188.

[54] D. Bandyopadhyay, A. Chattopadhyay, G. Ghosh, A.G. Datta, Oxidative stress-induced ischemic heart disease: protection by antioxidants, Curr. Med. Chem. 11 (2004) 369-387.

[55] D.E. Dolmans, D. Fukumura, R.K. Jain, Photodynamic therapy for cancer, Nature reviews cancer. 3 (2003) 380-387.

[56] E.D. Sternberg, D. Dolphin, C. Brückner, Porphyrin-based photosensitisers for use in photodynamic therapy, Tetrahedron. 54 (1998) 4151-4202.

[57] C.S. Foote, Definition of type I and type II photosensitised oxidation, Photochem. Photobiol. 54 (1991) 659-659.

[58] I.J. Macdonald, T.J. Dougherty, Basic principles of photodynamic therapy, Journal of Porphyrins and Phthalocyanines. 5 (2001) 105-129.

[59] F. Kamangar, C.C. Abnet, A.A. Hutchinson, C.J. Newschaffer, K. Helzlsouer, Y.Y. Shugart, P. Pietinen, S.M. Dawsey, D. Albanes, J. Virtamo, Polymorphisms in inflammation-related genes and risk of gastric cancer (Finland), Cancer Causes & Control. 17 (2006) 117-125.

[60] D. Nowis, T. Stokłosa, M. Legat, T. Issat, M. Jakóbisiak, J. Gołąb, The influence of photodynamic therapy on the immune response, Photodiagnosis and photodynamic therapy. 2 (2005) 283-298.

[61] M.R. Hamblin, T.N. Demidova, Mechanisms of low level light therapy, 6140 (2006) 1-12.

[62] N. Modi, A.J. Keay, Phototherapy for neonatal hyperbilirubinaemia: the importance of dose, Arch. Dis. Child. 58 (1983) 406-409.

[63] F. Faris, M. Thorniley, Y. Wickramasinghe, R. Houston, P. Rolfe, N. Livera, A. Spencer, Non-invasive in vivo near-infrared optical measurement of the penetration depth in the neonatal head, Clinical Physics and Physiological Measurement. 12 (1991) 353.

[64] L. Ventelon, S. Charier, L. Moreaux, J. Mertz, M. Blanchard-Desce, Nanoscale push–push dihydrophenanthrene derivatives as novel fluorophores for two-photon-excited fluorescence, Angewandte Chemie. 113 (2001) 2156-2159.

[65] M. Wainwright, Photodynamic therapy: the development of new photosensitisers, Anti-Cancer Agents in Medicinal Chemistry (Formerly Current Medicinal Chemistry-Anti-Cancer Agents). 8 (2008) 280-291.

[66] S. Pushpan, S. Venkatraman, V. Anand, J. Sankar, D. Parmeswaran, S. Ganesan, T. Chandrashekar, Porphyrins in photodynamic therapy-a search for ideal photosensitisers, Current Medicinal Chemistry-Anti-Cancer Agents. 2 (2002) 187-207.

[67] T. Patrice, Photodynamic Therapy, Royal Society of Chemistry, 2003.

[68] A.B. Ormond, H.S. Freeman, Dye sensitisers for photodynamic therapy, Materials. 6 (2013) 817-840.

[69] R.R. Allison, C.H. Sibata, Photodiagnosis for cutaneous malignancy: a brief clinical and technical review, Photodiagnosis and photodynamic therapy. 5 (2008) 247-250.

[70] L.R. Milgrom, Synthesis of some new tetra-arylporphyrins for studies in solar energy conversion, Journal of the Chemical Society, Perkin Transactions 1. (1983) 2535-2539.

[71] R. Bonnett, Photosensitisers of the porphyrin and phthalocyanine series for photodynamic therapy, Chem. Soc. Rev. 24 (1995) 19-33.

[72] T.J. Dougherty, An update on photodynamic therapy applications, J. Clin. Laser Med. Surg. 20 (2002) 3-7.

[73] A.d.C. Batlle, Porphyrins, porphyrias, cancer and photodynamic therapy—a model for carcinogenesis, Journal of Photochemistry and Photobiology B: Biology. 20 (1993) 5-22.

[74] C. Morton, S. Brown, S. Collins, S. Ibbotson, H. Jenkinson, H. Kurwa, K. Langmack, K. McKenna, H. Moseley, A. Pearse, Guidelines for topical photodynamic therapy: report of a workshop of the British Photodermatology Group, Br. J. Dermatol. 146 (2002) 552-567.

[75] J.C. Kennedy, R.H. Pottier, New trends in photobiology: endogenous protoporphyrin IX, a clinically useful photosensitiser for photodynamic therapy, Journal of Photochemistry and Photobiology B: Biology. 14 (1992) 275-292.

[76] W. Grant, A. MacRobert, S. Bown, C. Hopper, P. Speight, Photodynamic therapy of oral cancer: photosensitisation with systemic aminolaevulinic acid, The Lancet. 342 (1993) 147-148.

[77] J.D. Spikes, New trends in photobiology: Chlorins as photosensitisers in biology and medicine, Journal of Photochemistry and Photobiology B: Biology. 6 (1990) 259-274.

[78] R. Bonnett, Photosensitisers of the porphyrin and phthalocyanine series for photodynamic therapy, Chem. Soc. Rev. 24 (1995) 19-33.

[79] D.E. Dolmans, D. Fukumura, R.K. Jain, Photodynamic therapy for cancer, Nature reviews cancer. 3 (2003) 380-387.

[80] W. Kobayashi, Q. Liu, H. Nakagawa, H. Sakaki, B. Teh, T. Matsumiya, H. Yoshida, T. Imaizumi, K. Satoh, H. Kimura, Photodynamic therapy with mono-L-aspartyl chlorin e6 can cause necrosis of squamous cell carcinoma of tongue: experimental study on an animal model of nude mouse, Oral Oncol. 42 (2006) 45-49.

[81] H. Kato, K. Furukawa, M. Sato, T. Okunaka, Y. Kusunoki, M. Kawahara, M. Fukuoka, T. Miyazawa, T. Yana, K. Matsui, Phase II clinical study of photodynamic therapy using mono-L-aspartyl chlorin e6 and diode laser for early superficial squamous cell carcinoma of the lung, Lung Cancer. 42 (2003) 103-111.

[82] J. Usuda, H. Kato, T. Okunaka, K. Furukawa, H. Tsutsui, K. Yamada, Y. Suga, H. Honda, Y. Nagatsuka, T. Ohira, Photodynamic therapy (PDT) for lung cancers, Journal of Thoracic Oncology. 1 (2006) 489-493.

[83] J. Paczkowski, J. Lamberts, B. Paczkowska, D. Neckers, Photophysical properties of rose bengal and its derivatives (XII), J. Free Radic. Biol. Med. 1 (1985) 341-351.

[84] N. Houba-Herin, C. Calberg-Bacq, J. Piette, A. Van de Vorst, MECHANISMS FOR DYE-MEDIATED PHOTODYNAMIC ACTION: SINGLET OXYGEN PRODUCTION, DEOXYGUANOSINE OXIDATION AND PHAGE INACTIVATING EFFICIENCIES, Photochem. Photobiol. 36 (1982) 297-306.

[85] J. Lenard, A. Rabson, R. Vanderoef, Photodynamic inactivation of infectivity of human immunodeficiency virus and other enveloped viruses using hypericin and rose bengal: inhibition of fusion and syncytia formation, Proc. Natl. Acad. Sci. U. S. A. 90 (1993) 158-162.

[86] A. Bamias, P. Keane, T. Krausz, G. Williams, A.A. Epenetos, Intravesical administration of radiolabeled antitumor monoclonal antibody in bladder carcinoma, Cancer Res. 51 (1991) 724-728.

[87] D. Wöhrle, A. Hirth, T. Bogdahn-Rai, G. Schnurpfeil, M. Shopova, Photodynamic therapy of cancer: second and third generations of photosensitisers, Russian chemical bulletin. 47 (1998) 807-816.

[88] C.M. Allen, W.M. Sharman, J.E. Van Lier, Current status of phthalocyanines in the photodynamic therapy of cancer, Journal of Porphyrins and Phthalocyanines. 5 (2001) 161-169.

[89] A.E. O'Connor, W.M. Gallagher, A.T. Byrne, Porphyrin and nonporphyrin photosensitisers in oncology: preclinical and clinical advances in photodynamic therapy, Photochem. Photobiol. 85 (2009) 1053-1074.

[90] T. Rösch, R. Lorenz, C. Braig, S. Feuerbach, J.R. Siewert, V. Schusdziarra, M. Classen, Endoscopic ultrasound in pancreatic tumor diagnosis, Gastrointest. Endosc. 37 (1991) 347-352.

[91] G. Plattner, W. Renner, J. Went, L. Beaudette, G. Viau, Fetal sex determination by ultrasound scan in the second and third trimesters. Obstetrics & Gynecology. 61 (1983) 454-458.

[92] M.A. Röthlin, R. Näf, M. Amgwerd, D. Candinas, T. Frick, O. Trentz, Ultrasound in blunt abdominal and thoracic trauma. Journal of Trauma and Acute Care Surgery. 34 (1993) 488-495.

[93] V. Chan, A. Perlas, Basics of ultrasound imaging, in: Anonymous Atlas of Ultrasound-Guided Procedures in Interventional Pain Management, Springer, 2011, pp. 13-19.

[94] K. Hachimine, H. Shibaguchi, M. Kuroki, H. Yamada, T. Kinugasa, Y. Nakae, R. Asano, I. Sakata, Y. Yamashita, T. Shirakusa, Sonodynamic therapy of cancer using a novel porphyrin derivative, DCPH-P-Na (I), which is devoid of photosensitivity, Cancer science. 98 (2007) 916-920.

[95] S. Yoshino, T. Fukushima, S. Hayashi, M. Nonaka, K. Ogawa, K. Sasaki, S. Umemura, Effects of focused ultrasound sonodynamic treatment on the rat blood-brain barrier, Anticancer Res. 29 (2009) 889-895.

[96] R.R. Steuer, D.H. Harris, System for noninvasive hematocrit monitoring. (2004).

[97] C. Gong, D.P. Hart, Ultrasound induced cavitation and sonochemical yields, J. Acoust. Soc. Am. 104 (1998) 2675-2682.

[98] M. Pickworth, P. Dendy, T. Leighton, A. Walton, Studies of the cavitational effects of clinical ultrasound by sonoluminescence: 2. Thresholds for sonoluminescence from a therapeutic ultrasound beam and the effect of temperature and duty cycle, Phys. Med. Biol. 33 (1988) 1249.

[99] M. Pickworth, P. Dendy, T. Leighton, A. Walton, Studies of the cavitational effects of clinical ultrasound by sonoluminescence: 2. Thresholds for sonoluminescence from a therapeutic ultrasound beam and the effect of temperature and duty cycle, Phys. Med. Biol. 33 (1988) 1249.

[100] S.J. Putterman, Sonoluminescence: sound into light, Sci. Am. 272 (1995) 46-51.

[101] T.Y. Wu, N. Guo, C.Y. Teh, J.X.W. Hay, Theory and fundamentals of ultrasound, in: Anonymous Advances in Ultrasound Technology for Environmental Remediation, Springer, 2013, pp. 5-12.

[102] V. Mišík, P. Riesz, EPR characterization of free radical intermediates formed during ultrasound exposure of cell culture media, Free Radical Biology and Medicine. 26 (1999) 936-943.

[103] L.B. Feril, T. Kondo, Biological effects of low intensity ultrasound: the mechanism involved, and its implications on therapy and on biosafety of ultrasound, J. Radiat. Res. 45 (2004) 479-489.

[104] H. Tsuru, H. Shibaguchi, M. Kuroki, Y. Yamashita, M. Kuroki, Tumor growth inhibition by sonodynamic therapy using a novel sonosensitiser, Free Radical Biology and Medicine. 53 (2012) 464-472.

[105] Y. Li, X. Su, X. Wang, A.W. Leung, C. Xu, P. Wang, Q. Liu, Cytotoxic effect of protoporphyrin IX to human Leukemia U937 cells under ultrasonic irradiation, Cell. Physiol. Biochem. 33 (2014) 1186-1196.

[106] S. Umemura, N. Yumita, K. Umemura, R. Nishigaki, Sonodynamically induced effect of rose bengal on isolated sarcoma 180 cells, Cancer Chemother. Pharmacol. 43 (1999) 389-393.

[107] M. Nonaka, M. Yamamoto, S. Yoshino, S. Umemura, K. Sasaki, T. Fukushima, Sonodynamic therapy consisting of focused ultrasound and a photosensitiser causes a selective antitumor effect in a rat intracranial glioma model, Anticancer Res. 29 (2009) 943-950.

[108] E. Fischer, F. Varga, Hepatic storage and biliary excretion of rose bengal in the rat, Acta Physiol. Acad. Sci. Hung. 54 (1979) 89-94.

[109] N. Sugita, Y. Iwase, N. Yumita, T. Ikeda, S. Umemura, Sonodynamically induced cell damage using rose bengal derivative, Anticancer Res. 30 (2010) 3361-3366.

[110] N. Nomikou, C. Fowley, N.M. Byrne, B. McCaughan, A.P. McHale, J.F. Callan, Microbubble–sonosensitiser conjugates as therapeutics in sonodynamic therapy, Chemical Communications. 48 (2012) 8332-8334.

[111] J. Li, D. Song, Y. Xu, Z. Huang, W. Yue, In vitro study of haematoporphyrin monomethyl ether-mediated sonodynamic effects on C6 glioma cells, Neurological sciences. 29 (2008) 229-235.

[112] J. Li, W. Yue, Z. Huang, Z. Chen, Q. Zhan, F. Ren, J. Liu, S. Fu, Calcium overload induces C6 rat glioma cell apoptosis in sonodynamic therapy, Int. J. Radiat. Biol. 87 (2011) 1061-1066.

[113] S. Dai, S. Hu, C. Wu, Apoptotic effect of sonodynamic therapy mediated by hematoporphyrin monomethyl ether on C6 glioma cells in vitro, Acta Neurochir. 151 (2009) 1655-1661.

[114] Z. Tian, X. Quan, C. Xu, L. Dan, H. Guo, W. Leung, Hematoporphyrin monomethyl ether enhances the killing action of ultrasound on osteosarcoma in vivo, Journal of Ultrasound in Medicine. 28 (2009) 1695-1702.

[115] S. Nakajima, H. Hayashi, Y. Omote, Y. Yamazaki, S. Hirata, T. Maeda, Y. Kubo, T. Takemura, Y. Kakiuchi, Y. Shindo, The tumour-localizing properties of porphyrin derivatives, Journal of Photochemistry and Photobiology B: Biology. 7 (1990) 189-198.

[116] K. Sasaki, N. Yumita, R. Nishigaki, I. Sakata, S. Nakajima, S. Umemura, Pharmacokinetic Study of a Gallium-porphyrin Photo-and Sono-sensitiser, ATX-70, in Tumor-bearing Mice, Cancer Science. 92 (2001) 989-995.

[117] S. Umemura, K. Kawabata, N. Yumita, R. Nishigaki, K. Umemura, Sonodynamic approach to tumor treatment, (1992) 1231-1240.

[118] N. Yumita, K. Sasaki, S. Umemura, R. Nishigaki, Sonodynamically Induced Antitumor Effect of a Gallium-Porphyrin Complex, ATX-70, Cancer Science. 87 (1996) 310-316.

[119] F. Foglietta, R. Canaparo, A. Francovich, F. Arena, S. Civera, G. Cravotto, R. Frairia, L. Serpe, Sonodynamic treatment as an innovative bimodal anticancer approach: shock wave-mediated tumor growth inhibition in a syngeneic breast cancer model, Discovery medicine. 20 (2015) 197-205.

[120] C. Brazzale, R. Canaparo, L. Racca, F. Foglietta, G. Durando, R. Fantozzi, P. Caliceti, S. Salmaso, L. Serpe, Enhanced selective sonosensitizing efficacy of ultrasound-based anticancer treatment by targeted gold nanoparticles, Nanomedicine. 12 (2016) 3053-3070.

[121] A.P. McHale, J.F. Callan, N. Nomikou, C. Fowley, B. Callan, Sonodynamic therapy: concept, mechanism and application to cancer treatment, in: Anonymous Therapeutic Ultrasound, Springer, 2016, pp. 429-450.

[122] A.L. Klibanov, Ligand-carrying gas-filled microbubbles: ultrasound contrast agents for targeted molecular imaging, Bioconjug. Chem. 16 (2005) 9-17.

[123] E. Quaia, Contrast Media in Ultrasonography: Basic Principles and Clinical Applications, Springer, 2006.

[124] E.C. Unger, T.P. McCreery, R.H. Sweitzer, V.E. Caldwell, Y. Wu, Acoustically active lipospheres containing paclitaxel: a new therapeutic ultrasound contrast agent, Invest. Radiol. 33 (1998) 886-892.

[125] K. Tachibana, S. Tachibana, Application of ultrasound energy as a new drug delivery system, Japanese journal of applied physics. 38 (1999) 3014.

[126] K. Tachibana, S. Tachibana, The use of ultrasound for drug delivery, Echocardiography. 18 (2001) 323-328.

[127] G.A. Husseini, de la Rosa, Mario A Diaz, E.S. Richardson, D.A. Christensen, W.G. Pitt, The role of cavitation in acoustically activated drug delivery, J. Controlled Release. 107 (2005) 253-261.

[128] M.J. Shortencarier, P.A. Dayton, S.H. Bloch, P.A. Schumann, T.O. Matsunaga, K.W. Ferrara, A method for radiation-force localised drug delivery using gas-filled lipospheres, IEEE Trans. Ultrason. Ferroelectr. Freq. Control. 51 (2004) 822-831.

[129] P.A. Frenkel, S. Chen, T. Thai, R.V. Shohet, P.A. Grayburn, DNA-loaded albumin microbubbles enhance ultrasound-mediated transfection in vitro, Ultrasound Med. Biol. 28 (2002) 817-822.

[130] H.J. Kim, J.F. Greenleaf, R.R. Kinnick, J.T. Bronk, M.E. Bolander, Ultrasound-mediated transfection of mammalian cells, Hum. Gene Ther. 7 (1996) 1339-1346.

[131] M.A. Borden, C.F. Caskey, E. Little, R.J. Gillies, K.W. Ferrara, DNA and polylysine adsorption and multilayer construction onto cationic lipid-coated microbubbles, Langmuir. 23 (2007) 9401-9408.

[132] I. Lentacker, S.C. De Smedt, N.N. Sanders, Drug loaded microbubble design for ultrasound triggered delivery, Soft Matter. 5 (2009) 2161-2170.

[133] N.M. Green, Avidin, Adv. Protein Chem. 29 (1975) 85-133.

[134] E.P. Diamandis, T.K. Christopoulos, The biotin-(strept)avidin system: principles and applications in biotechnology, Clin. Chem. 37 (1991) 625-636.

[135] A.F. Lum, M.A. Borden, P.A. Dayton, D.E. Kruse, S.I. Simon, K.W. Ferrara, Ultrasound radiation force enables targeted deposition of model drug carriers loaded on microbubbles, J. Controlled Release. 111 (2006) 128-134.

[136] A. Kheirolomoom, P.A. Dayton, A.F. Lum, E. Little, E.E. Paoli, H. Zheng, K.W. Ferrara, Acoustically-active microbubbles conjugated to liposomes: characterization of a proposed drug delivery vehicle, J. Controlled Release. 118 (2007) 275-284.

[137] B. McCaughan, C. Rouanet, C. Fowley, N. Nomikou, A.P. McHale, P.A. McCarron, J.F. Callan, Enhanced ROS production and cell death through combined photo-and sono-activation of conventional photosensitising drugs, Bioorg. Med. Chem. Lett. 21 (2011) 5750-5752.

[138] C. McEwan, C. Fowley, N. Nomikou, B. McCaughan, A.P. McHale, J.F. Callan, Polymeric microbubbles as delivery vehicles for sensitisers in sonodynamic therapy, Langmuir. 30 (2014) 14926-14930.

[139] C. McEwan, J. Owen, E. Stride, C. Fowley, H. Nesbitt, D. Cochrane, C.C. Coussios, M. Borden, N. Nomikou, A.P. McHale, Oxygen carrying microbubbles for enhanced sonodynamic therapy of hypoxic tumours, J. Controlled Release. 203 (2015) 51-56.

[140] C. McEwan, S. Kamila, J. Owen, H. Nesbitt, B. Callan, M. Borden, N. Nomikou, R.A. Hamoudi, M.A. Taylor, E. Stride, Combined sonodynamic and antimetabolite therapy for the improved treatment of pancreatic cancer using oxygen loaded microbubbles as a delivery vehicle, Biomaterials. 80 (2016) 20-32.

[141] F. Yang, Y. Li, Z. Chen, Y. Zhang, J. Wu, N. Gu, Superparamagnetic iron oxide nanoparticle-embedded encapsulated microbubbles as dual contrast agents of magnetic resonance and ultrasound imaging, Biomaterials. 30 (2009) 3882-3890.

[142] J.I. Park, D. Jagadeesan, R. Williams, W. Oakden, S. Chung, G.J. Stanisz, E. Kumacheva, Microbubbles loaded with nanoparticles: a route to multiple imaging modalities, Acs Nano. 4 (2010) 6579-6586.

[143] E. Stride, C. Porter, A.G. Prieto, Q. Pankhurst, Enhancement of microbubble mediated gene delivery by simultaneous exposure to ultrasonic and magnetic fields, Ultrasound Med. Biol. 35 (2009) 861-868.

[144] H. Mulvana, R.J. Eckersley, R. Browning, J.V. Hajnal, E. Stride, T. Barrack, M. Tang, Q. Pankhurst, D. Wells, Enhanced gene transfection in vivo using magnetic localisation of ultrasound contrast agents: preliminary results, (2010) 670-673.

[145] L.M. Allen, T. Kent, C. Wolfe, C. Ficco, J. Johnson, MTCTM, in: Anonymous Scientific and Clinical Applications of Magnetic Carriers, Springer, 1997, pp. 481-494.

[146] W. Bonnar, Boyle's Law and gravitational instability, Monthly Notices of the Royal Astronomical Society. 116 (1956) 351-359.

[147] D. Mackay, W.Y. Shiu, A critical review of Henry's law constants for chemicals of environmental interest, Journal of physical and chemical reference data. 10 (1981) 1175-1199.

[148] M.K. Park, R.A. Myers, L. Marzella, Oxygen tensions and infections: modulation of microbial growth, activity of antimicrobial agents, and immunologic responses, Clinical infectious diseases. 14 (1992) 720-740.

[149] A. Gill, C.N. Bell, Hyperbaric oxygen: its uses, mechanisms of action and outcomes, QJM. 97 (2004) 385-395.

[150] B.A. Teicher, C.W. Rausch, E.H.I. Robert, Method for treating a tumor with a chemotherapeutic agent. (1998).

[151] M. Borad, S. Reddy, N. Bahary, H. Uronis, D. Sigal, A. Cohn, W. Schelman, J. Stephenson, C. Eng, D. Ryan, Gastrointestinal tumors, non-colorectal, Annals of Oncology. 23 (2012) ix224-ix257.

[152] S.M. Hameed, W.C. Aird, S.M. Cohn, Oxygen delivery, Crit. Care Med. 31 (2003) S658-67.

[153] J.L. Gainer, Trans-sodium crocetinate, methods of making and methods of use thereof. (2000).

[154] P. Judeinstein, C. Sanchez, Hybrid organic–inorganic materials: a land of multidisciplinarity, Journal of Materials Chemistry. 6 (1996) 511-525.

[155] J.L. Gainer, Trans-sodium crocetinate for treating hypoxia/ischemia, Expert Opin. Investig. Drugs. 17 (2008) 917-924.

[156] J. Gainer, A. Stennett, R. Murray, The effect of trans sodium crocetinate (TSC) in a rat oleic acid model of acute lung injury, Pulm. Pharmacol. Ther. 18 (2005) 213-216.

[157] C. Pierlot, V. Nardello, J. Schrive, C. Mabille, J. Barbillat, B. Sombret, J. Aubry, Calcium peroxide diperoxohydrate as a storable chemical generator of singlet oxygen for organic synthesis, J. Org. Chem. 67 (2002) 2418-2423.

[158] E. Olyaie, H. Banejad, A. Afkhami, A. Rahmani, J. Khodaveisi, Development of a cost-effective technique to remove the arsenic contamination from aqueous solutions by calcium peroxide nanoparticles, Separation and purification technology. 95 (2012) 10-15.

[159] D.P. Cassidy, R.L. Irvine, Use of calcium peroxide to provide oxygen for contaminant biodegradation in a saturated soil, J. Hazard. Mater. 69 (1999) 25-39.

[160] Y. Qian, X. Zhou, Y. Zhang, W. Zhang, J. Chen, Performance and properties of nanoscale calcium peroxide for toluene removal, Chemosphere. 91 (2013) 717-723.

[161] J. Ciccolini, C. Mercier, M. Blachon, R. Favre, A. Durand, B. Lacarelle, A simple and rapid high-performance liquid chromatographic (HPLC) method for 5-fluorouracil (5-FU) assay in plasma and possible detection of patients with impaired dihydropyrimidine dehydrogenase (DPD) activity, J. Clin. Pharm. Ther. 29 (2004) 307-315.

[162] L.C. Barnsley, D. Carugo, J. Owen, E. Stride, Halbach arrays consisting of cubic elements optimised for high field gradients in magnetic drug targeting applications, Phys. Med. Biol. 60 (2015) 8303.

[163] J. Khodaveisi, H. Banejad, A. Afkhami, E. Olyaie, S. Lashgari, R. Dashti, Synthesis of calcium peroxide nanoparticles as an innovative reagent for in situ chemical oxidation, J. Hazard. Mater. 192 (2011) 1437-1440.

[164] K. Komagoe, T. Katsu, Porphyrin-induced photogeneration of hydrogen peroxide determined using the luminol chemiluminescence method in aqueous solution: A structure-activity relationship study related to the aggregation of porphyrin, Analytical sciences. 22 (2006) 255-258.

[165] S.H. Choi, T.G. Park, G-CSF loaded biodegradable PLGA nanoparticles prepared by a single oil-in-water emulsion method, Int. J. Pharm. 311 (2006) 223-228.

[166] Invitrogen, TRIzol Reagent Guide, 2017 (2016).

[167] Roche, Transcriptor First Strand cDNA Synthesis Kit, 2017 (2006).

[168] K. Ishak, A. Baptista, L. Bianchi, F. Callea, J. De Groote, F. Gudat, H. Denk, V. Desmet, G. Korb, R.N. MacSween, Histological grading and staging of chronic hepatitis, J. Hepatol. 22 (1995) 696-699.

[169] D.E. Kleiner, E.M. Brunt, M. Van Natta, C. Behling, M.J. Contos, O.W. Cummings, L.D. Ferrell, Y. Liu, M.S. Torbenson, A. Unalp-Arida, Design and validation of a histological scoring system for nonalcoholic fatty liver disease, Hepatology. 41 (2005) 1313-1321.

[170] P. Duewell, E. Beller, S.V. Kirchleitner, T. Adunka, H. Bourhis, J. Siveke, D. Mayr, S. Kobold, S. Endres, M. Schnurr, Targeted activation of melanoma differentiation-associated protein 5 (MDA5) for immunotherapy of pancreatic carcinoma, Oncoimmunology. 4 (2015) e1029698.

[171] C. McEwan, J. Owen, E. Stride, C. Fowley, H. Nesbitt, D. Cochrane, C.C. Coussios, M. Borden, N. Nomikou, A.P. McHale, Oxygen carrying microbubbles for enhanced sonodynamic therapy of hypoxic tumours, J. Controlled Release. 203 (2015) 51-56.

[172] N. Bardeesy, R.A. DePinho, Pancreatic cancer biology and genetics, Nature Reviews Cancer. 2 (2002) 897-909.

[173] M. Rebucci, C. Michiels, Molecular aspects of cancer cell resistance to chemotherapy, Biochem. Pharmacol. 85 (2013) 1219-1226.

[174] A.E. Greijer, E. van der Wall, The role of hypoxia inducible factor 1 (HIF-1) in hypoxia induced apoptosis, J. Clin. Pathol. 57 (2004) 1009-1014.

[175] Z. Li, J.N. Rich, Hypoxia and hypoxia inducible factors in cancer stem cell maintenance, in: Anonymous Diverse Effects of Hypoxia on Tumor Progression, Springer, 2010, pp. 21-30.

[176] Y. Tsai, K. Wu, Hypoxia-regulated target genes implicated in tumor metastasis, J. Biomed. Sci. 19 (2012) 102.

[177] F. Otto, A.P. Thornell, T. Crompton, A. Denzel, K.C. Gilmour, I.R. Rosewell, G.W. Stamp, R.S. Beddington, S. Mundlos, B.R. Olsen, Cbfa1, a candidate gene for cleidocranial dysplasia syndrome, is essential for osteoblast differentiation and bone development, Cell. 89 (1997) 765-771.

[178] G. Browne, H. Nesbitt, L. Ming, G.S. Stein, J.B. Lian, S.R. McKeown, J. Worthington, Bicalutamide-induced hypoxia potentiates RUNX2-mediated Bcl-2 expression resulting in apoptosis resistance, Br. J. Cancer. 107 (2012) 1714-1721.

[179] H. Nesbitt, G. Browne, K.M. O'Donovan, N.M. Byrne, J. Worthington, S.R. McKeown, D.J. McKenna, Nitric Oxide Up-Regulates RUNX2 in LNCaP Prostate Tumours: Implications for Tumour Growth In Vitro and In Vivo, J. Cell. Physiol. 231 (2016) 473-482.

[180] G.L. Barnes, A. Javed, S.M. Waller, M.H. Kamal, K.E. Hebert, M.Q. Hassan, A. Bellahcene, A.J. Van Wijnen, M.F. Young, J.B. Lian, G.S. Stein, L.C. Gerstenfeld, Osteoblast-related transcription factors Runx2 (Cbfa1/AML3) and MSX2 mediate the expression of bone sialoprotein in human metastatic breast cancer cells, Cancer Res. 63 (2003) 2631-2637.

[181] H. Kayed, X. Jiang, S. Keleg, R. Jesnowski, T. Giese, M.R. Berger, I. Esposito, M. Lohr, H. Friess, J. Kleeff, Regulation and functional role of the Runt-related transcription factor-2 in pancreatic cancer, Br. J. Cancer. 97 (2007) 1106-1115.

[182] R.K. Boregowda, O.O. Olabisi, W. Abushahba, B. Jeong, K.K. Haenssen, W. Chen, M. Chekmareva, A. Lasfar, D.J. Foran, J.S. Goydos, RUNX2 is overexpressed in melanoma cells and mediates their migration and invasion, Cancer Lett. 348 (2014) 61-70.

[183] E. Zelzer, D.J. Glotzer, C. Hartmann, D. Thomas, N. Fukai, S. Soker, B.R. Olsen, Tissue specific regulation of VEGF expression during bone development requires Cbfa1/Runx2, Mech. Dev. 106 (2001) 97-106.

[184] J.M. Bailey, J. Alsina, Z.A. Rasheed, F.M. McAllister, Y. Fu, R. Plentz, H. Zhang, P.J. Pasricha, N. Bardeesy, W. Matsui, DCLK1 marks a morphologically distinct subpopulation of cells with stem cell properties in preinvasive pancreatic cancer, Gastroenterology. 146 (2014) 245-256.

[185] Y. Ohara, T. Oda, M. Sugano, S. Hashimoto, T. Enomoto, K. Yamada, Y. Akashi, R. Miyamoto, A. Kobayashi, K. Fukunaga, Histological and prognostic importance of CD44 /CD24 /EpCAM expression in clinical pancreatic cancer, Cancer science. 104 (2013) 1127-1134.

[186] A. Mohammed, N.B. Janakiram, M. Brewer, R.L. Ritchie, A. Marya, S. Lightfoot, V.E. Steele, C.V. Rao, Antidiabetic drug metformin prevents progression of pancreatic cancer by targeting in part cancer stem cells and mTOR signaling, Translational oncology. 6 (2013) 649IN7-659.

[187] L. Li, L. Borodyansky, Y. Yang, Genomic instability en route to and from cancer stem cells, Cell Cycle. 8 (2009) 1000-1002.

[188] S. Yabuuchi, S.G. Pai, N.R. Campbell, R.F. De Wilde, E. De Oliveira, P. Korangath, M.M. Streppel, Z.A. Rasheed, M. Hidalgo, A. Maitra, Notch signaling pathway targeted therapy suppresses tumor progression and metastatic spread in pancreatic cancer, Cancer Lett. 335 (2013) 41-51.

[189] G. Kroemer, G. Mariño, B. Levine, Autophagy and the integrated stress response, Mol. Cell. 40 (2010) 280-293.

[190] W. Kim, S.L. Flamm, A.M. Di Bisceglie, H.C. Bodenheimer, Serum activity of alanine aminotransferase (ALT) as an indicator of health and disease, Hepatology. 47 (2008) 1363-1370.

[191] Cancer Treatment Centers of America, **Blood counts**, 2017 (2017).

[192] E.N. Marieb, K. Hoehn, The cardiovascular system: blood vessels, Human anatomy & physiology. (2013) 703-720.

[193] R.K. Jain, T. Stylianopoulos, Delivering nanomedicine to solid tumors, Nature reviews Clinical oncology. 7 (2010) 653-664.

[194] L.C. Barnsley, D. Carugo, M. Aron, E. Stride, Understanding the dynamics of superparamagnetic particles under the influence of high field gradient arrays, Phys. Med. Biol. 62 (2017) 2333.

[195] C. Crake, J. Owen, S. Smart, C. Coviello, C. Coussios, R. Carlisle, E. Stride, Enhancement and Passive Acoustic Mapping of Cavitation from Fluorescently Tagged Magnetic Resonance-Visible Magnetic Microbubbles In Vivo, Ultrasound Med. Biol. 42 (2016) 3022-3036.

[196] This was informed by our clinical colleagues.

[197] T. Krings, J. Finney, P. Niggemann, P. Reinacher, N. Lück, A. Drexler, J. Lovell, A. Meyer, R. Sehra, P. Schauerte, Magnetic versus manual guidewire manipulation in neuroradiology: in vitro results, Neuroradiology. 48 (2006) 394-401.

[198] N. Nomikou, A.P. McHale, Exploiting ultrasound-mediated effects in delivering targeted, site-specific cancer therapy, Cancer Lett. 296 (2010) 133-143.

[199] The treatment schedule and termination date was informed by an earlier pilot study and supported by bioluminescent imaging. ,.

[200] S.P. Cregan, J.G. MacLaurin, C.G. Craig, G.S. Robertson, D.W. Nicholson, D.S. Park, R.S. Slack, Bax-dependent caspase-3 activation is a key determinant in p53-induced apoptosis in neurons, J. Neurosci. 19 (1999) 7860-7869.

[201] N. Henke, D.A. Lisak, L. Schneider, J. Habicht, M. Pergande, A. Methner, The ancient cell death suppressor BAX inhibitor-1, Cell Calcium. 50 (2011) 251-260.

[202] K. Miyake, K. Hayakawa, M. Nishino, T. Morimoto, S. Mukaihara, Effects of Oral 5-Fluorouracil Drugs on Hepatic Fat Content in Patients With Colon Cancer 1, Acad. Radiol. 12 (2005) 722-727.

[203] A.C. Koong, V.K. Mehta, Q.T. Le, G.A. Fisher, D.J. Terris, J.M. Brown, A.J. Bastidas, M. Vierra, Pancreatic tumors show high levels of hypoxia, International Journal of Radiation Oncology* Biology* Physics. 48 (2000) 919-922.

[204] M. Yoshimura, S. Itasaka, H. Harada, M. Hiraoka, Microenvironment and radiation therapy, BioMed research international. 2013 (2012).

[205] S. Rockwell, I.T. Dobrucki, E.Y. Kim, S.T. Marrison, V.T. Vu, Hypoxia and radiation therapy: past history, ongoing research, and future promise, Curr. Mol. Med. 9 (2009) 442-458.

[206] E. Racker, History of the Pasteur effect and its pathobiology, Mol. Cell. Biochem. 5 (1974) 17-23.

[207] J. Murtagh, D.O. Frimannsson, D.F. O'Shea, Azide conjugatable and pH responsive near-infrared fluorescent imaging probes, Org. Lett. 11 (2009) 5386-5389.

[208] C.S. Leopold, D. Eikeler, Eudragit® E as coating material for the pH-controlled drug release in the topical treatment of inflammatory bowel disease (IBD), J. Drug Target. 6 (1998) 85-94.

[209] F. McNeil-Watson, W. Tscharnuter, J. Miller, A new instrument for the measurement of very small electrophoretic mobilities using phase analysis light scattering (PALS), Colloids Surf. Physicochem. Eng. Aspects. 140 (1998) 53-57.

[210] K. Faulkner, I. Fridovich, Luminol and lucigenin as detectors for O 2 ṡ−, Free Radical Biology and Medicine. 15 (1993) 447-451.

[211] J. Fuchs, J. Thiele, The role of oxygen in cutaneous photodynamic therapy, Free Radical Biology and Medicine. 24 (1998) 835-847.

[212] H. Lin, Y. Shen, D. Chen, L. Lin, B.C. Wilson, B. Li, S. Xie, Feasibility study on quantitative measurements of singlet oxygen generation using singlet oxygen sensor green, J. Fluoresc. 23 (2013) 41-47.

[213] I. Yildiz, E. Deniz, B. McCaughan, S.F. Cruickshank, J.F. Callan, F.M. Raymo, Hydrophilic CdSe− ZnS core− shell quantum dots with reactive functional groups on their surface, Langmuir. 26 (2010) 11503-11511.

[214] S.C. Shekar, D. Lee, A. Ramamoorthy, Chemical shift anisotropy and offset effects in cross polarization solid-state NMR spectroscopy, Journal of Magnetic Resonance. 157 (2002) 223-234.

[215] J.W. Wojtkowiak, H.C. Cornnell, S. Matsumoto, K. Saito, Y. Takakusagi, P. Dutta, M. Kim, X. Zhang, R. Leos, K.M. Bailey, Pyruvate sensitises pancreatic tumors to hypoxia-activated prodrug TH-302, Cancer & metabolism. 3 (2015) 2.

[216] M. Nordsmark, M. Overgaard, J. Overgaard, Pretreatment oxygenation predicts radiation response in advanced squamous cell carcinoma of the head and neck, Radiotherapy and oncology. 41 (1996) 31-39.

[217] C. McEwan, J. Owen, E. Stride, C. Fowley, H. Nesbitt, D. Cochrane, C.C. Coussios, M. Borden, N. Nomikou, A.P. McHale, Oxygen carrying microbubbles for enhanced sonodynamic therapy of hypoxic tumours, J. Controlled Release. 203 (2015) 51-56.

[218] J.R. Eisenbrey, R. Shraim, J. Liu, J. Li, M. Stanczak, B. Oeffinger, D.B. Leeper, S.W. Keith, L.J. Jablonowski, F. Forsberg, Sensitization of hypoxic tumors to radiation therapy using ultrasound sensitive oxygen microbubbles, International Journal of Radiation Oncology• Biology• Physics. (2017).

Appendices

Appendix 1: This paper is related to chapter 4

Journal of Controlled Release 262 (2017) 192–200

Contents lists available at ScienceDirect

Journal of Controlled Release

journal homepage: www.elsevier.com/locate/jconrel

Magnetically responsive microbubbles as delivery vehicles for targeted sonodynamic and antimetabolite therapy of pancreatic cancer

Yingjie Sheng[a,1], Estelle Beguin[b,1], Heather Nesbitt[a,1], Sukanta Kamila[a], Joshua Owen[b], Lester C. Barnsley[b], Bridgeen Callan[a], Christopher O'Kane[c], Nikolitsa Nomikou[d], Rifat Hamoudi[d,h], Mark A. Taylor[e], Mark Love[f], Paul Kelly[g], Declan O'Rourke[g], Eleanor Stride[b,*], Anthony P. McHale[a,*], John F. Callan[a,*]

[a] Biomedical Sciences Research Institute, University of Ulster, Coleraine, Northern Ireland BT52 1SA, UK
[b] Institute of Biomedical Engineering, University of Oxford, OX3 7DQ, UK
[c] Department of Biomedical and Forensic Science, Anglia Ruskin University, Cambridge, CB1 1PT, UK
[d] Division of Surgery & Interventional Science, Faculty of Medical Sciences, University College London, UK
[e] Department of HPB Surgery, Mater Hospital, Belfast, Northern Ireland BT14 6AB, UK
[f] Imaging Centre, The Royal Victoria Hospital, Grosvenor Road, Belfast, Northern Ireland BT12 6BA, UK
[g] Department of Pathology, The Royal Victoria Hospital, Grosvenor Road, Belfast, Northern Ireland BT12 6BA, UK
[h] Sharjah Institute for Medical Research, College of Medicine, University of Sharjah, Sharjah, United Arab Emirates

ARTICLE INFO

Keywords:
Microbubbles
Magnetic targeting
Drug delivery
Hypoxia
5-Fluoruracil
Rose Bengal
Sonodynamic therapy
Antimetabolite therapy
Pancreatic cancer

ABSTRACT

Magnetically responsive microbubbles (MagMBs), consisting of an oxygen gas core and a phospholipid coating functionalised with Rose Bengal (RB) and/or 5-fluorouracil (5-FU), were assessed as a delivery vehicle for the targeted treatment of pancreatic cancer using combined antimetabolite and sonodynamic therapy (SDT). MagMBs delivering the combined 5-FU/SDT treatment produced a reduction in cell viability of over 50% when tested against a panel of four pancreatic cancer cell lines in vitro. Intravenous administration of the MagMBs to mice bearing orthotopic human xenograft BxPC-3 tumours yielded a 48.3% reduction in tumour volume relative to an untreated control group ($p < 0.05$) when the tumour was exposed to both external magnetic and ultrasound fields during administration of the MagMBs. In contrast, application of an external ultrasound field alone resulted in a 27% reduction in tumour volume. In addition, activated caspase and BAX protein levels were both observed to be significantly elevated in tumours harvested from animals treated with the MagMBs in the presence of magnetic and ultrasonic fields when compared to expression of those proteins in tumours from either the control or ultrasound field only groups ($p < 0.05$). These results suggest MagMBs have considerable potential as a platform to enable the targeted delivery of combined sonodynamic/antimetabolite therapy in pancreatic cancer.

1. Introduction

Pancreatic cancer has the lowest survival rate among the 21 most common forms of cancer with only 3% of patients surviving five years after their initial diagnosis [1]. While many other forms of cancer have seen survival rates increase significantly over the past four decades, the survival rate for pancreatic cancer has remained unchanged. Late presentation of patients due to the vague symptoms associated with the disease means only ~20% are eligible for potentially curative resection at the time of initial diagnosis [2]. Of the remaining ~80% of patients, ~50% present with metastatic disease and ~30% with locally advanced or borderline resectable pancreatic cancer (LAPC or BRPC) [3]. While earlier diagnosis and better awareness are key components of any future strategy to improve survival rates, there is also an urgent need for improved therapies. Several studies have investigated the potential of neo-adjuvant chemo- and/or radio-therapy to downstage tumours and increase the number of patients eligible for resection [3–5]. Unfortunately, such treatments are often associated with significant off-target effects due to the non-specific nature of the chemotherapy regimen. Therefore, the development of targeted treatments that reduce side-effects related to systemic chemotherapy have enormous potential as neo-adjuvant and palliative pancreatic cancer

* Corresponding authors.
E-mail addresses: eleanor.stride@eng.ox.ac.uk (E. Stride), j.callan@ulster.ac.uk (J.F. Callan).
[1] Joint first authors.

http://dx.doi.org/10.1016/j.jconrel.2017.07.040
Received 2 June 2017; Received in revised form 19 July 2017; Accepted 28 July 2017
Available online 29 July 2017

treatments by reducing tumour burden to either enable surgery or to provide symptom relief.

In a previous study, we demonstrated the utility of ultrasound responsive microbubbles (MBs) for delivery of drug payloads and encapsulated oxygen gas to pancreatic tumours [6]. MBs are lipid or polymer stabilised gas filled particles approved for use as contrast agents in diagnostic ultrasound [7]. At low ultrasound pressures, MBs oscillate in a relatively symmetric manner resulting in acoustic backscatter that enhances the quality of the diagnostic image [8]. Exposure of cells to low intensity ultrasound can also facilitate a phenomenon known as sonoporation which causes a transient 'poration' of cellular plasma membranes and the phenomenon is enhanced in the presence of exogenously-added MBs. Such an approach has been exploited to enhance the efficacy of gemcitabine therapy in pancreatic cancer patients [9,10]. In contrast, at higher acoustic pressures, collapse of the MB leads to rupture and release of the shell fragments at the target site [11]. This feature has been exploited by several groups investigating the potential of MBs as targeted delivery vehicles [12,13]. In our previous work, we attached the antimetabolite drug 5-fluouracil (5-FU) and the sonosensitiser Rose Bengal (RB) to the shell of oxygen-loaded lipid stabilised MBs for the combined antimetabolite and sonodynamic therapy (SDT) treatment of pancreatic cancer [6]. Significant reductions in the viability of three pancreatic cancer cell lines (BxPC3, MiaPaCa-2 and Panc-01) and inhibition of the growth of ectopic pancreatic BxPC-3 tumours were observed for the combined treatment when compared to either treatment alone. Antimetabolite therapy is an established treatment protocol for pancreatic cancer with 5-FU and gemcitabine among the most commonly used antimetabolite drugs [14]. In contrast, SDT is an emerging anti-cancer treatment that involves the activation of an otherwise inactive sensitiser drug using low-intensity ultrasound [15]. The combination of sensitiser and ultrasound, in the presence of molecular oxygen, generates cytotoxic levels of reactive oxygen species (ROS) causing cell death via oxidative stress [16]. As oxygen is a key substrate for the generation of ROS in SDT, and since pancreatic adenocarcinoma is characterised as extremely hypoxic, providing oxygen during SDT can improve the ROS yield and enhance the therapeutic outcome [17]. While our oxygen carrying MBs have shown great promise as a platform for targeted oxygen delivery and enhanced 5-FU/SDT treatment of pancreatic cancer, there remains a need to demonstrate the effectiveness of this method in an orthotopic tumour model following intravenous injection of the MB suspension. To this end, we have reasoned that an additional layer of targeting may be required to help retain MBs in the tumour vasculature after injection and enhance the quantity of MBs destroyed at the target site by ultrasound exposure. The incorporation of magnetic nanoparticles within the MB shell is one approach that has been explored to improve the targeting capability of MBs [18]. Previous work in our laboratory has demonstrated that externally applied magnetic fields may be used to enhance the retention of magnetically-responsive microbubbles at a target site in an ex vivo model under physiologically-relevant flow rates [19]. In this manuscript, we assess the ability of oxygen loaded magnetic MBs with 5-FU and Rose Bengal attached to their surface, as a targeted treatment for orthotopic human pancreatic BxPC-3 tumours in SCID mice. The benefit afforded by incorporating magnetic targeting into our delivery platform is demonstrated by studies in a flow-phantom and by therapeutic efficacy studies in vivo.

2. Materials and methods

2.1. Reagents and equipment

1,2-dibehenoyl-*sn*-glycero-3-phosphocholine (DBPC) and 1,2-distearoyl-*sn*-glycero-3-phosphoethanolamine-*N*-[methoxy(polyethylene glycol)-2000] (DSPE-PEG(2000)) and DSPE-PEG(2000)-biotin were purchased from Avanti Polar Lipids (Alabaster, Alabama, USA). Oxygen gas was purchased from BOC Industrial Gases UK and perfluorobutane (PFB) was purchased from Apollo Scientific Ltd. Phosphate Buffered Saline (PBS) was purchased from Gibco, Life Technologies, UK. Glycerol and propylene glycol (1 kg, hydrolysed) were purchased from Sigma Aldrich (UK). Superparamagnetic iron oxide nanoparticles (SPION): fluidMAG-Lipid (50 nm hydrodynamic diameter) were purchased from Chemicell (Berlin, Germany). The use of lipid conjugated SPION in this study was preferred over the use of previously reported isoparaffin stabilised SPION as the addition of lipids to lipid-shelled microbubbles is likely to be less disruptive to the acoustic response of the system compared to the addition of isoparaffin [19]. These microbubbles have been extensively characterised and successfully used in previous in vivo experiments [20]. The method for magnetic microbubble fabrication used in this study has then been adapted for the use of lipid conjugated SPION: fluidMAG-Lipid as presented in the following section. MBs were formed using a Microson ultrasonic cell disruptor, 100 W, 22.5 kHz, from Misonix Inc. (NY, USA). Optical microscope images were obtained using a Leica DM500 optical microscope. MB concentration and size were determined using purpose- written MATLAB software (2010B, MathWorks, Natick, MA, USA). Rose Bengal sodium salt, NHS-biotin, MTT assay kit, avidin, chloroacetic acid, 4-dimethylaminopyridine (DMAP), hydroxybenzotriazole (HOBt), *N,N′*-dicyclohexylcarbodiimide (DCC), anhydrous dimethylformamide (DMF), and ethanol were purchased from Sigma Aldrich (UK) at the highest grade possible. Biotin, 5-flurouracil, di(*N*-succinimidyl) carbonate and 2-aminoethanol were purchased from Tokyo Chemical Industry UK Ltd. Error was expressed as ± SEM (standard error of the mean) and statistical comparisons were established using ANOVA and un-paired Student's *t*-test.

2.2. Preparation of avidin functionalised magnetic microbubbles (MagPFBMBs)

Avidin functionalised magnetic MBs were prepared by dissolving DBPC (4.0 mg, 4.43 μmol), DSPE-PEG(2000) (1.35 mg, 0.481 μmol) and DSPE-PEG(2000)-biotin (1.45 mg, 0.481 μmol) at a molar ratio of 82:9:9 in chloroform (274 μL). The chloroform solvent was slowly evaporated by heating the lipid solution at 40 °C overnight to produce a dried lipid film. The lipid film was reconstituted in 2 mL of a PBS (pH 7.4 ± 0.1):propylene glycol:glycerol (8:1:1 v/v) mixture and the contents heated at 80 °C under stirring for 30 min in a water bath. FluidMAG-Lipids NPs (150 μL) were then added to the solution and the mixture was sonicated with a handheld sonicator probe for 1.5 min (100 W, 22.5 kHz, power setting 4). The headspace of the glass vial was then filled with perfluorobutane gas (PFB) and the gas/liquid interface was sonicated for 20 s (power setting 19), producing PFB-containing magnetic MBs (MagPFBMBs). The vial was immediately sealed and placed in an ice bath for 10 min. The MagPFBMB suspension was then centrifuged (100 RCF, 5 min) to remove the excess NPs and non-incorporated MB lipids by discarding the infranatant. The microbubble concentrate was re-suspended in 2 mL of PBS (pH 7.4 ± 0.1):propylene glycol:glycerol (8:1:1 v/v), avidin in PBS (50 μL, 10 mg/mL) was added to the suspension and the contents mixed for 10 min on a rotary shaker. The suspension was centrifuged (100 RCF, 5 min) to remove the excess avidin and the PFBMBs were again re-suspended in 2 mL of PBS (pH 7.4 ± 0.1):propylene glycol:glycerol (8:1:1 v/v). MagPFBMBs were analysed using a Leica DM500 optical microscope to obtain the size distribution and concentration. For this, 10 μL of suspension was diluted in 190 μL of PBS and examined using a haemocytometer (Bright-Line, Hausser Scientific, Horsham, PA, USA). 30 images were obtained with a 40 × objective lens and analysed with customised image analysis package in MATLAB (2010B, MathWorks, Natick, MA, USA). The iron content in the MagPFBMBs was determined by atomic absorption spectroscopy using a Varian fast sequential atomic absorption spectrometer. A calibration curve was constructed using known concentrations of Fe(III) in 0.5 M HCl. Readings were taken at 248.3 nm, 0.5 nm slit width, 10.0 mA lamp current, with the following flame settings; flame type: air/acetylene, air flow: 13.50 L/

min, acetylene flow: 2.00 L/min, burner height: 13.5 mm. A 300 μL sample of MagMBs was sonicated to destroy the bubbles and dissolved in 0.5 M HCl. The amount of Fe(III) present in the sample was calculated by reference to the calibration curve and the total iron content determined using a magnetite (Fe_3O_4) Fe(III):Fe(II) ratio of 2:1.

2.3. Preparation of $MagO_2$MB-Rose Bengal and $MagO_2$MB-5FU conjugates

The synthesis of biotin functionalised Rose Bengal [16] and biotin functionalised 5-FU [6] have been described by us in previous communications. Saturated solutions of biotin-RB and biotin 5-FU were prepared in a 0.5% (v/v) DMSO: PBS (pH 7.4 ± 0.1) solvent mixture. 100 μL of biotin-5FU and biotin-RB were added to separate samples (2 mL each) of MagPFBMBs and allowed to mix for 5 min on a rotary shaker. Both samples were centrifuged (100 RCF, 5 min) to remove unbound material and PFBMB conjugates were re-suspended in 1 mL of PBS solution (pH 7.4 ± 0.1). This conjugation/centrifugation process was repeated three times. The final PFBMB-RB and PFBMB-5FU conjugates were transferred to glass vials. $MagO_2$MB-RB and $MagO_2$MB-5FU conjugates were obtained by sparging the MagPFBMB-RB and MagPFBMB-5FU with pure O_2 gas for 2 min and sealing the vial via crimping. A small sample (100 μL) of both the $MagO_2$MB-RB and $MagO_2$MB-5FU conjugates was retained and the MB number again counted using a haemocytometer. The remaining sample was sonicated in an ultrasonic bath for 5 min to burst the MBs and the Rose Bengal and 5-FU concentration determined using UV–Vis (ultra violet – visible) spectroscopy and HPLC (high performance liquid chromatography) respectively [21].

2.4. Retention of MagMBs in a flow cell using an external magnetic field

MagPFBMBs without payload were used in this study to reduce wastage of biotin-5FU and biotin-RB. 1×10^7 MagPFBMBs were placed in a 1 mL syringe, connected to an ibidi μ-Slide VI flow chamber using silicone tubing (1.6 mm internal diameter) and placed in a peristaltic syringe pump. A single N52 grade NdFeB permanent magnet cube (12.7 mm) with an internal magnetization of 1.14×10^6 A/m was positioned 1 mm from the base of the flow chamber. Values for a field of 0.46 T and gradient of 83.1 T/m inside the flow chamber were calculated using a model described and experimentally verified previously [22], whereby the field was determined by breaking the magnet into a 3-dimensional lattice of evenly-distributed point moments, and summing the contributed dipole field from each moment. The MagPFBMBs were pumped through the flow chamber at a rate of 0.6 mL/min. Once the syringe was empty, the magnetic field was removed and 1 mL of PBS (pH 7.4 ± 0.1) added to the syringe to flush the flow chamber's content into a clean vial. Collected MBs were counted using the method described above. As a control, the experiment was repeated in the absence of a magnetic field but under otherwise identical conditions. The number of MBs collected during the PBS flush was again recorded.

2.5. In vitro cell viability

Human primary pancreatic adenocarcinoma cell lines Mia PaCa-2 and Panc-1, were maintained in DMEM medium. The mouse primary pancreatic adenocarcinoma T110299 derived from a GEM mouse (KPC and a gift from Prof. J. Siveke, Technical University of Munich, Germany), was also maintained in DMEM medium while the human primary pancreatic adenocarcinoma cell line BxPc-3 was maintained in RPMI-1640 medium, all of which were supplemented with 10% (v/v) foetal bovine serum and grown in a humidified 5% CO_2 atmosphere at 37 °C. These cells were plated into the wells of a 96-well tissue culture plate at a concentration of 5×10^3 cells per well and incubated for 24 h at 37 °C in a humidified 5% CO_2 atmosphere. The media was then removed from each well and replaced with 100 μL of treatment suspension and 100 μL of fresh medium. This resulted in a final MB count and RB or 5-FU concentration as follows: $MagO_2$MB-RB: 10^6 MB, [RB] = 5 μM; $MagO_2$MB-5FU; 10^7 MB, [5-FU] = 100 μM and combined $MagO_2$MB-RB/$MagO_2$MB-5FU: 10^7 MB, [RB] = 5 μM, [5-FU] = 100 μM. Where required, individual wells were then placed in direct contact with the emitting surface a Sonidel SP100 sonoporator with ultrasound gel used to mediate contact. Each well was treated with ultrasound for 30 s, using a frequency of 1 MHz, an ultrasound power density of 3.0 W cm^{-2} (I_{SATP}; spatial average, temporal peak) corresponding to a peak to peak pressure of 0.8 MPa in water and 0.5 MPa inside the well as measured with a needle hydrophone (Precision Acoustics, Dorset, UK); and a duty cycle of 50% (pulse frequency = 100 Hz). The solution was then removed from the wells and fresh medium added (200 μL). Plates were incubated in a humidified 5% CO_2 atmosphere at 37 °C for 21 h and cell viability determined using an MTT assay [23]. Results were compared with those obtained using untreated cells and cells exposed to ultrasound treatment alone.

2.6. Treatment of orthotopic BxPC-3 Luc tumours in SCID mice

All animals employed in this study were treated humanely and in accordance with licenced procedures under the UK Animals (Scientific Procedures) Act 1986. BxPc-3 Luc cells were maintained in RPMI-1640 medium supplemented with 10% foetal calf serum as described above. Cells (1×10^6) were re-suspended in 100 μL of Matrigel® and orthotopically implanted into the head of the pancreas of female Balb/c SCID (C·B-17/IcrHan®Hsd-Prkdcscid) mice. 19 days after implantation, animals were randomly distributed into 3 groups (n = 4). Following induction of anaesthesia (intraperitoneal injection of Hypnorm/Hypnovel), a 100 μL mixture of PBS containing $MagO_2$MB-RB/$MagO_2$MB-5FU (MB = 1.6×10^8, [RB] = 350 μM and [5-FU] = 700 μM) was administered by tail vein injection to Groups 2 & 3 while Group 1 received vehicle only. For Group 2, ultrasound (frequency = 1 MHz, ultrasound power density = 3.5 Wcm^{-2} I_{SATP}; spatial average temporal peak, corresponding to a free field peak to peak pressure of 0.85 MPa, duty cycle = 30% and pulse repetition frequency = 100 Hz) was directed to the tumour region (determined using prior bioluminescent imaging) via the abdomen for 3.5 min during and after injection (3.5 min total). For Group 3, in addition to ultrasound using the above parameters, a stack of permanent magnet discs (arranged to deliver the optimal magnetic force to the tumour region) [24] was directed to the tumour region (again via the abdomen) for 3.5 min during and after injection (3.5 min total), resulting in an approximate magnetic field at the tumour of 0.10 T and gradient 14.9 T/m. Treatments using the above conditions were repeated on Days 20 and 21 with animals sacrificed on Day 28. Tumours were then surgically excised and tumour volumes determined by direct measurement.

2.7. Determination of apoptotic marker expression in tumours post treatment

Following the determination of tumour volume a single cell suspension was prepared from the excised tumours. This involved homogenising the tumour tissue in 4% FCS in RPMI 160 μL (30 mg/mL) collagenase type II, 50 μL (2 μg/mL) DNAse and stirring for 15 min at room temperature. A further 160 μL of collagenase II was subsequently added and the contents stirred for a further 15 min. The mixture was filtered through a 100 μm filter, centrifuged at 1700 rpm for 5 min and re-suspended in 1 mL of Red Cell Lysis Buffer (RCLB) for 10 min. RCLB was neutralised by adding media containing FCS and cells were recovered by centrifuging at 1700 rpm. The pellet was washed twice with PBS, centrifuged and re-suspended in 700 μL PBS buffer. For BAX expression, 300 μL of single cell suspension in staining buffer was permeabilised using BD permeablisation buffer (BD Biosciences UK). Permeabilised cells were re-suspended in 300 μL of staining buffer

containing BAX antibody (Cell Signalling Technology, D2E11) (10 μg/mL) and incubated for 30 min at room temperature. The cells were washed in ice cold PBS and the cell pellet was re-suspended in FITC secondary antibody (Abcam, ab6717-1) for 1 h. Cells were washed three times by centrifugation at 400 RCF for 5 min in ice cold PBS, re-suspended in 650 μL of PBS buffer nd analysed by flow cytometry. For active caspase expression, the Pan Caspase NIR probe kit (Vergent Bioscience) was used according to the manufacturer's instructions. The kit utilizes the caspase family inhibitor VAD-FMK conjugated to a near IR dye (780-VAD-FMK) as a marker that irreversibly binds to activated caspases in apoptotic cells. Essentially, 300 μL of tumour single cell suspension diluted in staining buffer was centrifuged, the pellet re-suspended in 300 μL of 1XCAS-MAP NIR probe and incubated at room temperature in the dark for 1 h. Cells were washed three times by centrifugation at 400 RCF for 5 min in ice cold PBS and re-suspended in 650 μL of staining buffer and analysed by flow cytometry. qRT-PCR was used to investigate the expression of TMBIM1 in tumours as previously described [6]. Briefly, RNA was extracted from microdissected slides using the RecoverAll Kit (Life Technologies, Paisley, UK). cDNA synthesis was carried out using the Superscript III First Strand cDNA synthesis kit (Life Technologies, Paisley, UK) using the reverse primer of each of TMBIM1 (transmembrane BAX inhibitor motif containing 1) and the two housekeeping genes;18S rRNA and b-actin. qRT-PCR was carried out using the SYBR Green kit on the CFX96 instrument (BioRad, UK). The qRT-PCR cycle was as follows: 95C for 3 min, 95C for 10 s, 60C for 45 s for 40 cycles. For analysis, the geometric mean of 18S rRNA and b-actin was taken as the single housekeeping value. Statistical comparison between the groups was carried out using two-way ANOVA with Bonferroni post-hoc analysis. The primers used to investigate the TMBIM1 expression are shown in the table below.

Primer	Sequence
TMBIM1 Forward	CATCACTGCGGTGGTATCCA
TMBIM1_Reverse	GTATTGGAAGTAGAGCACAATGCTAGT
β-Actin Forward	CGTGGGCCGCCCTAGGCACCA
β-Actin Reverse	TTGGCCTTAGGGTTCAGGGGGG
18SrRNA_Forward	TGACTCAACACGGGAAACC
18SrRNA_Reverse	TCGCTCCACCAACTAAGAAC

2.8. Toxicity determination of $MagO_2$MB-5FU and $MagO_2$MB-RB conjugates

Healthy MF1 mice (8 weeks old) were randomly distributed into four groups (n = 10). Group 1 received no treatment; Groups 2 & 3 received a tail vein injection (100 μL) of 5-FU (115 mM) or RB (1.03 mM) respectively and Group 4 received a tail vein injection (100 μL) containing a suspension of $MagO_2$MB-RB/$MagO_2$MB-5FU ([MB] = 2.3×10^8, [RB] = 570 ± 15 μM, and [5FU] = 503 ± 7 μM]) on Day 1 and Day 8. Pre-treatment tail vein bleeds (0.10 mL) were collected in lithium heparinised tubes on Day 0 with the post-treatment bleeds taken in a similar manner on Day 15. Blood samples were sent to CTDS Ltd. (Leeds, UK) for whole blood and plasma biochemical analysis. Urea, alanine aminotransferase (ALT), red blood cell (RBC), haemoglobin (Hb), haematocrit (HCT), mean corpuscular volume (MCV), mean corpuscular haemoglobin (MCH), mean corpuscular haemoglobin concentration (MCHC), platelet, white blood cell, neutrophil and lymphocyte levels were determined using accredited protocols. Following the Day 15 bleed, mice were then sacrificed and the liver and kidneys were surgically excised and placed in a formalin free tissue fixative solution (Sigma-Aldrich) for 24 h. It should be noted that the liver was chosen in these studies because it has been shown that MB are removed from circulation by that organ following intravenous administration. The tissue was then placed in an automated Leica TP1020 tissue processor and passed between increasing concentrations of ethanol followed by xylene and paraffin wax 24 h later. The wax embedded tissue samples were placed in moulds containing paraffin wax. Once the wax blocks had solidified, 5 μm sections were cut, placed on a glass slide and stained with haematoxylin and eosin (H & E) using an automated staining protocol. In some cases, additional stains (i.e. reticulin, Masson's trichrome, Perl's Prussian blue stain) were used if required. The stained sections were reviewed histologically by pathologists with expertise in liver and renal pathology. Liver architecture was initially assessed to establish if there was significant remodelling or fibrosis. The various liver compartments were subsequently examined for pathological changes. Portal tract and lobular inflammation grading was adapted from the Ishak (modified HAI) system [25]. Portal tract inflammation was graded numerically from 1 (none) to severe, affecting all portal tracts (5). Lobular inflammation was assessed at 10 × magnification and graded as 1 (none) to 4 (severe, typically averaging > 10 foci per 10 × field). Fatty liver disease grading, referred to as steatosis/steatohepatitis, was undertaken based on parameters assessed in the NAFLD activity score [26]. In short, steatosis was graded based on a visual estimate of the percentage of liver cells affected as 1 = none or < 5%; 2 = mild, (5–33%); 3 = moderate (34–66%) and 4 = severe (> 67%). Kidney analysis was undertaken following a similar approach assessing the glomerular cellularity, glomerular basement membrane, tubular vacuolation, interstitial inflammation, interstitial fibrosis, vessel integrity and the collecting system. Statistical analysis was undertaken using a Student's *t*-test where the $MagO_2$MB-RB/$MagO_2$MB-5FU group was compared directly with the 5-FU, RB and untreated groups.

3. Results and discussion

Magnetic microbubbles (MagMBs) were prepared by sonication of DBPC, DSPE-PEG(2000) and DSPE-PEG(2000)-biotin lipids in the presence of PFB gas and superparamagnetic iron oxide nanoparticles (NPs). The magnetic nanoparticle formulation comprised an iron oxide core with a lipid coating to facilitate incorporation of the magnetic nanoparticles into the MB shell. The PFB containing MagMBs (MagPFBMBs) produced had an average diameter of 1–2 μm with a concentration of approximately 1×10^9 MB/mL as determined by analysis of optical microscopy images (Fig. 1).

The iron content of the MagPFBMBs was also determined using atomic absorption spectroscopy and revealed the MBs contained 0.286 mg/10^9 MBs total iron content. Following isolation of the MagPFBMBs by centrifugation and surface coating with avidin, biotinylated Rose Bengal and biotinylated 5-FU were added to separate batches of the MagPFBMBs to generate Rose Bengal loaded MagPFBMBs (MagPFBMB-RB) and 5-FU loaded MagPFBMBs (MagPFBMB-5FU) respectively. The PFB core gas was then exchanged with oxygen by sparging with pure oxygen gas for 2 min generating the $MagO_2$MB-RB and $MagO_2$MB-5FU conjugates (Scheme 1).

To determine the magnetic response of the MB platform, suspensions of MagMBs (1 mL) were placed in a syringe and pumped through a flow chamber (0.6 mL/min) with a fixed magnet (0.46 T) positioned on the underside of the flow chamber during the course of the experiment. A control study was also performed in the absence of a fixed magnet but under otherwise identical conditions. The number of MBs retained in the flow cell at the end of each experiment were counted and the results are shown in Fig. 2. A significant increase in the number of MBs ($p < 0.01$) was observed when the fixed magnet was present indicating the ability of the MagMBs to be retained against flow using an external magnetic field. Blood flow rates within the human body vary considerably depending on vessel type and size with blood leaving the aorta (2400 cm min^{-1}) at a flow rate approximately 3 orders of magnitude greater than in capillaries (1.8 cm min^{-1}) [27]. In tumours, the increased viscous and geometrical resistance presented by the vasculature can compromise its blood flow, meaning the average velocity of

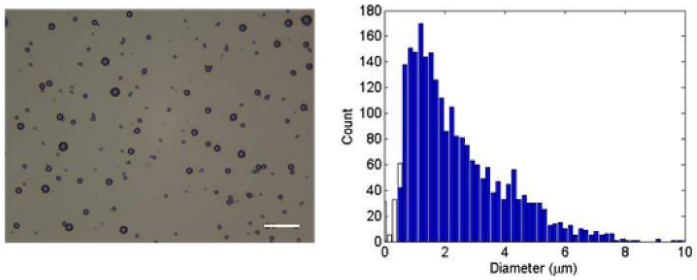

Fig. 1. (a) Photomicrograph taken with a 40× objective lens of MagMBs after centrifugation (300 RCF, 5 min) and after dilution (1:20) in PBS. Scale bar is 20 μm. (b) Size distribution of MagMBs obtained from analysis of 30 optical microscope images. White boxes on the left represent microbubbles detected by the image analysis software but smaller than 450 nm, the optical resolution of the system.

blood in tumour vessels can be an order of magnitude lower than in normal vessels [28]. Therefore, the flow rate used in the current study was towards the upper limit of rates chosen to study tumour perfusing resistivity which suggests that magnetic targeting may be effective in helping retain the MBs in the tumour vasculature and allowing a greater proportion to be destroyed in an applied acoustic field.

In order to retain a useful proportion (10%) of injected microbubbles at these blood flow rates, an estimated magnetic field gradient of 0.15 T/m would provide sufficient force to capture superparamagnetic particles flowing the capillary vessels [29]. When considering the possible translation of such technology to the clinic, both transabdominal and endoscopic sources are viable methods for the delivery of magnetic fields to the pancreas. In the context of the above capillary flow rates, optimized permanent magnet designs with a volume of 1.02 cm^3 [20] would be capable of targeting a tumour through the duodenal wall as part of an endoscopic probe, where the approximate distance to the head of the pancreas is in the region of 10 mm. In the case of transabdominal delivery, where the distances are more variable depending on the patient's body to mass index (BMI), the optimized permanent magnet volume would be in the region of 1.66 cm^3, based on a distance of 50 mm from the outside of the abdomen to the pancreas. Even at flow rates 5 times higher than the capillary flow rate used above, the estimated field gradient to retain the same fraction of

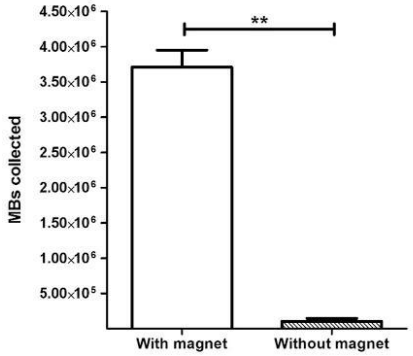

Fig. 2. Plot of MBs retained after injection through a flow-cell in the presence and absence of a fixed magnet.

MBs would be 2.48 T/m, requiring permanent magnet volumes in the region of 1.5 cm^3 for an endoscopic device, which is readily achievable [30]. Given endoscopic ultrasound (EUS) analysis is a common

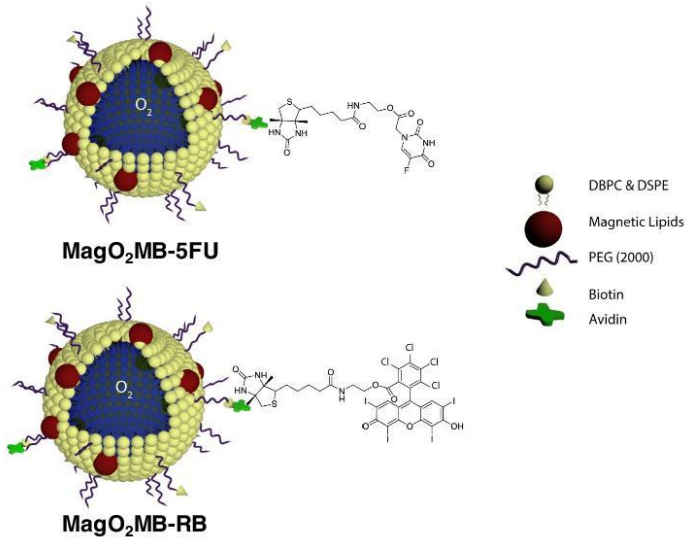

Scheme 1. Schematic representation of the $MagO_2$MB-5FU and $MagO_2$MB-RB conjugates.

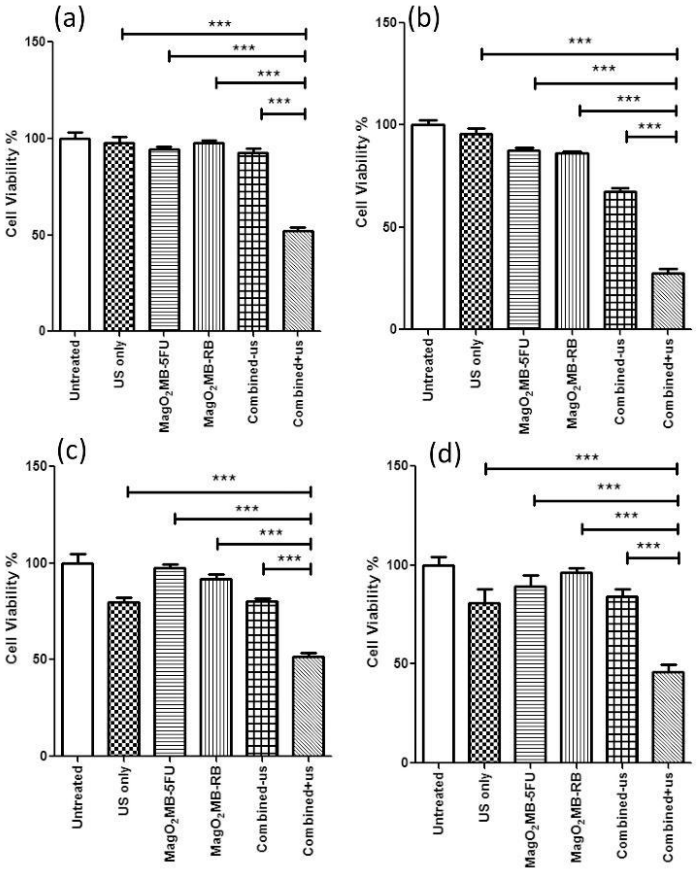

Fig. 3. Plot of % cell viability for (a) BxPC-3 (b) T110299 (c) MiaPaCa-2 and (d) Panc-01 after treatment with (i) untreated, (ii) ultrasound only (iii) $MagO_2$MB-5FU only (iv) $MagO_2$MB-RB only, (v) combined $MagO_2$MB-RB and $MagO_2$MB-5FU and (vi) combined $MagO_2$MB-RB and $MagO_2$MB-5FU plus ultrasound. ***$p < 0.001$ for (vi) compared to either (ii), (iii), (iv), or (v).

diagnostic tool used in staging pancreatic cancer, a EUS device configured to deliver both magnetic and ultrasonic fields is one possibility for the translation of this technology to clinic.

In a previous study, we demonstrated the benefit of combining Rose Bengal mediated SDT and 5-FU treatment, delivered using a non-magnetic O_2MB platform, for the treatment of pancreatic cancer [6]. In the current study, we were keen to ensure that the presence of redox active Fe(II) and Fe(III) in the MB shell, would not hamper the effectiveness of SDT or 5-FU treatment. Therefore, the next step was to determine the toxicity of the combined treatment in a panel of pancreatic cancer cell lines. Human pancreatic BxPC-3, MiaPaCa-2 and Panc-01 cells were chosen as targets in addition to the T110299 cell line [31]. The latter was isolated from a primary pancreatic tumour in the KPC model (Ptf1a-Cre; LSL-$Kras^{G12D}$ and Ptf1aCre; LSL-$Kras^{G12D}$; LSL-$Trp^{53fl/R172H}$ mice, respectively, that were back-crossed on a C57BL/6 background). The cells were seeded in 96 well plates and treated with a suspension of either $MagO_2$MB-5FU, $MagO_2$MB-RB or combined $MagO_2$MB-5FU/$MagO_2$MB-RB treatment in the presence of ultrasound. Untreated cells and cells treated with ultrasound only were used as controls.

The results are shown in Fig. 3 and reveal a significant reduction ($p < 0.001$) in cell viability for all cell lines that received combined SDT and 5-FU treatment with reductions > 50% relative to the untreated cells. In contrast, both the $MagO_2$MB-5FU and $MagO_2$MB-RB formulations demonstrated only minor reductions (< 10%) in the absence of ultrasound treatment meaning it was possible to control the generation of cytotoxicity using the ultrasound stimulus. Therefore, these results suggest that application of ultrasound not only disrupts the MBs releasing the encapsulated O_2 gas and the attached Rose Bengal/5-FU into the extracellular medium but also activates Rose Bengal leading to ROS generation and the observed cytotoxic effect [32]. It is also possible that application of the ultrasound could be enhancing the action of 5-FU by means of sonoporation. Indeed, it has been shown that this strategy can be employed to enhance the action of cancer chemotherapeutics by affording transient intracellular access of the drug via sonoporation [33].

While the in vitro cytotoxicity of the combined 5-FU/SDT treatment was encouraging, in vivo experiments are essential to identify the benefit of magnetic targeting. To this end, orthotopic human xenograft BxPC-3-Luc pancreatic tumours were established in SCID mice. Nineteen days following implantation the mice were randomly distributed into three groups (n = 4). Group 1 received no treatment; Group 2 received a $MagO_2$MB-5FU/$MagO_2$MB-RB suspension administered intravenously with the tumour region exposed to low-intensity ultrasound during and following injection for a total exposure of 3.5 min. Group 3 also received an IV injection of the $MagO_2$MB-5FU/$MagO_2$MB-RB suspension but in addition to ultrasound treatment, a

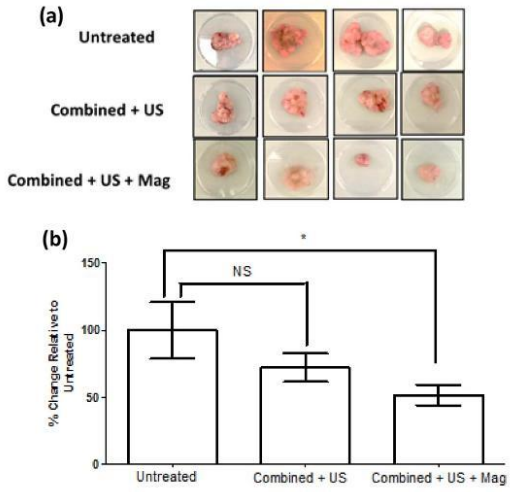

Fig. 4. (a) Photographs of orthotopic BxPC-3 Luc tumours removed from SCID mice 28 days following implantation after (i) no treatment (top), (ii) treatment with combined $MagO_2MB$-RB and $MagO_2MB$-FU plus ultrasound (middle) or (iii) treatment with $MagO_2MB$-RB and $MagO_2MB$-FU plus ultrasound and magnet (bottom). Treatments were administered on Day(s) 19, 20 and 21. (b) Plot of % change in tumour volume relative to untreated for mice treated with (ii) or (iii) above. *$p < 0.05$ for (iii) compared to (i). A one-way ANOVA, post-Hoc test showed the same significance as above.

permanent magnet was also directed at the tumour during ultrasound treatment (3.5 min). Treatments were repeated on Days 20 and 21 with the mice sacrificed on Day 28 [34]. This treatment schedule was determined on the basis of a previous pilot study where multiple treatments in close succession were shown to be beneficial over a single treatment. In addition, as our primary goal is to use this technology as a neo-adjuvant treatment to downstage tumours in advance of surgery, aggressive treatment of the tumours with three successive administrations was the preferred choice and as the technology is targeted, significantly lower concentrations of RB and 5-FU are used compared to standard systemic administration. Once the mice were sacrificed, the tumours were surgically excised and volumes determined with the results for the three groups shown in Fig. 4.

A statistically significant reduction in tumour volume of 48.3% ($p < 0.05$) was observed for Group 3 relative to control Group 1, while for Group 2 an obvious downward trend in tumour volume (27.9%) was detected although this was not found to be statistically significant. This improvement in efficacy in the presence of a magnetic field could be due to more MBs being retained in the tumour microenvironment, so that ultrasound exposure can enable enhanced deposition of MB payloads and subsequent activation of the sensitiser. Although the latter would require verification by further experimentation, our suggestion is corroborated by the observation that, activated caspase and BAX protein levels were both significantly elevated in tumours harvested from Group 3, when compared to expression of those proteins in tumours from either of the other 2 groups ($p < 0.05$) (Fig. 5).

Increases in activated caspase and BAX protein levels are indicative of increased apoptosis and consistent with the increased treatment efficacy observed for Group 3. Although BAX and caspase were not significantly increased in Group 2, a trend in tumour size reduction was observed for this group (Fig. 4). In addition, previous studies have shown that ectopic BxPC-3 tumours receiving the combined treatment in the absence of a magnetic field resulted in decreased tumour size and expressed markers for increased apoptosis [6]. Although significant differences exist in the manner in which this and the previous study

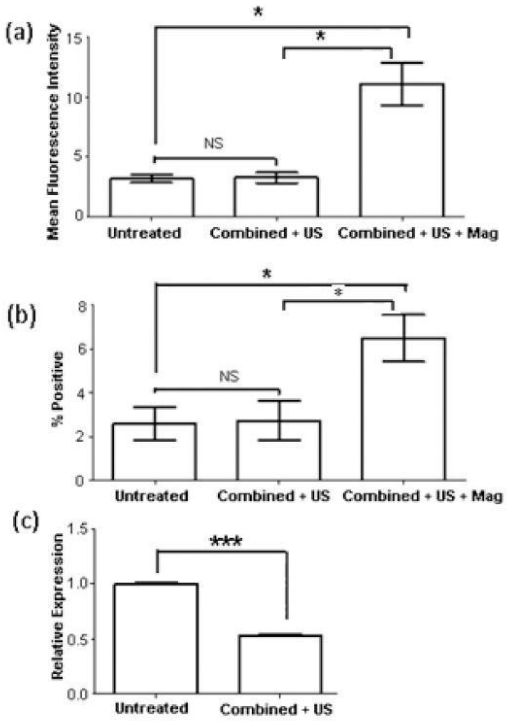

Fig. 5. (a) Plot showing presence of active caspase in single cell suspensions of tumours removed from SCID mice 38 days following implantation after treatment with (i) no treatment (left), (ii) treatment with combined $MagO_2MB$-RB and $MagO_2MB$-5FU plus ultrasound (middle) or (iii) treatment with $MagO_2MB$-RB and $MagO_2MB$-5FU plus ultrasound and magnet (right). Fluorescence indicates caspase activity which is reflective of apoptosis and was determined using the Pan Caspase probe (Pan Caspase NIR from Vergent Bioscience) via flow cytometry. Treatments were administered on Days 19, 20 and 21. (b) BAX protein expression of the same single cell suspensions via flow cytometry. *$p < 0.05$ for (iii) compared to (i). (c) Relative expression of TMBIM1 in untreated control tumours and those receiving combined treatment. ***$p < 0.001$.

were performed both from the perspective of the model type (orthotopic vs. ectopic) and that of the dosing regimen (multiple vs. single), it was felt that the reduction 'trend' observed in Group 2 in the current study (Fig. 4) warranted further consideration. To this end, we have been able to use qRT-PCR analysis to demonstrate that TMBIM1 (encoding transmembrane BAX inhibitor motif containing 1) was significantly downregulated in tumours receiving the combined treatment in the absence of a magnetic field (Fig. 5). Since TMBIM1 is an inhibitor of BAX [35], its down regulation in these tumours could lead to enhanced BAX-mediated apoptosis without an observable change in BAX concentration. However, the authors do realise that the data presented in Figs. 4 and 5 were derived from tumours removed at a specific time point (9 days) following treatment and these data may differ if longer or shorter time-points were chosen. Continuing studies will include a more in-depth examination of gene expression at various time points in order to more clearly elucidate the interplay between both of these genes and their role in treatment-induced apoptosis.

It was also found during the above studies that animals receiving the magnetically-responsive platform did not suffer any overt adverse effects and no significant change in body weight was observed over the course of the experiment (Fig. 6a). To investigate the aspect of safety

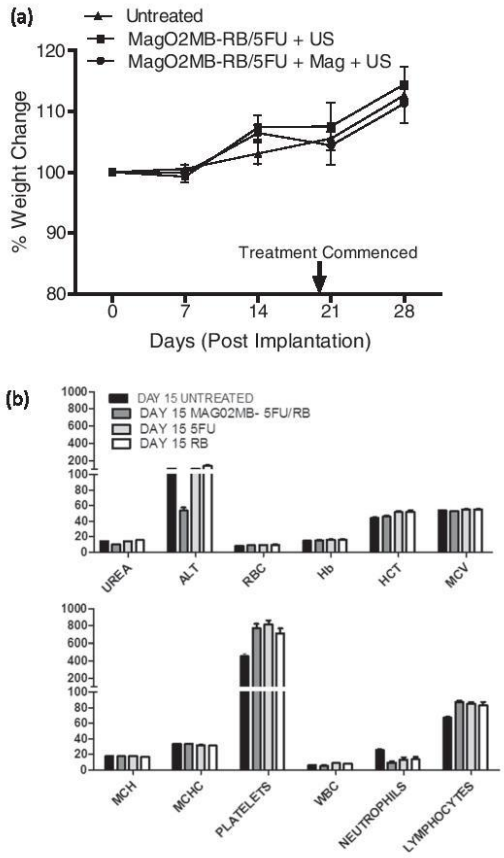

Fig. 6. (a) Average body weight of mice recorded following treatment with vehicle only (triangles), a suspension of $MagO_2$MB-RB/$MagO_2$MB-5FU + ultrasound (squares), or a suspension of $MagO_2$MB-RB/$MagO_2$MB-5FU + ultrasound + magnet (circles). (b) Whole blood and serum biochemistry analysis from healthy MF1 mice (i) untreated control, or treated with (ii) a suspension of $MagO_2$MB-RB/$MagO_2$MB-5FU, (iii) 5-FU alone, or (iv) RB alone.

further, a more detailed toxicology study was undertaken. This involved administering the $MagO_2$MB-5FU/$MagO_2$MB-RB suspension to 10 healthy non-tumour bearing MF1 mice by tail vein injection on Days 0 and 8. Similar experiments were undertaken involving MF1 mice treated with 5-FU or Rose Bengal alone at concentrations higher than those present on the MagMBs to reflect clinical doses, while untreated animals served as a control group. Blood samples were harvested from each group of animals on Day 15 and analysed for a range of key biochemical markers (Fig. 6b). No major differences in profile were observed between the $MagO_2$MB-5FU/$MagO_2$MB-RB group and the other groups that would raise any concern regarding toxicity of the combined MB-based treatment. Indeed ALT activity, which is a measure of liver function, was lower in the $MagO_2$MB-5FU/$MagO_2$MB-RB group compared to the other groups. While there was an increase in platelet and lymphocyte levels for the $MagO_2$MB-5FU/$MagO_2$MB-RB group relative to the untreated group, levels were also raised in 5-FU and Rose Bengal treated animals and the differences between these groups were not significant.

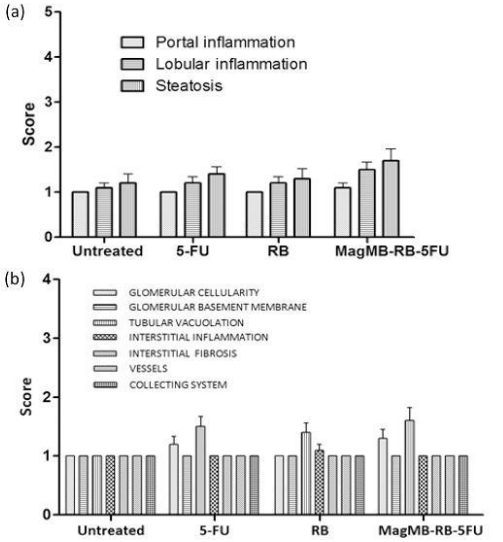

Fig. 7. Scoring for sections of (a) liver and (b) kidney following (i) no treatment, or treatment with (ii) 5-FU alone, (iii) RB alone, or (iv) a suspension of $MagO_2$MB-RB/$MagO_2$MB-5FU conjugates. Portal inflammation scored 1–5 while all other parameters were scored from 1 to 4. In each case a score of 1 = normal.

Similarly, there was evidence of mild neutropenia in the three treatment groups relative to the untreated group, but again the difference between the $MagO_2$MB-5FU/$MagO_2$MB-RB group and the 5-FU and RB groups was not significant. Furthermore, histological analysis of liver and kidney sections removed post-mortem on Day 16 also revealed no significant changes between the $MagO_2$MB-5FU/$MagO_2$MB-RB group and the 5-FU or RB treated groups (Fig. 7).

There was evidence of a slight increase in liver steatosis score for the $MagO_2$MB-5FU/$MagO_2$MB-RB group but this was not significant when compared to the 5-FU or RB groups. Liver steatosis, also known as fatty liver disease, is normally a consequence of dietary or lifestyle habits but can also be influenced by certain chemotherapeutic drugs including antimetabolites [36]. The slight increase in score for the $MagO_2$MB-5FU/$MagO_2$MB-RB group relative to 5-FU or RB may be due to the uptake and metabolism of the lipid component of the MBs and on that basis is likely a transient change of limited clinical significance. Analysis of kidney sections showed slightly raised levels of glomerular cellularity and tubular vacuolation for the $MagO_2$MB-5FU/$MagO_2$MB-RB group, but again these levels were also raised in the 5-FU and RB groups and the differences were non-significant. Some of the tubular vacuolation may have been artefactual, possibly fixation related, as it was observed in both treated and untreated groups. It must be stressed, however, that any effect observed in the liver or kidney histology analysis was deemed to be mild and in no case did the mean score exceed 2. Collectively, these results indicate the potential of O_2MagMBs as a safe and effective platform for the delivery of combined antimetabolite and SDT treatment of pancreatic cancer (Fig. 8).

4. Conclusions

Magnetically responsive MBs were successfully prepared and shown to be retained at a target site in the presence of an externally applied magnetic field. When decorated with the sensitiser Rose Bengal and the antimetabolite 5-FU, the $MagO_2$MB conjugates produced reductions of > 50% in the viability of four pancreatic cancer cell lines upon

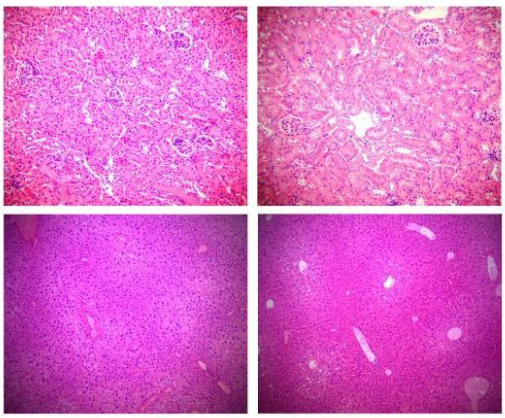

Fig. 8. Representative H & E stained microscope images of liver (top) and kidney (bottom) sections taken from animals sacrificed on Day 15 following treatment with a suspension of $MagO_2$MB-RB/$MagO_2$MB-5FU (right) or untreated (left).

exposure to relatively low intensity ultrasound. The combined application of external magnetic and ultrasound fields during IV delivery of the $MagO_2$MB conjugates resulted in a 48.3% reduction in orthotopic pancreatic tumour volumes 9 days after treatment relative to the control group, while the application of ultrasound alone resulted in a reduction of only 27.9%. In addition, a significant increase in apoptosis was observed in tumours that were treated with the MagMB conjugates and exposed to both magnetic and ultrasonic fields when compared to the ultrasound alone or untreated groups. These results highlight the potential of using a combination of magnetic and ultrasonic fields to retain and disrupt MBs in the tumour vasculature. The results also confirm the effectiveness of combined sonodynamic/antimetabolite therapy delivered using the $MagO_2$MB platform as a safe, highly targeted and efficacious treatment for pancreatic cancer.

Acknowledgements

JFC thanks Norbrook Laboratories Ltd. for an endowed chair. ES and JO thank the Engineering and Physical Sciences Research Council for support through grant EP/I021795/1. EB thanks the Research Councils UK Digital Economy Programme for support through grant EP/G036861/1 (Oxford Centre for Doctoral Training in Healthcare Innovation). We also thank Prof. Jens Siveke at Medizinische Klinik; Klinikum rechts der Isar; Technische Universität München; Munich, Germany for the KPC cell line. We acknowledge Dangoor Education for their supporting RH in this work.

References

[1] S. Badger, J. Brant, C. Jones, J. McClements, M. Loughrey, M. Taylor, T. Diamond, L. McKie, The role of surgery for pancreatic cancer: a 12-year review of patient outcome, Ulster Med. J. 79 (2010) 70–75.
[2] J. Li, M.G. Wientjes, J.L. Au, Pancreatic cancer: pathobiology, treatment options, and drug delivery, AAPS J. 12 (2010) 223–232.
[3] M.H. Katz, P.W. Pisters, D.B. Evans, C.C. Sun, J.E. Lee, J.B. Fleming, J.N. Vauthey, E.K. Abdalla, C.H. Crane, R.A. Wolff, Borderline resectable pancreatic cancer: the importance of this emerging stage of disease, J. Am. Coll. Surg. 206 (2008) 833–846.
[4] M. Tachezy, F. Gebauer, C. Petersen, D. Arnold, M. Trepel, K. Wegscheider, P. Schafhausen, M. Bockhorn, J.R. Izbicki, E. Yekebas, Sequential neoadjuvant chemoradiotherapy (CRT) followed by curative surgery vs. primary surgery alone for resectable, non-metastasized pancreatic adenocarcinoma: NEOPA-a randomized multicenter phase III study (NCT01900327, DRKS00003893, ISRCTN82191749), BMC Cancer 14 (2014) 1.
[5] C. Hamill, SBRT pre-operatively for borderline resectable pancreatic cancer, UK Clinical Trials Gateway website, 2014 (Study ID Numbers:OCTO_054).
[6] C. McEwan, S. Kamila, J. Owen, H. Nesbitt, B. Callan, M. Borden, N. Nomikou, R.A. Hamoudi, M.A. Taylor, E. Stride, Combined sonodynamic and antimetabolite therapy for the improved treatment of pancreatic cancer using oxygen loaded microbubbles as a delivery vehicle, Biomaterials 80 (2016) 20–32.
[7] S. Sirsi, M. Borden, Microbubble compositions, properties and biomedical applications, Bubble Sci. Eng. Technol. 1 (2009) 3–17.
[8] V. Stewart, P. Sidhu, New directions in ultrasound: microbubble contrast, Br. J. Radiol. 79 (2006) 188–194.
[9] G. Dimcevski, S. Kotopoulis, T. Bjånes, D. Hoem, J. Schjøtt, B.T. Gjertsen, M. Biermann, A. Molven, H. Sorbye, E. McCormack, A human clinical trial using ultrasound and microbubbles to enhance gemcitabine treatment of inoperable pancreatic cancer, J. Control. Release 243 (2016) 172–181.
[10] S. Kotopoulis, G. Dimcevski, O. Helge Gilja, D. Hoem, M. Postema, Treatment of human pancreatic cancer using combined ultrasound, microbubbles, and gemcitabine: a clinical case study, Med. Phys. 40 (2013).
[11] S. Umemura, N. Yumita, R. Nishigaki, K. Umemura, Mechanism of cell damage by ultrasound in combination with hematoporphyrin, Jap. J. Cancer Res. 81 (1990) 962–966.
[12] H. Chen, J.H. Hwang, Ultrasound-targeted microbubble destruction for chemotherapeutic drug delivery to solid tumors, J. Therapeutic Ultrasound 1 (2013) 1.
[13] S. Hernot, A.L. Klibanov, Microbubbles in ultrasound-triggered drug and gene delivery, Adv. Drug Deliv. Rev. 60 (2008) 1153–1166.
[14] M.M.A. Valenzuela, J.W. Neidigh, N.R. Wall, Antimetabolite treatment for pancreatic cancer, Chemotherapy 3 (2014).
[15] D. Costley, C. Mc Ewan, C. Fowley, A.P. McHale, J. Atchison, N. Nomikou, J.F. Callan, Treating cancer with sonodynamic therapy: a review, Int. J. Hyperth. 31 (2015) 107–117.
[16] N. Nomikou, C. Fowley, N.M. Byrne, B. McCaughan, A.P. McHale, J.F. Callan, Microbubble–sonosensitiser conjugates as therapeutics in sonodynamic therapy, Chem. Commun. 48 (2012) 8332–8334.
[17] C. McEwan, J. Owen, E. Stride, C. Fowley, H. Nesbitt, D. Cochrane, C.C. Coussios, M. Borden, N. Nomikou, A.P. McHale, Oxygen carrying microbubbles for enhanced sonodynamic therapy of hypoxic tumours, J. Control. Release 203 (2015) 51–56.
[18] Y. Gao, C.U. Chan, Q. Gu, X. Lin, W. Zhang, D.C.L. Yeo, A.M. Alsema, M. Arora, M.S.K. Chong, P. Shi, Controlled nanoparticle release from stable magnetic microbubble oscillations, NPG Asia Mater. 8 (2016) e260.
[19] J. Owen, P. Rademeyer, D. Chung, Q. Cheng, D. Holroyd, C. Coussios, P. Friend, Q.A. Pankhurst, E. Stride, Magnetic targeting of microbubbles against physiologically relevant flow conditions, Interface Focus 5 (2015) 20150001.
[20] C. Crake, J. Owen, S. Smart, C. Coviello, C. Coussios, R. Carlisle, E. Stride, Enhancement and passive acoustic mapping of cavitation from fluorescently tagged magnetic resonance-visible magnetic microbubbles in vivo, Ultrasound Med. Biol. 42 (2016) 3022–3036.
[21] J. Ciccolini, C. Mercier, M. Blachon, R. Favre, A. Durand, B. Lacarelle, A simple and rapid high-performance liquid chromatographic (HPLC) method for 5-fluorouracil (5-FU) assay in plasma and possible detection of patients with impaired dihydropyrimidine dehydrogenase (DPD) activity, J. Clin. Pharm. Ther. 29 (2004) 307–315.
[22] L.C. Barnsley, D. Carugo, J. Owen, E. Stride, Halbach arrays consisting of cubic elements optimised for high field gradients in magnetic drug targeting applications, Phys. Med. Biol. 60 (2015) 8303.
[23] A. McHale, L. McHale, Use of a tetrazolium based colorimetric assay in assessing photoradiation therapy in vitro, Cancer Lett. 41 (1988) 315–321.
[24] L.C. Barnsley, D. Carugo, E. Stride, Optimized shapes of magnetic arrays for drug targeting applications, J. Phys. D 49 (2016) 225501.
[25] K. Ishak, A. Baptista, L. Bianchi, F. Callea, J. De Groote, F. Gudat, H. Denk, V. Desmet, G. Korb, R.N. MacSween, Histological grading and staging of chronic hepatitis, J. Hepatol. 22 (1995) 696–699.
[26] D.E. Kleiner, E.M. Brunt, M. Van Natta, C. Behling, M.J. Contos, O.W. Cummings, L.D. Ferrell, Y. Liu, M.S. Torbenson, A. Unalp-Arida, Design and validation of a histological scoring system for nonalcoholic fatty liver disease, Hepatology 41 (2005) 1313–1321.
[27] E.N. Marieb, K. Hoehn, The cardiovascular system: blood vessels, human anatomy, Physiology (2013) 703–720.
[28] R.K. Jain, T. Stylianopoulos, Delivering nanomedicine to solid tumors, Nat. Rev. Clin. Oncol. 7 (2010) 653–664.
[29] L.C. Barnsley, D. Carugo, M. Aron, E. Stride, Understanding the dynamics of superparamagnetic particles under the influence of high field gradient arrays, Phys. Med. Biol. 62 (2017) 2333.
[30] T. Krings, J. Finney, P. Niggemann, P. Reinacher, N. Lück, A. Drexler, J. Lovell, A. Meyer, R. Sehra, P. Schauerte, Magnetic versus manual guidewire manipulation in neuroradiology: in vitro results, Neuroradiology 48 (2006) 394–401.
[31] P. Duewell, E. Beller, S.V. Kirchleitner, T. Adunka, H. Bourhis, J. Siveke, D. Mayr, S. Kobold, S. Endres, M. Schnurr, Targeted activation of melanoma differentiation-associated protein 5 (MDA5) for immunotherapy of pancreatic carcinoma, Oncoimmunology 4 (2015) e1029698.
[32] We have previously demonstrated in Ref 6 the effects of combined RB and 5-FU treatment (5 μM and 100 μM respectively) as free agents (i.e. not as MB conjugates) to cause between 20–30% reduction in viability in BxPC-3, MiaPaCa-2 and Panc-01 cell lines.
[33] N. Nomikou, A.P. McHale, Exploiting ultrasound-mediated effects in delivering targeted, site-specific cancer therapy, Cancer Lett. 296 (2010) 133–143.
[34] The treatment schedule and termination date was informed by an earlier pilot study and supported by bioluminescent imaging.
[35] D.A. Lisak, T. Schacht, V. Enders, J. Habicht, S. Kiviluoto, J. Schneider, N. Henke, G. Bultynck, A. Methner, The transmembrane Bax inhibitor motif (TMBIM) containing protein family: tissue expression, intracellular localization and effects on the ER CA 2 - filling state, Biochim. Biophys. Acta (BBA)-Mol. Cell Res. 1853 (2015) 2104–2114.
[36] K. Miyake, K. Hayakawa, M. Nishino, T. Morimoto, S. Mukaihara, Effects of oral 5-fluorouracil drugs on hepatic fat content in patients with colon cancer 1, Acad. Radiol. 12 (2005) 722–727.

Appendix 2: This paper is related to chapter 5.

Journal of Controlled Release 264 (2017) 333–340

Contents lists available at ScienceDirect

Journal of Controlled Release

journal homepage: www.elsevier.com/locate/jconrel

Oxygen generating nanoparticles for improved photodynamic therapy of hypoxic tumours

Yingjie Sheng[a], Heather Nesbitt[a], Bridgeen Callan[a], Mark A. Taylor[b], Mark Love[c], Anthony P. McHale[a,*], John F. Callan[a,*]

[a] Biomedical Sciences Research Institute, University of Ulster, Coleraine, Northern Ireland BT52 1SA, UK
[b] Department of HPB Surgery, Mater Hospital, Belfast, Northern Ireland BT14 6AB, UK
[c] Imaging Centre, The Royal Victoria Hospital, Grosvenor Road, Belfast, Northern Ireland BT12 6BA, UK

ARTICLE INFO

Keywords:
Hypoxia
Calcium peroxide
Photodynamic therapy
Pancreatic cancer

ABSTRACT

Photodynamic therapy (PDT) is a clinically approved anti-cancer treatment that involves the activation of an otherwise inactive sensitiser drug with light, which in the presence of molecular oxygen, generates cytotoxic reactive oxygen species (ROS). As oxygen is a key requirement for the generation of ROS in PDT and given the fact that hypoxia is a characteristic of most solid cancerous tumours, treating hypoxic tumours using PDT can be a challenge. In this manuscript, we have prepared a CaO_2 nanoparticle (NP) formulation coated with a pH-sensitive polymer to enable the controlled generation of molecular oxygen as a function of pH. The polymer coat was designed to protect the particles from decomposition while in circulation but enable their activation at lower pH values in hypoxic regions of solid tumours. The oxygen generating capability of the polymer coated NPs was demonstrated in aqueous solution with minimal oxygen produced at pH 7.4, whereas it increased significantly when the pH was reduced to 6.2. The polymer coated CaO_2 NPs were also observed to significantly increase tumour pO_2 levels ($p < 0.05$) in mice bearing ectopic human xenograft MIA PaCa-2 pancreatic tumours with an average increase in tumour pO_2 of 6.5 mm Hg in the period 10–30 min following administration. A statistically significant improvement in PDT mediated efficacy ($p < 0.001$) was also observed when the particles were administered to mice bearing the same tumours 20 min prior to PDT treatment. These results suggest that the polymer coated CaO_2 NP formulation offers significant potential as an *in situ* method for oxygen generation to enhance the efficacy of treatments that depend on the presence of oxygen to elicit a cytotoxic effect.

1. Introduction

Photodynamic therapy (PDT) is a cancer treatment that involves irradiating a photoactive drug with light, in the presence of molecular oxygen, to generate toxic levels of reactive oxygen species (ROS) ultimately resulting in cell death [1]. By carefully controlling light delivery to the target lesion, ROS generation can be localised with high precision in three dimensions sparing healthy surrounding tissue. While the targeted nature of PDT remains its greatest attraction, the technique is significantly limited by the inability of light to penetrate deeply through human tissue [2]. This has restricted PDT to the treatment of superficial lesions and hindered its ability to treat larger solid tumours. The development of near-infrared (NIR) absorbing sensitisers and the emergence of sonodynamic therapy (SDT) promise to overcome this limitation by enabling the activation of sensitisers at greater depths *in vivo* [3]. Combatting hypoxia presents another challenge in the treatment of solid tumours using PDT/SDT as oxygen is a key requirement for the generation of ROS. This is particularly true for tumours of the pancreas [4] and hypoxia is now recognised as an indicator of poor prognosis for many types of cancer [5,6]. Inefficient gas and mass transfer resulting from atypical vascularisation together with elevated oxygen demand by hyper-proliferating tissues results in hypoxia in most solid tumours. Once a hypoxic environment develops in the tumour, cell populations become resistant to many conventional cancer chemotherapeutic agents through a variety of adaptive survival mechanisms. Similarly, for radiotherapy, oxygen has been shown to play a very significant role in enhancing radiation induced damage to nucleic acid in target tissues [7]. One of the major challenges associated with the latter has been to provide oxygen to the target tissues during therapy. A number of approaches have been employed including, hyperbaric oxygen breathing and breathing pure oxygen or carbogen at atmospheric pressure [8]. Such approaches, however, have delivered limited success and there is still a significant un-met need in this area. We have recently demonstrated that the selective destruction of oxygen loaded

* Corresponding authors.
E-mail addresses: ap.mchale@ulster.ac.uk (A.P. McHale), j.callan@ulster.ac.uk (J.F. Callan).

http://dx.doi.org/10.1016/j.jconrel.2017.09.004
Received 2 July 2017; Received in revised form 28 August 2017; Accepted 1 September 2017
Available online 08 September 2017

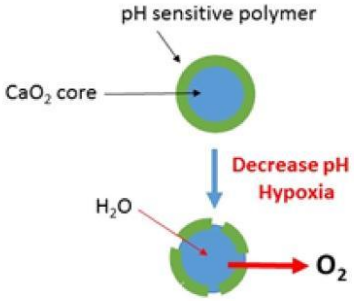

Scheme 1. Schematic illustration of how the polymer coat (green) protects the nanoparticle core (blue) from its aqueous environment at normal pH but at lower pH, the polymer coat dissolves, allowing access to the core by water with the resulting generation of oxygen.

microbubbles in the tumour microenvironment using low intensity ultrasound provided a temporary boost in tumour oxygen levels that enhanced the sonodynamic therapy (SDT) treatment of pancreatic tumours [9]. Inspired by these results, we are also focusing on the development of *in situ* oxygen generating nanoparticles as an alternative method to improve tumour oxygenation during PDT.

In this manuscript, we describe the preparation and characterisation of calcium peroxide (CaO_2) nanoparticles that generate molecular oxygen upon decomposition in water. The nanoparticles were coated with a pH-responsive methacrylate based *co*-polymer containing a tertiary amine residue that protects the nanoparticle core from water at pH values above 7.4. At lower pH values, the tertiary amine unit ionises resulting in dissolution of the polymer coat and exposure of the nanoparticle core to the aqueous environment resulting in oxygen generation (Scheme 1).

Tumour tissue interstitial fluid is more acidic (pH = ~6.0) than normal tissue, as hypoxia results in the accumulation of acid by inducing the production of energy from glycolysis *via* the Pasteur effect [10]. This difference in pH has been utilised in numerous pH-responsive cancer therapeutics and diagnostic probes [11]. Here, the pH-responsive polymer coat will limit NP decomposition in the blood and normal tissue while facilitating its decomposition in more acidic cancer tissue. The ability of the resulting oxygen generation to improve oxygenation in hypoxic environments and enhance the PDT-mediated treatment of BxPC-3 pancreatic cancer cells *in vitro* and human xenograft MIA-PaCa-2 pancreatic tumours *in vivo* is demonstrated.

2. Materials and methods

2.1. Reagents and equipment

Calcium chloride, PEG 200, 1 M ammonia solution, 35% hydrogen peroxide, sodium hydroxide, phosphate buffered saline (PBS), luminol, methanol, ethanol, hexane, chloroform, Rose Bengal (RB), singlet oxygen sensor green (SOSG), anhydrous tetrahydrofuran (THF), 2-(dimethylamino)ethyl methacrylate, methyl methacrylate, ethyl acrylate and 1,1′-Azobis(cyclohexanecarbonitrile) (ABCN) were purchased from commercial sources at the highest possible grade. BxPC-3 and MIA PaCa cells were obtained from the American Type Culture Collection (ATCC) and matrigel from BD Biosciences, Erembodegem, Belgium. SCID mice (C.B-17/IcrHanHsd-Prkdc^{SCID}) were bred in house. Scanning electron microscopy (SEM) analysis was conducted using an "FEI Quanta" scanning electron microscope while dynamic light scattering (DLS) measurements were performed using a Malvern Zetasizer 3000HSA (Malvern, Worcs., UK). Dissolved oxygen measurements were recorded using a Thermo Scientific™ DO Probe Orion™ 083005MD (Fisher Scientific, Ottawa, ON, Canada) while nanoparticle solutions were mixed using a Silverson homogenizer (Silverson Machines Ltd., Chesham, U.K.). Fluorescence measurements were undertaken using a Cary Eclipse spectrophotometer while 96 well plates were analysed using a Fluostar Omega plate reader. Tumour pO_2 measurements were performed using an Oxylite oxygen electrode sensor (Oxford Optronics, Oxford, UK). NMR spectra were obtained on Varian 500 MHz instrument at 25.0 ± 1 °C and processed using Bruker software. Mass spectra were obtained using a Finnegan LCQ-MS instrument. Error in measurements was expressed as % standard error of the mean while statistical analysis was undertaken using 2-tailed Students *t*-test.

2.2. Preparation of uncoated CaO_2 NPs

CaO_2 nanoparticles were prepared following the method described by Khodaveisi et al. [12] Ammonia solution (15.0 mL, 1 M) and PEG 200 (120.0 mL, 0.6744 mol) was added to a stirred solution of calcium chloride (3.0 g, 0.027 mol) in distilled water (30 mL). A solution of 35% H_2O_2 (15 mL, 0.17 mol) was then added to the mixture at a rate of 3 drops per minute and the colourless solution stirred for a further 2 h at room temperature. A NaOH solution (0.1 M) was then added until a pH value of 11.5 was achieved when the solution changed to a white coloured suspension. The precipitate was separated by centrifugation (8000 g, 5 min) and the resulting pellet washed three times with NaOH (25 mL, 0.1 M). The precipitate was then washed with distilled water until the filtrate pH reached 8.4 and the resulting solid dried *in vacuo* at 80 °C for 2 h. The resulting particles were suspended in ethanol and sonicated for 5 min. The suspension was passed through a Millex Filter Unit (0.45 μm) to isolate larger particles and the filtrate concentrated to dryness providing the uncoated CaO_2 nanoparticles as a white powder. The size of the nanoparticles was determined by SEM and DLS.

2.3. Determination of CaO_2 content in the uncoated CaO_2 NPs

The active CaO_2 content of the NPs was determined by reaction with luminol in PBS. A chemiluminescence/concentration calibration curve for the reaction of H_2O_2 with luminol was performed according to the procedure adopted by Komagoe et al. [13] CaO_2 NPs suspended in ethanol (50 μL, 35.6 μM) were added to a luminol solution (50 μL, 10 mg/mL in PBS) and the luminescence intensity determined using a plate reader. The CaO_2 content was determined by indirectly measuring the number of moles of H_2O_2 produced (by reference to a calibration graph) from the fixed mass of CaO_2 powder and assuming all the available CaO_2 was converted to H_2O_2.

2.4. Determination of singlet oxygen generation

The ability of the CaO_2 NPs to enhance PDT mediated singlet oxygen generation was determined using the singlet oxygen probe SOSG. CaO_2 NPs (2 mg) in de-oxygenated ethanol (1 mL) were added to a de-oxygenated PBS solution containing SOSG and RB resulting in final concentrations of 2.5 μM (SOSG), 5.0 μM (RB) and 35.6 μM (CaO_2 NPs). The solutions were then exposed to white light for 5 min (Fenix LD01 LED,50 mW output,113.0 J/cm^2) Control experiments were also undertaken and included (i) CaO_2 NP + light and (ii) RB + light. The intensity of SOSG fluorescence at 525 nm upon excitation at 505 nm was recorded at the beginning and at the end of each experiment.

2.5. In vitro PDT experiments

BxPc3 cells were seeded in a 96 well plate at a density of 5×10^4 cells per well and incubated in a hypoxic chamber at 37 °C ($O_2/CO_2/N_2$, 0.1: 5: 94.9, v/v/v) for 3 h. The cells were then treated with either (i) RB or (ii) RB with CaO_2 NPs to reach a final concentration per well of 1 μM (RB) and 25 μM (CaO_2) respectively. The CaO_2 NPs were initially prepared in EtOH that was diluted 1:1 v/v with PBS (100 μL total

volume) immediately before addition to wells containing 100 μL media leading to a total EtOH concentration of 25% v/v. Control wells containing untreated cells or cells treated with vehicle alone (*i.e.* EtOH/PBS 1:1 v/v 100 μL) were undertaken for comparative purposes. The cells were allowed to incubate with the drug/NPs/vehicle for 5 min, the medium was then removed and replaced with fresh media. The cells were then exposed to white light treatment for 30 s (Fenix LD01 LED,50 mW output,11.3 J/cm^2). Following light treatment cells were incubated for a further 3 h in the hypoxic chamber and then for a further 24 h under normoxic conditions in a humidified 5% CO_2 atmosphere at 37 °C. Cell viability was then determined using a MTT assay.

2.6. Preparation of polymer 1

2-(Dimethylamino)ethyl methacrylate (157.2 mg, 1 mmol), methyl methacrylate (100.1 mg, 2 mmol) and ethyl acrylate (100.1 mg, 1 mmol) and a catalytic amount of the free radical initiator (ABCN) were dissolved in anhydrous THF (5 mL) and placed in a Carious reaction vessel. The contents were then subjected to three freeze-pump-thaw cycles, sealed under vacuum and placed in a Carious oven at 80 °C for 72 h. The contents were removed and hexane (20 mL) added to the facilitate precipitation followed by centrifugation for 5 min at 3500 g. The supernatant was removed, the pellet containing **1** re-dissolved in anhydrous THF, precipitated again using hexane and centrifuged at 3743 × *g*. This purification procedure was repeated twice further before the pellet was dried *in vacuo* at 80 °C and characterised by ^{1}H NMR spectroscopy.

2.7. Coating of CaO_2 NPs with polymer 1 to form 1-CaO_2 NPs

CaO_2 NPs were coated with **1** using a modified single emulsion method [14]. CaO_2 NPs (10 mg) were dispersed in hexane (10 mL) and sonicated for 5 min. The NP suspension was then added dropwise at a rate of 2 mL/min to a solution of **1** (100 mg, 0.36 μmol) in ethanol (40 mL) using a Silverson homogenizer at 8000g for 5 min to ensure efficient mixing. After a further mixing period of 6 h, excess solvent was allowed to slowly evaporate and the **1**-CaO_2 NPs reconstituted in sterile water. Particle size was then determined using SEM and DLS.

2.8. Dissolved oxygen experiments

For the dissolved oxygen experiments involving the uncoated CaO_2 NPs, an ethanol solution containing the NPs (10.0 mg, 24 mmol) was added to 10 mL of de-oxygenated PBS solvent. The dissolved oxygen was then measured and recorded every minute using a dissolved oxygen meter. For dissolved oxygen experiments involving the **1**-CaO_2 NPs, separate solutions of de-oxygenated water were pH adjusted to pH 7.4 or 6.2. The **1**-CaO_2 NPs (2 mg) were then added to each solution and the dissolved oxygen measured using a dissolved oxygen meter 3 min following addition. Results were compared against identical solutions in the absence of **1**-CaO_2 NPs. Both sets of experiments were repeated in triplicate.

2.9. Solubility of 1-CaO_2 NPs with change in pH

The pH of an aqueous suspension containing **1**-CaO_2 NPs (2 mg in 10 mL) was lowered from pH 7.4 to pH 6.2 in approximate 0.1 pH increments following the addition of very small aliquots of 0.1 M HCl. Photographs of the resulting suspensions/solutions were taken at pH 7.4, 6.9 and 6.2.

2.10. Determination of tumour pO_2

All animals employed in this study were treated humanely and in accordance with licenced procedures under the UK Animals (Scientific Procedures) Act 1986. The ability of the **1**-CaO_2 NPs to influence tumour hypoxia was examined in a mouse xenograft tumour model of human pancreatic cancer. MIA PaCa-2 cells were maintained in RPMI-1640 medium supplemented with 10% foetal calf serum. Cells were cultured at 37 °C under 5% CO_2 in air. The cells (5×10^6) were re-suspended in 100 μL of Matrigel® (BD Biosciences, Erembodegem, Belgium) and implanted subcutaneously into the rear dorsum of male SCID mice. Tumour formation occurred approximately 5 weeks after implantation and tumour measurements were taken every other day using callipers. Once the tumours had reached an average volume of 254 ± 17 mm^3 calculated from the geometric mean diameter using the equation tumour volume = (W ∗ H ∗ L/2), animals were randomly distributed into two groups (n = 3): (i) **1**-CaO_2 NPs and (ii) vehicle only. Following induction of anaesthesia *via* intraperitoneal injection of Hyponym/Hypnovel (150 μL, i.p) of a mixture of 2:1:1; PBS: Hypnorm (0.315 mg/mL fentanyl citrate and fluanisone 10 mg/mL, VetaPharma Ltd., U.K.): Hypnovel (10 mg/mL midazolom, Roche, UK), the oxygen partial pressure (pO_2) of tumours was recorded using an Oxylite oxygen electrode sensor. A fibre optic probe was inserted into a 21-gauge needle before insertion into the centre of the tumour tissue. The needle was withdrawn and the probe readings allowed to stabilise for 5 min. The pO_2 in the tumours was recorded every second for 20 min. 100 μL aliquots of **1**-CaO_2 NPs in a PBS vehicle (2 mg/mL) or PBS alone were administered to the respective groups by tail-vein injection with pO_2 recorded every second for a further 40 min. This time period was chosen to avoid the need for re-administering anaesthesia.

2.11. Effect of 1-CaO_2 NPs on PDT efficacy in vivo

Mia-PaCa 2 xenograft tumours were established as described above. Once the tumours had reacted an average volume of 254 ± 17 mm^3 the mice were randomly separated into 4 groups (n = 5). Group 1 involved untreated animals, group 2 the PDT only group, Group 3 the **1**-CaO_2 NPs only group and group 4 the PDT + **1**-CaO_2 NPs group. For group 2 mice received an intratumoural injection (100 μL) of Rose Bengal (0.1 mg/mL) in a PBS solvent and the tumour was then exposed to a LED-based white light source for 3 × 3 min treatments (Fenix LD01 LED,50 mW output,205 J/cm^2) with a 1 min interval between each treatment. Group 3 received a tail vein injection (100 μL) of **1**-CaO_2 NPs in a PBS vehicle (2 mg/mL) while group 4 also received a tail vein injection (100 μL) of **1**-CaO_2 NPs in a PBS vehicle (2 mg/mL) in addition to an intratumoural injection (100 μL) of Rose Bengal (0.1 mg/mL) and light exposure administered 20 min after NP injection using the same conditions as described for group 2. The tumour volume was measured daily over the course of 6 days using callipers.

3. Results and discussion

CaO_2 NPs were prepared following a hydrolysis-precipitation procedure similar to that developed by J. Khodaveiside et al. that utilised $CaCl_2$ as a calcium precursor and polyethylene glycol 200 (PEG200) as a surface modifier. The resulting particles were analysed by SEM and found to be spherical in shape with an average diameter of 116.0 ± 7.6 nm (Fig. 1a). However, closer inspection of the particle morphology revealed the appearance of several smaller particles coalesced together to form the larger sized NPs. This was confirmed when an ethanol solution containing the NPs was analysed using DLS where the particle diameter was found to be much smaller at 21.0 nm ± 11 nm. (Fig. 1b). The amount of active CaO_2 contained within the NP powder was determined by measuring the luminescence generated when a fixed amount of the NP powder was dissolved in an aqueous luminol solution. The hydrogen peroxide generated from the reaction of CaO_2 with the aqueous medium (Eq. 1) subsequently reacts quantitatively with luminol to produce a chemiluminescence signal that is proportional to the amount of hydrogen peroxide present [15].

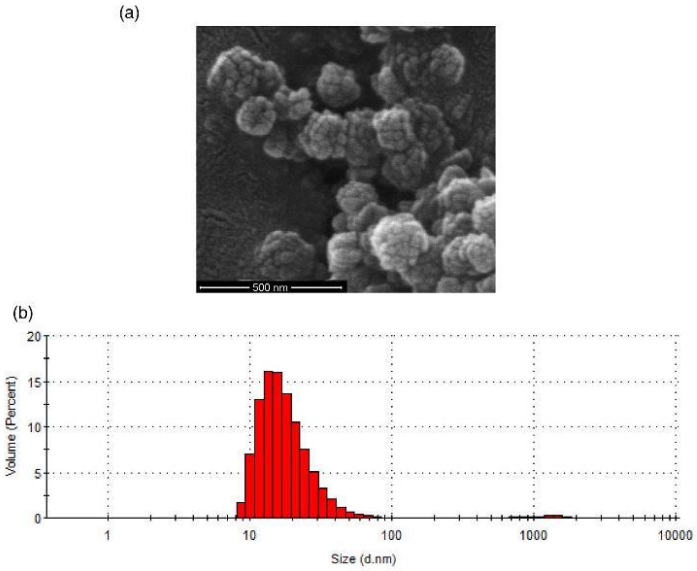

Fig. 1. (a) Representative SEM image and (b) DLS plot of CaO_2 NPs.

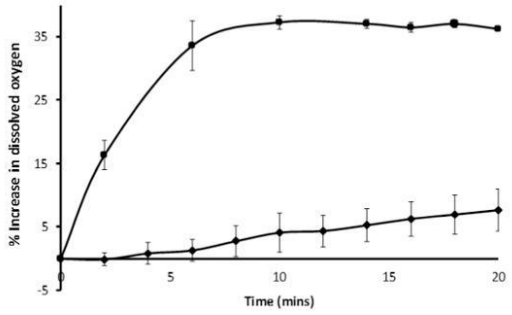

Fig. 2. Plot of % increase in dissolved oxygen against time for a solutions of de-oxygenated PBS with (squares) and without (diamonds) addition of CaO_2 NPs.

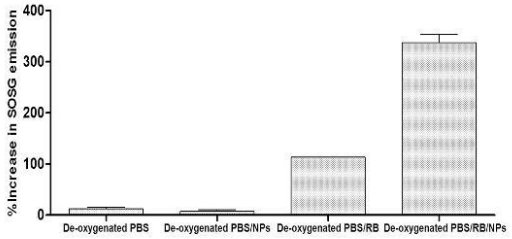

Fig. 3. Plot of % increase in SOSG fluorescence at 510 nm for solutions containing (i) degassed PBS (ii) deoxygenated PBS and CaO_2 NPs (iii) deoxygenated PBS and Rose Bengal (RB) and (iv) deoxygenated PBS, Rose Bengal and CaO_2 NPs. Groups (ii)–(iv) also received light treatment.

$$2CaO_2 + 4H_2O \rightarrow 2Ca(OH)_2 + 2H_2O_2 \rightarrow 2Ca(OH)_2 + 2H_2O + O_2 \quad (1)$$

Using this approach, the amount of active CaO_2 present in the NP

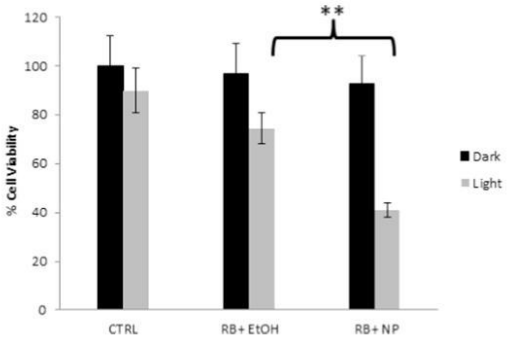

Fig. 4. Plot of cell viability for BxPC-3 cells, cultured under hypoxic conditions with (i) no treatment (CTRL dark bar) or after treatment with (ii) light only (CTRL light bar) (iii) RB only in an EtOH vehicle (RB + EtOH black bar) (iv) RB in an EtOH vehicle + light (RB + EtOH light bar) (v) RB + CaO_2 NP in an EtOH vehicle (RB + NP dark bar) (vi) RB + CaO_2 NP + light in an EtOH vehicle (RB + NP dark bar).

powder was determined as 44.9 ± 2.3% with the remaining mass due to excipients such as PEG.

To determine the ability of the uncoated CaO_2 NPs to generate molecular oxygen upon contact with water and improve oxygen levels in the immediate environment, a simulated hypoxic environment was generated by deoxygenating a solution of PBS (pH = 7.4 ± 0.1). A fixed amount of the CaO_2 NPs was added to the solution and the amount of dissolved oxygen present in the solution determined as a function of time. The results are shown in Fig. 2 and reveal a rapid increase in dissolved oxygen level (37.25%) 10 min after NP addition with no further increase observed over the next 10 min suggesting all the CaO_2 NPs were used. In contrast, a degassed PBS solution that was exposed to the open atmosphere increased by only 4.10% over the same time period. These results demonstrate that the CaO_2 NPs rapidly decompose when they come into contact with aqueous medium

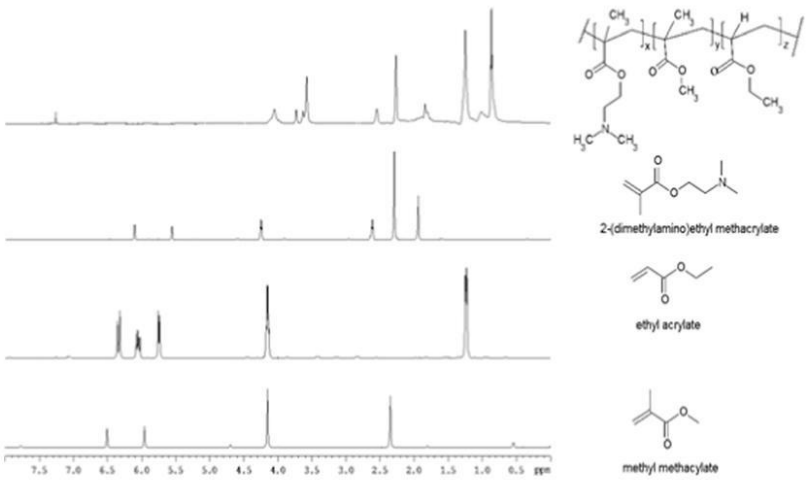

Fig. 5. Stacked ^{1}HNMR spectra of (i) methyl methacrylate (ii) ethyl acrylate (iii) 2-(dimethylamino)ethyl methacrylate and (iv) pH responsive polymer **1**.

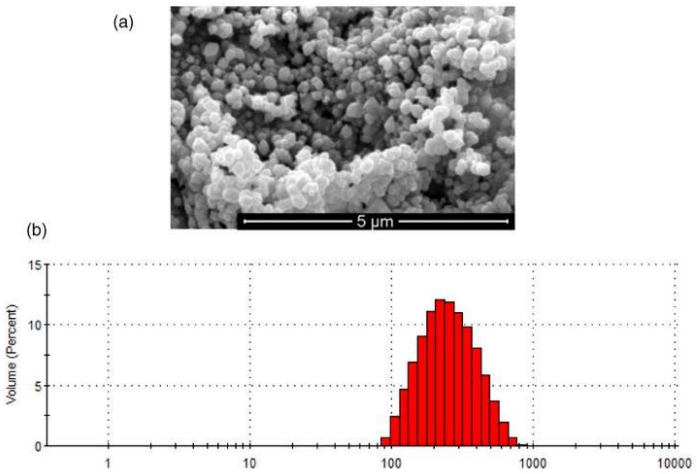

Fig. 6. (a) SEM image and (ii) DLS plot of **1**- CaO_2 NPs.

generating a significant enhancement in the oxygen levels their immediate environment.

It is well established that providing oxygen to an excited sensitiser during PDT can enhance the amount of ROS generated, particularly under hypoxic conditions [16]. To identify if the improved dissolved oxygen levels generated by the CaO_2 NPs would also translate to an increase in singlet oxygen quantum yield, the singlet oxygen probe sensor green (SOSG) was utilised. SOSG is inherently non-fluorescent but reacts with singlet oxygen to generate a fluorescent product with the fluorescence intensity being proportional to the amount of singlet oxygen generated. A de-oxygenated PBS solution (2:98; EtOH:H_2O) containing SOSG (2.5 µM) and the sensitiser Rose Bengal (5 µM) was prepared and an ethanol solution containing CaO_2 NPs (35.6 µM) added. Immediately, the solution was then irradiated with white light for 5 min at which point the fluorescence intensity at 530 nm was measured. Control experiments in the absence of the CaO_2 NPs (*i.e.* RB, SOSG and light) and CaO_2 NPs only (*i.e.* CaO_2 NPs, SOSG, and light) were also conducted for comparative purposes. The results are shown in Fig. 3 and reveal a significant increase (324.8%, $p < 0.001$) in the amount of SOSG fluorescence observed for the solution containing CaO_2 NPs, RB and treated with light compared to the control experiments, indicating the ability of the NPs to provide oxygen during the photodynamic event and enhance ROS generation in this simulated hypoxic environment.

Having determined the ability of the CaO_2 NPs to improve the light induced ROS generation of Rose Bengal in a simulated hypoxic environment, the next step was to determine if this improved ROS generation would also result in increased Rose Bengal mediated PDT induced toxicity using human BxPC-3 pancreatic cancer cells as a target. The cells were cultured in an anaerobic cabinet (O_2/CO_2/N_2, 0.1: 5: 94.9 v/v/v) for 3 h to generate a hypoxic environment and then treated with RB (1 µM) and incubated for a further 3 h under anaerobic conditions. This concentration of RB was identified from previous experiments to have a sub-lethal PDT effect in BxPC-3 cells cultured under

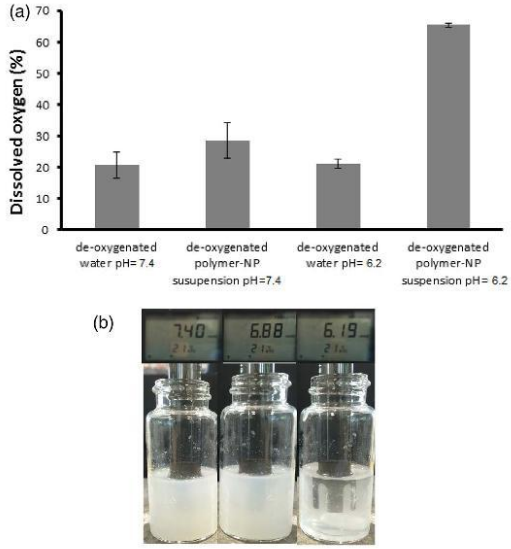

Fig. 7. (a) Plot of % dissolved oxygen for solutions of de-oxygenated water at pH 6.2 and pH 7.4 in the absence and presence of 1-CaO_2 NPs. (b) Photographs showing an aqueous suspension of the polymer coated NPs at pH 7.44, 6.88 and 6.19.

hypoxic conditions and would therefore identify any beneficial effect provided by the NPs [17]. The cells were then incubated with an ethanol: PBS (50:50) suspension of the NPs (100 μL, 50 μM) for 5 min before being subjected to light treatment for 30 s. The NP suspension was then removed, the cells washed with fresh PBS and incubated in fresh medium under normoxic conditions for a further 21 h before cell viability was determined using a MTT assay. The use of a 25% v/v ethanolic NP suspension in these experiments was not ideal but care was taken to ensure that contact time with the cells was kept to a minimum. We also conducted vehicle only, RB only, light only and NP only controls for comparative purposes. The results are shown in Fig. 4 and reveal a significant ($p < 0.01$) reduction in viability for those cells treated with PDT in the presence of CaO_2 NPs (57.9%) compared to PDT treatment alone (25.6%). In addition, there was no observable toxicity exhibited by the nanoparticles themselves at the concentration used in this experiment. These results suggest a synergistic effect between PDT and the CaO_2 NPs in this cell line under these experimental conditions and that treatment of hypoxic BxPC3 with CaO_2 NPs prior to PDT treatment can enhance oxygen levels improving the PDT mediated efficacy.

If CaO_2 NPs are to be used *in vivo* it is imperative they remain stable in circulation until taken up by tumour tissue so that inadvertent systemic activation is avoided. In theory, it should be possible to coat the NPs with a polymer that has low aqueous solubility at physiological pH (*i.e.* 7.4) but possesses increased solubility in environments where the pH is mildly acidic, as is the case in tumour extracellular fluid (pH = ~6.2). We prepared terpolymer **1**, similar in structure to Eudragit E, by the free radical *co*-polymerisation of 2-(dimethylamino) ethyl methacrylate, methylmethacyrlate and ethylmethacrylate in a 2:1:1 ratio. Eudragit E has been shown to suppress drug release at pH 7.4 when used as a tablet coating but rapidly dissolves in acidic medium to release the active drug [18]. Like Eudragit E, **1** contains a

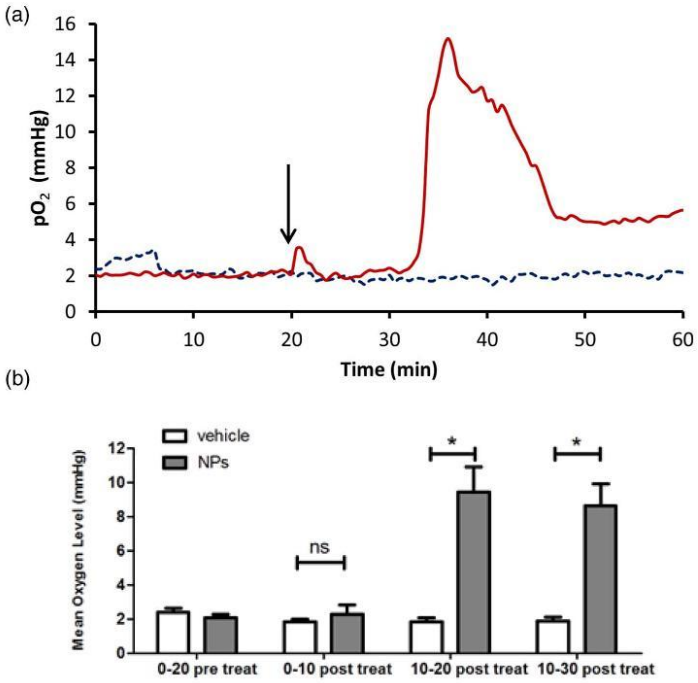

Fig. 8. (a) Plot of average tumour pO_2 in mice bearing ectopic MIA PaCa-2 pancreatic tumours recorded for 20 min before and 40 min following an IV injection of 1 CaO_2 NPs in a PBS (pH 7.4 ± 0.1) vehicle (red line) or vehicle only (blue dashed line). Arrow indicates when the injection occurred. (b) Plot showing the mean tumour pO_2 for various time intervals before and following IV administration of polymer coated CaO_2 NPs or vehicle only, obtained from integration of the plot shown in (a)., $^*p \leq 0.05$. (For interpretation of the references to colour in this figure legend, the reader is referred to the web version of this article.)

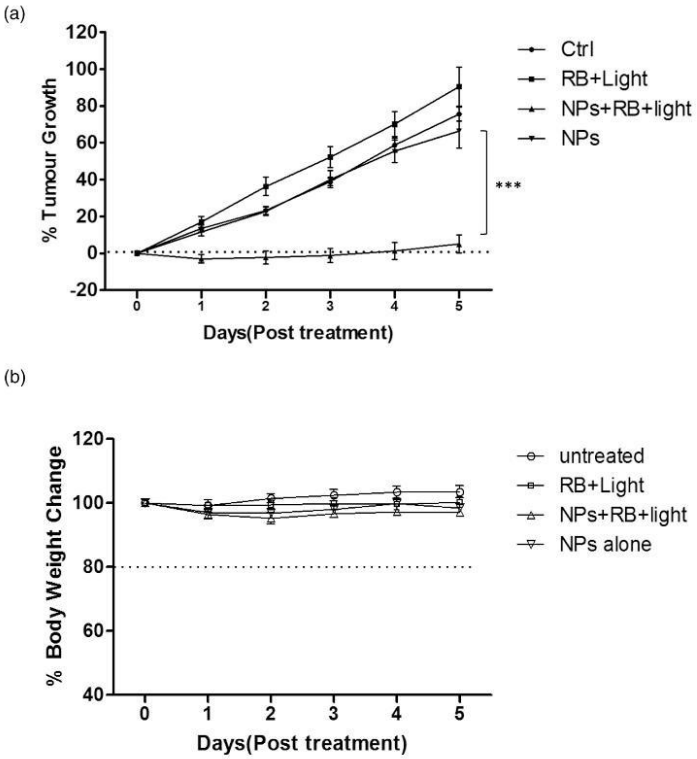

Fig. 9. (a) Plot of % change in tumour volume against time for SCID mice bearing human xenograft MIA PaCa 2 pancreatic tumours treated with (i) no treatment (squares) (ii) PDT only (circles) (iii) **1**-CaO_2 NPs only (diamonds) and (iv) **1**-CaO_2 NPs and PDT (triangles). (b) Plot of average body weight for each group of mice over the time course of the experiment. $^{***}p \leq 0.01$.

tertiary amine side chain making it possess low aqueous solubility as the free base but become soluble once ionised [19]. The successful preparation of **1** was confirmed by ^{1}H NMR spectroscopy with the stacked spectra of each monomer and **1** shown in Fig. 5. The olefinic protons present in the spectra of the monomers between 5.5 and 6.5 ppm were not present in **1** indicating they had been successfully polymerised to form the backbone of **1**. In addition, the peaks were much broader in the spectrum of **1** than in the monomers which is characteristic of protons in or near the backbone of polymers due to an ineffective averaging of their chemical shift anisotropies [20].

1 was then used to coat the CaO_2 NPs using a modified oil-in-water emulsion technique. A SEM image of the resulting **1**-CaO_2 NPs is shown in Fig. 6a and again reveals spherical particles with an average diameter of 248 ± 17 nm which was similar to the hydrodynamic diameter (278 ± 71 nm) determined by DLS.

The ability of the **1**-CaO_2 NPs to generate oxygen as a function of solution pH was determined by monitoring the increase in dissolved oxygen. Degassed aqueous solutions containing **1**-CaO_2 NPs (1 mg/mL) were pH adjusted to either pH 7.4 or pH 6.2 and the change in dissolved oxygen measured at each pH 5 min later. The results are shown in Fig. 7 and reveal a 45% increase in dissolved oxygen at pH 6.2 compared to only 7% increase at pH 7.4. This increase in dissolved oxygen results from dissolution of the polymer coat at lower pH that exposes the CaO_2 core to the aqueous environment. Indeed, when an aqueous suspension containing **1**-CaO_2 NPs was pH adjusted from pH 7.4 to pH 6.2, the visual appearance changed from a milky suspension to a more transparent colloidal suspension. These results suggest that the **1**-CaO_2 NPs should remain stable in the systemic circulation at pH = 7.4 but become activated to release O_2 when in the more acidic tumour microenvironment.

To determine the ability of the **1**-CaO_2 NPs to enhance tumour oxygenation in an *in vivo* model, ectopic human xenograft MIA PaCa-2 tumours were established in SCID mice. The MIA-PaCa-2 model is known to form hypoxic tumours and has previously been used in therapeutic efficacy experiments involving hypoxia activated prodrugs [21]. Unlike the BxPC-3 cell line, MIA PaCa-2 cells also express the KRAS mutation making it a more representative model of the disease *in vivo*. Once the tumours reached an average volume of 254 ± 17 mm^3, the mice were separated into two groups (n = 3). The treatment group received a tail vein injection of the **1**-CaO_2 NP suspension in a PBS buffer vehicle (pH 7.4 ± 0.1), with the control group receiving the same volume of vehicle only. Tumour pO_2 readings were recorded using an Oxylite oxygen electrode sensor for 20 min before and 40 min after injection.

The results are shown in Fig. 8 and reveal no significant change in the pO_2 reading in the 20 min period before injection for either group with a mean pO_2 reading of ~2.0 mm Hg. However, approximately 10 min after injection, tumour pO_2 levels in the **1**-CaO_2 NP group increased dramatically reaching a peak of 16 mm Hg before levelling off at ~6 mm Hg 30 min after injection. In contrast, mice treated with vehicle alone showed no noticeable change in tumour pO_2 over the time course of the experiment.

To put the above results in context, previous studies have indicated that the response to radiotherapy treatment is highly dependent upon tumour oxygenation with an increase from 2.5 mm Hg to 6 mm Hg significantly affecting loco-regional tumour control in advanced

squamous cell head and neck carcinoma [22]. While similar data are not available for PDT, the technique is known to be negatively impacted by hypoxia and the increase in tumour pO_2 levels provided by the **1**-CaO_2 NPs would be expected to have a beneficial effect on PDT mediated efficacy *in vivo* [23–26]. To confirm that this was the case, we treated the same MIA-PaCa-2 tumour model, described in the pO_2 study above, with PDT using a Rose Bengal sensitiser in the presence and absence of the **1**-CaO_2 NPs. Untreated animals and those treated with **1**-CaO_2 NPs alone were used as controls. The NPs were again delivered by IV injection while Rose Bengal was administered by intratumoral injection, to ensure a consistent dose was administered to all of the tumours. Twenty minutes following IV administration of the **1**-CaO_2 NPs, tumours were exposed to light treatment for 3 min. Tumour volume was monitored for 5 days following treatment and the results are shown in Fig. 9a. The results demonstrate that there was no significant difference in tumour volume for mice treated with PDT alone or with **1**-CaO_2 NPs alone 5 days after treatment, relative to the untreated control animals. In contrast, a significant reduction ($p \leq 0.001$) of 70.5% was observed for animals treated with the **1**-CaO_2 NPs and PDT over the same time period. In addition, there was no significant change in body weight in animals treated with the **1**-CaO_2 NPs alone or in combination with PDT suggesting the treatment was well tolerated (Fig. 9b). These results highlight the benefit of **1**-CaO_2 NPs in improving the PDT mediated treatment of hypoxic tumours such as pancreatic adenocarcinoma and may provide benefit in other treatments that are also compromised by hypoxia, most notably radiotherapy.

In summary, we have developed a CaO_2 containing nanoparticle formulation comprising a pH-responsive coating that enables the generation of molecular oxygen in response to changes in environmental pH. Specifically, the polymer coat maintains its integrity when in aqueous solution at pH 7.4, but rapidly dissolves when the pH is lowered to pH 6.2, exposing the CaO_2 particles to water resulting in oxygen generation. The ability of the coated particles to elevate tumour oxygen levels was also demonstrated in mice bearing human xenograft pancreatic tumours where significant elevations in tumour pO_2 were observed 10 mins following IV administration. This increase in tumour pO_2 was also shown to have a dramatic effect on the efficacy of PDT treatment with significant reductions in tumour growth observed in animals that received the coated particles prior to PDT treatment. The utility of this approach is not restricted to PDT but will surely also provide benefit in other treatments that are also negatively impacted by hypoxia.

Acknowledgements

JFC thanks Norbrook Laboratories Ltd for an endowed chair.

References

[1] S. Yano, S. Hirohara, M. Obata, Y. Hagiya, S. Ogura, A. Ikeda, H. Kataoka, M. Tanaka, T. Joh, Current states and future views in photodynamic therapy, J. Photochem. Photobiol. C 12 (2011) 46–67.
[2] S. Cui, D. Yin, Y. Chen, Y. Di, H. Chen, Y. Ma, S. Achilefu, Y. Gu, In vivo targeted deep-tissue photodynamic therapy based on near-infrared light triggered upconversion nanoconstruct, ACS Nano 7 (2012) 676–688.
[3] C. Taratula, M. Schumann, M. Naleway, A. Pang, K. Chon, O. Taratula, A multifunctional theranostic platform based on phthalocyanine-loaded dendrimer for image-guided drug delivery and photodynamic therapy, Mol. Pharm. 10 (2013) 3946–3958.
[4] A.C. Koong, V.K. Mehta, Q.T. Le, G.A. Fisher, D.J. Terris, J.M. Brown, A.J. Bastidas, M. Vierra, Pancreatic tumors show high levels of hypoxia, international journal of radiation oncology, Biol. Phys. 48 (2000) 919–922.
[5] M. Ilie, N. Mazure, V. Hofman, R. Ammadi, C. Ortholan, C. Bonnetaud, K. Havet, N. Venissac, B. Mograbi, J. Mouroux, High levels of carbonic anhydrase IX in tumour tissue and plasma are biomarkers of poor prognostic in patients with non-small cell lung cancer, Br. J. Cancer 102 (2010) 1627–1635.
[6] M. Hockel, P. Vaupel, Tumor hypoxia: definitions and current clinical, biologic, and molecular aspects, J. Natl. Cancer Inst. 93 (2001) 266–276.
[7] M. Yoshimura, S. Itasaka, H. Harada, M. Hiraoka, Microenvironment and radiation therapy, Biomed. Res. Int. 2013 (2012).
[8] S. Rockwell, I.T. Dobrucki, E.Y. Kim, S.T. Marrison, V.T. Vu, Hypoxia and radiation therapy: past history, ongoing research, and future promise, Curr. Mol. Med. 9 (2009) 442–458.
[9] C. McEwan, S. Kamila, J. Owen, H. Nesbitt, B. Callan, M. Borden, N. Nomikou, R.A. Hamoudi, M.A. Taylor, E. Stride, Combined sonodynamic and antimetabolite therapy for the improved treatment of pancreatic cancer using oxygen loaded microbubbles as a delivery vehicle, Biomaterials 80 (2016) 20–32.
[10] J.S. Fang, R.D. Gillies, R.A. Gatenby, Adaptation to hypoxia and acidosis in carcinogenesis and tumor progression, Semin. Cancer Biol. 18 (2008) 330–337.
[11] M. Oishi, S. Sumitani, Y. Nagasaki, On − off regulation of 19F magnetic resonance signals based on pH-sensitive PEGylated nanogels for potential tumor-specific smart 19F MRI probes, Bioconjug. Chem. 18 (2007) 1379–1382.
[12] J. Khodaveisi, H. Banejad, A. Afkhami, E. Olyaie, S. Lashgari, R. Dashti, Synthesis of calcium peroxide nanoparticles as an innovative reagent for in situ chemical oxidation, J. Hazard. Mater. 192 (2011) 1437–1440.
[13] K. Komagoe, T. Katsu, Porphyrin-induced photogeneration of hydrogen peroxide determined using the luminol chemiluminescence method in aqueous solution: a structure-activity relationship study related to the aggregation of porphyrin, Anal. Sci. 22 (2006) 255–258.
[14] S.H. Choi, T.G. Park, G-CSF loaded biodegradable PLGA nanoparticles prepared by a single oil-in-water emulsion method, Int. J. Pharm. 311 (2006) 223–228.
[15] K. Faulkner, I. Fridovich, Luminol and lucigenin as detectors for O2ś −, Free Radic. Biol. Med. 15 (1993) 447–451.
[16] J. Fuchs, J. Thiele, The role of oxygen in cutaneous photodynamic therapy, Free Radic. Biol. Med. 24 (1998) 835–847.
[17] Determined from a dose-response experiement conducted using BxPC-3 cells cultured under the conditions described in section 2.5.
[18] R. Sheshala, N. Khan, Y. Darwis, Formulation and optimization of orally disintegrating tablets of sumatriptan succinate, Chem. Pharm. Bull. 59 (2011) 920–928.
[19] M. Doreth, K. Löbmann, H. Grohganz, R. Holm, H.L. De Diego, T. Rades, P.A. Priemel, Glass solution formation in water-in situ amorphization of naproxen and ibuprofen with Eudragit® E PO, J. Drug Deliv. Sci. Technol. 34 (2016) 32–40.
[20] N. Singh, N. Kaur, J. Dunn, R. Behan, R.C. Mulrooney, J.F. Callan, A polymeric sensor for the chromogenic and luminescent detection of anions, Eur. Polym. J. 45 (2009) 272–277.
[21] J.W. Wojtkowiak, H.C. Cornnell, S. Matsumoto, K. Saito, Y. Takakusagi, P. Dutta, M. Kim, X. Zhang, R. Leos, K.M. Bailey, Pyruvate sensitizes pancreatic tumors to hypoxia-activated prodrug TH-302, Cancer Metab. 3 (2015) 2.
[22] M. Nordsmark, M. Overgaard, J. Overgaard, Pretreatment oxygenation predicts radiation response in advanced squamous cell carcinoma of the head and neck, Radiother. Oncol. 41 (1996) 31–39.
[23] Y. Cheng, H. Cheng, C. Jiang, X. Qiu, K. Wang, W. Huan, A. Yuan, J. Wu, Y. Hu, Perfluorocarbon nanoparticles enhance reactive oxygen levels and tumour growth inhibition in photodynamic therapy, Nat. Commun. 6 (2015) 8785.
[24] W. Zhu, Z. Dong, T. Fu, J. Liu, Q. Chen, Y. Li, R. Zhu, L. Xu, Z. Liu, Modulation of hypoxia in solid tumor microenvironment with MnO2 nanoparticles to enhance photodynamic therapy, Adv. Funct. Mater. 26 (2016) 5490–5498.
[25] S. Gao, G. Wang, Z. Qin, X. Wang, G. Zhao, Q. Ma, L. Zhu, Oxygen-generating hybrid nanoparticles to enhance fluorescent/photoacoustic/ultrasound imaging guided tumor photodynamic therapy, Biomaterials 112 (2017) 324–335.
[26] X. Song, L. Feng, C. Liang, K. Yang, Z. Liu, Ultrasound triggered tumor oxygenation with oxygen-shuttle nanoperfluorocarbon to overcome hypoxia-associated resistance in cancer therapies, Nano Lett. 16 (2016) 6145–6153.